

Nicolaus Copernicus Astronomical Center
Polish Academy of Sciences

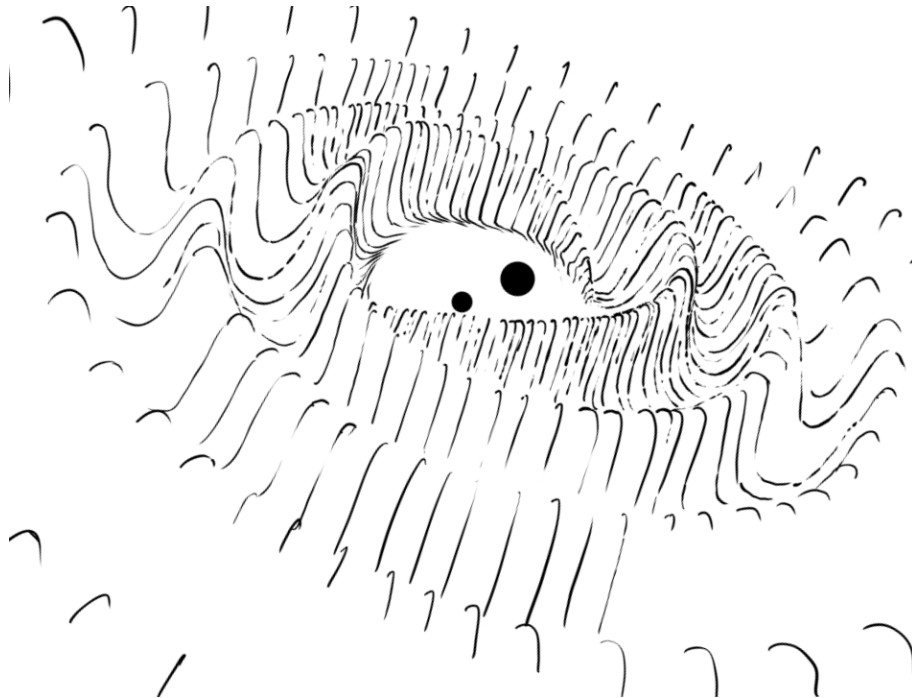


Doctoral dissertation:

The origin of binary black hole mergers
Isolated binary evolution scenarios with and without a common
envelope phase

Supervisor:
Prof. dr hab. Tomasz Bulik

Ph.D. candidate:
Ms. Aleksandra Maria Olejak



1

May 2023

I hereby declare that the content of this thesis was prepared and published between October 2019 and September 2023 during my studies at GeoPlanet Doctoral School at Nicolaus Copernicus Astronomical Center of the Polish Academy of Sciences. Any contributions and credits of others involved are indicated by references, co-authors' statements, figure captions, and acknowledgments.

Abstract

The origin of binary black hole mergers detected by gravitational wave detectors remains unknown and puzzles the astrophysical community. The literature suggests several possibly contributing formation channels. The most popular are the isolated evolution of massive binary star systems in galactic fields and dynamical pairing in dense clusters of stars.

In my thesis, I study the properties of gravitational wave sources formed via the isolated binary evolution channel. The two main scientific projects of my doctoral research concerned the influence of the criteria for unstable mass transfer (i.e., common envelope) development in massive stellar systems and the core-collapse supernovae physics on the population of compact object mergers. Especially, my interest focuses on evolutionary scenarios leading to the formation of binary black hole mergers with parameters similar to the detected population, including unusual events involving systems with unequal mass components or high inspiral effective spin parameters.

Both stability of mass transfer and core-collapse supernovae physics are poorly understood, with theory not well constrained by observations. In my doctoral research, I implement advancements in the studies of those highly uncertain astrophysical processes and examine the effect of various models on the synthetic population of gravitational wave sources. Different assumptions for the physics of the core-collapse supernova as well as the choice of criteria for common envelope development change the properties of compact object mergers, affecting the event rates, distribution of masses, systems' mass ratios, and spins. The choice of core-collapse supernova engine also affects the depth of the lower mass gap in the mass distribution between massive neutron stars and low-mass black holes. Restrictive criteria for common envelope development change the dominant formation scenario for binary black hole mergers. I present evolutionary scenarios with and without a common envelope phase, which reproduce a fraction of high-spinning binary black hole mergers consistent with gravitational wave detections.

Streszczenie

Pochodzenie populacji układów podwójnych czarnych dziur wykrytych dzięki emisji fal grawitacyjnych pozostaje niewiadomą i jest przedmiotem badań zyskującym popularność wśród astrofizyków. Literatura naukowa proponuje kilka scenariuszy mogących odpowiadać za tworzenie się zaobserwowanych układów obiektów zwartych. Najbardziej popularne scenariusze to odizolowana ewolucja masywnych układów podwójnych gwiazd w polach galaktyk oraz dynamiczne tworzenie par w gęstych gromadach gwiazd.

W mojej pracy doktorskiej zajmuję się badaniem populacji źródeł fal grawitacyjnych mogących tworzyć się w wyniku odizolowanej ewolucji układów podwójnych. Dwa główne projekty dotyczyły badania wpływu kryterium na stabilność transferu masy w masywnych układach gwiazdowych oraz fizyki przebiegu supernowej na właściwości tworzącej się populacji ciasnych układów obiektów zwartych. Szczególną uwagę poświęcam scenariuszom ewolucyjnym prowadzącym do powstania układów o parametrach zbliżonej do populacji zaobserwowanej przez detektory LIGO i Virgo, w tym nietypowych zdarzeń z udziałem układów podwójnych czarnych dziur o bardzo odmiennych masach, czy niezerowym efektywnym spinie.

Zarówno stabilność transferu masy, jak i mechanizm supernowej są słabo rozumianymi procesami astrofizycznymi, a istniejące modele teoretyczne nie są dobrze ograniczone przez obserwacje. Różne założenia dotyczące fizyki przebiegu supernowej, jak i wybór kryterium na stabilność transferu masy mają konsekwencje na tworzącą się populację ciasnych układów obiektów zwartych, wpływając na ich częstość łączenia, rozkłady masy, stosunku mas w układzie oraz spinów. Wybór silnika supernowej wpływa również na głębokość przerwy w rozkładzie masy między masywnymi gwiazdami neutronowymi, a mało masywnymi czarnymi dziurami. Restrykcyjne kryteria na rozwój wspólnej otoczki zmieniają natomiast dominujący scenariusz powstawania układów podwójnych czarnych dziur. W swojej pracy doktorskiej proponuję scenariusze ewolucyjne ze wspólną otoczką oraz stabilnym transferem masy, które odtwarzają frakcję układów z szybko rotującymi czarnymi dziurami, zgodną z populacją systemów wykrytą przez detektory fal grawitacyjnych.

List of publications

The link to my ADS public library:

<https://ui.adsabs.harvard.edu/public-libraries/U0LMup96RQe2hPXDjU3Mew>. To date, I have co-authored 16 peer-reviewed articles, 5 of which I am the principal author. Citation counts according to The SAO/NASA Astrophysics Data System. The total number of citations of co-authored articles: **707**. The total number of citations of my articles as the first-author: **183**.

Peer-reviewed

- [1] **Olejak A.**, Fryer C. L., Belczynski K., Baibhav V., 2022, MNRAS, 516, 2252. *The role of supernova convection for the lower mass gap in the isolated binary formation of gravitational wave sources*, doi:10.1093/mnras/stac2359, citations: 15.
- [2] **Olejak A.**, Belczynski K., 2021, ApJ Letters, 921, L2. *The Implications of High Black Hole Spins for the Origin of Binary Black Hole Mergers*, doi:10.3847/2041-8213/ac2f48, citations: 35.
- [3] **Olejak A.**, Belczynski K., Ivanova N., 2021, A&A, 651, A100. *Impact of common envelope development criteria on the formation of LIGO/Virgo sources*, doi:10.1051/0004-6361/202140520, citations: 44.
- [4] **Olejak A.**, Fishbach M., Belczynski K., Holz D. E., Lasota J.-P., Miller M. C., Bulik T., 2020, ApJ Letters, 901, L39. *The Origin of Inequality: Isolated Formation of a 30+10 Msun Binary Black Hole Merger*, doi:10.3847/2041-8213/abb5b5, citations: 47.
- [5] **Olejak A.**, Belczynski K., Bulik T., Sobolewska M., 2020, A&A, 638, A94. *Synthetic catalog of black holes in the Milky Way*, doi:10.1051/0004-6361/201936557, citations: 42.
- [6] Fryer C. L., **Olejak A.**, Belczynski K., 2022, ApJ, 931, 94. *The Effect of Supernova Convection On Neutron Star and Black Hole Masses*, doi:10.3847/1538-4357/ac6ac9, citations: 17.
- [7] Belczynski K., Doctor Z., Zevin M., **Olejak A.**, Banerje S., Chattopadhyay D., 2022, ApJ, 935, 126. *Black Hole-Black Hole Total Merger Mass and the Origin of LIGO/Virgo Sources*, doi:10.3847/1538-4357/ac8167, citations: 8.
- [8] Belczynski K., Romagnolo A., **Olejak A.**, Klencki J., Chattopadhyay D., Stevenson S., Coleman Miller M., et al., 2022, ApJ, 925, 69. *The Uncertain Future of Massive Binaries Obscures the Origin of LIGO/Virgo Sources*, doi:10.3847/1538-4357/ac375a, citations: 45.
- [9] Belczynski K., Klencki J., Fields C. E., **Olejak A.**, Berti E., Meynet G., Fryer C. L., et al., 2020, A&A, 636, A104. *Evolutionary roads leading to low effective spins, high black hole masses, and O1/O2 rates for LIGO/Virgo binary black holes*, doi:10.1051/0004-6361/201936528, citations: 310.
- [10] Romagnolo A., **Olejak A.**, Hypki A., Wiktorowicz G., Belczynski K., 2022, A&A, 667, A55. *Testing the presence of a dormant black hole inside HR 6819*, doi:10.1051/0004-6361/202141992, citations: 3

- [11] Leveque A., Giersz M., Askar A., Arca-Sedda M., **Olejak A.**, 2023, MNRAS, 520, 2593. *MOCCA-Survey Database: extra galactic globular clusters - III. The population of black holes in Milky Way and Andromeda-like galaxies*, doi:10.1093/mnras/stad240, citations: 2
- [12] Wang Y., Liao S., Giacobbo N., **Olejak A.**, Gao J., Liu J., 2022, A&A, 665, A111. *Astrometric mass measurement of compact companions in binary systems with Gaia*, doi:10.1051/0004-6361/202243684, citations: 1
- [13] Czerny B., **Olejak A.**, Rałowski M., Kozłowski S., Martinez Aldama M. L., Zajacek M., Pych W., et al., 2019, ApJ, 880, 46. *Time Delay Measurement of Mg II Line in CTS C30.10 with SALT*, doi:10.3847/1538-4357, citations: 41.
- [14] Prince R., Zajaček M., Czerny B., Trzcionkowski P., Bronikowski M., Sobrino Figaredo C., Panda S., et al., 2022, A&A, 667, A42. *Wavelength-resolved reverberation mapping of quasar CTS C30.10: Dissecting Mg II and Fe II emission regions*, doi:10.1051/0004-6361/202243194, citations: 7
- [15] Zajacek M., Czerny B., Martinez-Aldama M. L., Ralowski M., **Olejak A.**, Przyluski R., Panda S., et al., 2021, ApJ, 912, 10. *Time Delay of Mg II Emission Response for the Luminous Quasar HE 0435-4312: toward Application of the High-accretor Radius-Luminosity Relation in Cosmology* , doi:10.3847/1538-4357/abe9b2, citations: 30.
- [16] Zajacek M., Czerny B., Martinez-Aldama M. L., Ralowski M., **Olejak A.**, Panda S., Hryniewicz K., et al., 2020, ApJ, 896, 146. *Time-delay Measurement of Mg II Broad-line Response for the Highly Accreting Quasar HE 0413-4031: Implications for the Mg II-based Radius-Luminosity Relation* , doi:10.3847/1538-4357/ab94ae, citations: 29.

Other

- [1] Banerjee S., **Olejak A.**, Belczynski K., 2023, *Symmetry breaking in merging binary black holes from young massive clusters and isolated binaries*, arXiv, arXiv:2302.10851, citations: 2.
- [2] Belczynski K., Bulik T., **Olejak A.**, Chruslinska M., Singh N., Pol N., Zdunik L., et al., 2018, *Binary neutron star formation and the origin of GW170817* , arXiv, arXiv:1812.10065, citations: 29.

Contents

1	Introduction to GW astrophysics	3
1.1	Mass distribution of GW sources	4
1.1.1	Lower mass gap	5
1.1.2	Upper mass gap	6
1.1.3	Stellar winds	7
1.2	Spin distribution of GW sources	8
1.2.1	Spin measurements of detected BH-BH mergers	8
1.2.2	Astrophysical implications of BH spins	9
1.3	Merger rates evolution with redshift	11
1.4	Formation channels	12
1.4.1	Isolated binary systems	12
1.4.2	Dynamical formation in clusters	14
1.4.3	Isolated multiple systems	14
1.4.4	Active galactic nuclei	15
1.4.5	Population III stars	15
1.4.6	Primordial black holes	16
2	Method	17
2.1	Star formation history	17
2.2	Population synthesis	18
3	GW190412 and unequal mass binary black hole mergers	20
4	Common envelope vs stable mass transfer scenario	31
5	The implications of black hole spins	50
6	The role of supernova convection	58
7	Summary	80
7.1	Final conclusions	80
7.2	Future of gravitational wave astrophysics	80

1 Introduction to gravitational wave astrophysics

Gravitational wave (GW) astrophysics is young but a rapidly developing field. The first, ground-breaking detection of GW signal, GW150914 [1] started a new era in astrophysics, allowing for entirely new kinds of Universe studies. In my thesis, by GW astrophysics, I mean only a part of this field related to currently detected GW sources: mergers of binary compact object systems and their origin. However, it is an expanding scientific discipline with great potential to study many more astrophysical problems.

Current and forthcoming detections of GW sources will provide us with fundamental new information on the stellar evolution and the formation of systems hosting neutron stars (NSs) and black holes (BHs). Double compact object merger rates might also be a good tracer of star formation history and tell us a lot about the early ages of the Universe. However, in order to take full advantage of the detections and provide constraints for uncertain astrophysical processes, one needs to combine the parameters of the GW system with the advancements in numerical simulations. A deep understanding of the physical processes that are responsible for the double compact object mergers formation is needed to make any astrophysical inference based on the data provided by GW detections. Moreover, simultaneous analysis of the populations of the known NS and BH systems observed in the electromagnetic spectrum may close several gaps in our understanding of evolution and the final fate of massive stars. This will also bring us closer to answering the question about the origin and formation channels of detected GW sources.

This chapter will be a brief summary of the properties of GW sources provided in the cumulative third Gravitational-Wave Transient Catalog (GWTC-3) [2] with their possible astrophysical implications. I will provide a short overview of some of the most important topics that are currently puzzling scientists in the field of GW astrophysics, with a focus on the studies on the origin of detected compact object mergers.

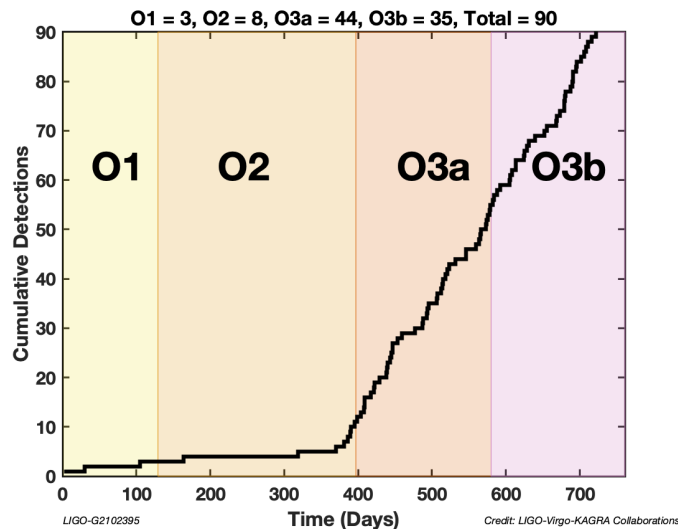


Fig. 1: The cumulative number of detections versus days in each observing run (O1, O2, O3a, O3b). Detections are classified as the candidates where the probability of astrophysical origin is greater than 0.5 for at least one analysis [2; 3]. Credit: The LIGO-Virgo-KAGRA (LVK) Collaboration, source: <https://dcc-lho.ligo.org>.

The public GW detection database after the first three observing runs: O1, O2, O3a and O3b [2–7] (See Fig. 1) contains around 90 detections of three event classes: mergers of binary black holes (BH-BH), binary neutron stars (NS-NS), and black hole-neutron star systems (BH-NS) [3]. Some events, e.g., GW190814, coalescence of a $23.2^{+1.0}_{-1.1} M_{\odot}$ BH and $2.59^{+0.08}_{-0.09} M_{\odot}$ compact

object [8], are however, not possible to classify as a mass of one component lies within the uncertain boundary between the maximum theoretical mass of a NS and the minimum mass of a BH. Due to their high masses, BH-BH mergers currently vastly dominate the catalog of GW detections.

Among the GW detections, there are several unexpected events challenging theoreticians, such as BH-BH merger with highly unequal mass components: $30.1^{+4.6}_{-5} M_{\odot} + 8.3^{+1.6}_{-0.9} M_{\odot}$. [9] or coalescence with one of the components within the lower mass gap range $\sim 2.5 - 5 M_{\odot}$ [8] (see more in Sec. 1.1.1) and the upper mass gap $m \geq 45 M_{\odot}$ [10] (see more in Sec. 1.1.2).

In my thesis, I will use the following notations related to GW detections consistent with works of LIGO-Virgo-KAGRA (unless expressly stated otherwise):

- m_1 is primary, the more massive of the merger components,
- m_2 is secondary, the less massive of the merger components,
- q is mass ratio of the merger components, defined as $\frac{m_1}{m_2}$.



Fig. 2: The popular graphic of so-called *Stellar Graveyard*, i.e., visualization of known compact object masses, black holes (blue and red), and neutron stars (yellow and orange) detected via gravitational waves (GWTC-3), and in the electromagnetic wave spectrum. Credit: LIGO-Virgo-KAGRA/Aaron Geller/Northwestern University.

1.1 Mass distribution of gravitational waves sources

As expected based on the observed initial mass distribution of stars [11], the intrinsic distribution of BH mass rapidly decreases as a function of mass [2], see Figure 3. However, mass distribution clearly includes several characteristic features, possibly of astrophysical origin. For example, LIGO-Virgo-KAGRA (LVK) collaboration finds some evidence for the lower mass gap based on a relative dearth of binaries with component masses between $3 M_{\odot}$ and $5 M_{\odot}$ [2], consistent with former Galactic observations [12–17]. LVK also reports two overdensities in the merger rate as a function of primary mass at $m_1 = 10^{+0.29}_{-0.59} M_{\odot}$ and $m_1 = 35^{+1.7}_{-2.9} M_{\odot}$ [2]. Similar substructures were already identified in the earlier analysis after O3a run [18] which may point towards the astrophysical origin of those features. Above the second peak, we observe a continuous, monotonically decreasing tail of more massive BHs.

Below, in Sections 1.1.1-1.1.3, I will briefly comment on the possible astrophysical mechanisms that could be responsible for the features observed in the mass distribution of GW sources.

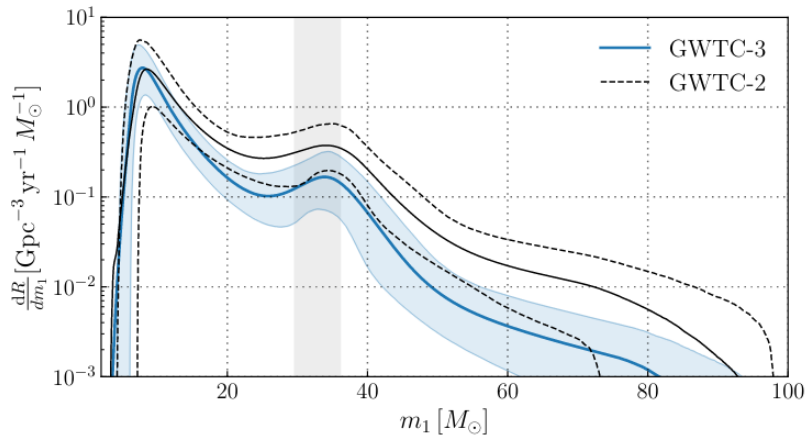


Fig. 3: The differential merger rate as a function of primary compact object mass, results of the fiducial model [2] with visible overdensities around $m_1 \approx 10 M_\odot$ and $m_1 \approx 35 M_\odot$. The solid blue line is the posterior population distribution with the 90% credible interval (shaded region), the result of GWTC-3 analysis [2]. The black solid and dashed lines are the results of GWTC-2 analysis [7]. Credit: [2].

1.1.1 Lower mass gap

The lower mass gap observed in the mass distribution of NSs and BHs has puzzled the astrophysical community for decades. The systematic dearth of $\sim 3 - 5 M_\odot$ compact objects among the observed population of X-ray binary systems [12–17] gave rise to the idea of a potential mechanism preventing the formation of objects in this mass regime. The latest population analyses of LVK collaboration [2; 3] seem to be consistent with former observations. LVK also reports on the rapid decrease in merger rates versus component mass between NS-like masses and BH-like mass, identifying relative suppression in rates of GW detections with component masses between $3 M_\odot$ and $5 M_\odot$ [2].

On the other hand, there are a few candidates for the compact objects with their masses possibly inside the gap, such as a low mass component of GW190814 merger [8]. The final products of, e.g., NS-NS mergers may naturally fill the lower mass gap range. That might indicate that even if the gap is real, it is not necessarily totally empty. There are ongoing discussions in the community about whether the lower mass gap has a physical origin, or it is only the effect of observational bias [19; 20].

The most natural mechanism, possibly responsible for limiting low-mass compact object formation, is core-collapse supernovae (SN). The physics behind core-collapse SN explosion is, however, so far poorly understood [21]. Especially, the final fate of progenitors with their initial masses in the range $20 - 40 M_\odot$, possible lower mass gap fillers, is highly uncertain and model dependent [22–25]. In particular, there are several SN models that fill the spectrum between reproducing a deep lower mass gap and a remnant mass distribution filled by massive NSs and low mass BHs [23–26].

Verifying the existence and characteristics of the lower mass gap may deliver a probe of core-collapse physics, ruling out incorrect SN models. However, the detection of compact objects within the lower mass gap might be also an indication of the second-generation merger and dynamical origin of the system. More information on the core-collapse SN physics, the lower mass gap, and implications for GW sources may be found in the article [26] constituting

Chapter 6 of the dissertation. The other suggested astrophysical process that could be partly responsible for the lower mass gap, but only in the case of GW detections, is the stable mass transfer BH-BH formation scenario [27].

1.1.2 Upper mass gap

Extreme physical conditions in the cores of very massive stars ($M_{\text{ZAMS}} \gtrsim 100M_{\odot}$), such as temperature reaching up to $\sim 5 \times 10^9$ K, are expected to allow for electron-positron pair production and lead to pulsational pair-instability SN (PPSN) or pair-instability SN (PSN) phenomena [28–32]. The production of electron-positron pairs reduces the radiation pressure due to the conversion of the energetic photons into the rest mass of the created pairs. In simple terms, the reduction in the radiation pressure supporting the gravity leads to a contraction of the core and therefore a temperature increase. That, on the other hand, causes the avalanche of electron–positron pairs production and acceleration of burning in runaway thermonuclear reactions in the outer core layers. Produced energy deposition can lead to a partial ejection of the outer layers of the core – PPSN, or even total disruption of the star in PSN, leaving no remnant behind. Explosions due to PPSN and PSN have been expected to prevent the formation of stellar origin BHs in the mass range $\sim 45M_{\odot} - 120M_{\odot}$ [28], the so-called upper mass gap. However, several recent studies indicate that the limit for PPSN/PSN might be easily shifted to the lower or upper mass regime, mainly due to a highly uncertain rate of $^{12}\text{C}(\alpha, \gamma)^{16}\text{O}$ reaction [32–34]. The dependence of the final outcome of the massive star evolution on the $^{12}\text{C}(\alpha, \gamma)^{16}\text{O}$ reaction rate and the mass of helium core is shown in the Figure 4 adopted from [33].

Former GW detections seemed to be consistent with the upper mass gap [4; 5] until the most massive GW190521 detection of $85_{-14}^{+21}M_{\odot} + 66_{-18}^{+17}M_{\odot}$ BH-BH merger [10] has been announced, causing consternation in the community. Both components’ masses were initially estimated within the upper mass gap range. However, few follow-up, independent analyses of the GW190521 event with different parameter inferences have argued that both BHs could have their masses as well outside this gap, with the primary above and the secondary below the limit [35; 36].

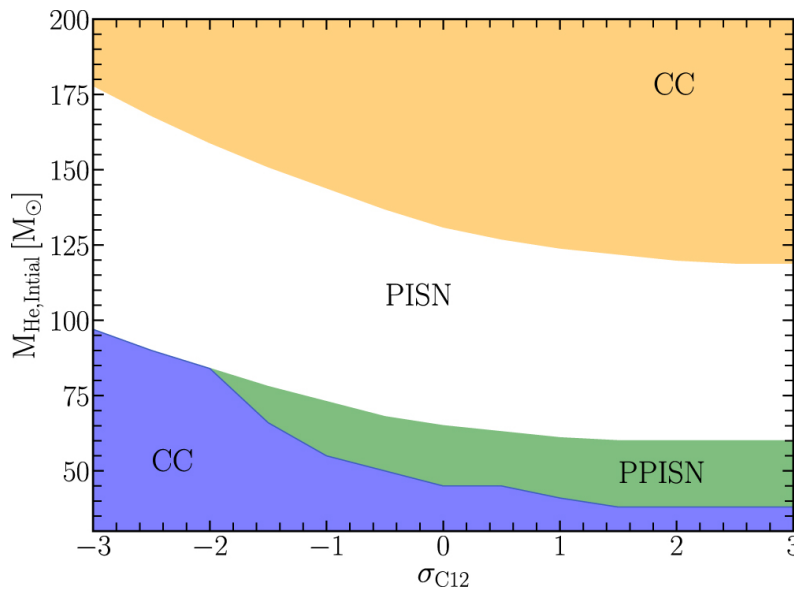


Fig. 4: The final outcome of a massive star evolution with a given helium core mass as a function of the adopted value of $^{12}\text{C}(\alpha, \gamma)^{16}\text{O}$ rate measured in standard deviation from the median [37]. Blue – core-collapse below the pair-instability supernovae mass gap; green - pulsational pair-instability supernovae; white – total disruption in a PSN; orange – black holes from core-collapse above the pair-instability mass gap. Credit: [33].

If PSN is a real phenomenon, the most natural explanation for GW190521 event could be its dynamical origin and formation in repeated BH-BH mergers [38; 39]. However, due to uncertain PSN limit related to unconstrained $^{12}\text{C}(\alpha, \gamma)^{16}\text{O}$ reaction rate, isolated binary evolution formation cannot be excluded for this event [40]

There are several unusually energetic SN observations that have been classified as possible candidates for PPSN and PSN events, e.g., SN 2007bi [41], SN 1000+0216 [42] and SN 2016iet [43]. Most recent LVK population study [2] find no evidence for or against the PSN-origin mass gap. However, if the future GW detections and analysis of the formation channels deliver robust evidence for the upper gap and its PSN origin (see sec. 1.1.3), it may be used to provide a constraint on $^{12}\text{C}(\alpha, \gamma)^{16}\text{O}$ reaction rate.

1.1.3 Stellar winds

The metallicity of the environment in which a star is born has important consequences on its formation, evolution, and final outcome [44–50]. Observation indicates that very massive stars, such as BH progenitors, with initial composition rich in metals lose most of their mass in stellar winds through their evolution [45; 47; 49]. For example, some recent stellar evolutionary models predict that the same progenitor star with its initial mass $M_{\text{ZAMS}} \approx 100M_{\odot}$ at the end of its evolution could retain around $55M_{\odot}$ for low metallicity $Z = 0.0002$ ($\sim 1\% Z_{\odot}$), around $40M_{\odot}$ for $Z = 0.002$ ($\sim 10\% Z_{\odot}$) and only around $15M_{\odot}$ for high, solar-like metallicity of $Z = 0.02$ [26; 48]. Therefore, the maximum possible mass of a stellar-origin BH is expected to be strongly dependent on the metallicity of the environment [48], see Figure 5. Observations of massive stellar-origin BHs in high metallicity environments, such as Cygnus X-1, its BH mass estimated at $M_{\text{BH}} = 21.2_{-2.2}^{2.2} M_{\odot}$ [51; 52], provide additional constraints for stellar winds efficiency.

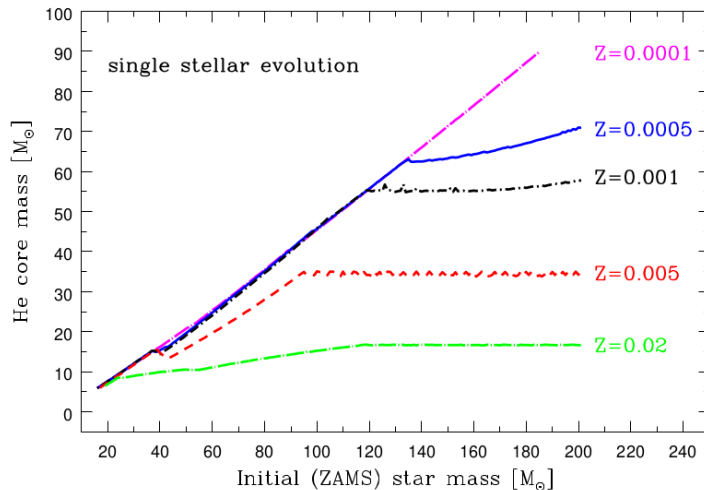


Fig. 5: The relation between the initial mass of the single stellar progenitor and the mass of the helium core at the late evolutionary stage obtained using StarTrack code [53]. Results for five metallicities. Credit: [54].

Stars with their initial masses over $M_{\text{ZAMS}} \gtrsim 30M_{\odot}$ may experience a few types of strong stellar winds at different evolutionary stages [55]: as the O type young main sequence stars [44; 45], as the late-type supergiants above the Humphreys-Davidson limit [56] (so-called luminous blue variables; LBV [57]), and as the late-type Wolf-Rayet stars [46; 49]. Increased mass loss in each type of stellar wind may result in distinctive features in the mass distribution of the final evolutionary outcome: NSs or BHs [26; 48], detected via GW.

The average metallicity in the Universe has been gradually increasing [58; 59] due to the production of heavy elements by massive stars' interiors and their SN explosions. Therefore, the mass of BH-BH mergers is expected to correlate with their redshift, e.g., [2; 53; 60; 61]. Sensitivity of improved LVK interferometers and the planned next-generation ground-based detectors: Einstein Telescope and the Cosmic Explorer will increase the number of detected compact object mergers by orders of magnitude and allow for GW detections at very high redshifts, approaching the edge of observable Universe [62; 63], see Figure 19. This will allow us to follow the evolution of compact object merger properties in the function of redshift and help to distinguish the origin of the different features in their mass distribution [62–64].

1.2 Spin distribution of gravitational sources

This section provides a brief summary of inferred BH-BH spin parameters of GWTC-3 [2]: subsection 1.2.1, and the possible astrophysical implications of those measurements: subsection 1.2.2.

1.2.1 Spin measurements of detected binary black hole mergers

BH spin distribution in GWTC-3, consistently with GWTC-2, is dominated by low-spinning BH population with a minor fraction of high-spinning BHs [2; 7]. Half of BH spins take value below $\chi_i \approx 0.25$, where $\chi_i = cJ_i/Gm_i^2$ is dimensionless BH spin magnitude. The distribution of BH spin magnitudes (see Fig. 6) peaks around $\chi_i \lesssim 0.2$, then there is a constant drop and a tail extending towards large spin values [2].

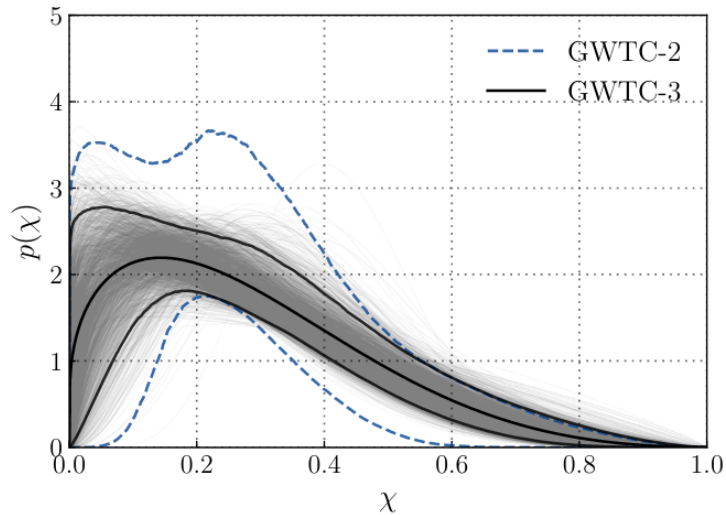


Fig. 6: Spin magnitudes χ_i distributions of BH-BH merger components. The median and central 90% credible bounds inferred on $p(\chi_i)$ using GWTC-3 are marked with solid black lines. The blue dashed lines show results obtained using GWTC-2. The light gray lines stand for individual draws from the posterior distribution of the DEAFULT spin model parameters, see more in [2] and [65]. Credit: [2].

Another provided spin parameter is the effective inspiral spin χ_{eff} [4], which can be measured more precisely than the individual BH spin magnitudes [66]. The effective spin parameter χ_{eff} is a mass-weighted linear combination of individual BH spin magnitudes and their alignment with the system orbit expressed by the formula:

$$\chi_{\text{eff}} = \frac{m_1 \chi_1 \cos \theta_1 + m_2 \chi_2 \cos \theta_2}{m_1 + m_2}$$

where: m_i -the mass of each BH, χ_i -each BH spin magnitude, θ_i is the angle between the orbital angular momentum axis and the individual BH spins. Therefore, χ_{eff} provides indirect information on spin misalignment and spin magnitude of the merging components, however, difficult to disentangle. Detected BH-BH systems point towards domination of mergers with positive $\chi_{\text{eff}} > 0$ and the mean value centered at $\chi_{\text{eff}} = 0.06^{+0.04}_{-0.05}$ [2; 67]. The inferred distribution (see Fig. 7) may possess an asymmetry relative to $\chi_{\text{eff}} = 0$, thus a possible fraction of negative effective spin mergers, even up to $f_{\chi_{\text{eff}} < 0} \lesssim 30\%$ [2].

On the other hand, BH-BH detection analyses with a prior allowing for a subpopulation of BHs with negligible spins, [67; 68] indicate that there is no certain evidence for any highly misaligned merger. The probability of negative $\chi_{\text{eff}} < 0$ mergers also weakens once the effective spin distribution is allowed to correlate with other BH-BH parameters, e.g., the system mass ratio [2; 69]. Correct and careful interpretation of GW detection data is required to make any astrophysical inference, e.g., on contributions of various formation channels.

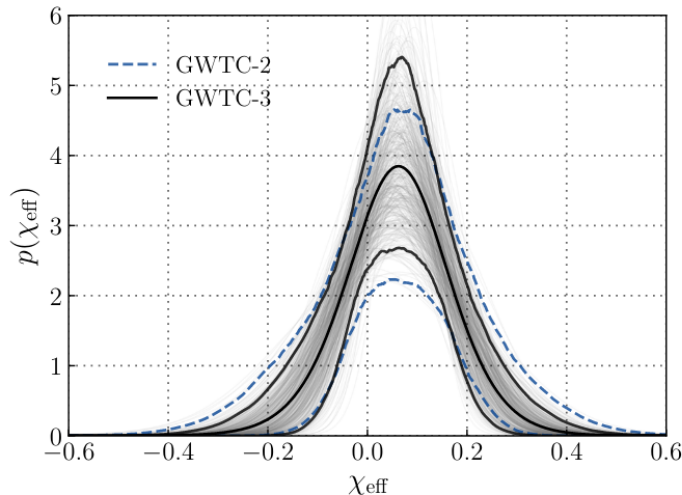


Fig. 7: Black solid line is the inferred distribution of χ_{eff} for GWTC-3 analysis. For comparison, the blue dashed lines are results derived for GWTC-2. Credit: [2].

Finally, LVK population studies and other data analysis report a possible negative correlation of spin and mass ratio [2; 70] such that BH-BH mergers with near equal mass component ($q \approx 1$) favor low, near zero $\chi_{\text{eff}} \approx 0$, while unequal mass ratio binaries tend to take positive values of χ_{eff} . Large spins of the more massive BH are naturally expected for hierarchical scenarios for which the products of next-generation mergers [71; 72]. However, a similar correlation may originate from mass reversal, stable mass transfer formation scenario in isolated binary evolution including efficient WR tidal spin-up. More details on this scenario may be found in Section 5.

1.2.2 Astrophysical implications of black hole spins

BH spins, their magnitudes, and orientations, may indicate the possible formation path of the given BH-BH merger. A rapidly increasing number of GW detections motivated several analyses of GW population properties, including spin parameters [2; 67–69]. Robust BH spin measurements could provide constraints on the mechanism of angular momentum transport in massive stars, as well as the possibility of BH spin-up due to tidal interactions or mass transfer.

The current BH-BH system database seems to be consistent with a low-spinning, but non-zero, BH population, with a possible tail extending towards large spin values [2]. On the contrary, X-ray binaries systematically result in very high spin measurements ($\chi > 0.8$) see e.g., [73; 74]. High-spinning BHs are crucial in the current understanding of the origin of Gamma Ray Bursts [75; 76]. The tension between the two BH populations is likely not the observational bias or limitations [77] and leads to inconsistent conclusions about typical BH spins. However, it may be explained by different evolutionary scenarios behind GW sources and X-ray binaries' formation (see [78] and references therein).

So far, both natal spins of BHs and the efficiency of possible spin-up mechanisms are uncertain. The natal spin of a BH depends on how efficient the angular momentum transport in the progenitor star is. If angular momentum transport between the stellar core and the envelope is efficient, the natal spin of a BH is low [53; 79–82]. Classic Tayler-Spruit magnetic dynamo results in low, but non-zero spin magnitudes [53; 79], see Figure 8. Efficient angular momentum transport and the assumption of effective Wolf-Rayet (WR) star tidal spin-up in very close, evolved systems [83–85] result in a minor fraction of high-spinning BHs in GW sources population, consistent with LVK detections [86–88], more details in Section 5.

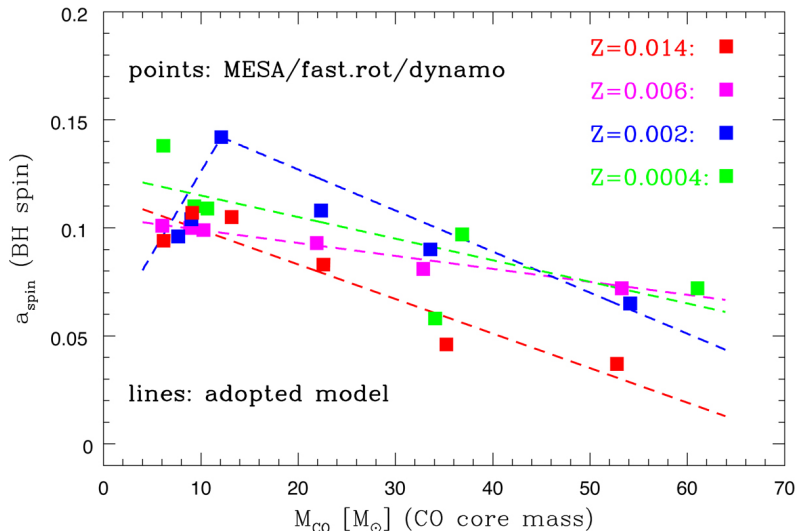


Fig. 8: Natal BH spin magnitudes as a function of the carbon-oxygen core mass of the BH progenitor before its collapse, results for the MESA stellar models [89–93] with 40% critical initial velocity and the Tayler-Spruit magnetic dynamo (efficient) angular momentum transport. Results for four metallicities. Credit: [53].

A significant fraction of highly misaligned BH-BH mergers might be the signature of the contribution of various formation channels. According to the generally used assumption, BH spins in isolated binary evolution channels may be misaligned with the orbit, mainly due to natal kicks [53; 86; 94]. Therefore, natal kicks may produce some fraction of negative $\chi_{\text{eff}} < 0$ [86]. The popular natal kick model used in population synthesis assumes that the more massive the BH is, the smaller probability of high natal kick [22; 95]. However, the nature of BH natal kicks is uncertain and almost not constrained by observations. Isolated binary evolution presumably favors nearly aligned mergers [53; 86; 96] with a rather low contribution of negative effective spins $f_{\chi_{\text{eff}} < 0} \lesssim 10\%$ (see more in Sec. 5), while dynamical paring, e.g., in globular clusters tend to produce an isotropic distribution of χ_{eff} with $f_{\chi_{\text{eff}} < 0} \approx 50\%$ [97–99]. Therefore, the mixed contribution of different channels could reconstruct well the observed properties of LVK mergers [100]. Alternatively, BH-BH mergers that originate from the young globular clusters could naturally possess asymmetry in χ_{eff} distribution, consistent with GWTC-3, due to the mixed contribution of a dynamically and primordially paired subpopulations [99], see

Figure 9.

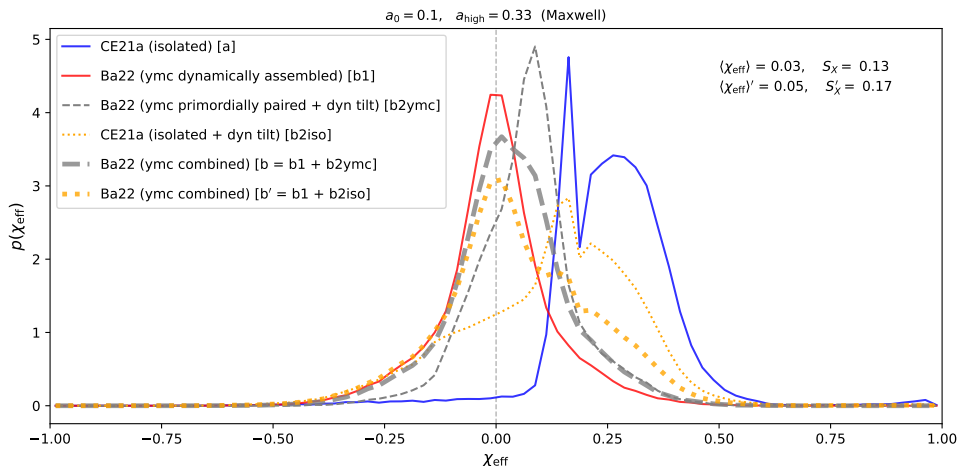


Fig. 9: Normalized intrinsic χ_{eff} distributions of BH-BH mergers from young massive clusters (mix of dynamically and primordially paired). Distributions for isolated binary evolution model [86] (blue line) and isotropic distribution of dynamically paired subpopulation (red solid line), for comparison. The thick dashed yellow line is a combination of a primordially paired subpopulation (isolated binaries with additional dynamical tilts) and purely dynamically assembled BH-BH mergers, see [99] for more details. Credit: [99].

1.3 Merger rates evolution with redshift

Analysis of the population properties of the detected compact objects after the end of the third observing run [2] constrained the increase of BH-BH coalescence rate with the redshift of the mergers z . BH-BH merger rate evolution was also found to be consistent with cosmic star formation rate (SFR), which points towards the stellar origin of the GW sources. Figure 10, adopted from [2], shows constraints on BH-BH merger rate evolution with redshift combined with the Madau–Dickinson model of SFR [58].

Parameterized as power-law, the BH-BH merger rate was found to be proportional to $(1+z)^\kappa$ with $\kappa = 2.9^{+1.7}_{-1.8}$ for $z < 1$. For comparison, the power-law at low redshift in the Madau–Dickinson SFR model corresponds to $\kappa_{\text{SFR}} \approx 2.7$. The observed evolution of the BH-BH merger rate with redshift is claimed to be confident, inferring that $\kappa < 0$ at 99.6% credibility [2].

It is worth noting that some deviations between the curve shapes of SFR and the merger rate evolution as a function of redshift are justified. The distribution of systems separation after both compact objects formation is uncertain, and therefore also the distribution of time delays, the periods between the systems formation and their merger due to GW emission [101]), is unknown. Such distribution not only depends on the formation channel (see Sec. 1.4) but also for a given channel it varies for different assumptions on highly uncertain astrophysical processes and parameters, e.g., mass transfer in massive star binaries [102–107].

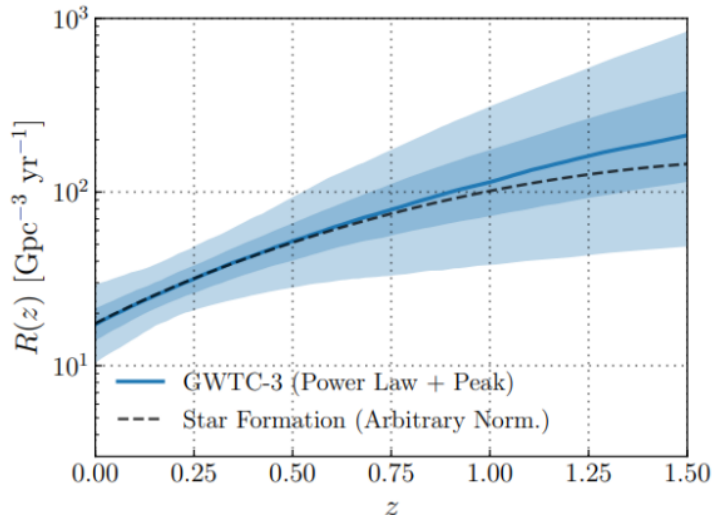


Fig. 10: Credible bounds on the BH-BH merger rate evolution with redshift: 50% (dark blue) and 90% (light blue). The dashed black line is the normalized rate of cosmic star formation [58]. Credit: [2]

1.4 Formation channels of binary black hole mergers

The contribution of different formation channels to the detected GW source population is still unknown. The possible mechanisms that could bring two compact objects close enough to allow them to merge in a period shorter than the current age of the Universe are unconstrained and poorly understood. However, studies on possible formation channels of compact object mergers became more and more intense after the first GW detection [1].

Currently, due to several uncertainties in modeling, it is even hard to define a parameter space e.g., for system masses, mass ratio, spin magnitudes, or misalignment for which we can safely exclude or confirm a given formation channel. There are degeneracies between the results of different models, and several formation channels are able to reconstruct at least part of the detected GW population properties.

This section briefly describes several popular formation channels for BH-BH mergers suggested by the literature. The isolated binary formation of BH-BH mergers is the main focus of this thesis. Moreover, the vast majority of current GW detections are classified as BH-BH mergers. Therefore, their formation is described in more detail.

1.4.1 Isolated binary systems

One of the most studied formation scenarios for GW sources is isolated binary evolution of massive binary stars, e.g., in galactic fields [96; 106; 108–129].

There are two major studied formation scenarios for merging BH-BH via isolated evolution of massive binary stars, see Figure 11 adopted from [130]. The first part of the evolution is similar for both of them. In the beginning, a binary system with two massive stars ($M_{ZAMS} \gtrsim 20 M_{\odot}$) is formed. Then, after a few million years, the more massive star leaves its main sequence. The star expands, filling its Roche Lobe and initiating the stable mass transfer. A fraction of the transferred mass is accreted on the companion, and the rest is lost from the system. During the first mass transfer phase, the donor star loses its hydrogen envelope and remains a naked helium core. Soon after that, the first BH is formed either by SN explosion or direct collapse (see more in Sec. 6).

The difference between the two BH-BH merger formation scenarios occurs during the second Roche Lobe Overflow (RLOF) after the second star leaves its main sequence. In the clas-

sical scenario, once the initially less massive star expands and fills its Roche Lobe, the binary system goes through an unstable mass transfer phase i.e., common envelope (CE) [118]. CE effectively tightens the orbit of the initially wide system, allowing the BH-BH system to merge in Hubble time. However, several recent studies report that mass transfer in massive binary systems is more stable than previously assumed [131–134]. CE in BH-BH progenitors is developed much less frequently than adopted in most of the rapid population synthesis codes used to study GW sources. Moreover, the successful ejection of the donor’s envelope is difficult to achieve [135] and possible only under very restrictive conditions. Therefore, the CE phase often leads to a donor and BH merger instead of a BH-BH binary formation. Recently, alternative isolated binary evolution scenario with stable mass transfer instead of CE [27; 78; 106; 121; 128; 134; 136; 137] is gaining popularity in the community. During my doctoral studies, I implemented and studied the impact of revised, more conservative than before, criteria for CE development in massive binaries on the population of BH-BH mergers [86; 106]. More details on this topic and the results of our studies are described in Section 4.

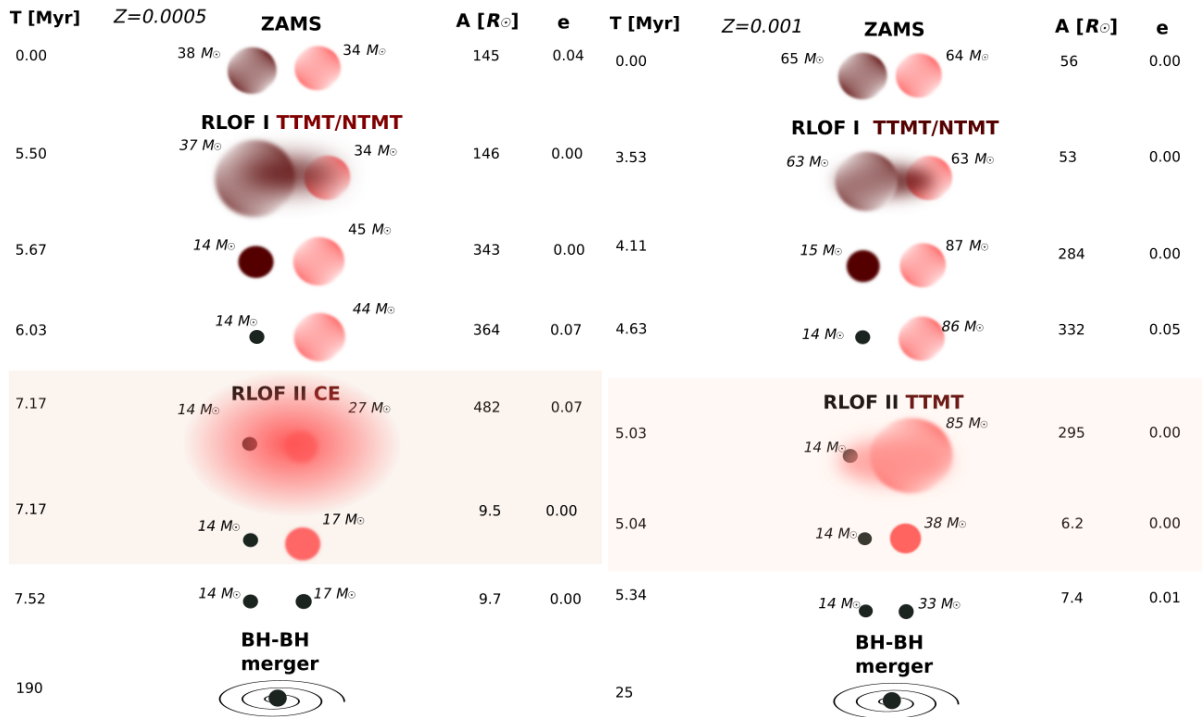


Fig. 11: Two most popular BH-BH formation scenarios for the isolated binary evolution channel: via common envelope (CE; left) and through the stable, thermal-timescale mass transfer (TTMT; right) during the second Roche Lobe Overflow (RLOF). Credit: [130].

Another, separate evolutionary path for isolated binaries, possibly leading to the formation of BH-BH mergers, is **chemically homogeneous** evolution of close massive binary star systems [138–143]. Chemically homogeneous evolution channel applies only to very tight, almost contact massive binaries with typical initial orbital period $P < 2$ days [141]. Young and relatively compact main sequence stars in such systems are expected to get tidally spun up. Rapid stellar rotation, on the other hand, induces efficient mixing from central parts throughout the star’s envelope. As a result, mixing provides the core with additional elements to continue nuclear burning. The most important consequence of high rotation and efficient mixing is the significant reduction in star expansion compared to the classical, non-rotating evolutionary models [144]. Therefore, the rapidly rotating stars may remain within their Roche Lobes throughout the core hydrogen burning phase and continue their evolution as a tight binary system, avoiding the stellar merger after the completion of hydrogen burning [145].

An important limitation of this formation channel is related to mass loss in stellar winds, which affects not only the masses of the stars but also the orbit of the system. Strong stellar winds from rich in metal stars may moderate the chemically homogeneous evolution of the system, as the angular momentum loss widens the separation between stars. That may lead to a star spin-down. Therefore, some studies of the chemically homogeneous channel indicate a high preference for the BH-BH progenitors with initially low metallicity [140].

As an increased fraction of star mass is processed by nuclear fusion, the chemically homogeneous formation channel naturally tends to produce massive BH-BH mergers with a total mass of $M_{\text{tot}} = M_{\text{BH}_1} + M_{\text{BH}_2} \in 50 - 110 M_{\odot}$ [141]. It also favors the formation of BH-BH mergers with a rather equal mass component, mass ratio $q \gtrsim 0.8$ [140; 141]. The first detected GW system GW150914 [1] with each BH mass of $\sim 30M_{\odot}$ is considered as a typical BH-BH merger that could have followed the chemically homogeneous formation path.

1.4.2 Dynamical formation in clusters

Globular clusters, nuclear star clusters, and young stellar clusters are dense environments commonly believed to enable the efficient formation of merging BH-BH systems via dynamical encounters [99; 105; 146–172]. Initially, single objects as well as primordially paired binaries are affected by common interactions with each other. Those interactions not only impact the orbital parameters but also may completely change the final evolutionary outcome of the system. Binaries with low binding energies might get disrupted, while single objects may become a part of new binaries. Binary systems in dense clusters may also exchange their companions [173] with tendencies to accelerate and eject the least massive ones [174]. Therefore, clusters favor the formation of massive binary systems [175].

Moreover, massive objects, such as BHs tend to sink and segregate into the cluster core due to dynamical friction [175–177], which increases the probability of two BHs encounter and merger. Cluster interiors may also allow for repeated mergers (second, third-generation) if the potential well is deep enough to retain the merger product once it receives a recoil kick [178]. Therefore, some of them are expected to host massive BHs [179] ($M_{\text{BH}} \gtrsim 50 M_{\odot}$) with their masses within or above the upper mass gap limit (see Sec. 1.1.2), even if PSN operates in massive, evolved stellar cores [28–32]. Some globular clusters may also contain intermediate mass BHs (IMBH) with masses in the range $M_{\text{BH}} \in 10^2 - 10^5 M_{\odot}$ [178]. Few candidates for IMBH in the center of clusters have been found based on measurements of the star velocities, however, so far none has been confirmed (e.g., [180]).

Interactions in clusters may also lead to the ejection of massive binary binaries, which later form compact object systems that merge in the galactic fields instead [175]. Each cluster has its individual set of features such as its mass, density, escape velocity, age, and metallicity of stellar populations. That impacts the number and properties (mass and spin distribution) of formed compact object systems.

Due to dynamical encounters and paring of randomly oriented objects, globular clusters are expected to produce isotropic χ_{eff} distribution of BH-BH mergers with a significant fraction of BH spins misaligned with the orbit (e.g., [97; 98]). This, in turn, may allow distinguishing the dynamical population of BH-BH mergers from those originating from isolated binaries, expected to be dominated by roughly aligned mergers. More on the topic of BH spin parameters in Sections 1.2.1 and 5.

1.4.3 Isolated multiple systems

Observations of early-type stars indicate that the stars with their initial masses $M \gtrsim 10M_{\odot}$ (i.e., NS and BH progenitors) tend to have one or more companion [181–183]. In particular, the more massive the star is, the higher probability it is part of a binary or multiple system (triple

or quadrupole) [183]. Many of the multiple systems are hierarchical [184], which means they may be divided into a few interacting subgroups. Each of the hierarchical subgroups is an approximately stable two-body system, while the closer pairs are treated as a single object. In the simplest case: the triple configuration, two of the stars form a close binary system (the inner system) while the third component orbits them in a much larger separation (the outer system). With more components, hierarchical structures become more diverse and complicated. When orbits of the inner and the outer systems are of similar sizes, the configuration may become unstable and result in complex movements of the components [185].

Under specific conditions, three-body interactions may lead to periodic eccentricity-inclination exchange, known as the Lidov-Kozai effect [186; 187]. The mechanism, observed for stars, planets as well as their satellites, affects the orbit of a binary system perturbed by the outer body. Due to imparted eccentricity, a near-circular system might evolve to relatively highly eccentric. Therefore, the Lidov-Kozai mechanism may play an important role also for BH-BH systems in triple configurations, which as isolated binaries would be too wide to merge in the Hubble time. The formation of GW sources via interactions in multiple systems has become a popular topic of study in the field of GW astrophysics [188–195],

1.4.4 Active galactic nuclei

Central parts of active galactic nuclei (AGN) are believed to host numerous stellar origin compact objects, also those in binary or multiple systems [196; 197]. Orbital motion in such systems might be significantly perturbed due to the presence of supermassive BH. Especially, binaries with their orbits highly inclined relative to their motion around the supermassive BH are expected to be strongly affected by the Lidov-Kozai mechanism [186; 187] (see also Sec. 1.4.3). That, on the other hand, may result in the shortened inspiral and accelerated merger of the BH-BH system, which would not merge in the Hubble time without interaction with supermassive BH. BH-BH mergers that followed this formation path are expected to enter the LVK detectable band with highly eccentric orbits [196], which may help to distinguish them from the isolated binary systems formed in the galactic field.

Another effect that could stimulate the formation of BH-BH mergers in AGN is the occurrence of torques exerted by the gas disk [198]. Such torques place compact objects in so-called migration traps. As stellar-origin BHs migrate toward such traps, pair up and form tight systems with short merger timescales. This process may continue, allowing also for repeated mergers of the higher generations [198].

AGN disk is a promising environment that may contribute to the formation of detected GW sources [196–201].

1.4.5 Population III stars

Population III stars are considered the primary origin of heavier elements, up to iron [202]. Although they constitute a promising piece of the puzzle that connects several observed features and cosmological theories of the early Universe, so far, there are only indirect premises for their existence, e.g., in the spectra of high redshift galaxies [203].

A fundamental property of this hypothetical stellar population is their metal-free chemical composition [204]. They are expected to consist only of hydrogen and helium, which are basically the only elements available at that Universe epoch [205]. The initial lack of metals determines other specific features predicted for the first stars, such as the limited expansion of the stellar radius [206] and low mass loss in stellar winds [207]. That makes them candidates for massive BHs progenitors (e.g., $M_{\text{BH}} \approx 100 M_{\odot}$), with masses difficult to achieve for BHs originating from younger stellar populations [208]. On the other hand, such massive population

III stars could also end their evolution in PSN [28–32] (see also Sec. 1.1.2) leaving no BH remnant [209].

Population III stars, either evolved in isolated binaries or in dense stellar clusters, are considered as possible formation channels for GW sources, especially massive BH-BH mergers [60; 114; 208; 210; 211]. Signals originating from population III stars are expected to dominate detections at very high redshifts (e.g., [211]). However, due to several uncertainties, there are large discrepancies between different studies in estimated rates for compact object mergers originating from the first stars. One of the major unknowns is the formation and initial parameter distributions of binary systems, which could be much different than observed for current stellar populations [114; 210; 212]. Future ground-based GW detectors, which are expected to detect massive BH-BH mergers at redshifts higher than $z \approx 10$ (see Fig. 19), will help to distinguish the origin of GW system between different stellar populations and put farther constraints on population III stars [62; 63; 213; 214].

1.4.6 Primordial black holes

The existence of primordial BHs (PBHs) is still unsolved and a hot topic of debate in modern astrophysics. Such hypothetical objects could have formed in the very early, non-homogeneous Universe as a product of the gravitational collapse of overdensities [215–217]. In contrast, with relatively well constrained by observations and theory stellar origin BHs, theoretical masses of PBHs could possibly take values that differ by several tens of orders of magnitude. PBHs are considered as the candidate for a fraction of the Universe’s dark matter [218–220]. However, recent surveys and experiments of various targets provide more and more limits on possible dark matter in the form of those exotic objects in the different mass ranges [221; 222], rather than evidence for their existence.

PBHs with masses below $\sim 10^{15}$ g are expected to be absent by now due to Hawking radiation [222; 223]. The abundance of such PBHs in the early Universe might still be constrained due to possible effects of evaporated particles on, e.g., the cosmic microwave background. The fraction of PBHs with masses larger than $\sim 10^{15}$ is constrained by e.g., gravitational lensing missions, dynamical effects, accretion, and GW detections (see [222] and references within).

Some recent studies argue that the detection of GW signals from merging PBH binaries can not be excluded by the current constraints on their parameters [224]. Due to huge knowledge gaps in possible PBH properties such as distributions of their masses and spins, as well as a lack of robust constraints in our understanding of other formation channels, it is not possible to rule out or prove some contribution of PBHs to the detected GW population. Therefore, bounded PBHs represent another possible origin of detected GW signals [225–230]. Confirmed detection of a merger involving subsolar-mass BH could be a promising premise for the existence of PBHs [231].

2 Method

To model properties of compact object mergers as a function of redshift and compare them with GW detection, many uncertain assumptions must be made as the simulation input. In particular, such simulations require some approximate model of the star formation history of the Universe, involving the rates of star formation and evolution of stellar metallicity with redshift. One also needs to adopt some initial distribution of masses as well as orbital parameters of newborn stellar binaries. Once we collect such information, we need another, separate tool that allows us to follow the evolution of a large sample of binary systems generated using our initial distributions, from ZAMS to the eventual formation of compact object mergers.

In my doctoral research, I mainly used StarTrack population synthesis code [53; 232] to study evolutionary tracks of isolated massive star binaries. Below, I briefly discuss the StarTrack code, the used model of star formation history, as well as the population synthesis method in general with its applications and limitations.

2.1 Star formation history

To study properties of the detected population of merging compact objects in the local Universe, $z \approx 0$, we need to consider that tightening of the system orbit due to GW emissions is happening on a very slow timescale [101]. Therefore, the time delay between the formation of a close compact object system and its merger may take, e.g., a thousand years as well as several billion years. Moreover, the majority of formed compact object binaries have their orbital separation too wide to merge in the Hubble time, see e.g., Table 13 in [233]. Therefore, to the currently detected GW signals might contribute a complex mix of systems formed in the early and late epochs of the Universe. Each Universe epoch is characterized by different averaged SFR and metallicity enrichment, which significantly influenced the number and properties of formed compact object systems [2; 53; 60; 61].

To properly capture the contribution of old and new stellar populations to the currently detected GW sources, we need to adopt some model of star formation history. For this purpose, results generated using StarTrack code are processed by the SFR model and metallicity distribution adopted from review studies of [58], commonly known as *Madau & Dickinson*, and its update for early epochs $4 < z < 10$ due to the uncertain contribution of the faint galaxies - *Madau & Fragos* [234], (see also Sec. 2.6 of [53]). The studies [58] and [234] summarize the results of several multiwavelength imaging and spectroscopic surveys to map the evolution of the SFR density and production of heavy elements from the dark Universe ages to the present day. According to the used models, the SFR density peaked around 10 Gyr ago, at $z \approx 2.0$, followed by an exponential decline to the recent times [53], see Figure 12.

In default StarTrack simulations for cosmic evolution of compact object mergers, a mix of 32 stellar populations with different metallicities is included [53]. The taken proportions of those populations change in different epochs of the Universe according to the mean stellar mass-weighted gas-phase metallicity value [234; 235]. In particular, the contribution of different stellar metallicities at given redshift z is a Gaussian distribution centered at the mean metallicity calculated as $\log(Z/Z_{\odot}) = 0.153 - 0.074z^{1.34}$ [53; 234].

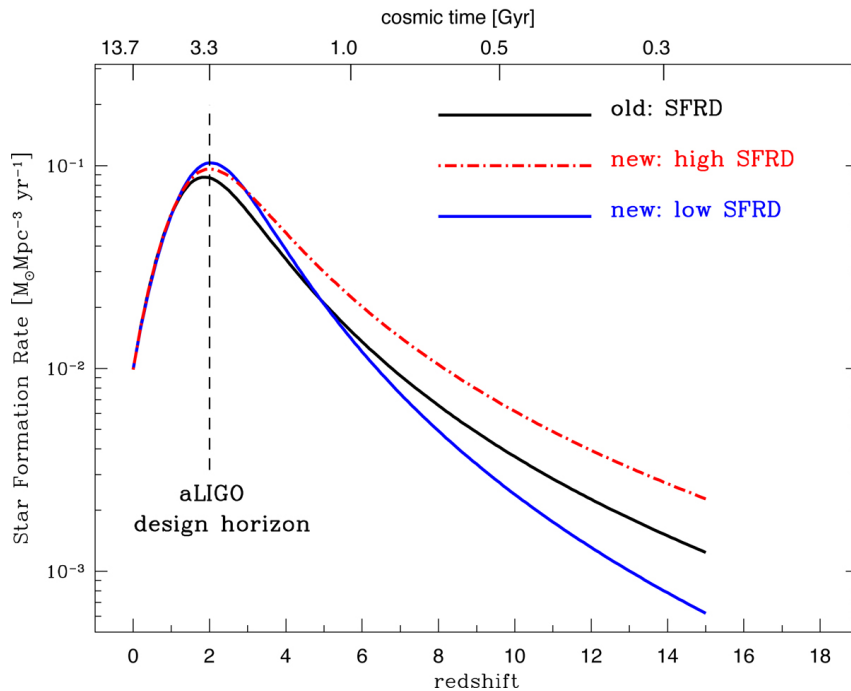


Fig. 12: Cosmic star formation rate density (SFRD) models as a function of redshift and cosmic time. Models adopted from [58] and [234] used for StarTrack simulations. The peak at redshift $z \approx 2$ and rates for low redshifts ($z \leq 2$) are common for both old SFRD model based on [58] (black) and new SFRD models based on updated studies [234]. New high SFRD (red) and new low SFRD (blue) models express the limits on the uncertain contribution of the faintest galaxies to the early SFRD [53]. Credit: [53].

2.2 Population synthesis

Rapid population synthesis code is a numerical tool commonly used to study the astrophysical origin of GW sources, as well as several other astrophysical phenomena. Examples of other research applications are cataclysmic variables [236–238], double white dwarf systems and SN type Ia [239], X-ray sources [240–242], Gamma Ray Bursts [243], Cepheid binaries [244] and many more [245].

In the case of compact object mergers, rapid population synthesis code allows following the evolutionary track of the massive stellar binaries from ZAMS to their final stage of evolution. StarTrack code [53; 232] enables to simulate evolution of isolated binaries for the wide range of initial parameters: masses, orbits, and metallicities. New binary systems are randomly sampled using probability distributions constrained by observations of young massive stars [11; 181; 182]. To follow the parameters of the components during the system evolution, rapid population synthesis codes, including StarTrack, often base on the analytical fits and extrapolations to a grid of the results derived using detailed stellar evolution codes. In particular, StarTrack adopts widely used fitting formulae employed for SSE code [246; 247]. Effects of binary interactions such as tides or mass transfer are usually included by approximated prescriptions calibrated to the observations or advancements in the theoretical modeling of given phenomena.

The approach adopted by rapid population synthesis allows evolving synthetic populations of many million binaries with low computational costs. However, it also results in several loose parameters and other inaccuracies, which may affect the robustness of simulation results and sometimes cause inconsistency with other, similar codes [248]. Different assumptions on highly uncertain and complex astrophysical phenomena such as mass transfer (see Sec.4) or core-

collapse SN (see Sec.6) may significantly impact the properties of the compact object mergers population. Therefore, the results of rapid population synthesis codes should be treated with proper caution. This tool should be rather used to build some intuition about studied phenomena, e.g., the formation of GW sources, and to test the general effects of physical assumptions on the studied population. Rapid population synthesis, despite its several shortcomings, is a widely used and important method that is very useful to plan new experiments and observation surveys. Synthetic populations are also used to understand the observational data and correct the observer bias [245]. In the case of GW sources, it allows, e.g., to develop intuition on possible evolutionary scenarios leading to the formation of compact object mergers.

More detailed 1D stellar evolution code, involving the structure of the star, such as MESA [89–93] are also commonly used tools to study the evolution of massive binary systems. However, due to the many gaps in our understanding of very massive stars (BH progenitors), detailed simulations may not necessarily provide more reliable results than rapid codes. Changing not-well-constrained input parameters of the stars within reasonable, physical ranges, e.g., overshooting, sometimes results in significantly different evolutionary tracks, properties of the star (structure, radius), and the final outcome [249; 250]. High computational costs allow using detailed modeling only for a small initial parameter space, e.g., several dozen systems. Such simulations are also often limited to the most interesting parts of system evolution, such as the first or the second mass transfer. Therefore, currently, those codes are mainly used to revisit and calibrate the most uncertain, complex evolutionary phases and create approximate models for rapid population synthesis [131–133; 251; 252].

3 GW190412 and unequal mass binary black hole mergers

Public announcement of GW190412 event [9], the first detection of a highly unequal mass BH-BH merger, caused a lot of excitement in the GW astrophysics community. The primary and secondary BH masses has been estimated for $30.1_{-5}^{+4.6}M_{\odot}$ and $8.3_{-0.9}^{+1.6}M_{\odot}$ respectively. In addition to the unusual components' mass ratio, the system is characterized by a relatively high measured effective spin $\chi_{\text{eff}} = 0.25_{-0.11}^{+0.08}$ [9]. Unequal mass ratio mergers, such as GW190412, emit GWs with increased contribution of higher multipoles [9]. Higher multipoles, on the other hand, provide additional information about the properties of the GW source, extractable by combining GW theory with data analysis. The contribution of higher multipoles in the signal waveform may improve constraints on source inclination and luminosity distance [9].

Soon, after the announcement of the detection, several possible evolutionary scenarios leading to the formation of a BH-BH merger with similar parameters as GW190412 have been considered [253–256]. Unequal mass ratio and significant effective spin were commonly seen as the possible signature of the hierarchical merger, with the more massive BH being a product of the former (one or multiple) repeated mergers [253–255].

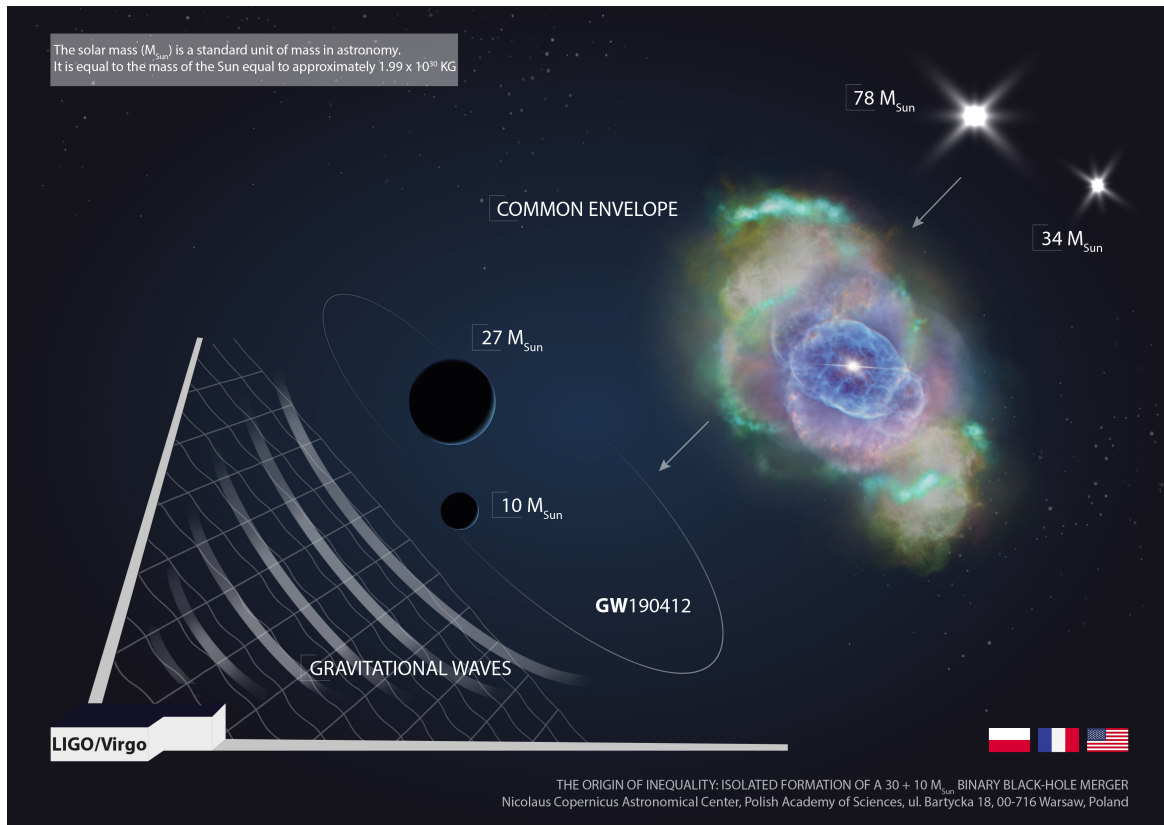


Fig. 13: A simplified diagram of the evolution of two massive stars leading to an unequal mass BH-BH merger formation with parameters consistent with GW190412. Credit: Katarzyna Drewniany. Figure prepared for popularizing our research group studies *The odd couple: how a pair of mismatched black holes formed* and *Scientists explain how two black holes of hugely different masses collided*.

In our letter [256] we show that contrary to community expectations, unequal-mass BH-BH mergers similar to GW190412 can originate from isolated massive binary star systems evolving in the galactic field. Therefore, the question about the formation channel is still relevant.

We present a possible evolutionary track of the GW190412-like progenitor system. At the late stage of its evolution, the binary system goes through an unstable mass transfer phase, which results in tightening the orbit. Then in a very close, evolved system, the first formed BH tidally spins up its companion – the naked helium core. Our scenario reconstructs both masses and effective spin parameter measured for GW190412 merger. Besides the formation scenario, we also present the mass ratio distribution of BH-BH mergers in our standard physical model and find the fraction of unequal-mass BH–BH mergers consistent with the LIGO and Virgo inference. We present the expected distribution of effective spin χ_{eff} and precession χ_p parameters for the entire population and for an unequal-mass subpopulation of BH-BH system which merge in Hubble time, testing various assumptions on uncertain efficiency of tidal spin-up. We try to put an upper limit on the precession of a tight BH-BH system formed via a classical isolated binary scenario with a common envelope by applying a model with very high BH natal kicks.



The Origin of Inequality: Isolated Formation of a 30+10 M_{\odot} Binary Black Hole Merger

A. Olejak¹, M. Fishbach², K. Belczynski¹, D. E. Holz², J.-P. Lasota^{1,3}, M. C. Miller⁴, and T. Bulik⁵

¹Nicolaus Copernicus Astronomical Center, Polish Academy of Sciences, ul. Bartycka 18, 00-716 Warsaw, Poland; aleksandra.olejak@wp.pl
²Enrico Fermi Institute, Department of Physics, Department of Astronomy & Astrophysics, KICP, University of Chicago, Chicago, IL 60637, USA
³Institut d'Astrophysique de Paris, CNRS et Sorbonne Université, UMR 7095, 98bis Bd Arago, F-75014 Paris, France
⁴Department of Astronomy and Joint Space-Science Institute, University of Maryland, College Park, MD 20742–2421, USA
⁵Astronomical Observatory, Warsaw University, Al. Ujazdowskie 4, 00-478 Warsaw, Poland

Received 2020 July 20; revised 2020 September 3; accepted 2020 September 5; published 2020 October 2

Abstract

The LIGO/Virgo Collaboration has reported the detection of GW190412, a black hole–black hole (BH–BH) merger with the most unequal masses to date. (Another system, with even more unequal-mass components, was recently published by LIGO/Virgo: GW190814 ($m_1 = 23 M_{\odot}$, $m_2 = 2.6 M_{\odot}$); however, it is not known whether it is a BH–BH or BH–NS merger (Abbott et al. 2020).) They are $m_1 = 24.4\text{--}34.7 M_{\odot}$ and $m_2 = 7.4\text{--}10.1 M_{\odot}$, corresponding to a mass ratio of $q = 0.21\text{--}0.41$ (90% probability range). Additionally, GW190412's effective spin was estimated to be $\chi_{\text{eff}} = 0.14\text{--}0.34$, with the spin of the primary BH in the range $a_{\text{spin}} = 0.17\text{--}0.59$. Based on this and prior detections, $\gtrsim 10\%$ of BH–BH mergers have $q \lesssim 0.4$. Major BH–BH formation channels (i.e., dynamics in dense stellar systems, classical isolated binary evolution, or chemically homogeneous evolution) tend to produce BH–BH mergers with comparable masses (typically with $q \gtrsim 0.5$). Here we test whether the classical isolated binary evolution channel can produce mergers resembling GW190412. We show that our standard binary evolution scenario, with the typical assumptions on input physics that we have used in the past, produces such mergers. For this particular model of the input physics the overall BH–BH merger rate density in the local universe ($z \sim 0$) is $73.5 \text{ Gpc}^{-3} \text{ yr}^{-1}$, while for systems with $q < 0.41$ the rate density is $6.8 \text{ Gpc}^{-3} \text{ yr}^{-1}$. The results from our standard model are consistent with the masses and spins of the black holes in GW190412, as well as with the LIGO/Virgo estimate of the fraction of unequal-mass BH–BH mergers. As GW190412 shows some weak evidence for misaligned spins, we provide distribution of the precession parameter in our models and conclude that if among the new LIGO/Virgo detections the evidence of system precession is strong and more than 10% of BH–BH mergers have large in-plane spin components ($\chi_p > 0.5$), then the common envelope isolated binary BH–BH formation channel can be excluded as their origin.

Unified Astronomy Thesaurus concepts: Black hole physics (159); High energy astrophysics (739); Black holes (162); Stellar evolution (1599); Stellar evolutionary models (2046); Compact objects (288); Common envelope binary stars (2156); Gravitational wave sources (677)

1. Introduction

The first confirmed double black hole (BH–BH) coalescence to be reported from the LIGO/Virgo O3 run, GW190412, differs from all previously announced BH–BH mergers in one important detail: it is the first BH–BH detection that has a mass ratio inconsistent with unity (The LIGO Scientific Collaboration & the Virgo Collaboration 2020). All 10 BH–BH mergers announced by the LIGO/Virgo team from the O1 and O2 observational campaigns were consistent with being equal-mass mergers (Abbott et al. 2019a, 2019b; Fishbach & Holz 2020). In contrast, GW190412's component masses are $m_1 = 29.7_{-5.3}^{+5.0} M_{\odot}$ and $m_2 = 8.4_{-1.0}^{+1.7} M_{\odot}$, with a mass ratio of $q = 0.28_{-0.07}^{+0.13}$ (median and 90% symmetric credible interval) and a maximum mass ratio of $q = 0.59$ (99% probability). The dimensionless spin of the primary (more massive) BH spin is estimated to be $a_{\text{spin1}} = 0.17\text{--}0.59$. The LIGO/Virgo Collaboration also gave their constraints on the system effective spin parameter, which is expressed by the formula

$$\chi_{\text{eff}} = \frac{m_1 a_{\text{spin1}} \cos \theta_1 + m_2 a_{\text{spin2}} \cos \theta_2}{m_1 + m_2} \quad (1)$$

where θ_i is the angle between the individual BH spin a_{spini} and the system orbital angular momentum. The estimated value of the system effective spin parameter is $\chi_{\text{eff}} = 0.25_{-0.11}^{+0.08}$

(90% probability). The inferred BH–BH merger rate density from O1/O2 is $9.7\text{--}101 \text{ Gpc}^{-3} \text{ yr}^{-1}$. From this and previous detections, $\gtrsim 10\%$ of BH–BH mergers have mass ratios $q < 0.40$ (The LIGO Scientific Collaboration & the Virgo Collaboration 2020).

It is expected that merging BH–BH systems may form through several channels. These include the classical isolated binary evolution channel (Bond & Carr 1984; Tutukov & Yungelson 1993; Lipunov et al. 1997; Voss & Tauris 2003; Belczynski et al. 2010b, 2016b; Dominik et al. 2012; Kinugawa et al. 2014; Eldridge & Stanway 2016; Hartwig et al. 2016; Spera et al. 2016; Woosley 2016; Stevenson et al. 2017; Hainich et al. 2018; Kruckow et al. 2018; Marchant et al. 2019; Spera et al. 2019; Bavera et al. 2020), the dense stellar system dynamical channel (Portegies Zwart & McMillan 2000; Miller & Hamilton 2002a, 2002b; Gültekin et al. 2004, 2006; Portegies Zwart et al. 2004; O'Leary et al. 2007; Sadowski et al. 2008; Downing et al. 2010; Antonini & Perets 2012; Benacquista & Downing 2013; Bae et al. 2014; Chatterjee et al. 2017; Hurley et al. 2016; Mapelli 2016; Rodriguez et al. 2016, 2018; VanLandingham et al. 2016; Arca-Sedda & Capuzzo-Dolcetta 2019; Askar et al. 2017; Samsing 2018; Banerjee 2018; Morawski et al. 2018; Di Carlo et al. 2019; Perna et al. 2019; Zevin et al. 2019; Kremer et al. 2020), isolated multiple (triple, quadruple) systems (Antonini et al. 2017; Silsbee & Tremaine 2017;

Arca-Sedda et al. 2018; Liu & Lai 2018; Fragione & Kocsis 2019), mergers of binaries in galactic nuclei (Antonini & Perets 2012; Hamers et al. 2018; Hoang et al. 2018; Fragione et al. 2019), and the chemically homogeneous evolution channel consisting of rapidly spinning stars in isolated binaries (de Mink & Mandel 2016; Mandel & de Mink 2016; Marchant et al. 2016; du Buisson et al. 2020).

In those formation scenarios BH–BH systems typically form with comparable mass components ($q \gtrsim 0.5$). These predictions are challenged by GW190412.

In this study we demonstrate that in the isolated binary channel a small but significant fraction of systems lead to a BH–BH merger similar to GW190412. We provide a proof-of-principle example of an isolated binary that is both qualitatively and quantitatively indistinguishable from GW190412. We emphasize that we have implemented only one model, incorporating our best estimates of the physics and astrophysics that set the evolution of stars in binary systems. We leave to future work a more extensive study, investigating a greater parameter space and exploring model uncertainties. Our results, when combined and contrasted with similar studies of other formation channels, suggest a plausible origin for GW190412.

2. Calculations

We use the population synthesis code *StarTrack* (Belczynski et al. 2002, 2008a) to test the possibility of the formation of a BH–BH merger resembling GW190412. We employ the rapid core-collapse supernova (SN) engine neutron star (NS)/BH mass calculation (Fryer et al. 2012), with weak mass loss from pulsational pair instability SNe (Belczynski et al. 2016a). We assume standard wind losses for massive stars: O/B star (Vink et al. 2001) winds and luminous blue variable (LBV) winds (specific prescriptions for these winds are listed in Section 2.2 of Belczynski et al. 2010a). BH natal spins are calculated under the assumption that angular momentum in massive stars is transported by the Tayler–Spruit magnetic dynamo as adopted in the MESA stellar evolutionary code (Spruit 2002). Such BH natal spins are at the level of $a_{\text{spin}} \sim 0.1$ (see Belczynski et al. 2020) and may be overridden if the immediate BH progenitor (Wolf–Rayet (WR)) stars in close binaries (orbital periods $P_{\text{orb}} < 1.3$ days) are subject to tidal interactions. In such cases we employ the scheme described in Section 2.5 of Belczynski et al. (2020). For BH–WR, WR–BH and WR–WR binary systems with orbital periods in the range $P_{\text{orb}} = 0.1$ –1.3 days the BH natal spin magnitude is fit from WR star spun-up MESA models (see Equation (15) of Belczynski et al. 2020), while for systems with $P_{\text{orb}} < 0.1$ day the BH spin is equal to 1.0. BH spins may be increased by accretion in binary systems. We treat accretion onto a compact object during Roche lobe overflow (RLOF) and from stellar winds using the analytic approximations presented in King et al. (2001) and Mondal et al. (2020). We adopted limited 5% Bondi accretion rate onto BHs during the common envelope (CE) phase (Ricker & Taam 2008; MacLeod & Ramirez-Ruiz 2015; MacLeod et al. 2017). The estimate of Bondi accretion rate during the CE phase is derived in Appendix B.

The most updated description of *StarTrack* is given in Belczynski et al. (2020). Here we use input physics from model M30 of that paper except for two important differences: First, instead of using the initial mass ratio distribution from Sana et al. (2012), which allows only $q = 0.1$ –1.0, we now extend

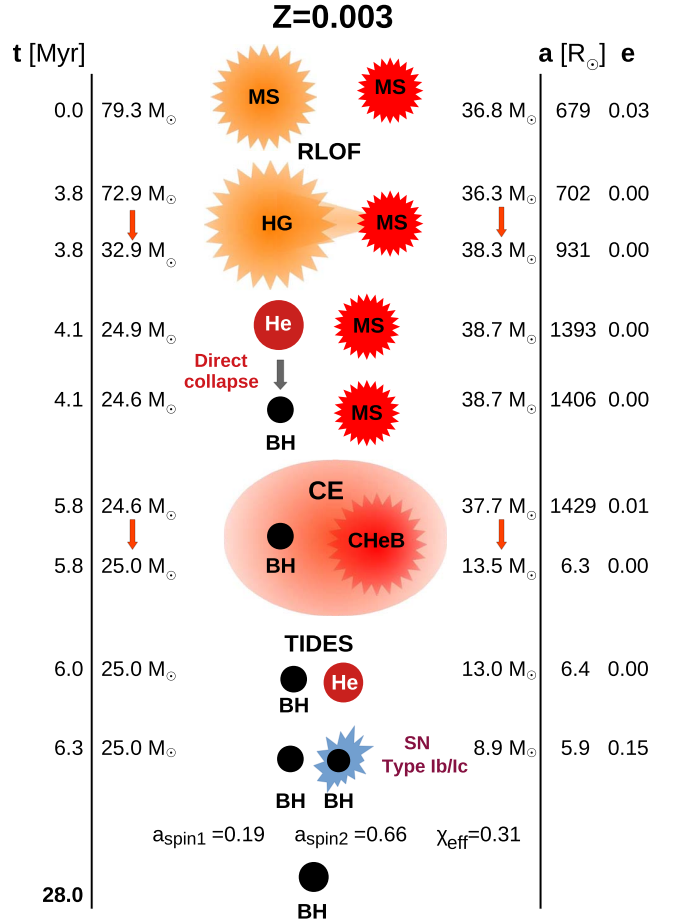


Figure 1. Evolution of an isolated binary system that produces a BH–BH merger resembling GW190412 (see Section 3 for details). MS: main sequence star, HG: Hertzsprung gap star, CHeB: core helium-burning star, He: naked helium star, BH: black hole, RLOF: Roche lobe overflow, CE: common envelope.

this distribution to lower mass ratios $q = q_{\text{min}} - 1.0$, where q_{min} is chosen in such a way that a star mass is allowed to reach the hydrogen burning limit $M_{\text{ZAMS}} = 0.08 M_{\odot}$. Second, for cases in which we do not know whether we should apply thermal timescale RLOF or CE for systems with NS/BH accretors, we use a specific diagnostic diagram to decide between thermal RLOF and CE (see Section 5.2 of Belczynski et al. 2008a). In this single step of binary evolution we previously applied our older numerical approximation of the calculation of accretion onto NS/BH presented in Belczynski et al. (2008b) instead of our newly adopted analytic approach (King et al. 2001; Mondal et al. 2020). These two changes increase the estimated total BH–BH merger rate in the local universe ($z \sim 0$) from $43.7 \text{ Gpc}^{-3} \text{ yr}^{-1}$ (model M30.B; Belczynski et al. 2020) to $73.5 \text{ Gpc}^{-3} \text{ yr}^{-1}$ (this study; see below).

3. Example of Evolution

In Figure 1 we present an example of the evolution of a binary system that leads to the formation of close BH–BH systems consistent with the parameters estimated for GW190412. This system was picked from the most populated formation channel of BH–BH mergers with $q < 0.41$ (see Table 1). This system has both BH masses and primary BH spin a_{spin1} within the range of 90% uncertainties given by The

Table 1
Evolutionary Channels for $q < 0.41$ BH–BH Mergers

No.	Evolutionary History ^a	\mathcal{R}_1^b	\mathcal{R}_2^c	\mathcal{R}_3^d	\mathcal{R}_4^e
1	RLOF1 BH1 CE2 BH2	5.90	0.49	0.11	0.11
2	RLOF1 BH1 RLOF2 CE2 BH2	0.76	0.04	0.01	0.01
3	RLOF1 BH1 CE2 RLOF2 BH2	0.02	0.01	0.00	0.00
4	OTHER CHANNELS	0.11	0.00	0.01	0.00
All		6.79	0.54	0.13	0.11

Notes.

^a RLOF: stable Roche lobe overflow, CE: common envelope, BH: black hole formation, 1: indicates primary (initially more massive star), 2: secondary star being donor in RLOF or CE.

^b Merger rate density ($\text{Gpc}^{-3} \text{yr}^{-1}$) for systems with $q < 0.41$.

^c Above and $24.4 < m_1/M_\odot < 34.7$ and $7.4 < m_2/M_\odot < 10.1$.

^d Above and $0.17 < a_{\text{spin},a} < 0.59$.

^e Above and $0.14 < \chi_{\text{eff}} < 0.34$.

LIGO Scientific Collaboration & the Virgo Collaboration (2020).

This system, with initial primary mass $\sim 79 M_\odot$ and secondary mass $\sim 37 M_\odot$, is formed in a low-metallicity environment $Z = 0.003$ ($\sim 0.1 Z_\odot$) with an initial separation of $a \sim 680 R_\odot$ and eccentricity $e \sim 0.03$. When the more massive star leaves the main sequence, the system circularizes ($e = 0.0$) at the onset of the stable RLOF phase, during which the donor (primary star) loses a significant amount (over 50%) of its mass. After finishing its nuclear evolution, the primary undergoes direct collapse and forms a first BH with no natal kick and no associated SN explosion. After the secondary leaves the main sequence and becomes a core helium-burning giant, the system enters a CE phase during which the secondary loses its H-rich envelope. The system separation decreases to only $a \sim 6 R_\odot$. After CE, the secondary is a massive naked helium WR star. The binary separation is so small that the secondary is subject to strong tidal interactions and is spun up. At time $t = 6.3 \text{ Myr}$ since the start of the evolution, the secondary explodes as a Type Ib/c SN (mass ejection of $\sim 3.0 M_\odot$; 3D natal kick of $v_{\text{kick}} = 98 \text{ km s}^{-1}$) and forms a second BH. Due to the small orbital separation, the two BHs, now with a mass ratio of $q = 0.36$, merge in just $\sim 21.7 \text{ Myr}$.

The first BH forms with a spin $a_{\text{spin}1} = 0.13$ (calculated from MESA single stellar models with Spruit 1999 angular momentum transport; see Figure 2 of Belczynski et al. 2020) that is perfectly aligned with the binary angular momentum ($\theta_1 = 0 \text{ deg}$). Had we adopted more efficient angular momentum transport in stars (Fuller & Ma 2019; Fuller et al. 2019; Ma & Fuller 2019) than employed in the standard MESA then primary BH spin would change to $a_{\text{spin}1} \sim 0.01$. This BH accretes in CE and during stable RLOF from its companion ($\sim 0.4 M_\odot$) and increases its spin to $a_{\text{spin}1} = 0.19$. The second, lower mass, BH forms with spin $a_{\text{spin}2} = 0.66$ that is slightly misaligned by its natal kick to $\theta_2 = 5 \text{ deg}$. The spin magnitude is obtained from rapidly spinning MESA naked helium star models with spins that correspond to a tidally locked star for a given orbital period in our binary models (see Equation (15) of Belczynski et al. 2020). The effective spin parameter of this BH–BH merger is $\chi_{\text{eff}} = 0.31$, within the LIGO/Virgo range for GW190412 (0.14–0.34). It is noted that, for the virtually aligned geometry of BH spins with binary angular momentum in this example, we do not expect any precession. Yet, there seems to be marginal evidence for precession in GW190412.

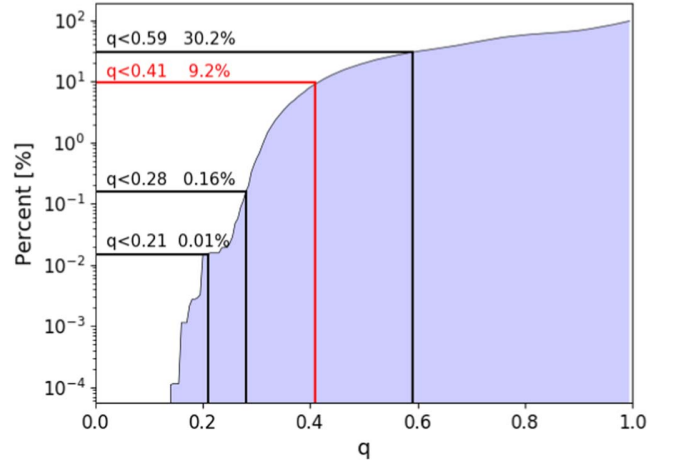


Figure 2. Cumulative fraction of merging BH–BH systems with mass ratio smaller than q in the local universe ($z \sim 0$). Fractions for selected mass ratios $q < 0.21$ (0.01%), $q < 0.28$ (0.16%), and $q < 0.59$ (30.2%) are marked with black lines. The red line marks $q < 0.41$, indicating that 9.2% of our simulated binary mergers at $z \sim 0$ are consistent with the 90% upper limit on q for GW190412.

We provide a discussion of precession in Section 5 and Appendix A.

One might be tempted to identify phase 4 (just before CE in Figure 1) of the evolution of our binary system with high-mass X-ray binaries of the Cyg X-1 type ($M_{\text{BH}} = 14.8 M_\odot$, O star companion $M_O = 19.2 M_\odot$ and orbital period of $P_{\text{orb}} = 5.6 \text{ days}$;⁶ this corresponds to a semimajor axis of $a = 43 R_\odot$). However, Cyg X-1 is an active system (it accretes from a wind), which implies an orbital separation that is too tight to allow survival of the subsequent CE phase (Belczynski et al. 2012). If it instead undergoes a stable RLOF (Pavlovskii & Ivanova 2015; Pavlovskii et al. 2017) then the orbit will widen beyond the limit ($a \sim 50 R_\odot$) for two BHs to merge within a Hubble time. We note that BH–BH progenitors in our simulations are initially very wide ($a \gtrsim 1000 R_\odot$) binaries so they can successfully survive the CE phase (de Mink & Belczynski 2015).

4. Population of Low- q BH–BH Mergers

Our simulation results in a $z \sim 0$ population of merging BH–BH systems with a local rate density of $\mathcal{R}_0 = 73.5 \text{ Gpc}^{-3} \text{yr}^{-1}$. The cumulative distribution of mass ratios for these mergers is presented in Figure 2. In this model the majority of BH–BH mergers ($\sim 80\%$) have large mass ratios ($q > 0.5$), consistent with previous results (Belczynski et al. 2016b). Here we focus on the tail of the distribution extending to more extreme mass ratios. Our model predicts very few systems with mass ratios smaller than the average value reported for GW190412: 0.16% of binaries have $q < 0.28$. However, we report a more significant fraction of systems with mass ratios smaller than the 90% upper bound on GW190412: 9.2% at $q < 0.41$. This fraction becomes significantly higher for the 99% upper bound on GW190412: 30.2% at $q < 0.59$.

In Table 1 we show evolutionary sequences that lead to the formation of BH–BH mergers with small mass ratios: $q < 0.41$. We list the merger rate density arising for typical evolutionary sequences. These are $z \sim 0$ rate densities and are

⁶ https://universeathome.pl/universe/black_holes.php

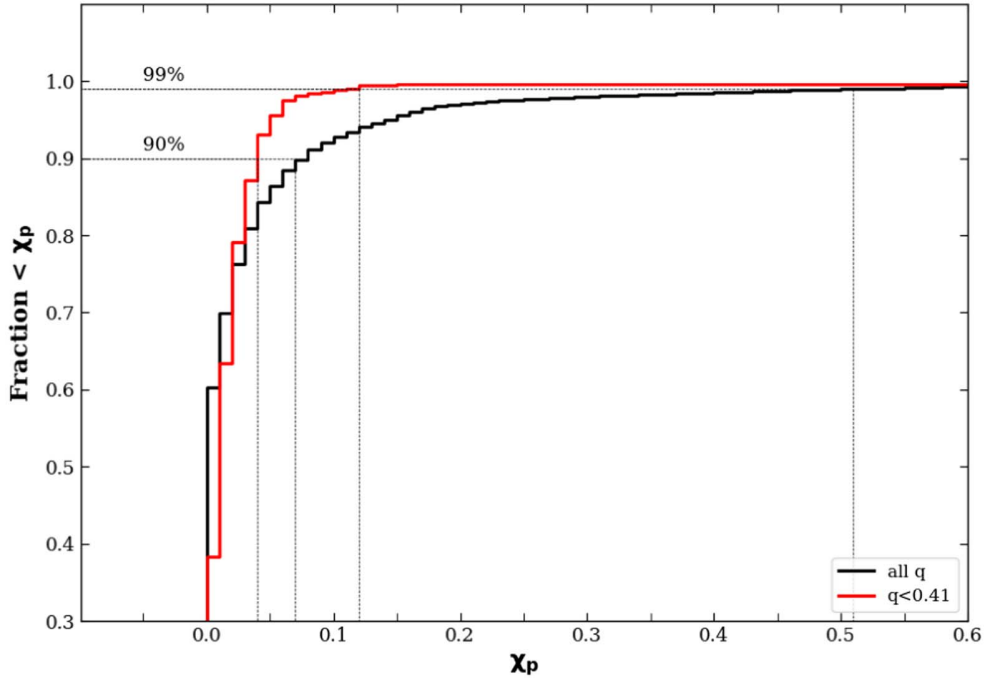


Figure 3. Cumulative distribution of precession parameter χ_p of BH–BH mergers in the local universe ($z \sim 0$). Black line—overall BH–BH population; red line—sub-population of BH–BH mergers with mass ratio $q < 0.41$. Results for standard model: Spruit–Taylor BH spins + natal kicks lowered by fallback and partial tidal interactions.

subpopulations of the overall local BH–BH merger population ($\mathcal{R}_0 = 73.5 \text{ Gpc}^{-3} \text{ yr}^{-1}$). The table presents merger rate densities for BH–BH systems that are increasingly constrained to resemble GW190412:

1. \mathcal{R}_1 : $q < 0.41$,
2. \mathcal{R}_2 : $q < 0.41$ and $24.4 < m_1/M_\odot < 34.7$ and $7.4 < m_2/M_\odot < 10.1$,
3. \mathcal{R}_3 : $q < 0.41$ and $24.4 < m_1/M_\odot < 34.7$ and $7.4 < m_2/M_\odot < 10.1$ and $0.17 < a_{\text{spin},a} < 0.59$,
4. \mathcal{R}_4 : $q < 0.41$ and $24.4 < m_1/M_\odot < 34.7$ and $7.4 < m_2/M_\odot < 10.1$ and $0.17 < a_{\text{spin},a} < 0.59$ and $0.14 < \chi_{\text{eff}} < 0.34$.

The overall rate of systems with $q < 0.41$ is $\mathcal{R}_1 = 6.8 \text{ Gpc}^{-3} \text{ yr}^{-1}$, which corresponds to $\sim 10\%$ of our overall predicted local merger rate density of BH–BH systems ($\mathcal{R}_0 = 73.5 \text{ Gpc}^{-3} \text{ yr}^{-1}$). This is consistent with the LIGO/Virgo estimate of the fraction of low-mass ratio systems as inferred from the detection of GW190412 combined with previous detections. We emphasize that Figure 2 shows the distribution of the mass ratios for *all* merging binaries in the local universe, which may be different from the distribution of *detected* binaries because it does not incorporate gravitational-wave (GW) selection effects. This is not expected to lead to a significant effect in the case of mass ratio distributions (e.g., see Figure 4 of Fishbach & Holz 2020). In addition, it is to be noted that the LIGO/Virgo estimate of $\gtrsim 10\%$ of binaries having $q \lesssim 0.4$ (The LIGO Scientific Collaboration & the Virgo Collaboration 2020) is for the true (intrinsic) population, not the detected population. This estimate is thus directly comparable to the results from Figure 2.

To produce a low-mass ratio system with a primary BH as massive as $30 M_\odot$, a progenitor binary needs to have (i) one very massive component ($M_{\text{ZAMS}} \gtrsim 70 M_\odot$), and (ii) rather

low initial stellar mass ratio ($q_{\text{ZAMS}} < 0.5$). In addition, the progenitor binary needs to have low metallicity $Z \lesssim 10\% Z_\odot$ ($\lesssim 0.002$; Belczynski et al. 2010a). These systems are uncommon, leading to a dearth of small mass ratio BH–BH mergers such as GW190412.

5. Discussion and Conclusions

The existence of unequal-mass binary BHs is to be expected within the isolated binary evolution formation scenario. The mass ratios of such systems were initially investigated by Bulik et al. (2004). They found that in the standard scenario one expects BH–BH systems with high mass ratios above 0.7 to dominate; however, varying the efficiency of the CE evolution phase leads to the formation of systems with mass ratios less than 0.5. Although our knowledge of binary evolution and BH–BH formation has subsequently improved, this result appears robust and remains valid. Dominik et al. (2012) have shown the distribution of mass ratios of BH–BH systems in their Figure 9. They find that for sub-solar metallicity a significant fraction of these mergers have mass ratio less than 0.5. An additional hint for the existence of unequal-mass BH–BH systems from isolated binary evolution comes from the analysis of the future evolution of Cyg X-3 (Belczynski et al. 2013). This system will lead to formation of either a BH–NS or BH–BH binary; in the latter case, the mass ratio is expected to be below 0.6. Systems with BH masses similar to GW190412 are also found in results from isolated binary evolution calculations by other groups (e.g., see Figure 5 of Eldridge & Stanway 2016).

The formation channel of GW190412 was considered by Di Carlo et al. (2020, p. 8) both through dynamical formation in open clusters and through the classical isolated binary evolution channel as discussed here. That group finds that systems like GW190412: “can be matched only by dynamical BH–BH born from metal-poor progenitors, because isolated

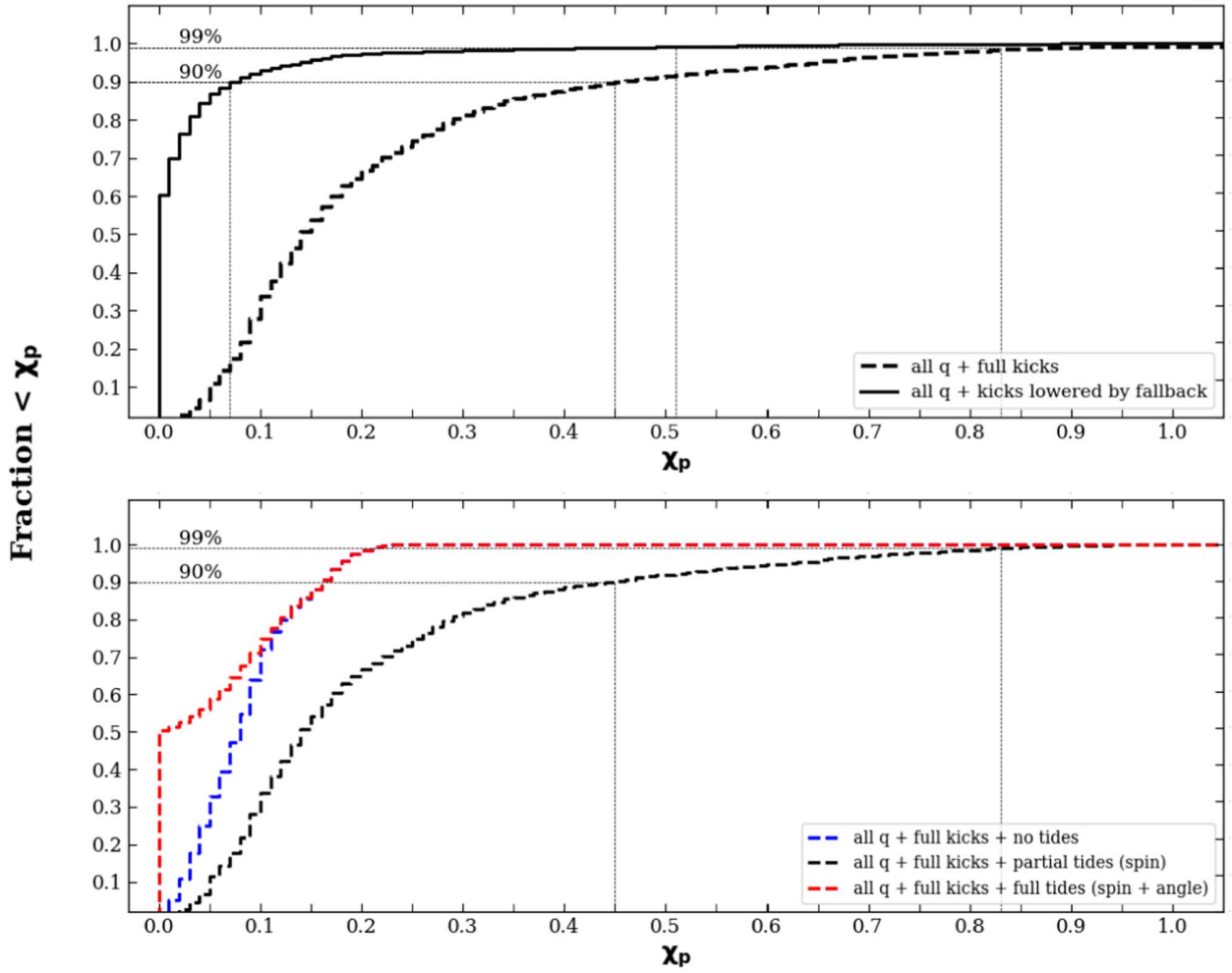


Figure 4. Cumulative distribution of precession parameter χ_p of BH–BH mergers in the local universe ($z \sim 0$). Top panel: solid black line—overall BH–BH population with standard natal kicks lowered by fallback; dashed black line—overall BH–BH population with full natal kicks. Bottom panel: blue dashed line—overall BH–BH population with full natal kicks and no tidal interactions on WR stars; black dashed line—overall BH–BH population with full natal kicks and partial tidal interactions on WR stars (spin magnitude); red dashed line—overall BH–BH population with full natal kicks and full tidal interactions on WR stars (spin magnitude and angles).

binaries can hardly account for its mass ratio in our models.” Unlike them, we find that systems like GW190412 are naturally formed by isolated binaries in a small but significant fraction of systems. Note also that the model that we use to account for the formation of GW190412 has also been used to explain the merger rates, masses, and low effective spins of the full O1/O2 LIGO/Virgo BH–BH merger sample (Belczynski et al. 2020).

Mandel & Fragos (2020) have questioned the LIGO/Virgo conclusion that the non-negligible positive effective spin parameter for GW190412 has its origin from a moderate/high spin of the primary (more massive) BH in GW190412 ($a_{\text{spin}1} = 0.17 - 0.59$). Instead, Mandel & Fragos (2020) point out that in the classical isolated binary evolution scenario some second-born BHs may form from tidally spun-up helium stars, and that the resulting BHs are expected to have high spins. Using priors consistent with this, they perform an alternate analysis of GW190412, which finds that the primary BH has negligible spin ($a_{\text{spin}1} \sim 0$) while the secondary BH has high spin ($a_{\text{spin}2} = 0.64 - 0.99$). This possibility is also consistent with our results: we find that in $\sim 30\%$ of local BH–BH mergers with $q < 0.41$, tidal interactions are strong enough to produce a lower mass BH with spin $a_{\text{spin}2} > 0.64$.

For example, in Figure 1 we show a system that forms a very close ($a \sim 4 R_\odot$) binary with a BH and a naked helium star (this is the evolutionary phase just prior BH–BH formation). This naked helium star is subject to tidal spin-up, and instead of forming a slowly spinning BH, it forms a rapidly spinning BH ($a_{\text{spin}2} = 0.66$). However, in contrast with Mandel & Fragos (2020) we do not assume that the primary BH spin is negligible. Instead, we calculate the natal BH spins (if not affected by tides) from single stellar models allow for spin increase due to accretion during binary mass transfer phases (see Section 2). The primary BH spins are found to be small, but not negligible. For the case shown in Figure 1, the natal primary BH spin is $a_{\text{spin}1} = 0.11$ and then it is increased to $a_{\text{spin}1} = 0.19$ through accretion in a CE event. Because both spins are closely aligned with the binary angular momentum (the secondary is slightly misaligned due to a small natal kick, to $\theta_2 = 5$ deg), the effective spin parameter of this system is $\chi_{\text{eff}} = 0.31$, which is consistent with the upper end of the LIGO/Virgo 90% probability estimate for GW190412.

GW190412 shows some weak evidence for misaligned spins, with a non-zero precession parameter: $\chi_p = 0.15 - 0.49$ (90% credible limits). In this system, the amount of observed

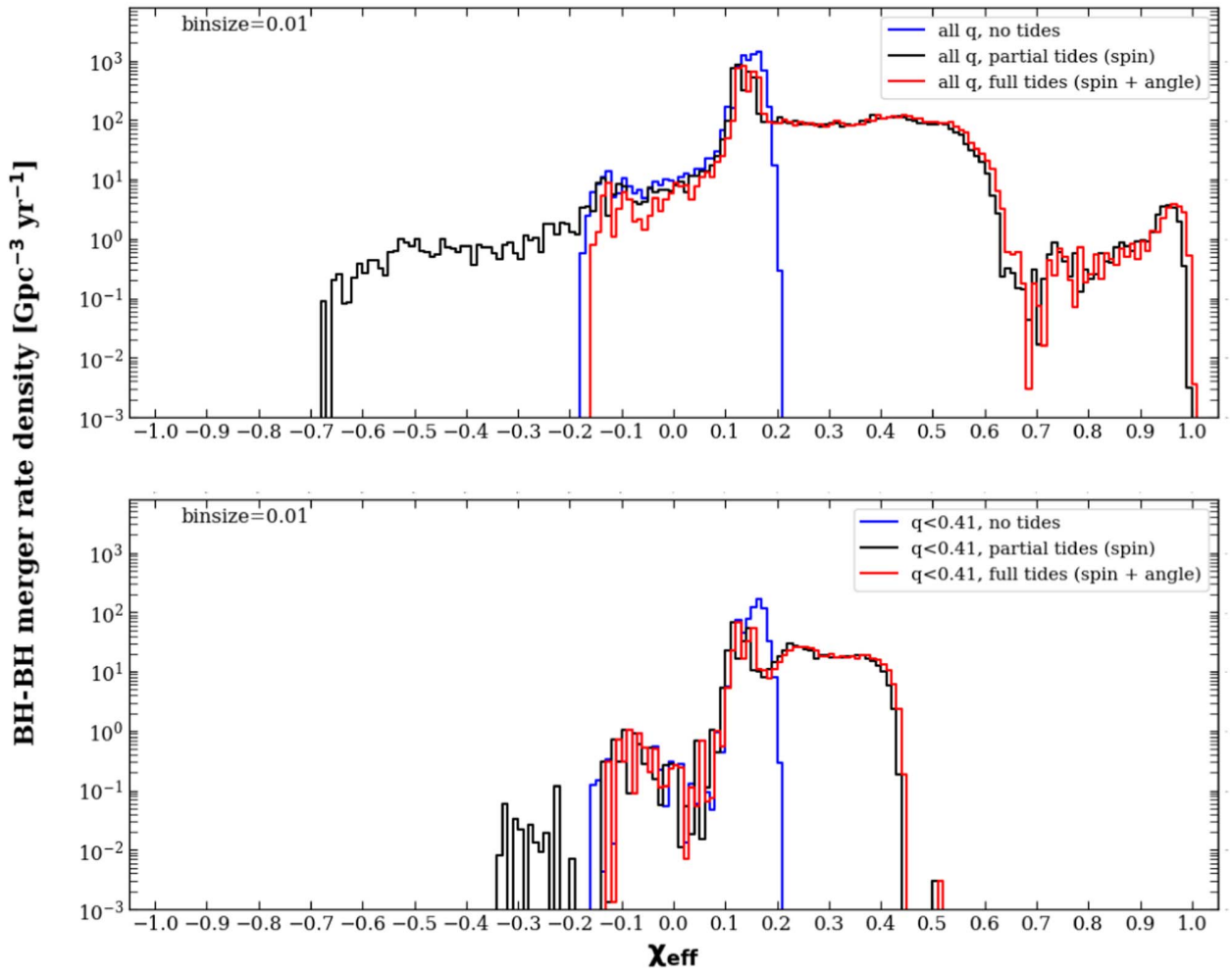


Figure 5. Distribution of effective spin parameter χ_{eff} of BH–BH mergers in the local universe ($z \sim 0$) for different approaches to tides: blue line—no tides; black line—partial tides; red line—full tides. Top panel: overall BH–BH population. Bottom panel: sub-population of BH–BH mergers with mass ratio $q < 0.41$. Results for standard model: Spruit–Tayler BH spins + natal kicks lowered by fallback.

precession is consistent with noise (see Figure 6 of The LIGO Scientific Collaboration & the Virgo Collaboration 2020), and the mild preference for $\chi_p > 0$ disappears when the GW data is re-analyzed with different priors on the spin magnitudes (Zevin et al. 2020). Nevertheless, it is interesting to explore whether a clear observation of precession would be consistent with our models. In our evolutionary example (see Figure 1) we do not expect to produce any precessing systems as both BHs are almost fully aligned with the binary angular momentum. Some degree of misalignment would appear in our model if, for example, we added a larger natal kick at the formation of the second BH. At this point the binary is so tight that even a large kick would have only a small chance to disrupt this binary. The small natal kick applied to the second BH formed through partial fallback results from the simple assumption that natal kicks scale inversely with the amount of the fallback (Fryer et al. 2012) but little is known about BH natal kicks (Repetto & Nelemans 2015; Belczynski et al. 2016c; Mandel 2016; Repetto et al. 2017; Gandhi et al. 2020). We have estimated the precession parameter for all the BH–BH mergers produced by our model (see Appendix A). The cumulative distribution of χ_p (Figure 3) shows that BH–BH mergers are dominated by low precession parameter values for our standard model (small

natal BH kicks). We calculated several additional models adopting high BH natal kicks, and a different approach to tidal spin-up of BH progenitors to be able to provide exclusion statements. If an analysis of the LIGO/Virgo BH–BH population finds that more than 10% of BH–BH mergers have large in-plane spin components ($\chi_p > 0.5$), then a CE isolated binary BH–BH formation channel can be excluded as their origin. This conclusion is valid if (i) stars in binaries are born with aligned spins, and (ii) angular momentum transport in massive stars is efficient (driven by magnetic dynamo) producing low natal BH spins ($a_{\text{spin}} < 0.2$), unless BH progenitor stars are subject to tidal spin-up. Furthermore, this conclusion is independent of the BH natal kick model or the action of tides on WR stars in close binaries. A similar statement can be made for possible future signals from highly mass asymmetric BH–BH systems with large $\chi_{\text{eff}} \gtrsim 0.5$. We show distributions of effective spin parameter for the overall local BH–BH mergers and the low-mass ratio BH–BH sub-population (Figure 5). This figure indicates that the effective spin values for low- q sub-population are systematically smaller and limited to $|\chi_{\text{eff}}| \leq 0.5$.

We have shown that the isolated classical binary evolution channel can form binaries similar to GW190412. This is an

important explicit proof-of-principle demonstration that the event GW190412 may be the result of isolated evolution. Furthermore, Figure 2 shows that the detection of a binary with a mass ratio of $q \lesssim 0.4$ is to be expected within the current GW sample, because this sub-population constitutes $\sim 10\%$ of the total population. We find that, if GW190412 formed via the classical isolated binary channel, it likely evolved from a low-metallicity ($Z < 10\% Z_{\odot}$) progenitor system with initial mass ratio $q < 0.5$ between the two massive stars, but that otherwise the system followed an evolutionary path that is typical of the majority of BH–BH mergers (Belczynski et al. 2016b). Over the coming years the population of GW BH–BH mergers is expected to grow to many hundreds of detections. These will facilitate detailed population studies, including a determination of the distribution of mass ratios. While the existing population of BH–BH mergers can be explained using classical isolated binary evolution, the discovery of a large population of binaries with mass ratio $q < 0.2$ would pose a significant challenge to our models.

We would like to thank the anonymous referee for their useful comments. K.B. and A.O. acknowledge support from the Polish National Science Center (NCN) grant Maestro (2018/30/A/ST9/00050). J.P.L. was supported in part by the French Space Agency CNES. T.B. was supported by TEAM/2016-3/19 grant from FNP. D.E.H. was supported by NSF grant PHY-1708081, as well as the Kavli Institute for Cosmological Physics at the University of Chicago through an endowment from the Kavli Foundation. D.E.H. also gratefully acknowledges support from the Marion and Stuart Rice Award. M.C.M. thanks the Radboud Excellence Initiative for supporting his stay at Radboud University.

Appendix A Precession Parameter

The LIGO/Virgo Collaboration gave an estimate of the GW190412 precession parameter χ_p , which is spin-dependent parameter expressed by the formula (Schmidt et al. 2015; Gerosa et al. 2020):

$$\chi_p = \max \left[a_{\text{spin1}} \sin \theta_1, a_{\text{spin2}} \sin \theta_2 \frac{q(4q+3)}{(4+3q)} \right]. \quad (2)$$

The value of χ_p given by LIGO/Virgo is in the range of 0.15–0.49 (90% credible limits). This is unique among the other BH–BH merger detections for which the precession parameter was uninformative, and consistent with $\chi_p = 0$ (corresponding to perfectly aligned spins). GW190412 shows weak evidence for precession, we note that the measurement remains inconclusive, and small values of $\chi_p < 0.1$ cannot be ruled out (The LIGO Scientific Collaboration & the Virgo Collaboration 2020; Zevin et al. 2020). Although χ_p is poorly measured for individual GW events, combining multiple observations will reveal the population distribution of χ_p . This will provide a powerful test of our models, as we discuss below.

We calculated distributions of precession parameter values for our standard model and its several variations.

The cumulative distribution of χ_p for our standard model is shown in Figure 3. For the overall BH–BH population merging at $z \sim 0$ as well as for the low-mass ratio sub-population

($q < 0.41$), the distribution is dominated by low precession parameters values: 90% of overall BH–BH binaries have precession parameter $\chi_p < 0.07$ while 99% have $\chi_p < 0.51$. Low mass ratio BH–BH mergers have even lower values: 90% of the systems have $\chi_p < 0.04$ and 99% have $\chi_p < 0.11$. The reason for the difference between those two populations is the relation between natal kicks and the mass of resulting compact object. Less massive BHs usually get higher natal kicks, so precession is more likely in mergers with low-mass BHs. In the low-mass ratio mergers, one of the BHs is always massive, and is formed through direct collapse (without a SN explosion). In contrast, in the overall BH–BH population, there are cases of mergers with two low-mass BHs that may form with high natal kicks. High natal kicks increase the degree of misalignment and subsequently increase χ_p .

To test the maximum allowed level of precession in our isolated binary evolution model, we increase BH natal kicks to the high speeds observed for single pulsars in the Galaxy (Maxwellian distribution with $\sigma = 265 \text{ km s}^{-1}$; Hobbs et al. 2005), and apply these natal kicks to all BHs independent of their mass. In this model, the distribution of precession parameters shifted to higher values, with 90% of all BH–BH mergers (any q) having $\chi_p < 0.43$ and 99% having $\chi_p < 0.82$ (see top panel of Figure 4). Note that our standard model employs BH natal kicks decreased by fallback, and in practice, massive BHs ($M \gtrsim 10\text{--}15 M_{\odot}$) do not receive natal kicks.

We have also tested the effect of tidal interactions between a WR star (an immediate BH progenitor in our models) and its massive companion on precession parameters. Three variants of approach to tides are shown in the bottom panel of Figure 4. Note that tides may change misalignment angles and BH natal spin magnitude affecting the value of χ_p . We perform this analysis on high natal BH kick model to maximize the effect of tides. We tested a variant with no tidal interactions on WR stars (no tides), a variant in which tides only affect spin magnitude (partial tides: our standard model approach), and a variant in which tides affect spin magnitude and cause alignment of a WR star with binary angular momentum (full tides; note that this star spin may be misaligned if earlier natal kick on the other star shifted binary angular momentum vector).

We find that among these three drastically different approaches to tides, our standard model (partial tides) may be considered as an upper limit on χ_p parameter value. For both the no-tides and full-tides variants 90% of systems have $\chi_p \lesssim 0.2$ while 99% of systems have $\chi_p \lesssim 0.15$, which is much less than for the variant with partial tides (for 90% $\chi_p < 0.43$ and for 99% $\chi_p < 0.82$). The lower limit on χ_p values in the no-tides variant is simply related to the fact that the BH spin magnitudes are not increased due to tidal interactions in the WR phase. In the case of full tides the sharp increase in fraction of systems near $\chi_p \sim 0$ is generated due to the assumption about the WR star spin alignment with the system angular momentum so the part of the formula corresponded to a given BH (Equation (2)) takes the value of zero. Those differences cause the removal of systems with high χ_p from the distribution for the no-tides and full-tides variants as contrasted with our partial-tides model.

In Figure 5 we present effective spin χ_{eff} distribution in our standard model for three different approaches to tides. In the top panel there is a distribution for overall BH–BH population merging at $z \sim 0$ and in the bottom panel we show distribution for low-mass ratio sub-population with $q < 0.41$. Adopted

tides approaches gives different results, especially for overall BH–BH population. In the no-tides approach both distributions (overall and low q) are similarly dominated by low effective spin parameter and the absolute value is limited to $|\chi_{\text{eff}}| < 0.2$. In the partial-tides and full-tides approaches the possible absolute value of effective spin widens to around $|\chi_{\text{eff}}| < 0.5$ for low-mass ratio sub-population while in overall population effective spin may take values up to 1.0. This is caused by the fact that for the overall BH–BH population there are more possible evolutionary scenarios in which both objects could be the subject of WR tides.

Based on our results we may conclude that if an analysis of the LIGO/Virgo BH–BH population reveals that more than 10% of systems have high precession ($\chi_p \leq 0.5$) then the CE isolated binary BH–BH formation channel can be excluded as their origin. This conclusion is valid if (i) stars in binaries are born with aligned spins and (ii) natal BH spins are low ($a_{\text{spin}} < 0.2$) unless their progenitor stars are subject to strong tidal interactions, and is independent of the BH natal kick model or the action of tides on WR stars in close binaries. We note that we have assumed in all our simulations that stellar spins are aligned with the binary angular momentum at zero-age main sequence, that only natal kicks at BH formation may misalign stellar/BH spins, and that only tidal interactions can realign stellar spins. A similar statement can be made for possible future signals from highly mass asymmetric BH–BH systems with large $\chi_{\text{eff}} \gtrsim 0.5$. Distributions indicates that the effective spin values for low- q sub-population are systematically smaller and limited to $|\chi_{\text{eff}}| \leq 0.5$.

Appendix B Accretion during CE Phase

Here we describe the procedure of calculating the accretion rate onto the BH during the CE phases. The procedure is based on Equations (5.3)–(5.7) of Bethe & Brown (1998) and Equations (A1)–(A10) from Belczynski et al. (2002).

In our calculations CE begins once BH companion (CE donor) expands beyond its Roche lobe and mass transfer is determined to proceed on a dynamical timescale (Belczynski et al. 2008a). CE evolution and accretion onto the BH ends when the donor’s envelope is ejected and the donor mass is reduced to the mass of its core. We use the following symbols: M_A —mass of the BH, M_B —mass of the donor, $M_{B,\text{core}}$ —mass of the donor’s core, A —orbital separation (semimajor axis).

First, we compare energy-loss rate related to the accretion onto the BH and the rate of the orbital energy dissipation due to the dynamical friction of BH in the donor’s envelope:

$$\dot{E}_{\text{acc}} = -\dot{E}_{\text{orb}}. \quad (3)$$

The formula for \dot{E}_{acc} is introduced by Equations (5.3)–(5.7) in Bethe & Brown (1998) and (A1) Belczynski et al. (2002) while \dot{E}_{orb} is expressed by Equation (A2) Belczynski et al. (2002). Note, that \dot{E}_{acc} include mass accretion rate \dot{M}_A given by the Bondi–Hoyle–Lyttleton theory. Comparing the time derivatives of both energies we obtain the first time-independent differential equation, which contains $\frac{dM_A}{dM_B}$ and $\frac{dA}{dM_B}$ (Equation (A3) of Belczynski et al. 2002).

Second, we compare the donor’s envelope binding energy with the orbital energy, since CE is ejected on the expense of the binary orbital energy with an efficiency described by parameter α_{CE} . Formulas for both energies are given by

Equations (A4) and (A5) of Belczynski et al. (2002). We then take donor’s mass derivative

$$\frac{dE_{\text{bind}}}{dM_B} = -\alpha_{\text{CE}} \left(\frac{E_{\text{orb}}}{dM_B} \right) \quad (4)$$

to obtain the second equation containing $\frac{dM_A}{dM_B}$ and $\frac{dA}{dM_B}$ (Equation (A7) of Belczynski et al. 2002). Therefore, we can rearrange the two above equations to have two ordinary differential equations, one for increasing mass of BH, and one for decreasing orbital separation. We solve them within realistic limits: using donor’s envelope mass (CE), which is known (in contrast to integrating over unknown timescale of CE). We integrate from pre-CE donor mass (M_B) to its post-CE mass ($M_{B,\text{core}}$) to obtain the final binary separation and final mass of the accreting BH.

We assume that accretion onto a BH is always set by the Bondi rate (as implemented above). However, we take into account the fact that not entire infalling/accreting mass is actually accumulated onto a BH. Some of the accreting mass is lost before reaching BH (e.g., angular momentum barrier in asymmetric flow around BH (MacLeod & Ramirez-Ruiz 2015), accretion disk winds; see Mondal et al. 2020 and references therein). We allow only some fraction of accreting mass to accumulate into a BH increasing its mass and spin. In particular, we estimate accretion mass ΔM_{bondi} assuming that accretion proceeds with Bondi rate (i.e., integrating Equation (A9) of Belczynski et al. 2002), and we adopt that only 5% of this mass actually accumulates on the BH (ΔM_{accu}):

$$\Delta M_{\text{accu}} = 0.05 \Delta M_{\text{bondi}}. \quad (5)$$

ORCID iDs

A. Olejak  <https://orcid.org/0000-0002-6105-6492>
M. Fishbach  <https://orcid.org/0000-0002-1980-5293>
D. E. Holz  <https://orcid.org/0000-0002-0175-5064>
J.-P. Lasota  <https://orcid.org/0000-0002-6171-8396>
M. C. Miller  <https://orcid.org/0000-0002-2666-728X>
T. Bulik  <https://orcid.org/0000-0003-2045-4803>

References

- Abbott, B. P., Abbott, R., Abbott, T. D., et al. 2019a, *ApJL*, **882**, L24
Abbott, B. P., Abbott, R., Abbott, T. D., et al. 2019b, *PhRvX*, **9**, 031040
Abbott, R., Abbott, T. D., Abraham, S., et al. 2020, *ApJL*, **896**, L44
Antonini, F., & Perets, H. B. 2012, *ApJ*, **757**, 27
Antonini, F., Toonen, S., & Hamers, A. S. 2017, *ApJ*, **841**, 77
Arca-Sedda, M., & Capuzzo-Dolcetta, R. 2019, *MNRAS*, **483**, 152
Arca-Sedda, M., Li, G., & Kocsis, B. 2018, arXiv:1805.06458
Askar, A., Szkudlarek, M., Gondek-Rosińska, D., Giersz, M., & Bulik, T. 2017, *MNRAS*, **464**, L36
Bae, Y.-B., Kim, C., & Lee, H. M. 2014, *MNRAS*, **440**, 2714
Banerjee, S. 2018, *MNRAS*, **473**, 909
Bavera, S. S., Fragos, T., Qin, Y., et al. 2020, *A&A*, **635**, A97
Belczynski, K., Bulik, T., & Fryer, C. L. 2012, arXiv:1208.2422
Belczynski, K., Bulik, T., Fryer, C. L., et al. 2010a, *ApJ*, **714**, 1217
Belczynski, K., Bulik, T., Mandel, I., et al. 2013, *ApJ*, **764**, 96
Belczynski, K., Dominik, M., Bulik, T., et al. 2010b, *ApJL*, **715**, L138
Belczynski, K., Heger, A., Gladysz, W., et al. 2016a, *A&A*, **594**, A97
Belczynski, K., Holz, D. E., Bulik, T., & O’Shaughnessy, R. 2016b, *Natur*, **534**, 512
Belczynski, K., Kalogera, V., & Bulik, T. 2002, *ApJ*, **572**, 407
Belczynski, K., Kalogera, V., Rasio, F. A., et al. 2008a, *ApJS*, **174**, 223
Belczynski, K., Klencki, J., Fields, C. E., et al. 2020, *A&A*, **636**, A104
Belczynski, K., Repetto, S., Holz, D. E., et al. 2016c, *ApJ*, **819**, 108

- Belczynski, K., Taam, R. E., Rantsiou, E., & van der Sluys, M. 2008b, *ApJ*, **682**, 474
- Benacquista, M. J., & Downing, J. M. B. 2013, *LRR*, **16**, 4
- Bethe, H. A., & Brown, G. E. 1998, *ApJ*, **506**, 780
- Bond, J. R., & Carr, B. J. 1984, *MNRAS*, **207**, 585
- Bulik, T., Gondek-Rosinska, D., & Belczynski, K. 2004, *MNRAS*, **352**, 1372
- Chatterjee, S., Rodriguez, C. L., Kalogera, V., & Rasio, F. A. 2017, *ApJL*, **836**, L26
- de Mink, S. E., & Belczynski, K. 2015, *ApJ*, **814**, 58
- de Mink, S. E., & Mandel, I. 2016, *MNRAS*, **460**, 3545
- Di Carlo, U. N., Giacobbo, N., Mapelli, M., et al. 2019, *MNRAS*, **487**, 2947
- Di Carlo, U. N., Mapelli, M., Giacobbo, N., et al. 2020, *MNRAS*, **498**, 495
- Dominik, M., Belczynski, K., Fryer, C., et al. 2012, *ApJ*, **759**, 52
- Downing, J. M. B., Benacquista, M. J., Giersz, M., & Spurzem, R. 2010, *MNRAS*, **407**, 1946
- du Buisson, L., Marchant, P., Podsiadlowski, P., et al. 2020, arXiv:2002.11630
- Eldridge, J. J., & Stanway, E. R. 2016, *MNRAS*, **462**, 3302
- Fishbach, M., & Holz, D. E. 2020, *ApJL*, **891**, L27
- Fragione, G., Grishin, E., Leigh, N. W. C., Perets, H. B., & Perna, R. 2019, *MNRAS*, **488**, 47
- Fragione, G., & Kocsis, B. 2019, *MNRAS*, **486**, 4781
- Fryer, C. L., Belczynski, K., Wiktorowicz, G., et al. 2012, *ApJ*, **749**, 91
- Fuller, J., & Ma, L. 2019, *ApJL*, **881**, L1
- Fuller, J., Piro, A. L., & Jermyn, A. S. 2019, *MNRAS*, **485**, 3661
- Gandhi, P., Rao, A., Charles, P. A., et al. 2020, *MNRAS: Letters*, **496**, L22
- Gerosa, D., Vitale, S., & Berti, E. 2020, *PhRvL*, **125**, 101103
- Gültekin, K., Miller, M. C., & Hamilton, D. P. 2004, *ApJ*, **616**, 221
- Gültekin, K., Miller, M. C., & Hamilton, D. P. 2006, *ApJ*, **640**, 156
- Hainich, R., Oskinova, L. M., Shenar, T., et al. 2018, *A&A*, **609**, A94
- Hamers, A. S., Bar-Or, B., Petrovich, C., & Antonini, F. 2018, *ApJ*, **865**, 2
- Hartwig, T., Volonteri, M., Bromm, V., et al. 2016, *MNRAS*, **460**, L74
- Hoang, B.-M., Naoz, S., Kocsis, B., Rasio, F. A., & Dosopoulou, F. 2018, *ApJ*, **856**, 140
- Hobbs, G., Lorimer, D. R., Lyne, A. G., & Kramer, M. 2005, *MNRAS*, **360**, 974
- Hurley, J. R., Sippel, A. C., Tout, C. A., & Aarseth, S. J. 2016, *PASA*, **33**, e036
- King, A. R., Davies, M. B., Ward, M. J., Fabbiano, G., & Elvis, M. 2001, *ApJL*, **552**, L109
- Kinugawa, T., Inayoshi, K., Hotokezaka, K., Nakauchi, D., & Nakamura, T. 2014, *MNRAS*, **442**, 2963
- Kremer, K., Ye, C. S., Rui, N. Z., et al. 2020, *ApJS*, **247**, 48
- Kruckow, M. U., Tauris, T. M., Langer, N., Kramer, M., & Izzard, R. G. 2018, *MNRAS*, **481**, 1908
- Lipunov, V. M., Postnov, K. A., & Prokhorov, M. E. 1997, *AstL*, **23**, 492
- Liu, B., & Lai, D. 2018, *ApJ*, **863**, 68
- Ma, L., & Fuller, J. 2019, *MNRAS*, **488**, 4338
- MacLeod, M., Antoni, A., Murguía-Berthier, A., Macias, P., & Ramirez-Ruiz, E. 2017, *ApJ*, **838**, 56
- MacLeod, M., & Ramirez-Ruiz, E. 2015, *ApJ*, **803**, 41
- Mandel, I. 2016, *MNRAS*, **456**, 578
- Mandel, I., & de Mink, S. E. 2016, *MNRAS*, **458**, 2634
- Mandel, I., & Fragos, T. 2020, *ApJL*, **895**, L28
- Mapelli, M. 2016, *MNRAS*, **459**, 3432
- Marchant, P., Langer, N., Podsiadlowski, P., Tauris, T. M., & Moriya, T. J. 2016, *A&A*, **588**, A50
- Marchant, P., Renzo, M., Farmer, R., et al. 2019, *ApJ*, **882**, 36
- Miller, M. C., & Hamilton, D. P. 2002a, *MNRAS*, **330**, 232
- Miller, M. C., & Hamilton, D. P. 2002b, *ApJ*, **576**, 894
- Mondal, S., Belczyński, K., Wiktorowicz, G., Lasota, J.-P., & King, A. R. 2020, *MNRAS*, **491**, 2747
- Morawski, J., Giersz, M., Askar, A., & Belczynski, K. 2018, *MNRAS*, **481**, 2168
- O'Leary, R. M., O'Shaughnessy, R., & Rasio, F. A. 2007, *PhRvD*, **76**, 061504
- Pavlovskii, K., & Ivanova, N. 2015, *MNRAS*, **449**, 4415
- Pavlovskii, K., Ivanova, N., Belczynski, K., & Van, K. X. 2017, *MNRAS*, **465**, 2092
- Perna, R., Wang, Y.-H., Farr, W. M., Leigh, N., & Cantiello, M. 2019, *ApJL*, **878**, L1
- Portegies Zwart, S. F., Baumgardt, H., Hut, P., Makino, J., & McMillan, S. L. W. 2004, *Natur*, **428**, 724
- Portegies Zwart, S. F., & McMillan, S. L. W. 2000, *ApJL*, **528**, L17
- Repetto, S., Igoshev, A. P., & Nelemans, G. 2017, *MNRAS*, **467**, 298
- Repetto, S., & Nelemans, G. 2015, *MNRAS*, **453**, 3341
- Ricker, P. M., & Taam, R. E. 2008, *ApJL*, **672**, L41
- Rodriguez, C. L., Amaro-Seoane, P., Chatterjee, S., et al. 2018, *PhRvD*, **98**, 123005
- Rodriguez, C. L., Haster, C.-J., Chatterjee, S., Kalogera, V., & Rasio, F. A. 2016, *ApJL*, **824**, L8
- Sadowski, A., Belczynski, K., Bulik, T., et al. 2008, *ApJ*, **676**, 1162
- Samsing, J. 2017, *PhRvD*, **10**, 103014
- Sana, H., de Mink, S. E., de Koter, A., et al. 2012, *Sci*, **337**, 444
- Schmidt, P., Ohme, F., & Hannam, M. 2015, *PhRvD*, **91**, 024043
- Silber, K., & Tremaine, S. 2017, *ApJ*, **836**, 39
- Spera, M., Giacobbo, N., & Mapelli, M. 2016, *MmSAI*, **87**, 575
- Spera, M., Mapelli, M., Giacobbo, N., et al. 2019, *MNRAS*, **485**, 889
- Spruit, H. C. 1999, *A&A*, **349**, 189
- Spruit, H. C. 2002, *A&A*, **381**, 923
- Stevenson, S., Vigna-Gómez, A., Mandel, I., et al. 2017, *NatCo*, **8**, 14906
- The LIGO Scientific Collaboration, & the Virgo Collaboration 2020, *PhRvD*, **102**, 043015
- Tutukov, A. V., & Yungelson, L. R. 1993, *MNRAS*, **260**, 675
- VanLandingham, J. H., Miller, M. C., Hamilton, D. P., & Richardson, D. C. 2016, *ApJ*, **828**, 77
- Vink, J. S., de Koter, A., & Lamers, H. J. G. L. M. 2001, *A&A*, **369**, 574
- Voss, R., & Tauris, T. M. 2003, *MNRAS*, **342**, 1169
- Woosley, S. E. 2016, *ApJL*, **824**, L10
- Zevin, M., Berry, C. P. L., Coughlin, S., Chatzioannou, K., & Vitale, S. 2020, *ApJL*, **899**, L17
- Zevin, M., Samsing, J., Rodriguez, C., Haster, C.-J., & Ramirez-Ruiz, E. 2019, *ApJ*, **871**, 91

4 Common envelope vs stable mass transfer scenario

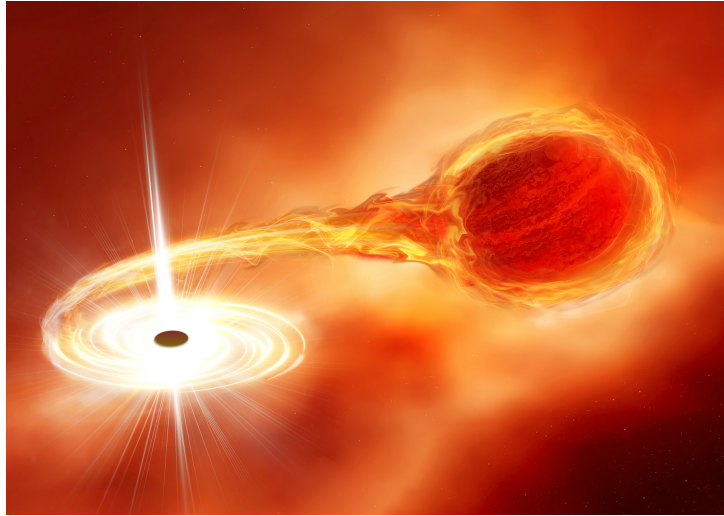


Fig. 14: Artistic vision of stable mass transfer in the massive binary system of a main sequence star and a BH. Credit: Katarzyna Drewniana.

Common envelope (i.e., unstable mass transfer, CE) is considered to be a promising mechanism for tightening the initially wide stellar binaries to very close, compact object systems [257–259]. The idea applies also to the formation of tight BH-BH binaries [118], with their final orbital separation small enough to allow them to merge in Hubble time only due to the orbital decay with GW radiation [101]. However, the development of CE, its course, and the physics behind is still poorly understood [259]. To estimate the CE outcome, rapid population synthesis codes often use a simplified, parameterized energy balance approach, known as α_{CE} formalism [258; 260]. However, such an approximate approach likely does not mimic well the complex, multistep evolution of the system through the CE phase [259].

Several recent studies, e.g., [131–134] indicate that mass transfer stability in massive binary systems, such as BH-BH mergers progenitors, is much more conservative than previously thought. Moreover, even if the CE develops, it is hard to avoid a stellar merger. Successful CE ejection is predicted to be possible only if the donor is a red supergiant with already well-developed, deep convective envelope [135]. Therefore, widely used rapid population synthesis codes are expected to significantly overestimate the number of successful CE ejections in massive binary systems. Such results challenge the classic isolated binary BH-BH mergers formation channel via CE developed during the second RLOF[118].

The figure 15 adopted from [133] well demonstrates the difference between the final outcomes for rapid population synthesis code COSMIC [261] and the detailed stellar evolution code MESA [89–93]. Simulations for both codes have been done for the same initial parameter grid of main sequence donors transferring mass on BH companion. The final evolutionary outcome such as stellar merger during CE, successful CE ejection, and formation of wide BH-BH systems or close BH-BH system (merger in Hubble time) are shown as a function of the initial orbital period and the system mass ratios. Results indicate that the widely used rapid population synthesis code favors the formation of BH-BH mergers via successful CE evolution, while detailed evolutionary codes tend to produce BH-BH mergers via stable mass transfer.

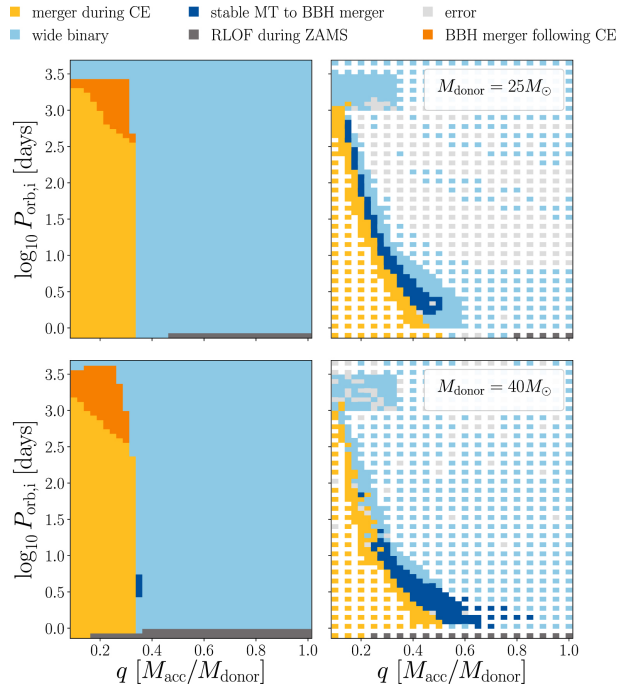




Fig. 15: The final evolutionary outcomes of simulations using COSMIC code (left) and MESA code (right). Top panels: results for $25M_{\odot}$ main sequence donor and BH binaries as a function of initial orbital period and the system mass ratio. Bottom panels: same as the top but for $40M_{\odot}$ main sequence donor. Main possible outcomes: formation of BH-BH merger via CE (orange) or via stable mass transfer (navy blue), formation of wide BH-BH system (blue), BH and main sequence star merger during CE (yellow). Credit: [133]

Motivated by similar studies, in our article [106] we implement, test, and study the impact of revised, more conservative criteria for CE development on the formation of GW sources. The revised criteria designed based on the results by [131] apply to massive binary systems with initial donor mass greater than $M_{ZAMS, \text{don}} > 18M_{\odot}$. Therefore, mostly evolution of BH-BH progenitors is affected. The previous, standard StarTrack CE development criteria strongly favor BH-BH mergers formation through the CE phase developed during second RLOF (over 90% of total merger rates). Revised criteria change the dominant formation scenario for BH-BH mergers, which instead of CE, consist of two stable (often rapid, thermal timescale) mass transfer phases. In our article [106] we demonstrate how assumption on uncertain CE development criteria impact: mass, mass ratio, and merger rates of GW sources.

The stability of mass transfer in massive binary systems is poorly understood, but has a crucial effect on the evolution of BH-BH mergers progenitors. Stable mass transfer, at least in widely used approaches, is much less effective in tightening the binary orbit than CE [26; 27; 106; 133]. That has consequences for the merger rates and other properties of GW sources. In StarTrack, less effective orbital tightening also results in the requirement of characteristic, unequal mass ratio at the onset of the second RLOF for stable mass transfer scenario. Only such highly unequal systems lose enough angular momentum in non-conservative mass transfer to tighten the BH-BH orbit enough to let the system merge in Hubble time. That, on the other hand, impacts the final distribution of BH-BH mergers mass ratio. Another consequence is that BH-BH merger progenitors in a stable mass transfer scenario tend to initiate the first mass transfer phase at the early evolutionary stage, quickly after leaving its main sequence, while in CE scenario it usually happens at later evolutionary stages.

Formation of BH-BH mergers via stable mass transfer is a relatively new and not well studied scenario, but it is recently gaining a lot of interest in the field of GW astrophysics [27; 121; 128; 133; 134; 136; 137].

Impact of common envelope development criteria on the formation of LIGO/Virgo sources

A. Olejak¹ , K. Belczynski¹, and N. Ivanova² 

¹ Nicolaus Copernicus Astronomical Center, Polish Academy of Sciences, ul. Bartycka 18, 00-716 Warsaw, Poland
e-mail: aolejak@camk.edu.pl, chrisbelczynski@gmail.com

² Department of Physics, University of Alberta, Edmonton, AB T6G 2E7, Canada

Received 9 February 2021 / Accepted 7 May 2021

ABSTRACT

The treatment and criteria for development of unstable Roche lobe overflow (RLOF) that leads to the common envelope (CE) phase have hindered the area of evolutionary predictions for decades. In particular, the formation of black hole-black hole (BH-BH), black hole-neutron star (BH-NS), and neutron star-neutron star (NS-NS) merging binaries depends sensitively on the CE phase in classical isolated binary evolution model. All these mergers are now reported as LIGO/Virgo sources or source candidates. CE is even considered by some as a mandatory phase in the formation of BH-BH, BH-NS, or NS-NS mergers in binary evolution models. At the moment, there is no full first-principles model for the development of the CE. We employed the StarTrack population synthesis code to test the current advancements in studies on the stability of RLOF for massive donors to assess their effect on the LIGO/Virgo source population. In particular, we allowed for more restrictive CE development criteria for massive donors ($M > 18 M_{\odot}$). We also tested a modified condition for switching between different types of stable mass transfer and between the thermal or nuclear timescale. The implemented modifications significantly influence the basic properties of merging double compact objects, sometimes in non-intuitive ways. For one of the tested models, with restricted CE development criteria, the local merger rate density for BH-BH systems increased by a factor of 2–3 due to the emergence of a new dominant formation scenario without any CE phase. We find that the changes in highly uncertain assumptions on RLOF physics may significantly affect: (i) the local merger rate density; (ii) shape of the mass and mass ratio distributions; and (iii) dominant evolutionary formation (with and without CE) scenarios of LIGO/Virgo sources. Our results demonstrate that without sufficiently strong constraints on RLOF physics, it is not possible to draw fully reliable conclusions about the population of double compact object systems based on population synthesis studies.

Key words. stars: black holes – gravitational waves – binaries: close – stars: statistics

1. Introduction

The concept behind the formation of close binary systems, such as merging double compact objects (DCO) or X-ray binaries, via the common envelope (CE) phase, began to appear in the literature nearly 50 years ago (Paczynski 1976; van den Heuvel 1976). Based on this concept, one binary component enters the other binary companion's envelope. The orbital energy is transferred to the envelope due to various drag forces, resulting in the binary orbit shrinking. Finally, the envelope either can be ejected from the system, leaving behind a newly formed close binary system, or the two stars can end up merging. One of the approaches to find the outcome of a CE event without doing detailed 3D simulations considers the energy budget of a CE event and is, hence, known as energy formalism. In its parameterized form, it has been introduced by Webbink (1984) and Livio & Soker (1988), and is known as “ α_{CE} -formalism”. Due to its simplicity, α_{CE} -formalism is still widely used in population synthesis studies (e.g., Vigna-Gómez et al. 2020). This simplified form of energy formalism equates only two energies: the envelope's binding energy (the energy required to eject the envelope to infinity) and the change in the orbital energy (the available energy source). This allows us to estimate the orbital separation after a CE event, assuming that envelope has been ejected:

$$\frac{GM_{\text{don},i}M_{\text{don,env}}}{\lambda R_{\text{don,lob}}} = \alpha_{\text{CE}} \left(\frac{GM_{\text{don},f}M_{\text{comp},f}}{2a_f} - \frac{GM_{\text{don},i}M_{\text{comp},i}}{2a_i} \right). \quad (1)$$

Here, $a_{i/f}$ is the initial or final orbital separation, $M_{\text{don},i/f}$ – initial or final donor mass, $M_{\text{comp},i/f}$ – initial or final companion mass, respectively, G – gravitational constant, $M_{\text{don,env}}$ – mass of the donor envelope, $R_{\text{don,lob}}$ – Roche lobe radius of the donor at the onset of Roche-lobe Overflow (RLOF), i and f – initial and final values of mass and separation, and λ – measure of the donor central concentration (de Kool 1990; Dewi & Tauris 2000; Xu & Li 2010).

Equation (1) postulates that the transfer of binary system orbital energy into the energy of the envelope takes place with some efficiency, α_{CE} , which, unless other energy sources are present, can not be more than one. Simulations and observations of CE phase indicates that the value of parameter is typically $\alpha_{\text{CE}} < 0.6$ –1.0 (Zuo & Li 2014; Nandez & Ivanova 2016; Clayton et al. 2017; Iaconi & De Marco 2019). On the other hand, if the simulations of a CE event are performed while including more physical processes, for example, accretion, the effective value of α_{CE} can be as high as 5 (e.g., see Fragos et al. 2019). A similar effect of increasing the apparent CE efficiency to more than one can be produced via exotic nucleosynthesis and jets (Podsiadlowski et al. 2010; Shiber et al. 2019; Zevin et al. 2021; Grichener & Soker 2021). Some population synthesis studies have already adopted such high values (e.g., see Santoliquido et al. 2020).

The CE efficiency parameter α_{CE} and the binding energy parameter λ are often coupled in population synthesis studies

or in observation analyses when energy formalism is applied. At the same time, each of them is subject to many uncertainties. For example, λ was introduced to relate the “true” binding energy of the envelope (as obtainable from detailed stellar models) to its simple parameterized form. However, the true binding energy of the donor continues to be a subject of discussion (e.g., see Sect. 3 in Ivanova et al. 2020). The CE efficiency parameter is expected to depend on the system specifics and which physical processes of energy creation or energy loss took place (e.g., on the system’s mass ratio, the evolutionary stage of the donor, or the nature of the companion). Values for α_{CE} , derived from observations, seem to be systematically lower for asymptotic giant branch (AGB) donors than for red giant branch (RGB) donors (Iaconi & De Marco 2019), which have different internal structures and envelope binding energy. The AGB donor envelopes are considered to be less tightly bound to the core than those of a RGB donors (Paczynski & Ziółkowski 1968; Han et al. 1994). However, even taking into account this AGB stars feature does not sufficiently help in successive envelope ejection (Sand et al. 2020). Numerical simulations encounter difficulties in successful envelope ejection unless some other energetic process (except orbital energy release) is included (e.g., Passy et al. 2012; Iaconi et al. 2017; Sand et al. 2020). In addition, recent studies by Klencki et al. (2021) have confirmed that even with the most favorable assumptions, a successful CE ejection in BH binaries is only possible if the donor is a massive convective-envelope giant. On the other hand, massive stars (BH progenitors) may be a subject of extensive mass loss through enhanced winds before they reach the RSG stage, which may even cause the spontaneous envelope loss (e.g., Vanbeveren 1991; Vanbeveren et al. 1998; Eggleton 2002).

The energy formalism in its parameterized form is a convenient way to predict CE outcomes, but, as it is argued now, it is not necessarily a well-founded method (Ivanova et al. 2020). While, at the moment, there is no comprehensive understanding of the CE evolution in all the cases, it is understood that the CE event could be preceded by stable mass transfer (MT) on different timescales. The criteria for the occurrence of CE phase are still under development as well.

New stellar mass loss models (Ge et al. 2010, 2015, 2020a,b) and detailed simulations for close, mass-exchanging binaries (Pavlovskii et al. 2017; Misra et al. 2020) have shown that RLOF may be stable over a much wider parameter space than previously thought. The same studies indicate that RLOF stability depends not only on the system mass ratio and the envelope type (convective or radiative), but also, for instance, on the metallicity, stellar type, or radius of the donor star. Those results can be confirmed via comparisons of the theoretical models with the observed systems (Cherepashchuk et al. 2019; Leiner & Geller 2021). A summary of the recent progress on RLOF stability has been summarized in Sect. 2.2 of Klencki et al. (2021). Unfortunately, due to a scarcity of observations for massive stellar systems during the ongoing RLOF phase and the high calculation costs, the current CE study (observations and simulations) usually refers to low-mass binary systems (Nandez et al. 2015; Nandez & Ivanova 2016; Jones 2020), which are not progenitors of BH-BH, BH-NS, or NS-NS binaries.

The CE phase is a key element in setting the formation of DCOs in the classical isolated binary evolution channel and therefore understanding of CE is crucial in studies of origin of merging DCOs. Recently more and more signals form BH-BH, BH-NS and NS-NS mergers have been detected by LIGO/Virgo instruments (Abbott et al. 2019a; The LIGO Scientific

Collaboration 2021) during the O1, O2 and O3 runs with reported parameters of systems such as the masses, spins and redshifts. It is still unknown what fraction of gravitational wave (GW) signal mergers formed through isolated binary evolution in the field (Bond & Carr 1984; Tutukov & Yungelson 1993; Lipunov et al. 1997; Voss & Tauris 2003; Belczynski et al. 2010; Dominik et al. 2012; Kinugawa et al. 2014; Mennekens & Vanbeveren 2014; Hartwig et al. 2016; Spera et al. 2016; Belczynski et al. 2016b; Eldridge & Stanway 2016; Woosley 2016; Stevenson et al. 2017; Kruckow et al. 2018; Hainich et al. 2018; Marchant et al. 2019; Spera et al. 2019; Bavera et al. 2020), the dense stellar system dynamical channel (Miller & Hamilton 2002b,a; Portegies Zwart et al. 2004; Gültekin et al. 2004, 2006; O’Leary et al. 2007; Sadowski et al. 2008; Downing et al. 2010; Antonini & Perets 2012; Benacquista & Downing 2013; Bae et al. 2014; Chatterjee et al. 2017; Mapelli 2016; Hurley et al. 2016; Rodriguez et al. 2016; VanLandingham et al. 2016; Askar et al. 2017; Morawski et al. 2018; Banerjee 2018; Di Carlo et al. 2019; Zevin et al. 2019; Arca-Sedda & Capuzzo-Dolcetta 2019; Rodriguez et al. 2018; Perna et al. 2019; Kremer et al. 2020); isolated multiple (triple, quadruple) systems (Antonini et al. 2017; Silsbee & Tremaine 2017; Arca-Sedda et al. 2021; Liu & Lai 2018; Fragione & Kocsis 2019), mergers of binaries in galactic nuclei (Antonini & Perets 2012; Hamers et al. 2018; Hoang et al. 2018; Fragione et al. 2019); the chemically homogeneous evolution channel consisting of rapidly spinning stars in isolated binaries (de Mink & Mandel 2016; Mandel & de Mink 2016; Marchant et al. 2016; du Buisson et al. 2020), or Population III origin DCO binary mergers (Bond & Carr 1984; Kinugawa et al. 2014; Tanikawa et al. 2021).

Over the years, various groups have developed their population synthesis codes to try and put better constraints on astrophysical processes by comparing theoretical model results with the known Galactic and extragalactic compact object population (e.g., Portegies Zwart & Verbunt 1996; Hurley et al. 2002; Kruckow et al. 2018; Belczynski et al. 2020; Han et al. 2020). Several uncertainties commonly encountered in population synthesis studies strongly influence formation of DCOs and therefore, are subjects of active research. Examples of uncertain processes and parameters that are crucial for DCO mergers evolution are: the metallicity-specific star formation rate density (Chruślińska et al. 2020; Santoliquido et al. 2021; Broekgaarden et al. 2021), NS and BH natal kicks (Mandel et al. 2021), or MT during stable or unstable RLOF (Vinciguerra et al. 2020; Howitt et al. 2020; Bavera et al. 2020).

In this paper, we study how the application of the most recent developments in the field of RLOF stability to the population synthesis affects DCOs formation. In Sect. 2 we describe the general method and the input physics implemented in the current version of StarTrack population synthesis code. In Sect. 3 we introduce the revised CE development criteria and modified stable RLOF treatment examined in this paper. In Sect. 4 we present the results of our simulations: DCO local merger rate density, BH-BH and BH-NS mass ratio distributions, and BH-BH mass distributions for three tested models. Section 5 is a description of evolutionary scenarios leading to the BH-BH and BH-NS mergers formation in three tested models. It also includes three diagrams with an example of systems evolution. Section 6 contains a brief discussion of our results together with the conclusions.

2. Method

In our simulation of the formation and mergers of DCO systems in the local Universe, we used the updated StarTrack

population synthesis code, developed over a number of years (Belczynski et al. 2002, 2008). The code allows us to simulate the evolution of a single star as well as of a binary star system for a wide range of initial conditions and physical parameters. The currently used version of implemented physics, adopted star formation history (SFH), and metallicity of the Universe is described in Belczynski et al. (2020), with two recent modifications, both explained in Sect. 2 of Olejak et al. (2020). We adopted three broken power-law initial mass function (IMF) Kroupa et al. (1993), Kroupa (2002), weak pulsation pair-instability supernovae (PPSN), and pair-instability supernovae (PSN) (Woosley 2017; Belczynski et al. 2016a). We applied procedures for accretion onto a compact object during stable RLOF and from stellar winds, based on the analytic approximations described in King et al. (2001) and Mondal et al. (2020). For non-degenerate accretors, we adopted a 50% non-conservative RLOF (Meurs & van den Heuvel 1989; Vinciguerra et al. 2020) with a fraction of the lost donor mass accreted onto the companion ($f_a = 0.5$), and the rest of the mass ($1 - f_a$), leaving the system together with part of the donor and orbital angular momentum (see Sect. 3.4 of Belczynski et al. 2008). We use 5% Bondi-Hoyle rate accretion onto the compact object during the CE phase (Ricker & Taam 2008; MacLeod & Ramirez-Ruiz 2015; MacLeod et al. 2017). The procedure is based on Eqs. (5.3)–(5.7) of (Bethe & Brown 1998) and Eqs. (A.1)–(A.10) of Belczynski et al. (2002), and has been recently summarized in Appendix B of Olejak et al. (2020). For stellar winds we use formulas based on theoretical predictions of radiation driven mass loss (Vink et al. 2001) with the inclusion of Luminous Blue Variable mass loss (Belczynski et al. 2010). All tested models have our standard physical values for the envelope ejection efficiency of $\alpha_{CE} = 1.0$ and Maxwellian distribution natal kicks with $\sigma = 265 \text{ km s}^{-1}$ (Hobbs et al. 2005) lowered by fallback (Fryer et al. 2012). We adopted solar metallicity $Z = 0.02$, in agreement with Pavlovskii et al. (2017).

We assume that systems with Hertzsprung gap (HG) donor star merge during CE phase (Belczynski et al. 2007). In the StarTrack code, the HG phase begins after leaving the main sequence – for both less and more massive stars, it is the period of intense star expansion (since, during the main sequence, stellar radius usually does not increase more than by a factor of few). Therefore, during the HG phase, stars often initiate TTMT and CE. At the onset of RLOF, such donors are often only partially expanded post-main sequence stars. Therefore, it is not well known whether such objects have an already well-separated core and envelope structure. In Fig. 1, we present the Hertzsprung-Russell evolution diagram for massive single stars. In the top panel of the figure, we mark that part of the evolution when stars are expected to have radiative or convective envelopes. In the bottom panel, we mark the part of the evolution where stars are defined in StarTrack as main sequence+HG or core helium burning.

We tested a delayed supernovae (SN) engine (Fryer et al. 2012; Belczynski et al. 2012), which affect the birth mass of NSs and BHs, allowing for the formation of the compact objects within the first mass gap ($\sim 2\text{--}5 M_\odot$). We assume that maximum mass of the NS is $2.5 M_\odot$ (Horvath et al. 2020) so more massive compact objects are BHs.

In this work, we present our results for three different evolutionary models: a model with standard Startrack treatment of RLOF: M380.B, along with the other two, which include the revised RLOF treatment: M480.B and M481.B. In these names, “M” stands for model, then the number is increasing with time to mark subsequent physical models. The ending “B” refers to

submodel B, which is often used in previous Startrack works, such as in Belczynski et al. (2020). In submodel B, all HG donor systems merge during the CE phase. The models are listed in Table 1.

3. RLOF

Two new types of instabilities were identified in RLOF binaries with massive donors, if such donors were allowed to evolve while they are exceeding their Roche lobe – the expansion and the convective instability (Pavlovskii et al. 2017). Expansion instability happens if an RLOF donor experiences a period of fast thermal-timescale expansion after its main sequence. This expansion may lead to the development of dynamical instability in a very short time (a few thousand years) after the start of thermal time-scale mass transfer (TTMT). The second type of instability, convection instability, is associated with developing a sufficiently deep convective envelope.

In this work, we implement, in our population synthesis code, the revised development criteria for the occurrence of the two instabilities and we examine how they influence the formation of DCO mergers. We base our criteria for checking whether any of the instabilities occur in a given donor on the numerical results of Pavlovskii et al. (2017), who report the boundaries between the instabilities using the radii of the donors of different masses and metallicities at the onset of RLOF. Following Pavlovskii et al. (2017), we defined two radii: R_U , the smallest radius for which the convection instability occurs, and R_S , the maximum radius when the expansion instability can take place.

In our approximation, the values of R_U and R_S are the averages of the ranges obtained and given in Table 1 of Pavlovskii et al. (2017). The specific values of R_U and R_S used in this work are given in Table 2. We note that simulations by Pavlovskii et al. (2017) were performed for the systems with BH companion. In our work, we extend the results and treat the same way binary systems with any other companion types (e.g., main-sequence stars, neutron stars, etc.). If the radius, R_{don} , of a given donor at the onset of RLOF is found within the range $R_S - R_U$ for $Z \leq 0.5 Z_\odot$ or below $R_{\text{don}} < R_U$ for $Z > 0.5 Z_\odot$, then we assume a stable RLOF; otherwise, CE evolution is applied. We note that stars of a higher metallicity were not found to undergo such an expansion instability (Pavlovskii et al. 2017).

3.1. CE development criteria

In the revised treatment, we require the following four conditions to be met simultaneously for CE development:

The condition based on the donor type. Revised RLOF instability criteria are applied if, during the RLOF, the donor is an H-rich envelope giant of one of the following types: HG star, first giant branch, core helium burning, early asymptotic giant branch, or thermally pulsing asymptotic giant branch. However, for HG donors, we assume that CE always leads to a merger, and we halt this system binary evolution (see Sect. 2).

The condition based on the donor mass. Revised RLOF instability criteria are applied only to the systems with initially massive donor stars with $M_{Z_{\text{AMS}},\text{don}} > 18 M_\odot$.

The condition based on the system mass ratio. The ratio of companion masses, M_{comp} , to donor masses M_{don} (see Table 2) represents the border between regimes of always stable and possibly unstable RLOF. Therefore, from Table 2 we can obtain the limit value of mass ratio, $q_{\text{CE}} = M_{\text{comp}}/M_{\text{don}}$, for the binary

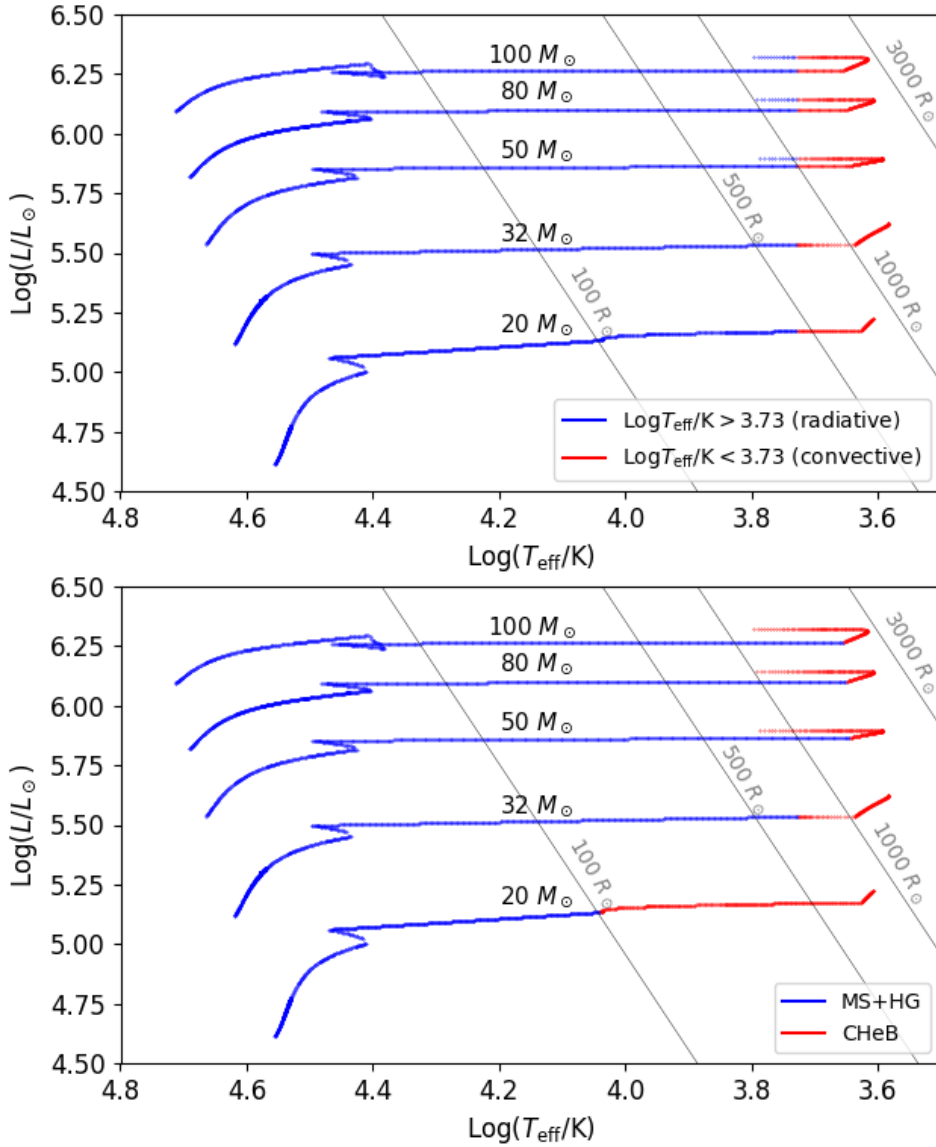


Fig. 1. Hertzsprung-Russell diagram for massive stars with ZAMS masses: $20 M_{\odot}$, $32 M_{\odot}$, $50 M_{\odot}$, $80 M_{\odot}$, and $100 M_{\odot}$ at metallicity $Z = 0.007$; evolution of single star since main sequence to core helium burning. In the top panel, we marked stars cooler than $\log(T_{\text{eff}}/K) < 3.73$ with the red line and with the blue line, those stars with $\log(T_{\text{eff}}/K) > 3.73$. It is expected that the red line represents stars having convective envelopes, while the blue line is for radiative envelopes (Ivanova & Taam 2004; Belczynski et al. 2008). In the bottom panel, we marked with the blue line, the star main sequence and Hertzsprung gap phases and with the red line, the core helium burning phase. Evolutionary stages are defined as in formulas by Hurley et al. (2002) and Belczynski et al. (2008). With the grey lines, we marked the borders corresponding to stellar radii: $100 R_{\odot}$, $500 R_{\odot}$, and $1000 R_{\odot}$.

to enter a potentially unstable RLOF regime. For metallicities $Z \leq 0.5 Z_{\odot}$ and for different donor mass, M_{don} ranges the q_{CE} values are following:

$$\begin{aligned} q_{\text{CE}} &= 0.36 \text{ for } M_{\text{don}} \in (18, 60)M_{\odot} \\ q_{\text{CE}} &= 0.21 \text{ for } M_{\text{don}} \in [60, 80)M_{\odot} \\ q_{\text{CE}} &= 0.19 \text{ for } M_{\text{don}} \geq 80M_{\odot}, \end{aligned} \quad (2)$$

whereas for metallicities $Z > 0.5 Z_{\odot}$

$$\begin{aligned} q_{\text{CE}} &= 0.36 \text{ for } M_{\text{don}} \in (18, 60)M_{\odot} \\ q_{\text{CE}} &= 0.29 \text{ for } M_{\text{don}} \in [60, 80)M_{\odot} \\ q_{\text{CE}} &= 0.19 \text{ for } M_{\text{don}} \geq 80M_{\odot}. \end{aligned} \quad (3)$$

If the mass ratio of the binary system is greater than q_{CE} , we assume stable RLOF.

The condition based on the donor radius. Finally, if all four conditions are met, we use stability diagrams presented in Figs. 2 and 3 to decide between stable RLOF and CE development. The diagrams pertain to two metallicities corresponding to the simulations performed by Pavlovskii et al. (2017):

$Z = 0.1 Z_{\odot}$ and $Z = 1.0 Z_{\odot}$, respectively. We marked the values of R_{U} and R_{S} with the corresponding donor masses taken from the Table 2 and fit functions to the simulation points. We extend our model for wider metallicity ranges and follow different procedures for metallicities smaller than $0.5 Z_{\odot}$ and greater than $0.5 Z_{\odot}$.

For $Z \leq 0.5 Z_{\odot}$, we used simulation data for $Z = 0.1 Z_{\odot}$ and we fit a second-degree polynomial to R_{S} points with the following coefficients:

$$R_{\text{S}} = -0.29M_{\text{don}}^2 + 30.3M_{\text{don}} - 498, \quad (4)$$

and a straight line to R_{U} :

$$R_{\text{U}} = 26.3M_{\text{don}} + 262. \quad (5)$$

If a donor during ongoing RLOF has a radius $R_{\text{don}} < R_{\text{S}}$ or $R_{\text{don}} > R_{\text{U}}$, RLOF is unstable (CE).

For $Z > 0.5 Z_{\odot}$ we used simulation data for $Z = 1.0 Z_{\odot}$. In this case, we had only R_{U} points and we fit a straight line with the equation:

$$R_{\text{U}} = 62.3M_{\text{don}} - 515. \quad (6)$$

Table 1. List of tested evolutionary models.

Model	CE development criteria	MT switch
M380.B	Standard	Standard
M480.B	Revised	Standard
M481.B	Revised	Modified

Table 2. Boundary radii values between the stable and unstable RLOF, values based on data from Pavlovskii et al. (2017).

$M_{\text{don}}[M_{\odot}]$	$M_{\text{comp}}[M_{\odot}]$	$R_S[R_{\odot}]$	$R_U[R_{\odot}]$
Metallicity $Z \leq 0.5 Z_{\odot}$			
19.6	7	stable	703.5
29.1	7	47.5	1057.5
37.6	7	331.5	1293.5
56.8	7	unstable	
56.8	10	355.0	1747.5
56.8	12	148.0	1823.5
74.5	7	unstable	
74.5	10	stable	2229.0
74.5	14	144.5	2150.5
Metallicity $Z > 0.5 Z_{\odot}$			
19.6	7	stable	736.0
26.6	7	stable	1159.0
32.5	7	stable	1407.5
41	10	stable	2103.5
41	12	stable	2033.0

Notes. If the radius, R_{don} , of a given donor during the ongoing RLOF is found within range R_S – R_U for $Z \leq 0.5 Z_{\odot}$ or below $R_{\text{don}} < R_U$ for $Z > 0.5 Z_{\odot}$ then we assume stable RLOF, otherwise CE evolution is applied. There are cases where expansion instability was not found for any radius (stable) and where cases where RLOF is unstable over the whole radius range (unstable).

If a donor radius during ongoing RLOF is $R_{\text{don}} > R_U$, RLOF is unstable (CE).

M_{don} in Eqs. (4)–(6) stands for the mass of the donor at a given RLOF time step, such that only 1% of donor mass is transferred (see Sect. 5.1, Belczynski et al. 2008).

In detailed simulations, RLOF is always unstable if $q < 0.123$ (see also Table 2). We therefore adopt the premise that CE events always start in binaries where at the onset of RLOF the mass ratio is

$$\frac{M_{\text{comp}}}{M_{\text{don}}} < q_{\text{crit}} = 0.125. \quad (7)$$

Unfortunately, the He giant donors do not have envelopes similar to hydrogen stars to make a straightforward connection and use revised RLOF stability diagrams. Therefore, in this work, for He stars – as well as cases where the donor is a main sequence star (H-rich; core H-burning and He-rich; core He-burning main sequence) or a giant of $M_{\text{ZAMS, don}} < 18 M_{\odot}$ – we follow the standard StarTrack CE development criteria and stable RLOF treatment (Belczynski et al. 2008).

3.2. Stable RLOF

In this study, we also test a modification of the condition for switching from TTMT to nuclear-timescale stable MT in the StarTrack code. So far, once the TTMT began, the issued MT

was continued until the donor star’s radius R_{don} decreased below 1.1 of its Roche lobe radius R_{lobe} . Then the type of MT was selected based on the comparison of MT timescale τ_{eq} (Eq. (46) from Belczynski et al. 2008) and thermal timescale τ_{thermal} . For τ_{thermal} , we use the approximation from Kalogera & Webbink (1996):

$$\tau_{\text{thermal}} \approx 30 \left(\frac{M_{\text{don}}}{M_{\odot}} \right)^2 \left(\frac{R_{\text{don}}}{R_{\odot}} \right)^{-1} \left(\frac{L_{\text{don}}}{L_{\odot}} \right)^{-1} \text{ Myr}. \quad (8)$$

If $\tau_{\text{eq}} > \tau_{\text{thermal}}$, it was assumed that MT is driven on nuclear timescale. If $\tau_{\text{eq}} \leq \tau_{\text{thermal}}$, it was assumed that the MT proceeds on a thermal timescale.

In one of the tested models of this work, we modified this condition by allowing for the switch from TTMT to nuclear timescale stable MT that is always based on the timescale comparison in the given RLOF time step (not only if $R_{\text{don}} < 1.1 R_{\text{lobe}}$). We note that this modification is applied to all binaries during their RLOF, regardless of component masses or types (as opposed to the new CE development criteria described in Sect. 3.1).

The evolutionary formulas we employ to evaluate star properties (e.g., radii, mass, luminosity) based on Hurley et al. (2000) are not applicable for thermal-timescale changes of the star outside of thermal-timescale evolution that is intrinsic to normal single stars (e.g., post-main-sequence expansion). Therefore, we cannot properly evaluate the donor’s properties during ongoing TTMT, as then the donor is out of its thermal equilibrium. We obtain TTMT rate using the mass, radius, and luminosity that the donor had when the TTMT had just started. Hence, the donor is still in thermal equilibrium. Therefore, we assume that the donor’s properties should still be well approximated by our parameterized equations. This obtained TTMT rate is kept constant for as long as the TTMT proceeds. We have to resort to this simplified method of obtaining the MT rate since, as the TTMT proceeds, our evolutionary formulas generate unreliable values for the star’s radius and luminosity.

However, we go on to use the onset RLOF parameters to construct our switches. In the first (original StarTrack) switch from TTMT to nuclear timescale MT, we wait until the donor’s radius (as given by the evolutionary formula) becomes comparable to the size of the donor’s Roche lobe. Then we assume that the star is back (or close) to its thermal equilibrium. Then we use the new donor’s properties to decide whether to continue TTMT (with a new MT rate based on the current donor mass, radius, and luminosity) or to switch to nuclear timescale MT.

In the modified approach that we test in this work, at each time step of the ongoing TTMT, we use the evolutionary formulae and calculate the current thermal and nuclear timescales. Suppose we get that the updated nuclear timescale is longer than the updated thermal timescale and the donor radius is still larger than its Roche lobe radius. In that case, we assume that the donor has regained its thermal equilibrium and we proceed with the MT on the new nuclear timescale. This usually happens earlier in the ongoing TTMT than meeting the original condition, $R_{\text{don}} < 1.1 R_{\text{lobe}}$. With this new additional condition, a numerical artifact is plausible: the donor star’s radius may significantly exceed its Roche lobe when we change MT to nuclear timescale. In this case we apply a “safety” condition, such that if:

$$R_{\text{don}} > 2.0 R_{\text{lobe}}, \quad (9)$$

we proceed with CE evolution for giant donors, or assume merger for main sequence donors (both H-core burning H-rich and He-core burning He-rich main sequence stars).

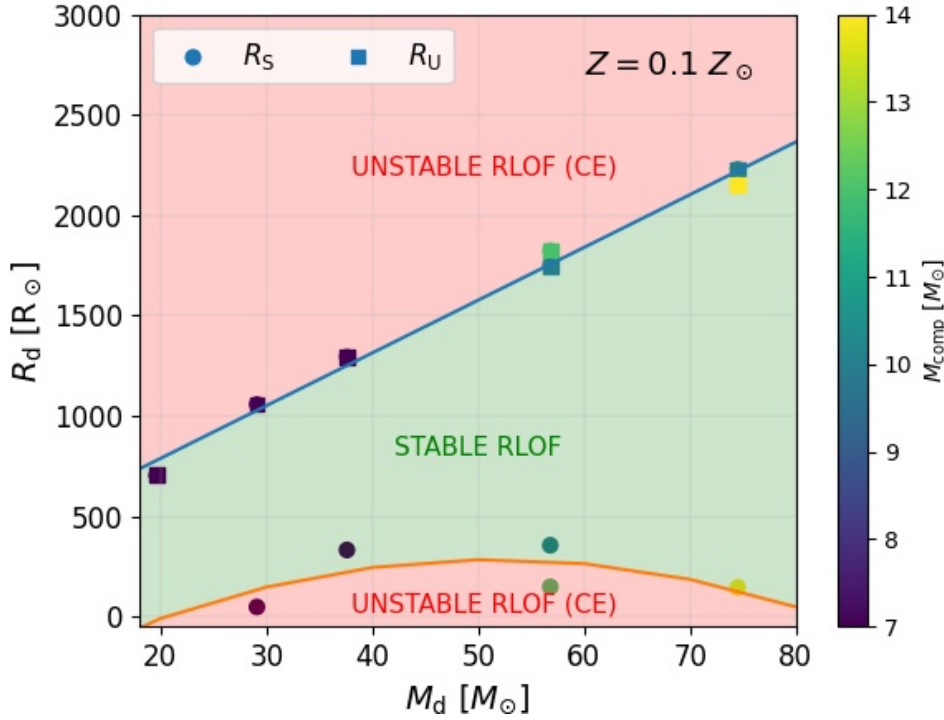


Fig. 2. Revised CE development criteria for stars with 10% of solar metallicity. On horizontal axis is the mass of the donor star. On the vertical axis is the radius of the donor. The circle and square points mark values of R_S and R_U , respectively (see Table 2). We fit lines to these data (see Eqs. (4)–(6)) to show regions of stable RLOF and unstable RLOF (CE). The color coded bar on the right denotes companion mass.

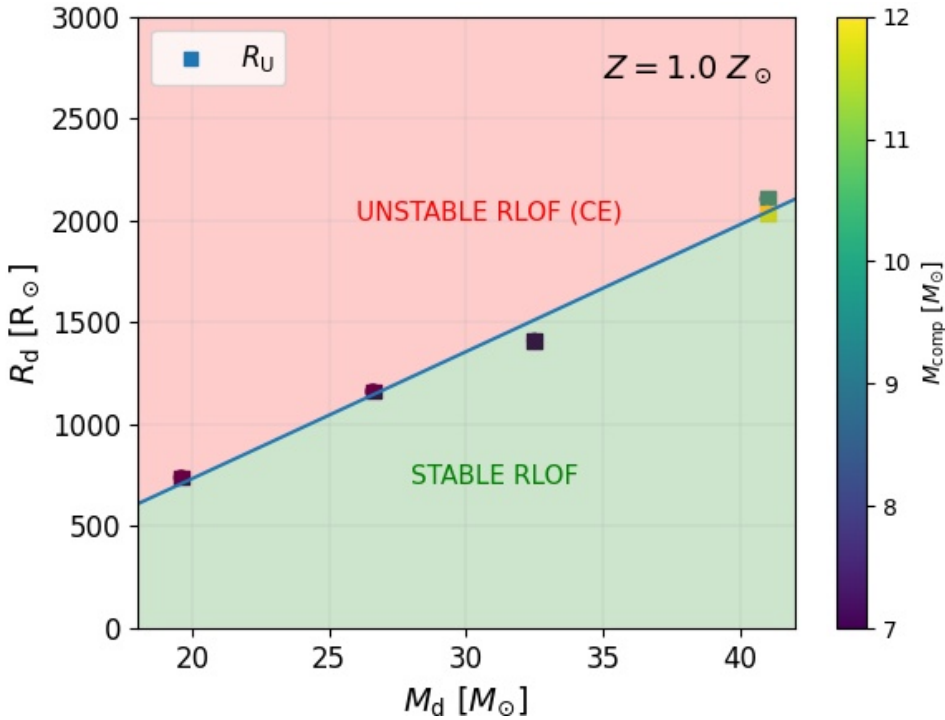


Fig. 3. Revised CE development criteria for stars with 100% of solar metallicity. Notation is the same as on Fig. 2.

Using either the original switch or the modified one is not perfect. Since we cannot be sure which transition condition from TTMT to nuclear timescale MT would correspond better to detailed MT calculations, we will present models with both treatments.

3.3. Other cases of unstable RLOF

There are other situations when RLOF is unstable, leading to a CE phase. We take into account the following two of the known scenarios: (i) in case of the Darwin instability, due to

an extreme mass ratio (Lai et al. 1993); (ii) if the accretion flow is so strong that photons are trapped in it, building up an envelope around a compact accretor in excess of its Roche lobe radius (Begelman 1979). For these, we use standard StarTrack procedures (Belczynski et al. 2008).

4. Results

4.1. NS-NS, BH-NS, and BH-BH local merger rate density

We present local merger rate densities ($z \sim 0$) for different types of DCO systems corresponding to the tested physical models

with standard (M380.B) and revised RLOF treatment (M480.B, M481.B) listed in the Table 3. Our rates are placed together with values recently estimated by LIGO/Virgo (90% credible limits): $23.9^{+14.9}_{-8.6} \text{ Gpc}^{-3} \text{ yr}^{-1}$ for BH-BH mergers, $320^{+490}_{-240} \text{ Gpc}^{-3} \text{ yr}^{-1}$ for NS-NS mergers (The LIGO Scientific Collaboration 2021) and previously given range for BH-NS mergers: $0\text{--}610 \text{ Gpc}^{-3} \text{ yr}^{-1}$ (Abbott et al. 2019a).

The effect of revised CE development criteria (separate from other tested changes) on the merger rates is visible by comparing results of model M380.B and M480.B. It seems to be rather counterintuitive as the rate for BH-BH and BH-NS mergers increased under more restricted conditions for CE initiation. In the standard model (M380.B), the local merger rate densities were for BH-BH: $62 \text{ Gpc}^{-3} \text{ yr}^{-1}$ and for BH-NS: $13 \text{ Gpc}^{-3} \text{ yr}^{-1}$ while in M480.B they slightly increased to $88 \text{ Gpc}^{-3} \text{ yr}^{-1}$ and $16 \text{ Gpc}^{-3} \text{ yr}^{-1}$, respectively. This is caused by the fact that in the revised treatment during the RLOF some of the systems with HG star donor instead of entering the unstable RLOF regime (which always lead to the merger, Sect. 2), go through the period of TTMT which allows for further binary evolution and potential formation of BH-BH systems. On the other hand, systems initiate CE phase much less often and as the consequence we obtain new, dominant evolutionary scenario leading to formation of BH-BH mergers without any CE phase. In other words, the early (HG donors) development of CE during TTMT eliminates many progenitors of BH-BH systems from dominant formation channel of model M480.B and the restricted (in terms of mass and mass ratio) development of CE reduces number of BH-BH mergers from the dominant formation channel in model M380.B. For details about the new evolutionary scenario see Sect. 5. The rate for NS-NS mergers (model M480.B), $\sim 150 \text{ Gpc}^{-3} \text{ yr}^{-1}$, is the same as in the standard model (M380.B), as the revised CE development criteria were adopted only to the systems with initially massive donors ($M_{ZAMS} > 18 M_{\odot}$, see Sect. 3.1) which are mainly BH progenitors. Therefore NS-NS systems formation was not significantly influenced and the merger rate is within LIGO/Virgo range as it used to be for the standard approach. Rates for BH-NS systems for both M380.B and M480.B models are also consistent with the given LIGO/Virgo range, which is wide, due to the limited detection data for BH-NS mergers (The LIGO Scientific Collaboration 2021). BH-BH merger rates for the same two models are about 1.5–2.0 times larger than the upper limit given by LIGO/Virgo.

Model M481.B includes both implemented changes to our standard approach (M380.B): revised CE development criteria and modified condition for the switch between TTMT and nuclear timescale stable MT. As the second change was implemented in all systems (regardless components masses or types), it affected also NS-NS merger rate (for M481.B equal $\sim 320 \text{ Gpc}^{-3} \text{ yr}^{-1}$), increasing it about twofold in comparison with the M380.B and M480.B models. The additional modification implemented in model M481.B leads, however, to a decrease in the rate for BH-BH and BH-NS mergers ($18 \text{ Gpc}^{-3} \text{ yr}^{-1}$ and $4 \text{ Gpc}^{-3} \text{ yr}^{-1}$ respectively) by a factor of $\sim 4\text{--}5$ comparing to the model M480.B. The effect described in previous paragraph – leading to the increase in the number of the surviving BH binaries progenitors due to the entry into the stable RLOF instead of early CE with HG donors – does not apply here. Due to the modification of condition for switch between MT types, TTMT stops faster than in the standard approach. At the same time the radius of the donor, derived from the formula for stars in equilibrium (see Sect. 3.2) is large ($R_{\text{don}} > 2.0R_{\text{lobe}}$), leading to early CE initiation (and merger of all HG donor systems). The new dominant BH-BH merger formation channel

Table 3. Local ($z \sim 0$) merger rate densities [$\text{Gpc}^{-3} \text{ yr}^{-1}$] for different types of DCO systems.

Model	$\mathcal{R}_{\text{BH-BH}}$	$\mathcal{R}_{\text{BH-NS}}$	$\mathcal{R}_{\text{NS-NS}}$
LIGO/Virgo	23.9	–	320
	15.3–38.8	0–610	80–810
M481.B	17.9	4.1	322
M380.B	61.7	13.1	148
M480.B	88.4	15.6	148

Notes. In bold, we mark the model for which BH-BH, BH-NS and NS-NS merger rates are within ranges given by LIGO/Virgo (Abbott et al. 2019a; The LIGO Scientific Collaboration 2021).

emerges in this model and it is different from the dominant BH-BH formation channels in models M380.B and M480.B. This channel includes TTMT that develops into late CE with a core helium burning donor (for details see Sect. 5). Merger rates for all types of DCOs in this (M481.B) model are in good agreement with recent LIGO/Virgo estimates.

4.2. BH-NS and BH-BH mass ratio distribution

Until the O3 data became available, all ten detected O1/O2 BH-BH mergers published by LIGO/Virgo team were consistent with being equal-mass mergers (Abbott et al. 2019b,c; Fishbach & Holz 2020). The latest detections, however, have indicated that the distribution of BH-BH mergers mass ratio may be more complex and wide-ranging. Recently, two detections of DCO mergers with highly asymmetric masses were announced (The LIGO Scientific Collaboration & the Virgo Collaboration 2020; Abbott et al. 2020a). The events GW190412 ($\sim 30 M_{\odot}$ BH and $\sim 8 M_{\odot}$ BH) and GW190814 ($\sim 23 M_{\odot}$ BH and $\sim 2.6 M_{\odot}$ NS or BH) were caused by DCO mergers in which one of the objects was less massive than the second by a factor of $0.28^{+0.12}_{-0.07}$ and $0.112^{+0.008}_{-0.009}$, respectively. We check how revised CE development criteria and stable RLOF treatment influence the mass ratio distribution of BH-BH, and BH-NS mergers, and if we are still able to reconstruct asymmetric mass BH-BH and BH-NS mergers as in previous models (Olejak et al. 2020; Drozda et al. 2020). In our study, we define the mass ratio of merging components, q , as the ratio of the less massive compact object to the more massive compact object, in agreement with LIGO/Virgo definition. In Figs. 4 and 5 we present the distributions of mass ratio of BH-BH and BH-NS mergers ($z \sim 0$) for two models with revised RLOF treatment (red line): M480.B and M481.B, respectively.

We calculated the percent of asymmetric mass BH-BH mergers with $q < 0.4$, which has been constrained after GW190412 detection to constitute $\geq 10\%$ of the overall BH-BH merger population (The LIGO Scientific Collaboration & the Virgo Collaboration 2020). In the standard StarTrack models with rapid (M230.B, Olejak et al. 2020) and delayed (M380.B) SN engine (Fryer et al. 2012), those fractions are 9% and $\sim 30\%$, respectively. We find that our tested revised CE development criteria reduced the fraction of unequal BH-BH mergers in comparison to model M380.B. Percent of BH-BH mergers with $q < 0.4$ for model M480.B constitute $\sim 2\%$ while for M481.B it is $\sim 6\%$. The main formation channel for the formation of unequal mass BH-BH binaries in standard approach (see Table 1 of Olejak et al. 2020) is missing for the revised CE treatment (see Table 4, Sect. 5). Systems that would produce unequal mass BH-BH mergers, in the revised treatment instead of CE, enter the stable RLOF regime and finally form wide BH-BH binaries, which

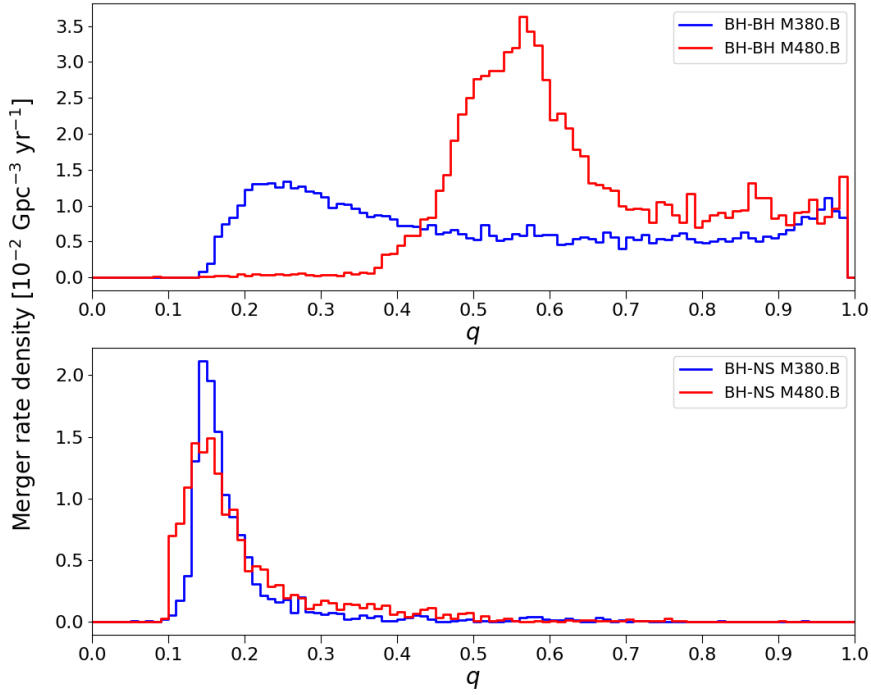


Fig. 4. Distribution of mass ratio in BH-BH and BH-NS mergers ($z \sim 0$). *Top panel:* BH-BH mergers, on the *bottom panel* BH-NS mergers. Blue line – results for standard CE development criteria with delayed SN engine (M380.B). Red line – results for revised CE development criteria (M480.B).

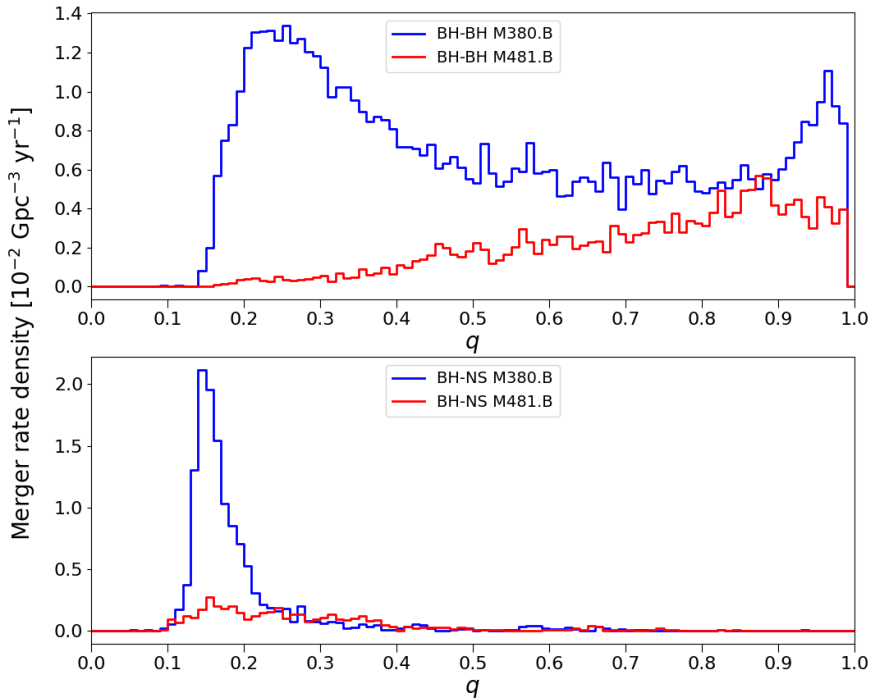


Fig. 5. Distribution of mass ratio in BH-BH and BH-NS mergers ($z \sim 0$). On the *top panel* BH-BH mergers, on the *bottom panel* BH-NS mergers. Blue line – results for standard CE development criteria with delayed SN engine (M380.B). Red line – results for revised CE development criteria and revised stable RLOF treatment (M481.B).

do not merge in *Hubble* time. The lowest BH-BH merger mass ratio achieved in tested models is $q \sim 0.06$ for the M480.B and $q \sim 0.1$ for M481.B.

In distribution of BH-BH mergers for model M480.B there is a large peak in the range of $q \approx 0.4$ – 0.6 , which is not present in distributions for other models. Vast majority (94%) of BH-BH mergers in M480.B forms via evolutionary scenario without any CE phase (see Table 4 and Fig. 9). Binary separation, instead during CE phase as in the standard *Startrack* approach, is reduced as the donor mass is ejected from the system together with the orbital angular momentum during stable RLOF. The

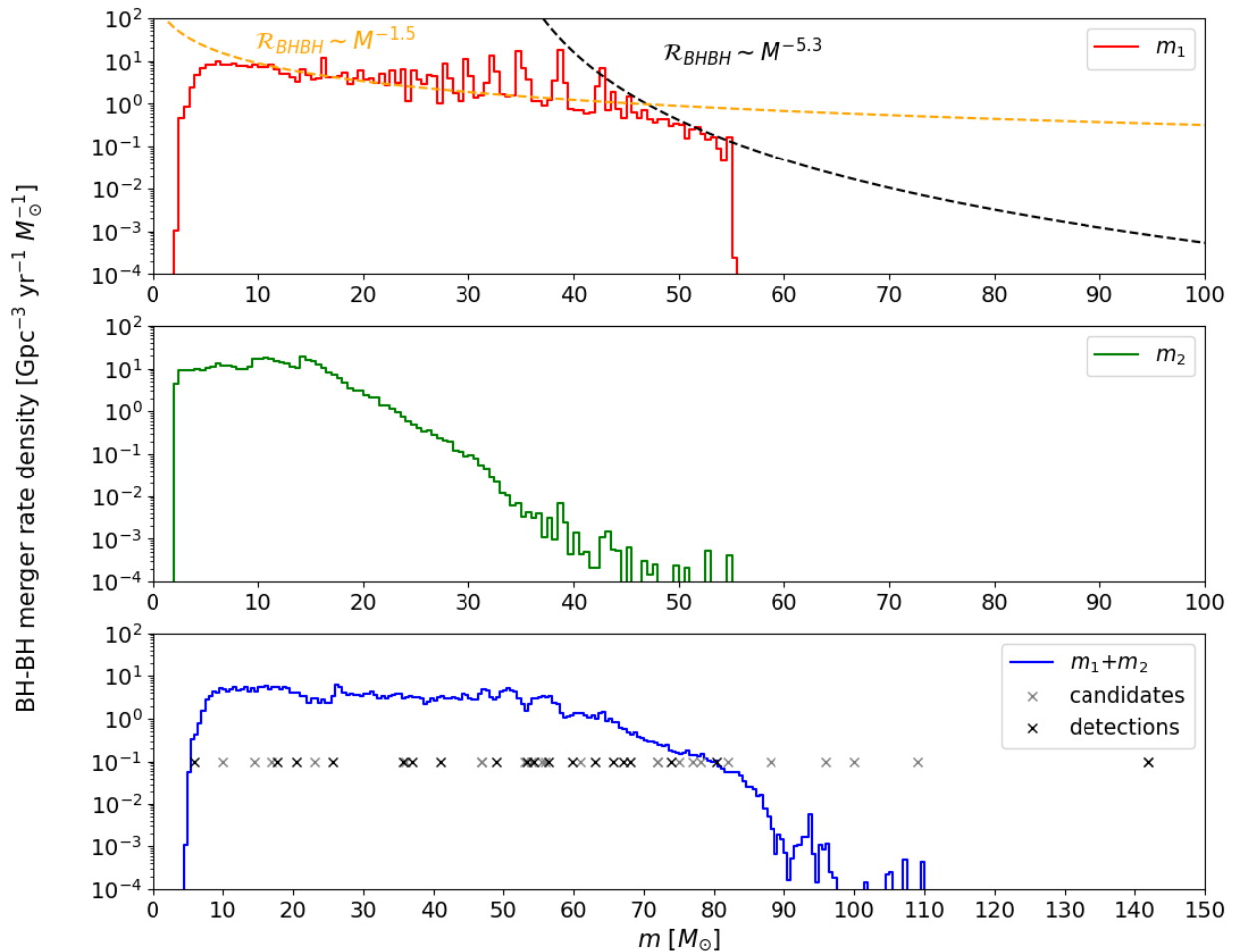
described mechanism of orbital shrinkage is effective only for unequal mass binary components, when the donor mass at the RLOF onset is significantly larger than the companion’s mass (van den Heuvel et al. 2017; Marchant et al. 2021). In our simulations such systems usually end their evolution as BH-BH binaries with mass ratio close to $q = 0.5$ (Fig. 9).

Mass ratio distribution for BH-NS mergers is strongly dominated with low mass ratio systems, what has been already reported and described for example by Drozda et al. (2020). For both models M480.B and M481.B, $\sim 90\%$ of the BH-NS mergers have $q < 0.35$. However, the lowest achieved mass

Table 4. Local ($z \sim 0$) merger rate densities [$\text{Gpc}^{-3} \text{yr}^{-1}$] for different BH-BH formation scenarios.

No.	BH-BH formation scenario	$\mathcal{R}_{M480.B}$	$\mathcal{R}_{M481.B}$	$\mathcal{R}_{M380.B}$
1.	MT1(1/2/4/5-1/4)/MT2(7-4) BH1 MT2(14-2/4/5/7/8) BH2	83.1	0.4	0.3
2.	MT1(1/2/4-1) BH1 MT2(14-2/4) SW CE2(14-4/5:14-7/8/14) BH2	0.4	12.5	0.0
3.	MT1(1/2/4-1) BH1 CE2(14-4/5:14-7/8/14) BH2	2.1	2.0	51.2
4.	MT1(1/2/4-1) BH1 MT2(14-2/4) CE2(14-4/5:14-7/8/14) BH2	1.1	1.0	1.6
5.	MT1(4-2/4) MT2(4/5/7/8-4) CE12(4/5/8-4:14-7) BH1 BH2	1.4	1.4	2.0
6.	Other scenarios	0.3	0.6	6.6
	Total	88.4	17.9	61.7

Notes. The main formation scenario for given model is marked in bold. MT1-stable RLOF, donor is initially more massive star; MT2-stable RLOF, donor is initially less massive star; BH1-formation of black hole by initially more massive star; BH2-formation of black hole by initially less massive star; CE1-common envelope initiated by initially more massive star; CE2-common envelope initiated by initially less massive star; CE12-double common envelope initiated by two giants; SW – switch from TTMT to CE based on the revised condition (see Sects. 3.2 and 5). The numeric types are consistent with Hurley et al. (2002): 0 – main sequence star with $M \leq 0.7 M_{\text{sun}}$ (deeply or fully convective) 1 – main sequence star with $M > 0.7 M_{\text{sun}}$ 2 – Hertzsprung gap star 3 – first giant branch star 4 – core helium burning star 5 – early asymptotic giant branch star 6 – thermally pulsing asymptotic giant branch star 7 – main sequence naked helium star 8 – Hertzsprung gap naked helium star 9 – giant branch naked helium star 10 – helium white dwarf 11 – carbon or oxygen white dwarf 12 – oxygen or neon white dwarf 13 – neutron star 14 – black hole 15 – massless remnant. The values in the brackets (e.g., 1/2/4) refer to different possible variants of the evolutionary types of binary components during given phase. The type of an initially more massive component is given first and the type that is initially less massive component comes second (after the dash). In the case of a CE phase type, those at the onset are given as first, the next types after envelope ejection (after the colon).


Fig. 6. Intrinsic BH-BH merger ($z < 2$) mass distributions: More massive BH mass (*top panel*), less massive BH mass (*middle panel*), and total mass (*bottom panel*). We also show total mass estimates for LIGO/Virgo BH-BH mergers from O1, O2 and O3. Results for model M480.B.

ratios for BH-NS merger (~ 0.1) is not that extreme as it used to be in standard model M380.B (0.03). Similarly as in case of the BH-BH system, the main formation channel leading to the

formation of extreme mass ratios (see Fig. 6 in Drozda et al. 2020) is reduced as during the first RLOF instead of CE systems goes through period of stable RLOF.

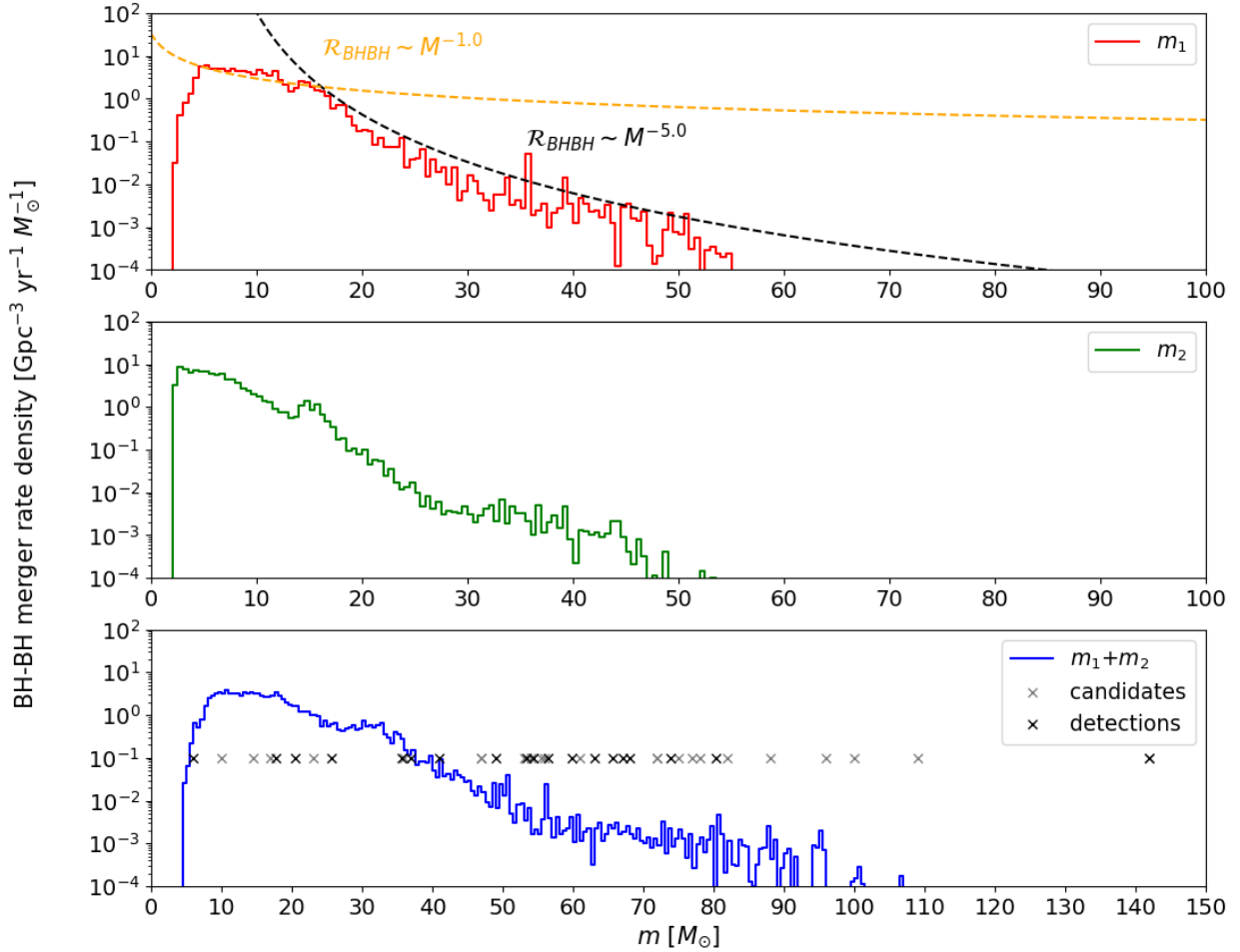


Fig. 7. Intrinsic BH-BH merger ($z < 2$) mass distributions: More massive BH mass (*top panel*), less massive BH mass (*middle panel*), and total mass (*bottom panel*). We also show total mass estimates for LIGO/Virgo BH-BH mergers from O1, O2, and O3. Results for model M481.B.

4.3. BH-BH mass distributions

The LIGO Scientific Collaboration (2021) gives recent estimations on the possible shape of mass distribution for the more massive of the merging BHs (m_1) based on so far detected BH-BH mergers. The proposed fit is a power-law mass function $p(m_1) \propto m_1^{-\alpha}$, with a break around $40 M_\odot$, with the first exponent for the masses $m_1 \lesssim 40 M_\odot$, $\alpha_1 = 1.58^{+0.82}_{-0.86}$ and the second exponent for $m_1 \gtrsim 40 M_\odot$, $\alpha_2 = 5.6^{+4.1}_{-2.5}$.

We present the distributions of more massive, less massive BH masses, and total mass of BH-BH systems which merged at redshifts $z < 2$ for two tested models with revised RLOF physics. Figures 6 and 7 shows results for models M480.B and M481.B, respectively. We approximate more BH mass distributions (Figs. 6 and 7; top panels) with power-law function for an easy visual comparison with the LIGO/Virgo estimate.

The shape of more massive BH distribution for our model M480.B is in very good agreement with the shape of the BH-BH detections (Fig. 6, top panel). The distribution for this model may be divided as well into two parts, with the break around $45 M_\odot$. The first part, up to the break is characterized by a slow decrease corresponding to the exponent $\alpha_1 \approx 1.5$ while after the break, the curve become much steeper with $\alpha_2 \approx 5.3$ and the cut at $\sim 55 M_\odot$ (PSN, beginning of the second mass gap). We note that this model distribution is a better match to the LIGO/Virgo estimate than recently published StarTrack results (see Fig. 15 for model M30.B in Abbott et al. (2020b): sin-

gle power-law with index $\alpha = 3.6$). The LIGO/Virgo total BH-BH system masses are within range of our simulated population of BH-BH mergers for model M480.B. The only exception is GW190521: the most massive detected BH-BH merger (Abbott et al. 2020b), which has both BHs ($85 M_\odot + 66 M_\odot$) within our adopted pair-instability mass gap: $55\text{--}135 M_\odot$ (Belczynski et al. 2020). However, even such massive BHs can be possibly produced by massive stars if uncertainties on nuclear reaction rates and mixing in stellar interiors are taken into account (Belczynski 2020).

In the case of model M481.B, the more massive BH mass distribution is not a good match to LIGO/Virgo data. Although two power-law exponents ($\alpha_1 \approx 1.0$ and $\alpha_2 \approx 5.0$) are within LIGO/Virgo estimates, the break appears at quite a low mass $M_{\text{break}} \approx 15\text{--}20 M_\odot$. We note also the total BH-BH mass distribution ends at lower mass ($M_{\text{cutoff}} = 100 M_\odot$) as compared with model M480.B ($M_{\text{cutoff}} = 110 M_\odot$).

We also plot mass distributions for the model M380.B which represents our standard RLOF physics (Fig. 8). Similarly to M481.B, the break point of more massive BH mass distribution is at rather low BH masses, $M_{\text{break}} \approx 15\text{--}20 M_\odot$. However, in this case for masses $m_1 < M_{\text{break}}$ the distribution is increasing with BH mass ($\propto M^{+2.7}$), which is inconsistent with the LIGO/Virgo estimates. For masses $m_1 > M_{\text{break}}$ we fit power-law exponent $\alpha_2 = 3.3$. The maximum total mass ($m_1 + m_2$) of the BH-BH merger for model M380.B is $110 M_\odot$.

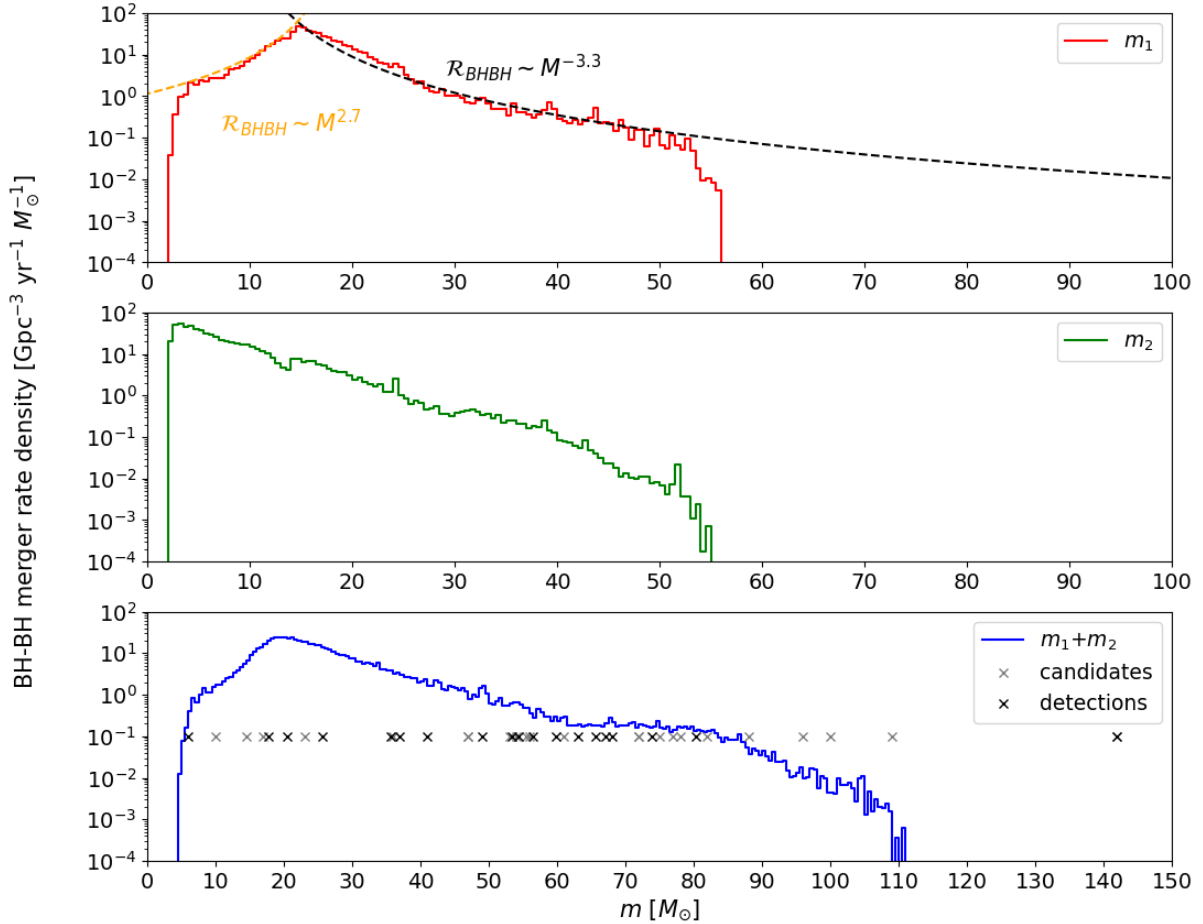


Fig. 8. Intrinsic BH-BH merger ($z < 2$) mass distributions: More massive BH mass (*top panel*), less massive BH mass (*middle panel*), and total mass (*bottom panel*). We also show total mass estimates for LIGO/Virgo BH-BH mergers from O1, O2 and O3. Results for model M380.B (standard).

Our results indicate that modifications in RLOF physics approach may drastically influence the BH mass distribution of BH-BH mergers. Some approaches (M480.B) allow to match nicely the empirical data for more massive BH mass distribution while for others distribution shape is rather off (M380.B and M481.B).

5. Formation scenarios

5.1. BH-BH formation scenarios

In Table 4, we provide evolutionary scenarios which lead to the formation of local ($z \sim 0$) BH-BH mergers for tested models with revised CE development criteria (M480.B and M481.B) and standard StarTrack criteria (M380.B). For each model the dominant formation scenario, which constitutes the highest merger rate density fraction (marked with the bold text) is different. In Figs. 9 and 10 we present diagrams with the example for the dominant BH-BH formation scenario in model M480.B (without CE phase), together with alternative evolution of the same system (the same initial conditions), but in models M380.B and M481.B. The Fig. 9 is an example of a low-mass BH-BH merger formation, for which significant natal kick (received after second SN explosion) plays an important role. The second example (Fig. 10) is massive BH-BH merger formation in which two BHs form via direct collapse.

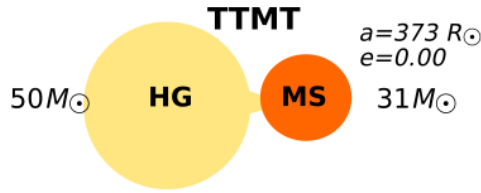
For model M480.B (revised CE development criteria and standard switch from TTMT to nuclear-timescale stable MT), the dominant BH-BH mergers formation scenario is without any CE phase. Similar channels were reported in many other recent works (van den Heuvel et al. 2017; Andrews et al. 2020; Zevin et al. 2021; Bavera et al. 2020; Marchant et al. 2021), as a possible formation scenario of LIGO/Virgo sources via isolated binary evolution. The typical evolution of binary system in model M480.B is as follow: When the primary (initially more massive star) leaves its main sequence and expands, system goes through a period of TTMT. We note that in some cases the donor star enters TTMT while it is at its HG. Survival of a binary through this phase is facilitated by high TTMT rate from the donor star. This removes most of (or entire) donor’s H-rich envelope and does not allow for a significant increase in donor radius, which, in turn, does not allow for development of CE phase and possible merger of the donor with its companion. After RLOF, the primary becomes a naked helium star. When the primary star completes its evolution, the first BH is formed. In the meantime, the secondary evolves off the main sequence, expands, and initiates a second phase of TTMT. The second RLOF, as well as the first one, is often initiated by a HG stars expanding on the thermal scales. If the system components have highly unequal masses (the donor mass is by a factor of 3 or more greater than the BH mass), the substantial mass loss from the system carries away also lots of the orbital angular momentum (even 90%

Time [Myr]

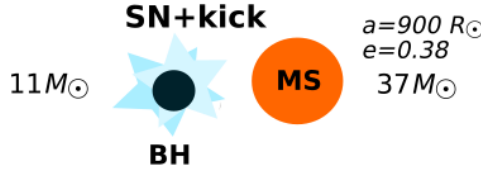
-0.00

 $Z=0.0085$

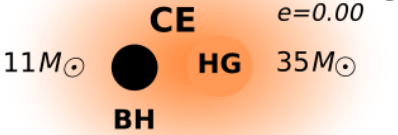
-4.34



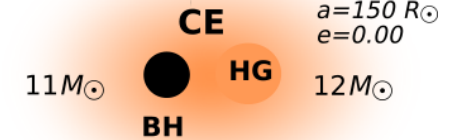
-4.84



-6.50

M380**M480****M481**

-6.54

BH+HG star merger

-7.15

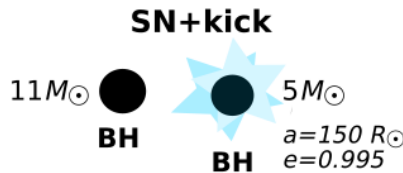
**BH+HG star merger****BH+BH merger**

Fig. 9. Typical local ($z \approx 0$) BH-BH mergers formation scenarios for model M480.B together with the alternative evolution of the same system in models M380.B and M481.B. For all models we begin with the same initial conditions, massive system of $55 M_{\odot}$ primary and $35 M_{\odot}$ secondary on the orbit of $350 R_{\odot}$ and with metallicity $Z = 0.0085$. In all scenarios, the primary initiates TTMT when it leaves the main sequence and begins to expand in thermal timescale during the HG phase. After 4.8 Myr the primary finishes evolution and explodes as type Ib/Ic SN leaving behind a $11 M_{\odot}$ BH remnant. Next, after the secondary leaves main sequence, due to more restricted condition for CE development, in the cases of model M480.B and 481.B system goes through TTMT instead of CE phase as in standard M380.B model. During TTMT the secondary loses a substantial percentage of its mass (over 60%), together with the system orbital angular momentum. Therefore, the orbit tightens (by a factor of ~ 4). After TTMT, in model 480.B, the system remains a BH-He system on the orbit of $150 R_{\odot}$. Due to the high natal kick after the second SN explosion, the orbital eccentricity significantly increases to $e = 0.995$, which allows the BH-BH system to merge in *Hubble* time. In standard (M380.B) scenario systems goes through CE phase with HG donor and we assume system a merger (see Sect. 2). In model M481.B due to modified condition for switch between the TTMT and nuclear-timescale stable MT, and the “safety” condition (see Sect. 3.2) after TTMT system also enters the CE phase with the HG donor and merges, leaving behind a single BH. The “He” in the diagram stands for a stripped helium core.

comparing with the amount at the second RLOF onset). This leads to significant orbit tightening. Such a mechanism was reported previously, for instance, by van den Heuvel et al. (2017), Marchant et al. (2021). After MT, the secondary

becomes naked helium star, and next it forms a second, typically less massive BH.

In all tested models of BHs with masses $M_{\text{BH}} < 10\text{--}15 M_{\odot}$, they may receive a natal kick at the time of their formation

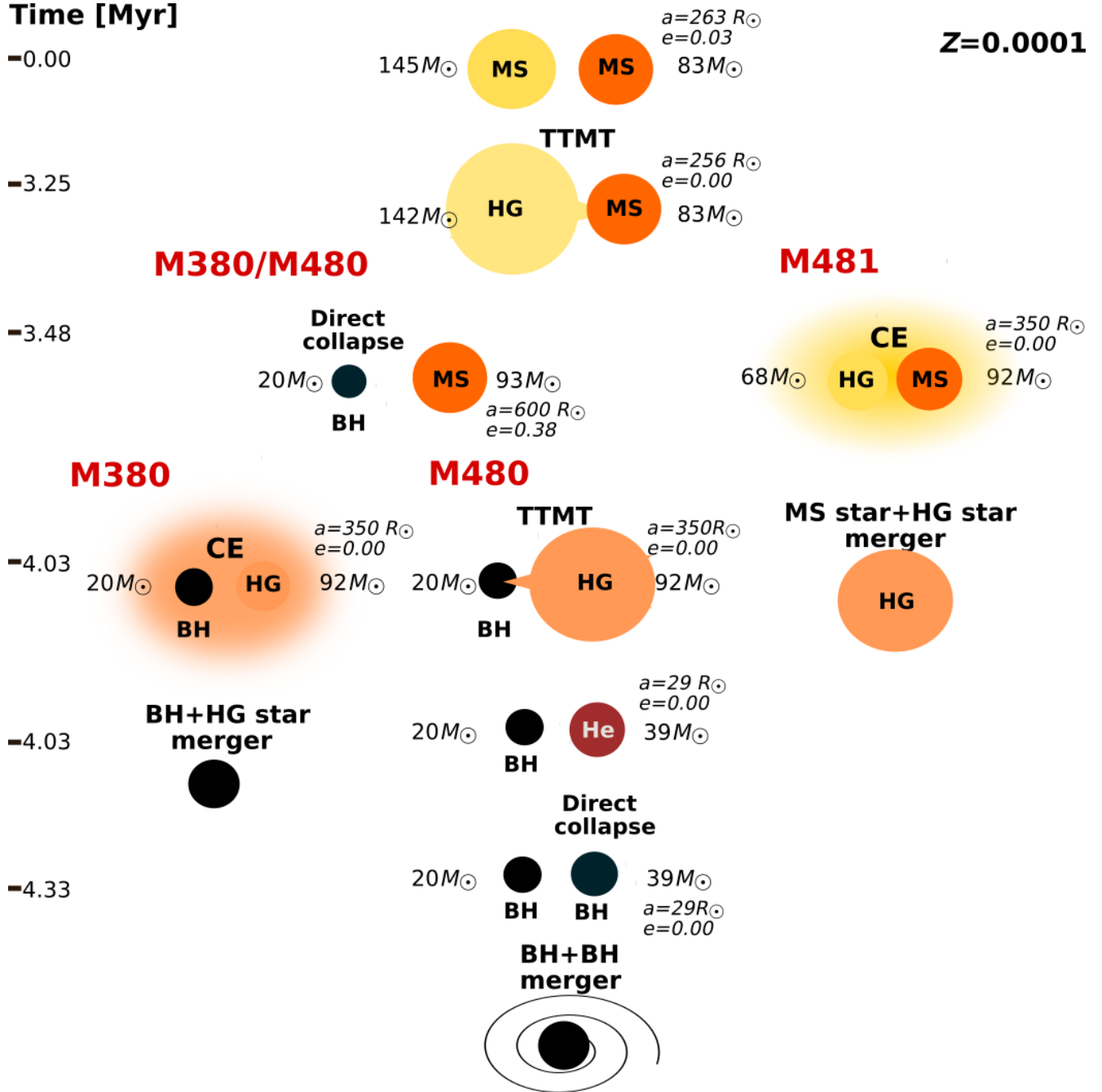


Fig. 10. Typical local ($z \approx 0$) BH-BH mergers formation scenarios for model M480.B, together with the alternative evolution of the same system in models M380.B and M481.B. For all models, we begin with the same initial conditions, massive system of $145 M_{\odot}$ primary and $83 M_{\odot}$ secondary on the orbit of $263 R_{\odot}$ and with metallicity $Z = 0.0001$. In all scenarios, the primary initiates TTMT when it leaves main sequence and begins to expand in thermal timescale during the HG phase. When TTMT finishes, in case of models M380.B and M480.B secondary loses envelope. A BH with stripped helium core companion on the orbit of $350 R_{\odot}$ is left. In model M481.B due to modified condition for switch between the TTMT and nuclear-timescale stable MT, and the “safety” condition (read Sect. 3.2) when TTMT ends, the system goes through the CE phase. As the donor is a HG star, the CE ends with the system merger leaving behind an unevolved single star. After 3.3 Myr, in models M380.B and M340.B, the primary finishes evolution and collapse to a $20 M_{\odot}$ BH remnant. Next, after the secondary leaves main sequence, due to more restricted conditions for CE development, in cases of model M480.B system goes through TTMT instead of CE phase as in standard M380.B model. At the onset of TTMT, the secondary (donor) is over four times more massive than a BH companion. During the TTMT, the donor star loses $\sim 60\%$ of its mass together with the system orbital angular momentum. This leads to the significant orbit tightening by a factor of ~ 12 . Efficient orbital angular momentum loss during TTMT allows for the subsequent formation of $20 M_{\odot}$ BH and $30 M_{\odot}$ BH systems to merge in *Hubble* time. In the scenario for M380.B, the highly unequal mass system enters the CE phase with the HG donor. The binary system does not survive CE phase leaving behind a single BH. The “He” in the diagram stands for stripped helium core.

(see Sect. 2). The lower the BH mass, the greater probability of a high natal kick. Therefore, in the BH-BH formation scenario the second-born BH (usually the less massive one)

may receive a significant kick. High natal kick may impart significant eccentricity to newly formed BH-BH system what decreases the inspiral timescale $T_{\text{ins}} \sim (1 - e^2)^{7/2}$, (Peters 1964),

Table 5. Local ($z \sim 0$) merger rate densities [$\text{Gpc}^{-3} \text{yr}^{-1}$] for different BH-NS formation scenarios.

No.	BH-NS formation scenario	$\mathcal{R}_{\text{M480.B}}$	$\mathcal{R}_{\text{M481.B}}$	$\mathcal{R}_{\text{M380.B}}$
1.	MT1(1/2/4-1) BH CE2(14-4/5:14-7/8/14) MT2(14-8/9) NS	11.6	0.7	6.6
2.	MT1(1/2/4/5-1/4)/MT2(7-4) BH MT2(14-2/4/5/7/8) NS	1.2	0.0	0.0
3.	MT1(1/2/4-1) BH CE2(14-4/5:14-7/8/14) NS	1.0	0.8	3.5
4.	MT1(1/2/4-1) BH CE2(14-4/5:14-7/8) MT2(14-8) SW CE2(14-9:14-13) NS	0.0	1.5	0.0
5.	Other scenarios	1.8	1.1	3.0
	Total	15.6	4.1	13.1

Notes. The main formation scenario for given model is marked with the bold text. Abbreviations are analogous to those described in Table 4.

allowing such BH-BH system to merge in *Hubble* time. For example BH-BH system of $25 M_{\odot}$ and $10 M_{\odot}$ on the wide orbit of $\sim 900 R_{\odot}$ may merge in ~ 10 Gyr if the eccentricity is as high as $e = 0.992$. For a comparison, in the case of circular orbit ($e = 0$) initial separation of the same BH-BH system would have to be less than $\sim 30 R_{\odot}$, for eccentricity $e = 0.7$ less than $\sim 45 R_{\odot}$, and for $e = 0.9$ less than $\sim 110 R_{\odot}$. The first stable RLOF phase in this scenario (M480.B) would be replaced in our standard model (M380.B) with the CE phase for many binaries as revised CE development criteria is more restrictive. Obviously, CE may lead in some cases to binary component merger and formation of a massive single stars. We note however, that even in our standard scenario dominant formation channel, the first RLOF is stable TTMT from HG star (compare dominant path 3 for model M380.B with dominant path 1 for model M480.B in Table 4). The second stable RLOF phase would be replaced by CE in the standard model. The CE during second RLOF is the main phase which leads the orbit size decrease for final BH-BH system to merge within *Hubble* time (see path 3 in Table 4 for model M380.B).

For Model M481.B (revised CE development criteria and modified condition for switch from TTMT to nuclear timescale MT), the main BH-BH formation channel also differs from the one in the standard Startrack approach (M380.B). Most of the evolution resembles the scenario described for M480.B: first TTMT initiated by the primary, then the first BH formation with a possible natal kick and the second TTMT initiated by the secondary. However, in model M481.B, due to a modified condition for switch from the TTMT to nuclear-timescale stable MT, and the “safety” condition (see Sect. 3.2), when TTMT ends, the system goes through the CE phase. If the system survives CE, the separation is reduced and the secondary’s envelope is ejected, leaving behind a naked helium core. Soon thereafter, in the CE phase (in some cases also already during CE), the secondary’s core collapse and the second (typically less massive) BH is formed.

5.2. BH-NS formation scenarios

In Table 5, we provide formation scenarios for local ($z \approx 0$) BH-NS mergers for tested models with revised CE development criteria (M480.B and M481.B) and standard Startrack criteria (M380.B). For each model, the dominant formation scenario which constitutes the highest merger rate density fraction is marked with the bold text. For two models M380.B and M480.B, the dominant formation scenario is the same, however, for model M480.B, it constitutes over 70%, while for M380.B about 50% of total BH-NS merger rates. The evolutionary diagrams with the dominant formation scenarios are shown in Fig. 11.

Most of the evolutionary phases are common for all three tested models. The evolutionary scenario transpires as follows: the once primary, initially more massive star, leaves the main sequence, it expands and initiates the first stable RLOF. System goes through the stable MT, after which the donor (primary) star loses its envelope becoming a stripped helium star. Next, the primary forms a BH through SN explosion or via direct collapse (depends on the final star mass). When the secondary star leaves its main sequence it expands and initiates unstable MT. The CE development leads to the secondary’s envelope removal and significant contraction of the system separation. Close system of BH and naked helium star is formed. Since, following the CE phase, the secondary is a main sequence or HG helium star, it still expands initiating a stable RLOF. At the end of the TTMT, the evolutionary scenarios for different models begin to diverge. In the case of models M380.B and M480.B, after the TTMT system is close to the BH-He binary. Next, a SN explosion takes place, followed by NS formation. In scenario M481.B, due to a modified condition for the switch between the TTMT and nuclear-timescale stable MT, and the “safety” condition (read Sect. 3.2), the system ends stable RLOF with CE phase. The orbit is tightened once again. During the second CE phase, the NS is formed.

6. Conclusions and discussion

In this work, we implement the revised RLOF stability diagram for binary systems with initially massive donors ($M_{\text{ZAMS}} > 18 M_{\odot}$) into StarTrack population synthesis code. The revised diagram is based on MT simulations performed by Pavlovskii et al. (2017) using the 1D hydrodynamical stellar code MESA. They found that RLOF is stable over a much wider parameter space than previously thought if the MT is allowed to proceed until outflows from the outer Langrangian points develop. For one tested model, we also modify the conditions for switching between TTMT and nuclear timescale MT. We used the most updated version of StarTrack code to calculate local merger rate density and mass ratio distribution of the synthetic population of DCOs mergers.

We compare the results of the revised RLOF treatment with the standard StarTrack method. We also check if the new results are consistent with the recent estimates of LIGO/Virgo collaboration, comparing local merger rate density, the fraction of unequal mass mergers, and the shape of BH-BH mergers mass distribution.

We present the results of three models; our standard StarTrack input physics model with delayed SN engine (M380.B) and two models with revised RLOF treatment (M480.B and M481.B). Model M480.B differs from our standard M380.B

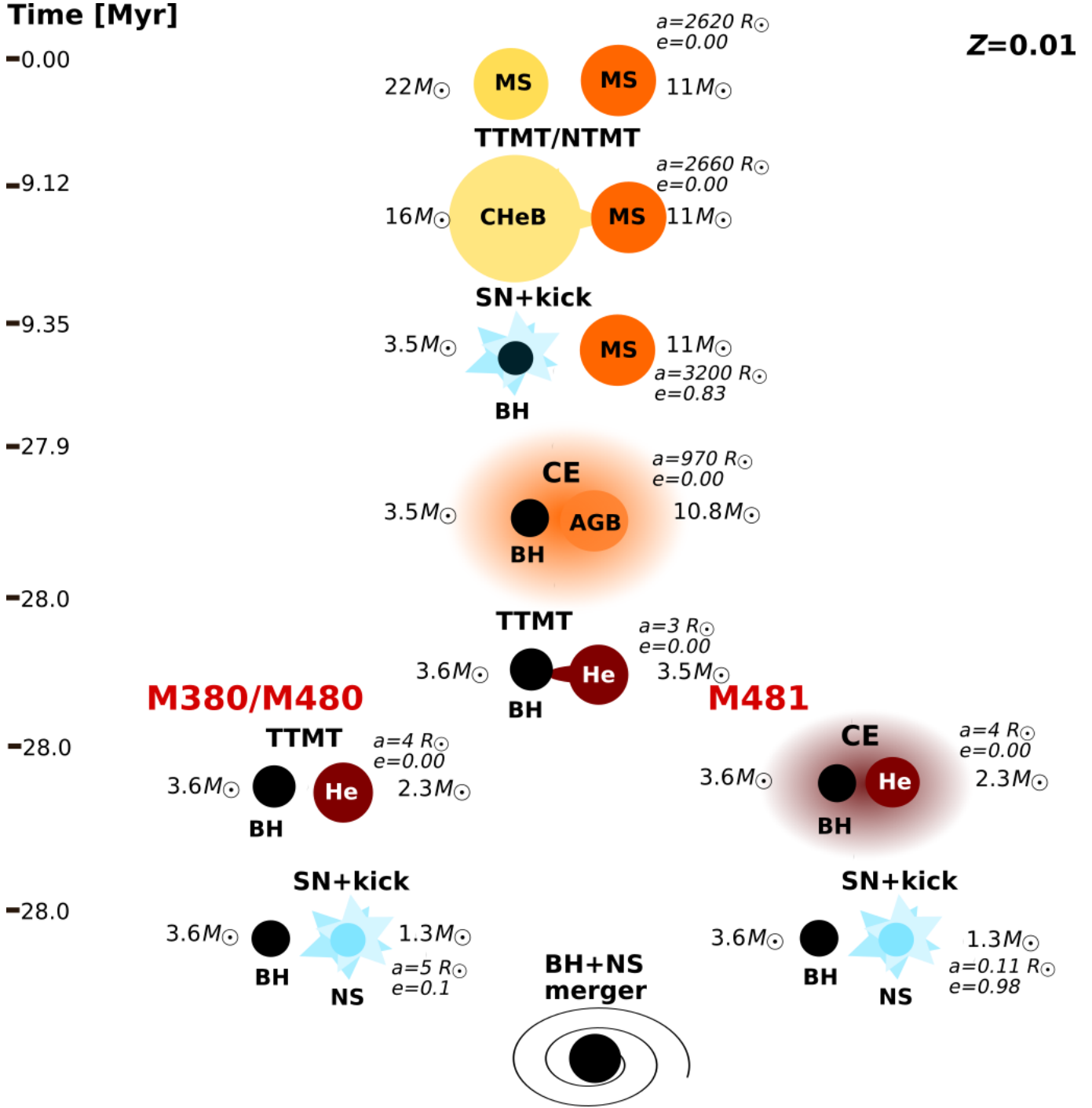


Fig. 11. Typical local ($z \approx 0$) BH-NS mergers formation scenarios for three tested models M380, M480, and M481 (for models M380 and M480 the scenario is the same). For all models, we begin with the same initial conditions: a wide binary system with $22 M_{\odot}$ primary and $11 M_{\odot}$ secondary on the orbit of $\sim 2600 R_{\odot}$ with metallicity $Z = 0.01$. Most of the evolutionary phases are common for all three models. When the primary leaves main sequence it expands, first as an HG star and then as core helium burning giant. The system goes through stable RLOF phase with TTMT and nuclear-timescale MT episodes. After MT the donor loses its envelope and soon explodes as SN. A low-mass BH ($3.5 M_{\odot}$) is formed with the accompanying high natal kick which causes the system eccentricity increase to $e = 0.83$. Next, the secondary leaves main sequence and begins to expand. At the same time the orbit gets circularized by the tides. System goes through the CE phase, the secondary loses its envelope. After CE separation decreases to only $3 R_{\odot}$. Close system of BH and helium star is formed. As after CE the secondary is a main sequence or HG naked helium star, it expands initiating a stable RLOF. The system goes through another TTMT, which in model M481 ends with the second CE phase and formation of a very close ($0.11 R_{\odot}$) BH-NS system. In the case of models M380 and M480, once TTMT ends, the system remains a close BH-He star binary and soon the secondary explodes forming a NS.

model only by the revised CE development criteria, while M481.B additionally includes the modified condition for the switch from TTMT to nuclear timescale MT.

Various changes related to assumptions about RLOF physics may strongly affect (sometimes in a non-intuitive way) the formation of DCO mergers: impacting merger rates and physical

properties of merging objects. For the three presented models, we obtained not only different local merger rate densities or BH mergers mass distributions, but also the dominant evolutionary scenarios for BH-BH formation changes.

In model M480.B (with revised CE development criteria), the most common scenario for BH-BH merger formation is without any CE phase. In model M481.B (with revised CE development criteria and modified switch from TTMT to nuclear timescale MT), BH-BH dominant formation scenario involves CE that is preceded by short TTMT phase.

Among the tested models, we did not find one that would be fully consistent with the merger rates for NS-NS, BH-NS, and BH-BH given by LIGO/Virgo and at the same time would produce the reported more massive BH mass distribution for BH-BH mergers. While the shape of the more massive BH mass distribution in model M480.B fits two exponent values well as well as the break point given (The LIGO Scientific Collaboration 2021), the total rates for BH-BH mergers are too high by a factor of $\sim 2-3$. Additionally, the fraction of unequal BH-BH mergers is not high enough. For Model M481.B, the total local rate density for all types of DCO mergers are aptly consistent with the most recent LIGO/Virgo estimates, but the shape of the more massive BH distribution seems too steep. Obviously, we could try to modify RLOF physics further or even change other parts of input physics (e.g., increasing the BH natal kicks to lower BH-BH merger rates) to fit LIGO/Virgo data for some models. However, the aim of this paper is only to demonstrate how uncertain ingredients of population synthesis codes may dramatically alter predictions.

We checked that the fraction of accreted mass during non-conservative RLOF (non-degenerate accretors, see Sect. 2) does not significantly influence the population of BH-BH and BH-NS mergers in the tested model M380.B. Beside the standard Startrack value $f_a = 0.5$, we tested models with values $f_a = 0.8$ and $f_a = 0.2$ for accreted mass fraction (the fraction $1 - f_a$ of transferred mass is ejected from the system). We found that merger rates for BH-BH and BH-NS systems change about 3% for $f_a = 0.8$ and about 20% for $f_a = 0.2$ comparing to the model with $f_a = 0.5$. Also, the mass and mass ratio distribution for three tested values are similar, with m_1 (more massive of merging components) slightly shifted to the lower mass values in the model with the lowest accretion fraction $f_a = 0.2$. Different adopted values of f_a influence, however, the local merger rate density for NS-NS systems. In both $f_a = 0.2$ and $f_a = 0.8$ models, the rate for NS-NS systems decreased by a factor of ~ 2 in comparison to the standard $f_a = 0.5$ model. The drop in NS-NS rates is a complex mix of multiple overlapping physical processes, for instance different amounts of lost mass (together with orbital angular momentum) leads to different types of system separation after the first RLOF, which further leads to a different evolutionary type of the donor during the second RLOF (CE phase with HG donor ends with a system merger).

In earlier works based on StarTrack code, two main variants of CE treatment were usually considered (referred to as submodel A and B). Submodel B (the one presented in this work, see Sect. 2) assumes that all HG donor systems merge during the CE phase. In contrast, submodel A allows such binary systems to survive if the energy budget calculations allow. We decided to present only the results for submodel B for two main reasons: First, we checked that typically HG donors which initiate CE in StarTrack are only partially expanded stars, shortly after their main sequence. Such stars likely do not have a clear core-envelope boundary and, therefore, it seems

more physical to assume their merger (as we do for main sequence stars). Second, the merger rates for DCOs, especially BH-BH systems in submodel A (see Belczynski et al. 2020) are often much larger (up to 30 times) than estimated by LIGO/Virgo.

The central message of our rapid population synthesis study is that the choice of our RLOF treatment produces noticeably different populations of GW sources. Our results highlight the need for caution when makes inferences from stellar and binary evolution models, as applied to LIGO/Virgo results. Similar cautionary notes are also found through more detailed evolutionary calculations with hydrodynamical stellar codes (Klencki et al. 2021; Decin 2020). If we suppose a population synthesis study is performed with variations of only natal kicks and CE efficiency, and the match to LIGO/Virgo rates is achieved for some specific CE efficiency and natal kicks assumption, it cannot be expected that we have already constrained these uncertain components of the input physics.

Acknowledgements. We would like to thank anonymous referee for their useful comments. K.B. and A.O. acknowledge support from the Polish National Science Center (NCN) grant Maestro (2018/30/A/ST9/00050). N.I. acknowledges support from CRC program and funding from NSERC Discovery under Grant No. NSERC RGPIN-2019-04277.

References

- Abbott, B., Abbott, R., Abbott, T., et al. 2019a, *Phys. Rev. X*, 9, 031040
 Abbott, B. P., Abbott, R., Abbott, T. D., et al. 2019b, *ApJ*, 882, L24
 Abbott, B. P., Abbott, R., Abbott, T. D., et al. 2019c, *Phys. Rev. X*, 9, 031040
 Abbott, R., Abbott, T. D., Abraham, S., et al. 2020a, *ApJ*, 896, L44
 Abbott, R., Abbott, T. D., Abraham, S., et al. 2020b, *Phys. Rev. Lett.*, 125, 101102
 Andrews, J. J., Cronin, J., Kalogera, V., Berry, C., & Zezas, A. 2020, *ApJ*, 914, L32
 Antonini, F., & Perets, H. B. 2012, *ApJ*, 757, 27
 Antonini, F., Toonen, S., & Hammers, A. S. 2017, *ApJ*, 841, 77
 Arca-Sedda, M., & Capuzzo-Dolcetta, R. 2019, *MNRAS*, 483, 152
 Arca-Sedda, M., Li, G., & Kocsis, B. 2021, *A&A*, 650, A189
 Askar, A., Szkudlarek, M., Gondek-Rosińska, D., Giersz, M., & Bulik, T. 2017, *MNRAS*, 464, L36
 Bae, Y.-B., Kim, C., & Lee, H. M. 2014, *MNRAS*, 440, 2714
 Banerjee, S. 2018, *MNRAS*, 473, 909
 Bavera, S. S., Fragos, T., Qin, Y., et al. 2020, *A&A*, 635, A97
 Begelman, M. C. 1979, *MNRAS*, 187, 237
 Belczynski, K. 2020, *ApJ*, 905, L15
 Belczynski, K., Kalogera, V., & Bulik, T. 2002, *ApJ*, 572, 407
 Belczynski, K., Taam, R. E., Kalogera, V., Rasio, F. A., & Bulik, T. 2007, *ApJ*, 662, 504
 Belczynski, K., Kalogera, V., Rasio, F. A., et al. 2008, *ApJS*, 174, 223
 Belczynski, K., Dominik, M., Bulik, T., et al. 2010, *ApJ*, 715, L138
 Belczynski, K., Wiktorowicz, G., Fryer, C. L., Holz, D. E., & Kalogera, V. 2012, *ApJ*, 757, 91
 Belczynski, K., Holz, D. E., Bulik, T., & O’Shaughnessy, R. 2016a, *Nature*, 534, 512
 Belczynski, K., Heger, A., Gladysz, W., et al. 2016b, *A&A*, 594, A97
 Belczynski, K., Klencki, J., Fields, C. E., et al. 2020, *A&A*, 636, A104
 Benacquista, M. J., & Downing, J. M. B. 2013, *Liv. Rev. Rel.*, 16, 4
 Bethe, H. A., & Brown, G. E. 1998, *ApJ*, 506, 780
 Bond, J. R., & Carr, B. J. 1984, *MNRAS*, 207, 585
 Broekgaarden, F. S., Berger, E., Neijssel, C. J., et al. 2021, ArXiv e-prints [arXiv:2103.02608]
 Chatterjee, S., Rodriguez, C. L., Kalogera, V., & Rasio, F. A. 2017, *ApJ*, 836, L26
 Cherepashchuk, A. M., Postnov, K. A., & Belinski, A. A. 2019, *MNRAS*, 485, 2638
 Chruślińska, M., Jeřábková, T., Nelemans, G., & Yan, Z. 2020, *A&A*, 636, A10
 Clayton, M., Podsiadlowski, P., Ivanova, N., & Justham, S. 2017, *MNRAS*, 470, 1788
 de Kool, M. 1990, *ApJ*, 358, 189
 de Mink, S. E., & Mandel, I. 2016, *MNRAS*, 460, 3545

- Decin, L. 2020, ArXiv e-prints [arXiv:2011.13472]
- Dewi, J. D. M., & Tauris, T. M. 2000, *A&A*, **360**, 1043
- Di Carlo, U. N., Giacobbo, N., Mapelli, M., et al. 2019, *MNRAS*, **487**, 2947
- Dominik, M., Belczynski, K., Fryer, C., et al. 2012, *ApJ*, **759**, 52
- Downing, J. M. B., Benacquista, M. J., Giersz, M., & Spurzem, R. 2010, *MNRAS*, **407**, 1946
- Drozda, P., Belczynski, K., O’Shaughnessy, R., Bulik, T., & Fryer, C. L. 2020, ArXiv e-prints [arXiv:2009.06655]
- du Buisson, L., Marchant, P., Podsiadlowski, P., et al. 2020, *MNRAS*, **499**, 5941
- Eggleton, P. P. 2002, *ApJ*, **575**, 1037
- Eldridge, J. J., & Stanway, E. R. 2016, *MNRAS*, **462**, 3302
- Fishbach, M., & Holz, D. E. 2020, *ApJ*, **891**, L27
- Fragione, G., & Kocsis, B. 2019, *MNRAS*, **486**, 4781
- Fragione, G., Grishin, E., Leigh, N. W. C., Perets, H. B., & Perna, R. 2019, *MNRAS*, **488**, 47
- Fragos, T., Andrews, J. J., Ramirez-Ruiz, E., et al. 2019, *ApJ*, **883**, L45
- Fryer, C. L., Belczynski, K., Wiktorowicz, G., et al. 2012, *ApJ*, **749**, 91
- Ge, H., Hjellming, M. S., Webbink, R. F., Chen, X., & Han, Z. 2010, *ApJ*, **717**, 724
- Ge, H., Webbink, R. F., Chen, X., & Han, Z. 2015, *ApJ*, **812**, 40
- Ge, H., Webbink, R. F., & Han, Z. 2020a, *ApJS*, **249**, 9
- Ge, H., Webbink, R. F., Chen, X., & Han, Z. 2020b, *ApJ*, **899**, 132
- Grichener, A., & Soker, N. 2021, ArXiv e-prints [arXiv:2101.05118]
- Gültekin, K., Miller, M. C., & Hamilton, D. P. 2004, *ApJ*, **616**, 221
- Gültekin, K., Miller, M. C., & Hamilton, D. P. 2006, *ApJ*, **640**, 156
- Hainich, R., Oskinova, L. M., Shenar, T., et al. 2018, *A&A*, **609**, A94
- Hamers, A. S., Bar-Or, B., Petrovich, C., & Antonini, F. 2018, *ApJ*, **865**, 2
- Han, Z., Podsiadlowski, P., & Eggleton, P. P. 1994, *MNRAS*, **270**, 121
- Han, Z.-W., Ge, H.-W., Chen, X.-F., & Chen, H.-L. 2020, *Res. Astron. Astrophys.*, **20**, 161
- Hartwig, T., Volonteri, M., Bromm, V., et al. 2016, *MNRAS*, **460**, L74
- Hoang, B.-M., Naoz, S., Kocsis, B., Rasio, F. A., & Dosopoulou, F. 2018, *ApJ*, **856**, 140
- Hobbs, G., Lorimer, D. R., Lyne, A. G., & Kramer, M. 2005, *MNRAS*, **360**, 974
- Horvath, J. E., Rocha, L. S., Bernardo, A. L. C., de Avellar, M. G. B., & Valentim, R. 2020, ArXiv e-prints [arXiv:2011.08157]
- Howitt, G., Stevenson, S., Vigna-Gómez, A., et al. 2020, *MNRAS*, **492**, 3229
- Hurley, J. R., Pols, O. R., & Tout, C. A. 2000, *MNRAS*, **315**, 543
- Hurley, J. R., Tout, C. A., & Pols, O. R. 2002, *MNRAS*, **329**, 897
- Hurley, J. R., Sippel, A. C., Tout, C. A., & Aarseth, S. J. 2016, *MNRAS*, **33**
- Iaconi, R., & De Marco, O. 2019, *MNRAS*, **490**, 2550
- Iaconi, R., Reichardt, T., Staff, J., et al. 2017, *MNRAS*, **464**, 4028
- Ivanova, N., & Taam, R. E. 2004, *ApJ*, **601**, 1058
- Ivanova, N., Justham, S., & Ricker, P. 2020, *Common Envelope Evolution* (IOP Publishing), 2514
- Jones, D. 2020, *Rev. Frontiers Mod. Astrophys.*, 123
- Kalogera, V., & Webbink, R. F. 1996, *ApJ*, **458**, 301
- King, A. R., Davies, M. B., Ward, M. J., Fabbiano, G., & Elvis, M. 2001, *ApJ*, **552**, L109
- Kinugawa, T., Inayoshi, K., Hotokezaka, K., Nakauchi, D., & Nakamura, T. 2014, *MNRAS*, **442**, 2963
- Klencki, J., Nelemans, G., Istrate, A. G., & Chruslinska, M. 2021, *A&A*, **645**, A54
- Kremer, K., Ye, C. S., Rui, N. Z., et al. 2020, *ApJS*, **247**, 48
- Kroupa, P. 2002, *Science*, **295**, 82
- Kroupa, P., Tout, C. A., & Gilmore, G. 1993, *MNRAS*, **262**, 545
- Kruckow, M. U., Tauris, T. M., Langer, N., Kramer, M., & Izzard, R. G. 2018, *MNRAS*, **481**, 1908
- Lai, D., Rasio, F. A., & Shapiro, S. L. 1993, *ApJS*, **88**, 205
- Leiner, E. M., & Geller, A. 2021, *ApJ*, **908**, 229
- Lipunov, V. M., Postnov, K. A., & Prokhorov, M. E. 1997, *Astron. Lett.*, **23**, 492
- Liu, B., & Lai, D. 2018, *ApJ*, **863**, 68
- Livio, M., & Soker, N. 1988, *ApJ*, **329**, 764
- MacLeod, M., & Ramirez-Ruiz, E. 2015, *ApJ*, **803**, 41
- MacLeod, M., Antoni, A., Murguía-Berthier, A., Macias, P., & Ramirez-Ruiz, E. 2017, *ApJ*, **838**, 56
- Mandel, I., & de Mink, S. E. 2016, *MNRAS*, **458**, 2634
- Mandel, I., Müller, B., Riley, J., et al. 2021, *MNRAS*, **500**, 1380
- Mapelli, M. 2016, *MNRAS*, **459**, 3432
- Marchant, P., Langer, N., Podsiadlowski, P., Tauris, T. M., & Moriya, T. J. 2016, *A&A*, **588**, A50
- Marchant, P., Renzo, M., Farmer, R., et al. 2019, *ApJ*, **882**, 36
- Marchant, P., Pappas, K. M. W., Gallegos-Garcia, M., et al. 2021, *A&A*, **650**, A107
- Mennekens, N., & Vanbeveren, D. 2014, *A&A*, **564**, A134
- Meurs, E. J. A., & van den Heuvel, E. P. J. 1989, *A&A*, **226**, 88
- Miller, M. C., & Hamilton, D. P. 2002a, *MNRAS*, **330**, 232
- Miller, M. C., & Hamilton, D. P. 2002b, *ApJ*, **576**, 894
- Misra, D., Fragos, T., Tauris, T. M., Zapartas, E., & Aguilera-Dena, D. R. 2020, *A&A*, **642**, A174
- Mondal, S., Belczynski, K., Wiktorowicz, G., Lasota, J.-P., & King, A. R. 2020, *MNRAS*, **491**, 2747
- Morawski, J., Giersz, M., Askar, A., & Belczynski, K. 2018, *MNRAS*, **481**, 2168
- Nandez, J. L. A., & Ivanova, N. 2016, *MNRAS*, **460**, 3992
- Nandez, J. L. A., Ivanova, N., & Lombardi, J. C. J. 2015, *MNRAS*, **450**, L39
- O’Leary, R. M., O’Shaughnessy, R., & Rasio, F. A. 2007, *Phys. Rev. D*, **76**, 061504
- Olejak, A., Fishbach, M., Belczynski, K., et al. 2020, *ApJ*, **901**, L39
- Paczynski, B. 1976, in *Structure and Evolution of Close Binary Systems*, eds. P. Eggleton, S. Mitton, & J. Whelan, *IAU Symp.*, **73**, 75
- Paczynski, B., & Ziółkowski, J. 1968, *Acta Astron.*, **18**, 255
- Passy, J.-C., De Marco, O., Fryer, C. L., et al. 2012, *ApJ*, **744**, 52
- Pavlovskii, K., Ivanova, N., Belczynski, K., & Van, K. X. 2017, *MNRAS*, **465**, 2092
- Perna, R., Wang, Y.-H., Farr, W. M., Leigh, N., & Cantiello, M. 2019, *ApJ*, **878**, L1
- Peters, P. C. 1964, PhD Thesis, California Institute of Technology
- Podsiadlowski, P., Ivanova, N., Justham, S., & Rappaport, S. 2010, *MNRAS*, **406**, 840
- Portegies Zwart, S. F., & Verbunt, F. 1996, *A&A*, **309**, 179
- Portegies Zwart, S. F., Baumgardt, H., Hut, P., Makino, J., & McMillan, S. L. W. 2004, *Nature*, **428**, 724
- Ricker, P. M., & Taam, R. E. 2008, *ApJ*, **672**, L41
- Rodriguez, C. L., Haster, C.-J., Chatterjee, S., Kalogera, V., & Rasio, F. A. 2016, *ApJ*, **824**, L8
- Rodriguez, C. L., Amaro-Seoane, P., Chatterjee, S., et al. 2018, *Phys. Rev. D*, **98**, 123005a
- Sadowski, A., Belczynski, K., Bulik, T., et al. 2008, *ApJ*, **676**, 1162
- Sand, C., Ohlmann, S. T., Schneider, F. R. N., Pakmor, R., & Röpke, F. K. 2020, *A&A*, **644**, A60
- Santoliquido, F., Mapelli, M., Bouffanais, Y., et al. 2020, *ApJ*, **898**, 152
- Santoliquido, F., Mapelli, M., Giacobbo, N., Bouffanais, Y., & Artale, M. C. 2021, *MNRAS*, **502**, 4877
- Shiber, S., Iaconi, R., De Marco, O., & Soker, N. 2019, *MNRAS*, **488**, 5615
- Silber, K., & Tremaine, S. 2017, *ApJ*, **836**, 39
- Spera, M., Giacobbo, N., & Mapelli, M. 2016, *Mem. Soc. Astron. It.*, **87**, 575
- Spera, M., Mapelli, M., Giacobbo, N., et al. 2019, *MNRAS*, **485**, 889
- Stevenson, S., Vigna-Gómez, A., Mandel, I., et al. 2017, *Nat. Commun.*, **8**, 14906
- Tanikawa, A., Susa, H., Yoshida, T., Trani, A. A., & Kinugawa, T. 2021, *ApJ*, **910**, 30
- The LIGO Scientific Collaboration & the Virgo Collaboration, 2020, ArXiv e-prints [arXiv:2004.08342]
- The LIGO Scientific Collaboration, the Virgo Collaboration (Abbott, R., et al.) 2021, *ApJ*, **913**, L7
- Tutukov, A. V., & Yungelson, L. R. 1993, *MNRAS*, **260**, 675
- van den Heuvel, E. P. J. 1976, in *Structure and Evolution of Close Binary Systems*, eds. P. Eggleton, S. Mitton, & J. Whelan, *IAU Symp.*, **73**, 35
- van den Heuvel, E. P. J., Portegies Zwart, S. F., & de Mink, S. E. 2017, *MNRAS*, **471**, 4256
- Vanbeveren, D. 1991, *A&A*, **252**, 159
- Vanbeveren, D., De Donder, E., Van Bever, J., Van Rensbergen, W., & De Loore, C. 1998, *New Astron.*, **3**, 443
- VanLandingham, J. H., Miller, M. C., Hamilton, D. P., & Richardson, D. C. 2016, *ApJ*, **828**, 77
- Vigna-Gómez, A., MacLeod, M., Neijssel, C. J., et al. 2020, *PASA*, **37**
- Vinciguerra, S., Neijssel, C. J., Vigna-Gómez, A., et al. 2020, *MNRAS*, **498**, 4705
- Vink, J. S., de Koter, A., & Lamers, H. J. G. L. M. 2001, *A&A*, **369**, 574
- Voss, R., & Tauris, T. M. 2003, *MNRAS*, **342**, 1169
- Webbink, R. F. 1984, *ApJ*, **277**, 355
- Woosley, S. E. 2016, *ApJ*, **824**, L10
- Woosley, S. E. 2017, *ApJ*, **836**, 244
- Xu, X.-J., & Li, X.-D. 2010, *ApJ*, **716**, 114
- Zevin, M., Samsing, J., Rodriguez, C., Haster, C.-J., & Ramirez-Ruiz, E. 2019, *ApJ*, **871**, 91
- Zevin, M., Bavera, S. S., Berry, C. P. L., et al. 2021, *ApJ*, **910**, 152
- Zuo, Z.-Y., & Li, X.-D. 2014, *MNRAS*, **442**, 1980

5 The implications of black hole spins

Detections of GWs from merging compact objects allow for a new, independent way of measuring and studying BH spins [2; 4; 7]. Inference on spin magnitudes of the merging components and their alignment with the orbit provides new insight into the evolution of massive stars and their final fate. Measured spin parameters also carry signatures of the GW sources formation scenarios. So far, detected GW sources seem to be consistent with a low spinning, but non-zero BH population with a possible tail extending towards high spin values [2; 7] (see Fig. 6) More comments on the current LVK spin distributions and their astrophysical implications may be found in Sec. 1.2.1.

In our article [86] we present the spin distribution of BH-BH mergers formed via isolated binary evolution. In particular, we focus on a high-spinning subpopulation of BH-BH mergers. We describe two possible evolutionary scenarios for BH-BH mergers with high effective spin χ_{eff} : via classical CE evolution and via stable mass transfer. Each of those scenarios dominates the formation of high-spinning BH-BH mergers, depending on the adopted CE development criteria [256].

In our studies [86] we show that efficient angular momentum transport [262] combined with the possibility of WR-BH and WR-WR tidal spin-up in very tight, evolved binary systems [83] result in a spin distribution consistent with LVK [2]. Our two standard models which differ by CE development criteria produce a minor but significant fraction of high-spinning BH-BH mergers. Effective spin distribution derived for both tested CE development criteria formation channels looks relatively similar.

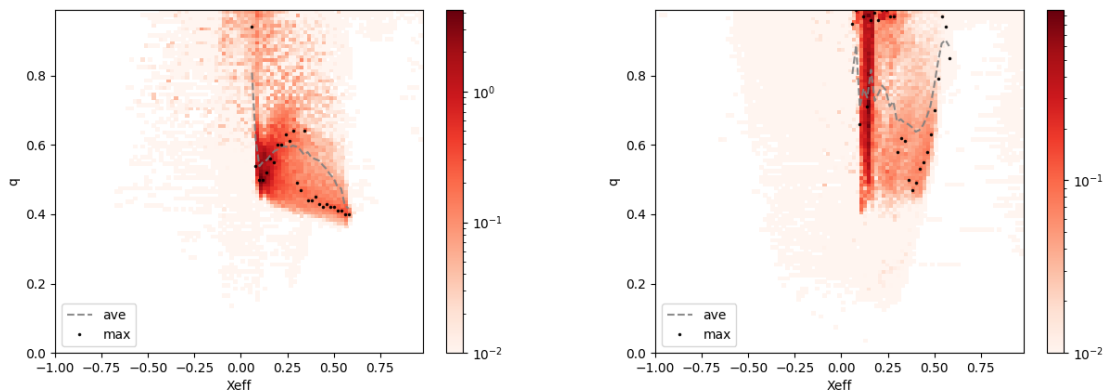



Fig. 16: 2-dimensional histogram of effective spin χ_{eff} and mass ratio q for BH-BH mergers formed via stable mass transfer (left) and CE (right). Detection-weighted results of StarTrack population synthesis code. Results not published.

However, the evolutionary formation scenario leading to a high-spinning subpopulation is different and has interesting consequences for the BH-BH mergers population. With less restrictive CE development criteria, for which BH-BH are formed through CE evolution, the second-born BH (tidally spun up) is usually the less massive one. In the CE scenario, there are also cases in which systems with almost equal mass components pass through a close WR-WR phase and both of them are spun up. With more restrictive CE development criteria, for which the majority of BH-BH mergers form through stable mass transfer, the second-born BH (tidally spun up) is usually the more massive one instead. This is due to common for this channel mass reversal scenario. As stable mass transfer in our approach is much less efficient in tightening the orbit than CE evolution, the system needs to have a highly unequal mass ratio at the onset of the second RLOF in order to enter the WR tidal regime.

The requirement of highly unequal masses to produce high-spinning BH-BH merger through stable mass transfer has resulted in the relation between χ_{eff} and mass ratio, see the left panel of Figure 16. In a stable mass transfer formation channel, BH-BH mergers with near equal mass components take rather low, near zero $\chi_{\text{eff}} \approx 0$, while mergers with unequal mass components take a broad spectrum of χ_{eff} values and tend to be more positive. The similar, negative correlation of spin and mass ratio has been reported by LVK population studies as well as other recent data analysis of GW data [2; 70]



The Implications of High Black Hole Spins for the Origin of Binary Black Hole Mergers

A. Olejak  and K. Belczynski

Nicolaus Copernicus Astronomical Center, Polish Academy of Sciences, ul. Bartycka 18, 00-716 Warsaw, Poland; aleksandra.olejak@wp.pl,
chrisbelczynski@gmail.com

Received 2021 September 22; revised 2021 October 12; accepted 2021 October 12; published 2021 October 26

Abstract

The LIGO–Virgo collaboration has reported 50 black hole–black hole (BH–BH) mergers and 8 candidates recovered from digging deeper into the detector noise. The majority of these mergers have low effective spins pointing toward low BH spins and efficient angular momentum (AM) transport in massive stars as proposed by several models (e.g., the Tayler–Spruit dynamo). However, out of these 58 mergers, 7 are consistent with having high effective-spin parameter ($\chi_{\text{eff}} > 0.3$). Additionally, two events seem to have high effective spins sourced from the spin of the primary (more massive) BH. These particular observations could be used to discriminate between the isolated binary and dynamical formation channels. It might seem that high BH spins point to a dynamical origin if AM in stars is efficient and forms low-spinning BHs. In such a case dynamical formation is required to produce second and third generations of BH–BH mergers with typically high spinning BHs. Here we show, however, that isolated binary BH–BH formation naturally reproduces such highly spinning BHs. Our models start with efficient AM in massive stars that is needed to reproduce the majority of BH–BH mergers with low effective spins. Later, some of the binaries are subject to a tidal spin-up allowing the formation of a moderate fraction ($\sim 10\%$) of BH–BH mergers with high effective spins ($\chi_{\text{eff}} \gtrsim 0.4\text{--}0.5$). In addition, isolated binary evolution can produce a small fraction of BH–BH mergers with almost maximally spinning primary BHs. Therefore, the formation scenario of these atypical BH–BH mergers remains to be found.

Unified Astronomy Thesaurus concepts: [Black holes \(162\)](#); [Compact objects \(288\)](#); [Massive stars \(732\)](#)

1. Introduction

The LIGO–Virgo collaboration has announced detection of gravitational waves from ~ 50 double black hole (BH–BH) mergers (Abbott et al. 2019a, 2019b, 2021a; Fishbach & Holz 2020). An additional eight BH–BH merger candidates have been recently reported (Abbott et al. 2021b). The majority of all these events have low effective spins parameters: $\chi_{\text{eff}} = \frac{m_1 a_1 \cos \theta_1 + m_2 a_2 \cos \theta_2}{m_1 + m_2} \approx 0$, where m_i are BH masses, $a_i = cJ_i/Gm_i^2$ are dimensionless BH spin magnitudes (J_i being the BH angular momentum (AM), c the speed of light, G the gravitational constant), and θ_i are angles between the individual BH spins and the system orbital AM.

However, among the detections there are also several BH–BH mergers that are characterized by higher (nonzero) positive effective spins. In Table 1 we list the parameters of the five BH–BH mergers with the highest effective spins reported by Abbott et al. (2021a) with an additional two high effective-spin systems reported by Abbott et al. (2021b).

The formation of close BH–BH systems is an open issue with several formation channels proposed and discussed in the context of the LIGO–Virgo mergers. The major formation scenarios include the isolated binary evolution (Bond & Carr 1984; Tutukov & Yungelson 1993; Lipunov et al. 1997; Voss & Tauris 2003; Belczynski et al. 2010b; Dominik et al. 2012; Kinugawa et al. 2014; Belczynski et al. 2016a; de Mink & Mandel 2016; Eldridge & Stanway 2016; Hartwig et al. 2016; Mandel & de Mink 2016; Marchant et al. 2016; Spera et al. 2016; Woosley 2016; van den Heuvel et al. 2017;

Stevenson et al. 2017; Hainich et al. 2018; Kruckow et al. 2018; Marchant et al. 2019; Neijssel et al. 2019; Spera et al. 2019; Bavera et al. 2020, 2021; du Buisson et al. 2020; Qin et al. 2021), the dense stellar system dynamical channel (Portegies Zwart & McMillan 2000; Miller & Hamilton 2002a, 2002b; Gültekin et al. 2004, 2006; Portegies Zwart et al. 2004; O’Leary et al. 2007; Sadowski et al. 2008; Downing et al. 2010; Antonini & Perets 2012; Benacquista & Downing 2013; Bae et al. 2014; Mennekens & Vanbeveren 2014; Chatterjee et al. 2017; Hurley et al. 2016; Mapelli 2016; Rodriguez et al. 2016, 2018; VanLandingham et al. 2016; Arca-Sedda & Capuzzo-Dolcetta 2019; Askar et al. 2017; Banerjee 2018; Morawski et al. 2018; Samsing 2018; Di Carlo et al. 2019; Perna et al. 2019; Zevin et al. 2019; Kremer et al. 2020), isolated multiple (triple, quadruple) systems (Antonini et al. 2017; Silsbee & Tremaine 2017; Arca-Sedda et al. 2021; Liu & Lai 2018; Fragione & Kocsis 2019), mergers of binaries in galactic nuclei (Antonini & Perets 2012; Hamers et al. 2018; Hoang et al. 2018; Fragione et al. 2019), and primordial BH formation (Sasaki et al. 2016; Clesse & García-Bellido 2017; Green 2017; Carr & Silk 2018; De Luca et al. 2021).

BH spins and their orientations can play an important role in distinguishing between various BH–BH formation models. If the BH spins are not small, then their orientation may possibly distinguish between a binary evolution origin (predominantly aligned spins) and dynamical formation channels (more or less isotropic distribution of spin orientations). If the BHs formed out of stars have small spins (Spruit 2002; Hotokezaka & Piran 2017; Zaldarriaga et al. 2018; Fuller et al. 2019; Qin et al. 2019; Bavera et al. 2020; Belczynski et al. 2020; Olejak et al. 2020) then BH–BH mergers with high effective spins may challenge their isolated evolution origin. In dense stellar clusters, BHs may merge several times easily producing BHs with high spins and making a dynamical channel a prime site

Table 1
BH–BH Mergers with High Effective Spins

No.	Name ^a	χ_{eff}	m_1	m_2	a_1
1	GW190517	$0.52^{+0.19}_{-0.19}$	$37.4^{+11.7}_{-7.6}$	$25.3^{+7.0}_{-7.3}$...
2	GW170729	$0.37^{+0.21}_{-0.25}$	$50.2^{+16.2}_{-10.2}$	$34.0^{+9.1}_{-10.1}$...
3	GW190620	$0.33^{+0.22}_{-0.25}$	$57.1^{+16.0}_{-12.7}$	$35.5^{+12.2}_{-12.3}$...
4	GW190519	$0.31^{+0.20}_{-0.22}$	$66.0^{+10.7}_{-12.0}$	$40.5^{+11.0}_{-11.1}$...
5	GW190706	$0.28^{+0.26}_{-0.29}$	$67.0^{+14.6}_{-13.3}$	$38.2^{+14.6}_{-13.3}$...
6	GW190403	$0.70^{+0.15}_{-0.27}$	$88.0^{+28.2}_{-32.9}$	$22.1^{+23.8}_{-9.0}$	$0.92^{+0.07}_{-0.22}$
7	GW190805	$0.35^{+0.30}_{-0.36}$	$48.2^{+17.5}_{-12.5}$	$32.0^{+13.4}_{-11.4}$	$0.74^{+0.22}_{-0.60}$

Note.

^a Names are abbreviated. We include candidate detections as full astrophysical events. Parameters of the first five events are from original LIGO–Virgo analysis (Abbott et al. 2021a), while the remaining two are from deeper searches into the detector noise (Abbott et al. 2021b).

for such events (Fishbach et al. 2017; Gerosa & Berti 2017). However, the assumption about the BH natal spin (and the AM transport efficiency) also plays a role in the effective-spin distribution for the dynamical channel (Banerjee 2021).

In this study we show that the current understanding of stellar/binary astrophysics (Belczynski et al. 2021) and the degeneracy between the different formation channels do not allow for such a simple test of the origin of the LIGO–Virgo BH–BH mergers. To demonstrate this we show that although the isolated binary evolution channel produces mostly BH–BH mergers with low effective spins, a small but significant fraction of mergers is expected to have moderate or even high effective spins. Despite the assumption that stars slow down their rotation due to efficient AM transport, we find that tidal interactions are capable of spinning up some stars allowing formation of rapidly spinning BHs (Detmers et al. 2008; Kushnir et al. 2017; Qin et al. 2018).

2. Method

We use the population synthesis code *StarTrack* (Belczynski et al. 2002, 2008) with a model of star formation rates and metallicity distribution based on Madau & Dickinson (2014) described in Belczynski et al. (2020). We employ the delayed core-collapse supernova (SN) engine for neutron star/BH mass calculation (Fryer et al. 2012), with weak mass loss from pulsation pair instability supernovae (Belczynski et al. 2016b). BH natal kicks are calculated from a Maxwellian distribution with $\sigma = 265 \text{ km s}^{-1}$ and decreased by fallback during core collapse; this makes a significant fraction of BHs form without a natal kick (Mirabel & Rodrigues 2003). We assume our standard wind losses for massive O/B stars (Vink et al. 2001) and Luminous Blue Variable (LBV) winds (specific prescriptions for these winds are listed in Section 2.2 of Belczynski et al. 2010a). BH natal spins are calculated under the assumption that AM in massive stars is transported by the Tayler–Spruit magnetic dynamo (Spruit 2002) as adopted in the MESA stellar evolutionary code (Paxton et al. 2015). Such BH natal spins take values in the range $a \in 0.05\text{--}0.15$ (see Belczynski et al. 2020). Note that the modified classic Tayler–Spruit dynamo with a different nonlinear saturation mechanism of the Tayler instability (Fuller & Ma 2019; Fuller et al. 2019) causes larger magnetic field amplitudes, more efficient AM transport, and even lower final natal spins ($a \sim 0.01$). BH spin

may be increased if the immediate BH progenitors (Wolf–Rayet, WR) stars in close binaries are subject to tidal spin-up. In our calculations for BH–WR, WR–BH, and WR–WR binary systems with orbital periods in the range $P_{\text{orb}} = 0.1\text{--}1.3$ days the BH natal spin magnitude is fit from WR star spun-up MESA models (see Equation 15 of Belczynski et al. 2020), while for systems with $P_{\text{orb}} < 0.1$ day the BH spin is taken to be equal to $a = 1$. BH spins may also be increased by accretion in binary systems. We treat accretion onto a compact object during Roche-lobe overflow (RLOF) and from stellar winds using the analytic approximations presented in King et al. (2001) and Mondal et al. (2020). In the adopted approach the accumulation of matter on a BH is very inefficient so accretion does not noticeably affect the final BH spin. However, note that, e.g., Van Son et al. (2020) or Bavera et al. (2021) tested different super-Eddington accretion prescriptions finding that some BHs may be significantly spun up by accretion.

For common-envelope (CE) evolution we assume a 100% ($\alpha_{\text{CE}} = 1$) orbital energy transfer for CE ejection and we adopt 5% Bondi accretion rate onto the BHs during CE (Ricker & Taam 2008; MacLeod & Ramirez-Ruiz 2015; MacLeod et al. 2017). During the stable RLOF (whether it is a thermal- or nuclear-timescale mass transfer, TTMT/NTMT) we adopt the following input physics. If an accretor is a compact object (neutron star or BH) we allow for super-Eddington accretion with excess transferred mass lost with an AM specific to the accretor (Mondal et al. 2020). In all other cases, we allow a fraction of the transferred mass of $f_a = 0.5$ to be lost from the binary with a specific AM of the binary orbit $j_{\text{loss}} = 1.0$ (expressed in units of $2\pi A^2/P_{\text{orb}}$, A being an orbital separation; see Equation (33) of Belczynski et al. 2008).

RLOF stability is an important issue in the context of BH–BH system formation in the framework of the isolated binary evolution (Neijssel et al. 2019; Belczynski et al. 2021; Gallegos-Garcia et al. 2021; Marchant et al. 2021; Olejak et al. 2021). In the standard *StarTrack* evolution we impose rather liberal limits for CE (dynamical-timescale RLOF) to develop (see Belczynski et al. 2008): binaries with a donor star more massive than 2–3 times the mass of the accretor are subject to CE. In this model (for simplicity tagged here as CE model) the vast majority of BH–BH mergers form through CE evolution, although we find some cases ($\lesssim 1\%$) of BH–BH merger formation without any CE event. In the alternative model (non-CE model; detailed description in Olejak et al. 2021) we allow CE to be suppressed for some systems even with a mass ratio as high as 6–8 (Pavlovskii et al. 2017). In this model the majority of the BH–BH mergers form without any CE event (the orbital decrease is obtained through angular momentum loss during stable RLOF), although some ($< 10\%$) BH–BH mergers form with the assistance of CE.

For each model we calculate the evolution of 64 million massive, Population I/II binary systems. We use the star formation history and chemical evolution of the universe to obtain the BH–BH merger properties within an approximate reach of LIGO–Virgo (redshift $z < 1$). We use the same method as described in Belczynski et al. (2020).

3. Results

Figure 1 shows a typical example of binary system evolution without a CE phase leading to the formation of a BH–BH merger with a tidally spun-up primary BH (restricted RLOF stability criteria; Olejak et al. 2021). The rather unequal-mass

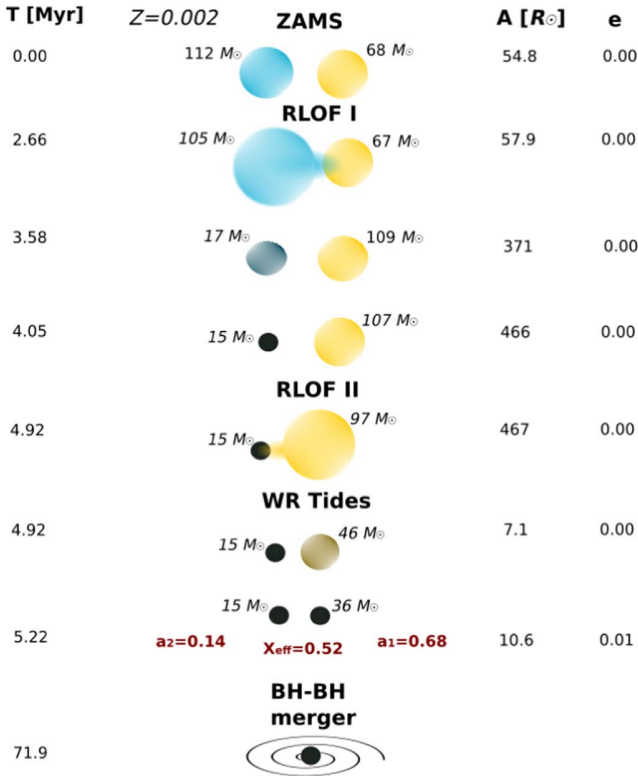


Figure 1. Typical example of a non-CE evolutionary scenario leading to the formation of a BH–BH merger with a tidally spun-up primary: $a_1 = 0.68$ and $\chi_{\text{eff}} = 0.52$. The binary system goes through two phases of RLOF with episodes of nuclear- and thermal-timescale mass transfer. RLOF I ends with the system mass ratio reversal. After RLOF II the system orbital separation significantly decreases and the WR star is a subject to tidal spin-up by a BH. Soon thereafter the close BH–BH system is formed with a short merger time of ~ 67 Myr (see Section 3).

massive stellar system ($112 M_{\odot}$ and $68 M_{\odot}$) with a metallicity of $Z = 0.002$ goes through two RLOF events. RLOF I is initiated by the more massive star; first by an NTMT when the donor is still on the main sequence and then through a TTMT when the donor evolves off the main sequence. After RLOF I, the system mass ratio is reversed: the initially more massive star lost over 80% of its mass while the companion gained $\sim 40 M_{\odot}$. Next, the initially more massive star ends its evolution directly collapsing to the less massive (secondary) BH with a mass of $m_2 = 15 M_{\odot}$ and spin $a_2 = 0.14$. When the companion star expands, it initiates a second stable RLOF. At the onset of RLOF II the system has highly unequal masses: the donor is almost 6.5 times more massive than the BH. The thermal timescale for a donor with mass $M_{\text{don}} \approx 97 M_{\odot}$, radius $R_{\text{don}} \approx 300 R_{\odot}$, and luminosity $L_{\text{don}} \approx 3 \times 10^6 L_{\odot}$ (parameters at the RLOF II onset¹) calculated with the formula by Kalogera & Webbink (1996) is $\tau_{\text{th}} \approx 330$ yr. It corresponds to a very high mass transfer rate $\dot{M} = M_{\text{don}}/\tau_{\text{th}} \approx 0.3 M_{\odot} \text{ yr}^{-1}$ that does not allow the BH to accrete much mass (despite the fact that we allow for super-Eddington accretion). Half of the donor’s mass is lost from the binary with the specific AM of the BH (as the matter was transferred to the vicinity of the BH accretor). This has a huge effect on the orbital separation that decreases from $A = 467 R_{\odot}$ to only $A = 7.1 R_{\odot}$. After RLOF II the binary

¹ Such parameter values are in line with other predictions for massive stars, e.g., using Geneva stellar evolution code (Yusof et al. 2013).

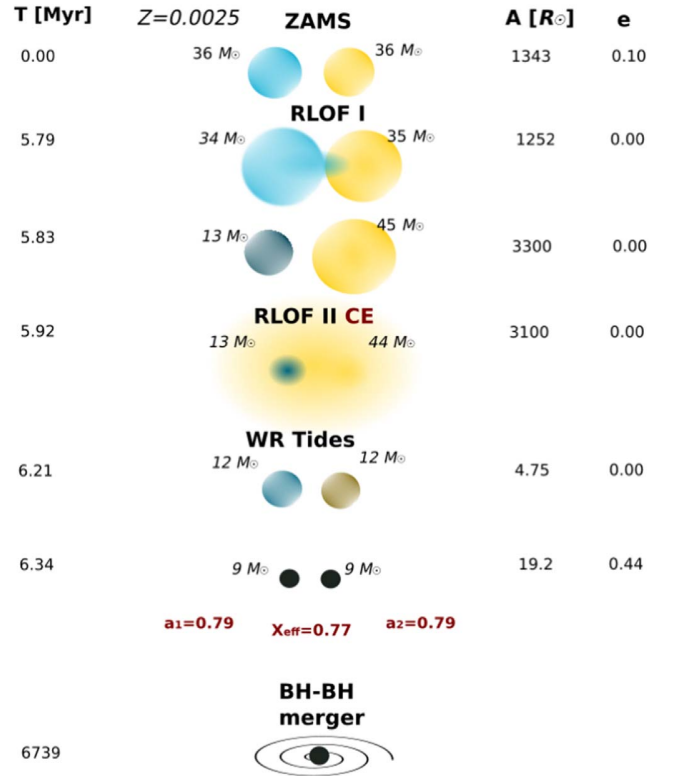


Figure 2. Typical example of an evolutionary scenario with the CE phase leading to the formation of a BH–BH merger with $a_1 = 0.79$, $a_2 = 0.79$, and $\chi_{\text{eff}} = 0.77$. First, the binary system goes through a stable RLOF phase with episodes of nuclear- and thermal-timescale mass transfer initiated by the initially more massive star. Then initially less massive star expands and initiates CE, after which the orbital separation is significantly decreased. After CE, the binary hosts two compact WR stars that are subject to tidal spin-up. Both stars explode as supernovae and form BHs on an eccentric orbit with a merger time of ~ 6.7 Gyr (see Section 3).

consists of a BH and a WR star that are close enough to allow for the tidal spin-up of the WR star. Finally, the WR star directly collapses to the more massive (primary) BH with a mass $m_1 = 36 M_{\odot}$ and spin $a_1 = 0.68$. The BH–BH system merges after ~ 67 Myr.

Figure 2 shows a typical CE evolution scenario (standard StarTrack RLOF stability criteria) leading to the formation of a BH–BH merger with both BHs spun up by tidal interactions. At the beginning, the binary system of two $\sim 36 M_{\odot}$ stars with $Z = 0.0025$ is on a wide ($A \approx 1340 R_{\odot}$) and eccentric ($e = 0.1$) orbit. When the initially more massive star expands the system goes through a stable RLOF, after which the donor loses its H-rich envelope and the orbit circularizes. Soon after RLOF I, the system goes through another (unstable) RLOF initiated by the initially less massive companion star. The ensuing CE evolution leads to significant orbital contraction from $A = 3100 R_{\odot}$ to $A = 4.5 R_{\odot}$ and leaves two WR stars subject to strong tidal interactions. Both stars end their evolution at a similar time forming via supernovae explosions two $\sim 9 M_{\odot}$ BHs. At the formation, both BHs get significant natal kicks that make the system orbit larger $A \approx 19 R_{\odot}$ and eccentric $e = 0.44$, leading to a merger time of ~ 6.7 Gyr.

In Table 2 we present the statistical spin properties of BH–BH systems merging at redshifts $z < 1$ for the two tested RLOF stability criteria models. In rows (1)–(6) we list the percentage of the BH–BH mergers with effective-spin parameter values

Table 2
Predictions for BH–BH Mergers from Binary Evolution

No.	Condition ^a	CE Model	Non-CE Model
1	$\chi_{\text{eff}} > 0.0$	97%	93%
2	$\chi_{\text{eff}} > 0.1$	95%	85%
3	$\chi_{\text{eff}} > 0.2$	70%	60%
4	$\chi_{\text{eff}} > 0.3$	36%	39%
5	$\chi_{\text{eff}} > 0.4$	10%	21%
6	$\chi_{\text{eff}} > 0.5$	2%	7%
7	$a_1 > 0.5$	3%	34%
8	$a_1 > 0.7$	2%	15%
9	$a_1 > 0.9$	1%	1%
10	$a_2 > 0.5$	52%	11%
11	$a_2 > 0.7$	33%	7%
12	$a_2 > 0.9$	12%	2%

Note.

^a We list fractions of BH–BH mergers (redshift $z < 1$) produced in our two population synthesis models satisfying a given condition.

$\chi_{\text{eff}} > 0.0, 0.1, 0.2, 0.3, 0.4,$ and 0.5 . In rows (7)–(9) we list the percentages of BH–BH mergers with a highly spinning primary BH $a_1 > 0.5, 0.7,$ and 0.9 while rows (10)–(12) give the percentages of mergers with a highly spinning secondary BH $a_2 > 0.5, 0.7,$ and 0.9 . The full distribution of the primary-spin, the secondary-spin, and the effective-spin parameters for both the CE and non-CE evolution is plotted in Figure 3 in the [Appendix](#).

4. Discussion and Conclusions

The rapidly increasing number of detected BH–BH mergers allows for some general population statements (Abbott et al. 2021b; Galadage et al. 2021; Roulet et al. 2021). It appears that (i) the majority ($\sim 70\%$ – 90%) of BH–BH mergers have low effective spins consistent with $\chi_{\text{eff}} \approx 0$ and that (ii) a small fraction ($\sim 10\%$ – 30%) of mergers have positive nonzero spins that can be as high as $\chi_{\text{eff}} \gtrsim 0.5$. Additionally, the population is consistent with (iii) no systems having negative effective spins and (iv) a nonisotropic distribution of effective spins (which could indicate dynamical origin). Finally, (v) there is at least one case of a primary BH (more massive) in a BH–BH merger with very high spin ($a_1 > 0.7$ at 90% credibility). These properties are noted to be broadly consistent with BH–BH mergers being formed in an isolated binary evolution.

In our study we have tested whether we can reproduce the above spin characteristics with our binary evolution models that employ efficient AM transport in massive stars and that impose tidal spin-up of compact massive Wolf–Rayet stars in close binaries. The two presented models employ our standard input physics but allow for the formation of BH–BH mergers assisted either by a CE or by a stable RLOF. We find that the observed population and its spin characteristics (i)–(v) are consistent with our isolated-binary-evolution predictions (see Table 2). In particular, we find that the majority of BH–BH mergers have small positive effective spins: $\sim 70\%$ mergers have $0 < \chi_{\text{eff}} < 0.3$ (efficient AM transport), while a small fraction have significant spins: 36%–39% mergers have $\chi_{\text{eff}} > 0.3$ and 2%–7% mergers have $\chi_{\text{eff}} > 0.5$ (tidal spin-up). The fraction of systems with negative effective spins is small (3%–7%) as most BHs do not receive strong natal kicks in our simulations. Individual BH spins can reach high values. A large fraction (11%–52%) of secondary BHs may have

significant spin values ($a_2 > 0.5$) as it is the less massive stars that are most often subject to tidal spin-up. Nevertheless, primary BHs may also form with high spins (3%–34% with $a_1 > 0.5$) if both stars have similar masses and both are subject to tidal spin-up (see Figure 2) or due to mass ratio reversal caused by the RLOF (see Figure 1). We also note the formation of a small fraction of almost maximally spinning BHs: 2%–12% for $a_2 > 0.9$ (secondary BH) and 1% for $a_1 > 0.9$ (primary BH). These results on effective spins and individual BH spins are consistent with the current LIGO–Virgo population of BH–BH mergers. Note that Qin et al. (2021) came to different conclusions, finding the high spinning detections challenging for the Tayler–Spruit dynamo, especially for the unequal-mass event with a high spinning primary (GW190403). Our non-CE model reproduces this type of merger due to the mass ratio reversal (see Figure 1). In this channel, at the onset of the second stable RLOF, the donor may be even 5–6 times more massive than the accretor, ending as an unequal-mass ($q \leq 0.4$) BH–BH merger. Qin et al. (2021) have not considered the case of a stable RLOF in such unequal-mass systems.

The above fractions correspond to just two different modes of spinning up during the classical isolated binary BH–BH formation. Had we varied several other factors that influence BH spins and their orientations in BH–BH mergers, the ranges of these fractions would have broadened. Some obvious physical processes that can affect BH spins and their orientations include initial star spin alignment (or lack thereof) with the binary AM, the alignment of stellar spins (or lack thereof) during RLOF phases, the treatment of accretion, the initial mass ratio distribution that can alter the ratio of systems going through stable and unstable (CE) RLOF, and the natal kicks that can misalign spin orientations. Above all, the three major uncertainties include the initial stellar rotation of stars forming BHs, the efficiency of AM transport, and the strength of tides in close binary systems. All of the above are only weakly constrained. Note that this is a proof-of-principle study that is limited only to BH spins in BH–BH mergers. In particular, we did not try to match BH masses and BH–BH merger rates for the highly spinning LIGO–Virgo BHs. In this study we have only shown that it is possible to produce highly spinning BHs by tidal interactions of stars in close binaries in evolution that include and do not include CE. Our two examples of evolution (Figures 1 and 2) have much smaller masses than the LIGO–Virgo mergers with highly spinning BHs (Table 1). Note, however, that we have not used the input physics here that allows for the formation of BHs with mass over $50 M_{\odot}$. Such a model is already incorporated and tested within our population synthesis code (Belczynski 2020). An attempt to match all observed parameters simultaneously is projected to happen in the future when LIGO–Virgo will deliver a larger sample of highly spinning BHs.

Given the results presented in this study, alas limited only to BH spins, we conclude that (i) the isolated binary evolution channel reproduces well the BH spins of the LIGO–Virgo mergers; (ii) if, in fact, the binary channel is producing the majority of the LIGO–Virgo BH–BH mergers, then this indicates that the AM transport is efficient in massive stars and the tidal interactions in close binaries are strong.

We thank the anonymous reviewer, Jean-Pierre Lasota, Ilya Mandel, and Sambaran Banerjee for their useful comments on the manuscript. K.B. and A.O. acknowledge support from the

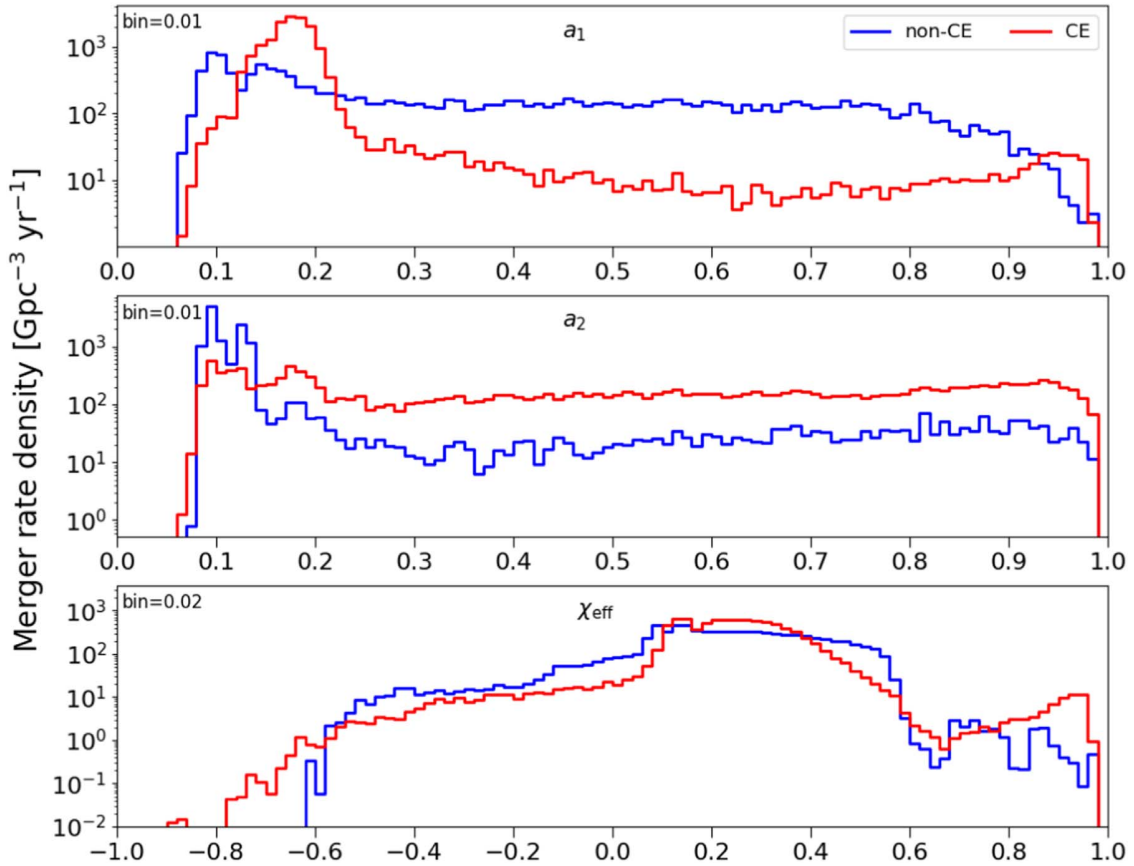


Figure 3. Distribution of (top panel) primary BH spin (a_1), (middle panel) secondary BH spin (a_2), and (bottom panel) effective-spin parameter (χ_{eff}) of BH–BH mergers at redshifts $z < 1.0$. The results are for two tested models: the non-CE model plotted with the red line, and the CE model plotted with the blue line. The figure is a supplement to the statistical spin predictions shown in Table 2 and described in Section 3.

Polish National Science Center (NCN) grant Maestro (2018/30/A/ST9/00050).

Appendix

In Figure 3 we plot the full distribution of the primary-spin, the secondary-spin and the effective-spin parameter for both the CE and non-CE evolution channels. The figure is a supplement to the statistical spin predictions shown in Table 2 and described in Section 3.

ORCID iDs

A. Olejak  <https://orcid.org/0000-0002-6105-6492>

References

- Abbott, B. P., Abbott, R., Abbott, T. D., et al. 2019a, *ApJL*, **882**, L24
 Abbott, B. P., Abbott, R., Abbott, T. D., et al. 2019b, *PhRvX*, **9**, 031040
 Abbott, R., Abbott, T. D., Abraham, S., et al. 2021a, *PhRvX*, **11**, 021053
 Abbott, R., Abbott, T. D., Acernese, F., et al. 2021b, arXiv:2108.01045
 Antonini, F., & Perets, H. B. 2012, *ApJ*, **757**, 27
 Antonini, F., Toonen, S., & Hamers, A. S. 2017, *ApJ*, **841**, 77
 Arca-Sedda, M., & Capuzzo-Dolcetta, R. 2019, *MNRAS*, **483**, 152
 Arca-Sedda, M., Li, G., & Kocsis, B. 2021, *A&A*, **650**, A189
 Askar, A., Szkudlarek, M., Gondok-Rosińska, D., Giersz, M., & Bulik, T. 2017, *MNRAS*, **464**, L36
 Bae, Y.-B., Kim, C., & Lee, H. M. 2014, *MNRAS*, **440**, 2714
 Banerjee, S. 2018, *MNRAS*, **473**, 909
 Banerjee, S. 2021, *MNRAS*, **500**, 3002
 Bavera, S. S., Fragos, T., Qin, Y., et al. 2020, *A&A*, **635**, A97
 Bavera, S. S., Fragos, T., Zevin, M., et al. 2021, *A&A*, **647**, A153
 Belczynski, K. 2020, *ApJL*, **905**, L15
 Belczynski, K., Bulik, T., Fryer, C. L., et al. 2010a, *ApJ*, **714**, 1217
 Belczynski, K., Dominik, M., Bulik, T., et al. 2010b, *ApJL*, **715**, L138
 Belczynski, K., Heger, A., Gladysz, W., et al. 2016b, *A&A*, **594**, A97
 Belczynski, K., Holz, D. E., Bulik, T., & O’Shaughnessy, R. 2016a, *Natur*, **534**, 512
 Belczynski, K., Kalogera, V., & Bulik, T. 2002, *ApJ*, **572**, 407
 Belczynski, K., Kalogera, V., Rasio, F. A., et al. 2008, *ApJS*, **174**, 223
 Belczynski, K., Klencki, J., Fields, C. E., et al. 2020, *A&A*, **636**, A104
 Belczynski, K., Romagnolo, A., Olejak, A., et al. 2021, arXiv:2108.10885
 Benacquista, M. J., & Downing, J. M. B. 2013, *LRR*, **16**, 4
 Bond, J. R., & Carr, B. J. 1984, *MNRAS*, **207**, 585
 Carr, B., & Silk, J. 2018, *MNRAS*, **478**, 3756
 Chatterjee, S., Rodriguez, C. L., Kalogera, V., & Rasio, F. A. 2017, *ApJL*, **836**, L26
 Clesse, S., & García-Bellido, J. 2017, *PDU*, **15**, 142
 De Luca, V., Desjacques, V., Franciolini, G., Pani, P., & Riotto, A. 2021, *PhRvL*, **126**, 051101
 de Mink, S. E., & Mandel, I. 2016, *MNRAS*, **460**, 3545
 Detmers, R. G., Langer, N., Podsiadlowski, P., & Izzard, R. G. 2008, *A&A*, **484**, 831
 Di Carlo, U. N., Giacobbo, N., Mapelli, M., et al. 2019, *MNRAS*, **487**, 2947
 Dominik, M., Belczynski, K., Fryer, C., et al. 2012, *ApJ*, **759**, 52
 Downing, J. M. B., Benacquista, M. J., Giersz, M., & Spurzem, R. 2010, *MNRAS*, **407**, 1946
 du Buisson, L., Marchant, P., Podsiadlowski, P., et al. 2020, *MNRAS*, **499**, 5941
 Eldridge, J. J., & Stanway, E. R. 2016, *MNRAS*, **462**, 3302
 Fishbach, M., & Holz, D. E. 2020, *ApJL*, **891**, L27
 Fishbach, M., Holz, D. E., & Farr, B. 2017, *ApJL*, **840**, L24
 Fragione, G., Grishin, E., Leigh, N. W. C., Perets, H. B., & Perna, R. 2019, *MNRAS*, **488**, 47
 Fragione, G., & Kocsis, B. 2019, *MNRAS*, **486**, 4781
 Fryer, C. L., Belczynski, K., Wiktorowicz, G., et al. 2012, *ApJ*, **749**, 91

- Fuller, J., & Ma, L. 2019, *ApJL*, **881**, L1
- Fuller, J., Piro, A. L., & Jermyn, A. S. 2019, *MNRAS*, **485**, 3661
- Galatage, S., Talbot, C., Nagar, T., et al. 2021, arXiv:2109.02424
- Gallegos-Garcia, M., Berry, C. P. L., Marchant, P., & Kalogera, V. 2021, arXiv:2107.05702
- Gerosa, D., & Berti, E. 2017, *PhRvD*, **95**, 124046
- Green, A. M. 2017, *PhRvD*, **96**, 043020
- Gültekin, K., Miller, M. C., & Hamilton, D. P. 2004, *ApJ*, **616**, 221
- Gültekin, K., Miller, M. C., & Hamilton, D. P. 2006, *ApJ*, **640**, 156
- Hainich, R., Osinkova, L. M., Shenar, T., et al. 2018, *A&A*, **609**, A94
- Hammers, A. S., Bar-Or, B., Petrovich, C., & Antonini, F. 2018, *ApJ*, **865**, 2
- Hartwig, T., Volonteri, M., Bromm, V., et al. 2016, *MNRAS*, **460**, L74
- Hoang, B.-M., Naoz, S., Kocsis, B., Rasio, F. A., & Dosopoulou, F. 2018, *ApJ*, **856**, 140
- Hotokezaka, K., & Piran, T. 2017, *ApJ*, **842**, 111
- Hurley, J. R., Sippel, A. C., Tout, C. A., & Aarseth, S. J. 2016, *PASA*, **33**, e036
- Kalogera, V., & Webbink, R. F. 1996, *ApJ*, **458**, 301
- King, A. R., Davies, M. B., Ward, M. J., Fabbiano, G., & Elvis, M. 2001, *ApJL*, **552**, L109
- Kinugawa, T., Inayoshi, K., Hotokezaka, K., Nakauchi, D., & Nakamura, T. 2014, *MNRAS*, **442**, 2963
- Kremer, K., Ye, C. S., Rui, N. Z., et al. 2020, *ApJS*, **247**, 48
- Kruckow, M. U., Tauris, T. M., Langer, N., Kramer, M., & Izzard, R. G. 2018, *MNRAS*, **481**, 1908
- Kushnir, D., Zaldarriaga, M., Kollmeier, J. A., & Waldman, R. 2017, *MNRAS*, **467**, 2146
- Lipunov, V. M., Postnov, K. A., & Prokhorov, M. E. 1997, *AstL*, **23**, 492
- Liu, B., & Lai, D. 2018, *ApJ*, **863**, 68
- MacLeod, M., Antoni, A., Murguía-Berthier, A., Macias, P., & Ramirez-Ruiz, E. 2017, *ApJ*, **838**, 56
- MacLeod, M., & Ramirez-Ruiz, E. 2015, *ApJ*, **803**, 41
- Madau, P., & Dickinson, M. 2014, *ARA&A*, **52**, 415
- Mandel, I., & de Mink, S. E. 2016, *MNRAS*, **458**, 2634
- Mapelli, M. 2016, *MNRAS*, **459**, 3432
- Marchant, P., Langer, N., Podsiadlowski, P., Tauris, T. M., & Moriya, T. J. 2016, *A&A*, **588**, A50
- Marchant, P., Pappas, K. M. W., Gallegos-Garcia, M., et al. 2021, *A&A*, **650**, A107
- Marchant, P., Renzo, M., Farmer, R., et al. 2019, *ApJ*, **882**, 36
- Mennekens, N., & Vanbeveren, D. 2014, *A&A*, **564**, A134
- Miller, M. C., & Hamilton, D. P. 2002a, *MNRAS*, **330**, 232
- Miller, M. C., & Hamilton, D. P. 2002b, *ApJ*, **576**, 894
- Mirabel, I. F., & Rodrigues, I. 2003, *Sci*, **300**, 1119
- Mondal, S., Belczyński, K., Wiktorowicz, G., Lasota, J.-P., & King, A. R. 2020, *MNRAS*, **491**, 2747
- Morawski, J., Giersz, M., Askar, A., & Belczynski, K. 2018, *MNRAS*, **481**, 2168
- Neijssel, C. J., Vigna-Gómez, A., Stevenson, S., et al. 2019, *MNRAS*, **490**, 3740
- O’Leary, R. M., O’Shaughnessy, R., & Rasio, F. A. 2007, *PhRvD*, **76**, 061504
- Olejak, A., Belczynski, K., & Ivanova, N. 2021, *A&A*, **651**, A100
- Olejak, A., Fishbach, M., Belczynski, K., et al. 2020, *ApJL*, **901**, L39
- Pavlovskii, K., Ivanova, N., Belczynski, K., & Van, K. X. 2017, *MNRAS*, **465**, 2092
- Paxton, B., Marchant, P., Schwab, J., et al. 2015, *ApJS*, **220**, 15
- Perma, R., Wang, Y.-H., Farr, W. M., Leigh, N., & Cantiello, M. 2019, *ApJL*, **878**, L1
- Portegies Zwart, S. F., Baumgardt, H., Hut, P., Makino, J., & McMillan, S. L. W. 2004, *Natur*, **428**, 724
- Portegies Zwart, S. F., & McMillan, S. L. W. 2000, *ApJL*, **528**, L17
- Qin, Y., Fragos, T., Meynet, G., et al. 2018, *A&A*, **616**, A28
- Qin, Y., Marchant, P., Fragos, T., Meynet, G., & Kalogera, V. 2019, *ApJL*, **870**, L18
- Qin, Y., Wang, Y.-Z., Dong-Hong, et al. 2021, arXiv:2108.04821
- Ricker, P. M., & Taam, R. E. 2008, *ApJL*, **672**, L41
- Rodriguez, C. L., Amaro-Seoane, P., Chatterjee, S., et al. 2018, *PhRvD*, **98**, 123005
- Rodriguez, C. L., Haster, C.-J., Chatterjee, S., Kalogera, V., & Rasio, F. A. 2016, *ApJL*, **824**, L8
- Roulet, J., Chia, H. S., Olsen, S., et al. 2021, *PhRvD*, **104**, 083010
- Sadowski, A., Belczynski, K., Bulik, T., et al. 2008, *ApJ*, **676**, 1162
- Samsing, J. 2018, *PhRvD*, **97**, 103014
- Sasaki, M., Suyama, T., Tanaka, T., & Yokoyama, S. 2016, *PhRvL*, **117**, 061101
- Silber, K., & Tremaine, S. 2017, *ApJ*, **836**, 39
- Spera, M., Giacobbo, N., & Mapelli, M. 2016, *MmSAI*, **87**, 575
- Spera, M., Mapelli, M., Giacobbo, N., et al. 2019, *MNRAS*, **485**, 889
- Spruit, H. C. 2002, *A&A*, **381**, 923
- Stevenson, S., Vigna-Gómez, A., Mandel, I., et al. 2017, *NatCo*, **8**, 14906
- Tutukov, A. V., & Yungelson, L. R. 1993, *MNRAS*, **260**, 675
- van den Heuvel, E. P. J., Portegies Zwart, S. F., & de Mink, S. E. 2017, *MNRAS*, **471**, 4256
- Van Son, L. A. C., De Mink, S. E., Broekgaarden, F. S., et al. 2020, *ApJ*, **897**, 100
- VanLandingham, J. H., Miller, M. C., Hamilton, D. P., & Richardson, D. C. 2016, *ApJ*, **828**, 77
- Vink, J. S., de Koter, A., & Lamers, H. J. G. L. M. 2001, *A&A*, **369**, 574
- Voss, R., & Tauris, T. M. 2003, *MNRAS*, **342**, 1169
- Woosley, S. E. 2016, *ApJL*, **824**, L10
- Yusof, N., Hirschi, R., Meynet, G., et al. 2013, *MNRAS*, **433**, 1114
- Zaldarriaga, M., Kushnir, D., & Kollmeier, J. A. 2018, *MNRAS*, **473**, 4174
- Zevin, M., Samsing, J., Rodriguez, C., Haster, C.-J., & Ramirez-Ruiz, E. 2019, *ApJ*, **871**, 91

6 The role of supernova convection

Massive stars, with their initial mass above $M_{\text{ZAMS}} \gtrsim 10 M_{\odot}$, pass through hydrogen, helium, carbon, neon, oxygen, and silicon fusion stages, finally producing an iron core of $\sim 1.5 M_{\odot}$ in the center [21]. Then, in simplified terms, no further energy is released by nuclear fusion to prevent the stellar core against collapse. The physical conditions: high temperature and density, lead to electron capture by nuclei. The core, which is mostly supported by the degeneracy pressure of electrons, is therefore thrown out of balance and contracts. The contracting core heats up, producing high-energy photons, which decompose iron nuclei into helium via photodisintegration. The outer layers of the collapsing core fall toward the star center, reaching velocities nearly a quarter of the light speed [21]. The inner collapse of the core is eventually halted by short-range nuclear force once the matter density is comparable to two times that of an atomic nucleus. The core becomes a proto-neutron star with a radius of approximately ~ 30 km [21]. When the core collapse is halted, the falling matter rebounds and generates a shock wave. This shock propagates outwards, gradually losing its energy, and eventually stalls due to photodisintegration and loss of neutrinos [21]. At this moment, the proto-neutron star is expected to accrete mass from the outer layers at a very high rate of a few tenths of a solar mass per second. Therefore, the timescales since the shock to the eventual supernovae (SN) explosion might be crucial for the final SN outcome (NS or BH) and the remnant mass [22; 263]. Understanding SN development might be the key to identifying the origin of the lower mass gap – the suppressed number of detected low mass compact objects in the mass range $\sim 2 - 5 M_{\odot}$ [22; 25]. See Section 1.1.1 for more comments on the lower mass gap and its current status.

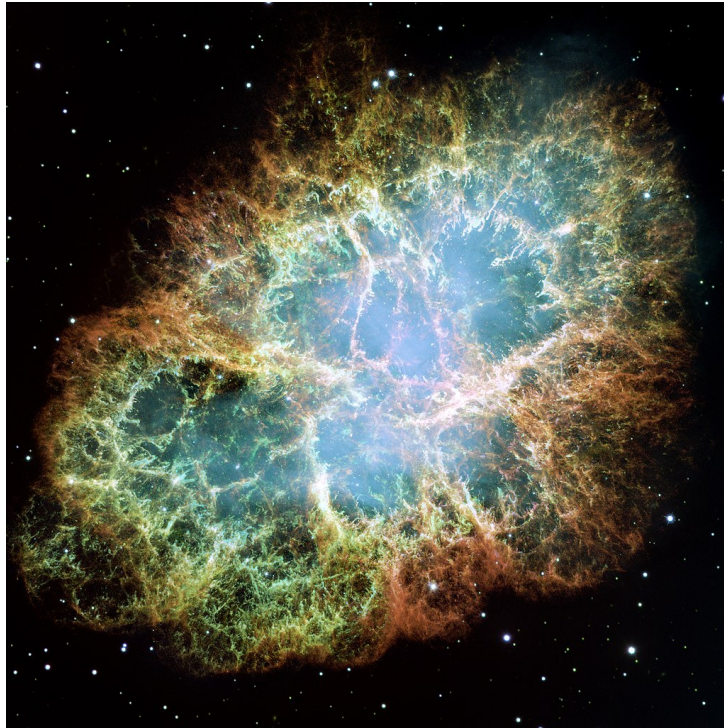


Fig. 17: The Crab Nebula, supernova remnant, image by NASA’s Hubble Space Telescope. Credit: NASA, ESA, J. Hester, and A. Loll (Arizona State University).

Our understanding of the mechanism behind core-collapse SN is still insufficient [21]. Those incredible astrophysical laboratories are still a big challenge for theoretical modeling, due to the complex physics, only a few observational constraints, and numerical viscosity that makes 3-dimensional simulations unreliable. Several approaches have been proposed to mimic the real SN engine [263–270].

In our recent studies [26] we implement in the StarTrack population synthesis code the advancements for the convection-enhanced SN engine [22; 25; 270–272], the approach based on the assumption that convection is the key to SN modeling. In the article [26] we adopt and test results for improved 1-dimensional mixing models driving SN explosion given by [25] which tie the pre-SN stellar structure with the final mass of a NS or a BH. The aim of the work was to study how different assumptions on SN convection growth affects the population of merging compact remnants, with a particular focus on the lower mass gap region. The new formulas by [25], in contrast to previous, widely used extreme cases of the so-called rapid and delayed SN engines [22], allow for testing a broad spectrum of the convection growth timescales. Different variants of the formulas result in a smooth transition between having a deep mass gap and a mass distribution rich in massive NSs and low-mass BHs. In our article, we present the distribution of masses, mass ratios, and the local density merger rates predicted for different SN convection growth variants. We also test the impact of new SN models along with various assumptions on highly uncertain criteria for CE development and the limit for PSN-origin upper mass gap.

The role of supernova convection for the lower mass gap in the isolated binary formation of gravitational wave sources

Aleksandra Olejak ¹, ¹★ Chris L. Fryer ^{2,3,4,5,6} Krzysztof Belczynski ¹ and Vishal Baibhav ⁷

¹*Nicolaus Copernicus Astronomical Center, Polish Academy of Sciences, 18 Bartycka Street, PL-00-716 Warsaw, Poland*

²*Center for Theoretical Astrophysics, Los Alamos National Laboratory, Los Alamos, NM 87545, USA*

³*Computer, Computational, and Statistical Sciences Division, Los Alamos National Laboratory, Los Alamos, NM 87545, USA*

⁴*Physics Department, University of Arizona, Tucson, AZ 85721, USA*

⁵*Department of Physics and Astronomy, The University of New Mexico, Albuquerque, NM 87131, USA*

⁶*Department of Physics, The George Washington University, Washington, DC 20052, USA*

⁷*Center for Interdisciplinary Exploration and Research in Astrophysics (CIERA), Northwestern University, 1800 Sherman Ave, Evanston, IL 60201, USA*

Accepted 2022 August 19. Received 2022 August 1; in original form 2022 April 21

ABSTRACT

Understanding the astrophysical phenomena involving compact objects requires an insight about the engine behind the core-collapse supernovae (SNe) and the fate of the stellar collapse of massive stars. In particular, this insight is crucial in developing an understanding of the origin and formation channels of the growing populations of the detected black hole–black hole, black hole–neutron star, and neutron star–neutron star mergers. The time-scale of convection growth may have a large effect on the strength of SN explosion and therefore also on the mass distribution of stellar remnants. We adopt new formulas for the relation between the pre-SN star properties and their remnants and check how they impact the population of double compact object (DCO) mergers formed via the isolated binary evolution. The new formulas give one the ability to test a wide spectrum of assumptions on the convection growth time. In particular, the different variants allow for a smooth transition between having a deep mass gap and a remnant mass distribution filled by massive neutron stars and low-mass black holes. We present the distribution of masses, mass ratios, and the local merger rate densities of DCO for the different variants of new formulas and test them together with different approaches to other highly uncertain processes. We find that the mass distribution of DCO mergers is sensitive to the adopted assumption on the SN convection growth time-scale up to $m_1 + m_2 \lesssim 35 M_\odot$. Between the two extreme tested variants the probability of compact object formation within the mass gap may differ by up to approximately two orders of magnitude.

Key words: Physical data and processes: gravitational waves – Stars: black holes – Stars: binaries – Transients: black hole mergers – Transients: neutron star mergers – Transients: black hole – neutron star mergers – Transients: supernovae.

1 INTRODUCTION

Recent surveys provide more and more candidates and confirmed observations for black hole (BH) and neutron star (NS) systems in the Universe. Especially, the increasing amount of gravitational wave (GW) detections significantly enriched the data base with known compact objects, opening new possibilities for studying and constraining their formation. So far, LIGO/Virgo/KAGRA collaboration announced the detection of GW signals from around ~ 90 sources (Abbott et al. 2019a, b, 2021a, b). One of the most important questions in GW astrophysics is about the origin of compact binaries and the formation scenario of the detected double compact object (DCO) mergers. The popular formation scenarios in the literature include the isolated binary evolution (Bond & Carr 1984; Tutukov & Yungelson 1993; Lipunov, Postnov & Prokhorov 1997; Belczynski et al. 2010b; Kinugawa et al. 2014; Mennekens & Vanbeveren 2014a; de Mink & Mandel 2016; Eldridge & Stanway 2016; Hartwig et al.

2016; Mandel & de Mink 2016; Marchant et al. 2016, 2019; Woosley 2016; Stevenson et al. 2017; van den Heuvel, Portegies Zwart & de Mink 2017; Hainich et al. 2018; Neijssel et al. 2019; Spera et al. 2019; du Buisson et al. 2020; Bavera et al. 2021; Olejak & Belczynski 2021; van Son et al. 2021; Qin et al. 2022), the dense stellar system dynamical channel (Portegies Zwart & McMillan 2000; Miller & Hamilton 2002; Gültekin, Miller & Hamilton 2004, 2006; O’Leary, O’Shaughnessy & Rasio 2007; Sadowski et al. 2008; Downing et al. 2010; Antonini & Perets 2012; Benacquista & Downing 2013; Bae, Kim & Lee 2014; ; Hurley et al. 2016; Mapelli 2016; Rodriguez et al. 2016; VanLandingham et al. 2016; Askar et al. 2017; Chatterjee et al. 2017; Banerjee 2018; Belczynski et al. 2018; Morawski et al. 2018; Rodriguez et al. 2018; Samsing 2018; Arca-Sedda & Capuzzo-Dolcetta 2019; Di Carlo et al. 2019; Perna et al. 2019; Zevin et al. 2019; Kremer et al. 2020), isolated multiple (triple, quadruple) systems (Toonen, Hamers & Portegies Zwart 2016; Antonini, Toonen & Hamers 2017; Silsbee & Tremaine 2017; Liu & Lai 2018; Fragione & Kocsis 2019; Arca-Sedda, Li & Kocsis 2021; Vigna-Gómez et al. 2021; Stegmann et al. 2022), and mergers of binaries in galactic nuclei (Antonini & Perets 2012; Hamers et al. 2018; Hoang

* E-mail: aleksandra.olejak@wp.pl, aolejak@camk.edu.pl

et al. 2018; Fragione et al. 2019; Tagawa, Haiman & Kocsis 2020; Tagawa et al. 2021). Progress in understanding the origin of compact binaries requires having a reliable relation between properties of pre-supernova (SN) star and its remnant mass (NS, BH, or no stellar remnant). Conversely, in order to have a reliable distribution of remnant masses, scientists need to constrain the existing SN models by comparing results of population synthesis models with the detected and observed population of compact objects. Several recent studies applied population synthesis calculations to predict mass distributions of Galactic or cosmological DCO population adopting different SN prescriptions (Zevin et al. 2020; Dabrowny, Giacobbo & Gerosa 2021; Shao & Li 2021; Zevin & Bavera 2022). Such comparisons will become much more reliable in the near future as the predicted number of DCO mergers will increase significantly after the O4 run (e.g. Magee & Borhanian 2022) and later, due to the development of the next-generation ground-based GW detectors (Borhanian & Sathyaprakash 2022).

There are several approaches trying to mimic the true SN engine in order to predict the final fate of massive stars and estimate the remnant masses. However, the final faith of progenitors with their initial masses in the range $20\text{--}40 M_{\odot}$, so eventual lower mass gap fillers, is especially challenging as the outcome may drastically differ depending on the accumulated explosion energy (Fryer et al. 2012; Liu et al. 2021).

Due to the complexity of the problem and the emergence of numerical viscosity in the three-dimensional modelling, some find it more reliable using the one-dimensional codes with artificially altered energy deposition into the pre-SN star in order to get an explosion. One approach is to alter the neutrino luminosity or absorption to increase the energy deposited (Fröhlich et al. 2006; Fischer et al. 2010; Ugliano et al. 2012; Perego et al. 2015; Ertl et al. 2016; Prša et al. 2016). Another approach is to implement the one-dimensional mixing models to drive explosions (Fryer et al. 2018; Couch, Warren & O’Connor 2020). In this study, we assume that convection dominates the matter motion above the proto NS (Herant et al. 1994; Blondin, Mezzacappa & DeMarino 2003; Fryer & Young 2007; Melson et al. 2015; Burrows et al. 2018; Fields & Couch 2021) and therefore is crucial for SN engine modelling. We implement and test new results for different one-dimensional mixing prescriptions of Fryer, Olejak & Belczynski (2022). The time-scale of convection growth significantly affects the course of eventual SN explosion and therefore also the final distribution of compact object remnants (Fryer & Young 2007).

The new formulas give one the ability to test a wide spectrum of assumptions on the convection growth time. In particular, the different variants of the formulas allow for a smooth transition between having a deep lower mass gap and a remnant mass distribution filled by massive NSs and low-mass BHs. The dearth of compact objects with the masses in the range $\sim 3\text{--}5 M_{\odot}$ among the observed population of X-ray binary systems (Bailyn et al. 1998; Özel et al. 2010; Farr et al. 2011) has led to the idea of potential mass gap between the maximum mass of an NS and the minimum mass of a BH. Also, the latest discoveries and analyses of The LIGO Scientific Collaboration (2021a, b) point to the possible existence of an NS/BH mass gap. On the other hand, some recent estimates for isolated compact objects detected via microlensing provide candidates for NS/BH mass in a gap range (Mroz et al. 2021; Lam et al. 2022; Sahu et al. 2022). Due to a relatively small sample of known compact objects and usually significant error bars on their mass estimates, it is not yet clear whether the mass gap is a real phenomenon. The possible physical mechanism responsible for the formation of the gap, the rapid SN time-scale of the convection

growth, was suggested by Fryer et al. (2012) and Belczynski et al. (2012). This work is an update and a continuation of those studies. In this study, we implement new formulas for the SN remnant masses into the `STARTRACK` population synthesis code and test how the different variants of mixing (corresponding to different convection growth time-scales) change the distribution of DCO mergers masses, mass ratios, and local merger rate density. Section 2 explains the used method, including a brief description of the `STARTRACK` code. It contains our main adopted physical assumptions, especially the description of the new adopted prescriptions for remnant masses. In Section 3, we present the relation between the properties of pre-SN stars (NS or BH progenitor) and their new remnant masses in a single star evolution, together with a comparison with the previously used models. In Section 4, we present the results of the isolated binary evolution for different types of DCO mergers. Section 6 includes the summary of the results and conclusions. Furthermore, Appendix A demonstrates how the different assumptions on the mass threshold for BH formation (instead of NS) influence the lower mass gap. In Appendix B, we attach the redshift evolution of BH–BH merger rate densities for two formation channels with and without the common envelope phase (CE). Appendix C includes the effect of eventual stochasticity in pre-SN stellar structure on the mass distribution of DCO mergers. In Appendix D, we briefly compare our new SN prescriptions with other parametrized prescription for stellar remnant masses proposed by a recent study (Dabrowny et al. 2021).

2 METHOD

2.1 STARTRACK code

In this study, we generate a population of cosmological DCO mergers using the `STARTRACK` population synthesis code (Belczynski, Kalogera & Bulik 2002; Belczynski et al. 2008). The version of the code used in this paper is the same as the one described in section 2 of Olejak, Belczynski & Ivanova (2021) with two important modifications: the first is the new remnant mass formulas (see Section 2.2) and the second is a different approach to pair-instability supernovae (PPSN)/pair-instability supernovae (PSN). In this study, we test the two different prescriptions for PSN. In the first approach we adopt a strong PPSN/PSN which limits the mass of BHs to $\sim 45 M_{\odot}$ as adopted in Belczynski et al. (2016). The second approach is a revised prescription from Belczynski (2020) in which a star experiences disruption in PSN if the final mass of its helium core is in the range $90 M_{\odot} < M_{\text{He}} < 175 M_{\odot}$. The revised PSN model does not include any mass-loss in PPSN and allows for the formation of BH with mass up to $90 M_{\odot}$. In the strong PPSN/PSN model we use the initial mass function (IMF) with the maximum mass for a star limited to $150 M_{\odot}$, while we extend it to $200 M_{\odot}$ in the revised PSN model, similarly as done for Belczynski (2020).

We use a model of star formation history and metallicity distribution in the Universe (Madau & Fragos 2017) described in Belczynski et al. (2020). The adopted procedures for accretion on to a compact object during stable Roche lobe overflow (RLOF) and from stellar winds are based on the analytic approximations (King et al. 2001), implemented as in Mondal et al. (2020). For the non-compact accretors, we assume a 50 per cent non-conservative RLOF (Meurs & van den Heuvel 1989; Vinciguerra et al. 2020) with a fraction of the donor mass $(1 - f_a)$ lost from the system together with the corresponding part of the donor and orbital angular momentum (see section 3.4 of Belczynski et al. 2008). In the current

version of `STARTTRACK` code, we limit the mass accretion rate on to a non-compact accretor to the Eddington limit. We use the following formula:

$$\dot{M}_{\text{Edd}} = \frac{4\pi c R}{\eta k_{th}}. \quad (1)$$

The adopted limit is derived under the assumptions that accretion goes to a star radius R , and that there are no outflows/jets, so $\eta = 1$. Here, c is the speed of light and k_{th} is the Thomson scattering opacity. The Eddington limit for a non-compact accretor may be exceeded in our simulations in case of a thermal-time-scale mass transfer from massive, rapidly expanding donor on its Hertzsprung gap. We adopt 5 per cent Bondi–Hoyle rate accretion on to the compact object during the CE phase (Ricker & Taam 2008; MacLeod & Ramirez-Ruiz 2015; MacLeod et al. 2017) and standard `STARTTRACK` physical value for the envelope ejection efficiency $\alpha_{\text{CE}} = 1.0$. For the stellar wind mass-loss we use the formulas based on theoretical predictions of radiation-driven mass-loss (Vink, de Koter & Lamers 2001) with the inclusion of the Luminous Blue Variable (LBV) mass-loss (Belczynski et al. 2010b). We adopt a Maxwellian distribution natal kicks with $\sigma = 265 \text{ km s}^{-1}$ (Hobbs et al. 2005) lowered by fallback (Fryer et al. 2012) at NS and BH formation.

While presenting the results for binary evolution, we distinguish between the two prescriptions for stability of RLOF: the standard CE development criteria described in section 5.2 of Belczynski et al. (2008) and the revised mass transfer stability criteria based on the results of Pavlovskii et al. (2017), implemented and tested in Olejak et al. (2021). The revised RLOF stability criteria applies only to the systems with massive donors (mainly BH progenitors) with their initial masses over $20 M_{\odot}$. It allows for CE development under much more restricted conditions than the standard `STARTTRACK` criteria, taking into account the system mass ratio at the RLOF onset, the radius of the donor, and metallicity. For details, see Section 3.1 or the revised stability diagrams plotted in figs 2 and 3 of Olejak et al. (2021). Simplifying, the typical critical mass ratio (of donor to accretor) for a system to develop CE instead of stable RLOF is around 4–5 for the revised criteria, while it is rather 2–3 for the standard `STARTTRACK` criteria.

2.2 New formulas for remnant masses

The main modification in the `STARTTRACK` code tested in this paper is the implementation of new formulas for remnant masses (NSs and BHs) given by Fryer et al. (2022). In their study, Fryer et al. (2022) apply sub-grid mixing algorithms to the profile of post-bounce pre-SN cores in order to follow the convection growth above proto-NSs, and estimate explosion energies and the final remnant masses. In particular, the new formulas represent analytical fits to different solutions obtained for a set of one-dimensional core-collapse models based on the mixing-length theory and a Reynolds-averaged Navier–Stokes approach (Livescu et al. 2009). For more details, see sections 2 and 3 of Fryer et al. (2022).

Fryer et al. (2022) predict the final masses of the formed NS and BH by capturing how the differences in convection growth time-scales associated with variations in mixing affect the final stellar remnant masses. Increasing the mixing length tends to accelerate the growth of convection making explosion more likely. Such a trend is commonly observed in the one-dimensional simulations results. Based on those results, Fryer et al. (2012) obtained simple mathematical fits which incorporate the pre-SN stellar structure, to estimate the remnant mass for a given progenitor.

In contrast to the previously used rapid and delayed SN models given by formulas 5 and 6 of Fryer et al. (2012), which may be treated as the two extremes, the new formula gives one the ability to test the remnant masses for a wide spectrum of assumptions on convection growth time-scales. Formula 2 allows to calculate the remnant masses assuming smooth relation with pre-SN carbon–oxygen core mass M_{CO} and varying different mixing efficiency (f_{mix}) set by the convection growth time.

$$M_{\text{rem}} = 1.2 + 0.05 f_{\text{mix}} + 0.01 (M_{\text{CO}} / f_{\text{mix}})^2 + e^{f_{\text{mix}}(M_{\text{CO}} - M_{\text{crit}})}, \quad (2)$$

where M_{rem} is the remnant mass (NS or BH), f_{mix} is the convection mixing parameter which takes value in the range 0.5–4.0, M_{CO} is the mass of the carbon–oxygen core of the pre-SN star in M_{\odot} unit (in `STARTTRACK` it is the value at the end of star core helium-burning phase), and $M_{\text{crit}} = 5.75 M_{\odot}$ is the assumed critical mass of carbon oxygen core for a BH formation (the switch from NS to BH formation). Note that the mass of the remnant is calculated using equation (2) till some M_{CO} value, which depends on the steepness of the exponent (so the adopted f_{mix} value). If M_{rem} from equation (2) exceeds the value of the total mass of pre-SN star ($M_{\text{pre-SN}}$), then we assume the direct collapse of the star to a BH with only mass-loss in the form of neutrinos (1 per cent of pre-SN mass):

$$M_{\text{rem}} = \min(M_{\text{eq. 2}}, M_{\text{pre-SN}}). \quad (3)$$

Convection mixing parameter f_{mix} (equation 2) is inversely proportional to the convection growth time. Therefore, $f_{\text{mix}} = 4.0$ corresponds to the rapid growth of the convection < 10 ms that then develops an explosion in the first 100 ms (depending on mass), while $f_{\text{mix}} = 0.5$ corresponds to a growth time closer to 100 ms where the explosion can take up to 1s. The new formula with the adopted value $f_{\text{mix}} \approx 0.5$ results in a shallow or no mass gap similarly to the previous delayed SN model (Fryer et al. 2012), while a high value of $f_{\text{mix}} \approx 4.0$ results in a deep mass gap, similarly to the previous rapid SN model. The applied formulas are for non-rapidly rotating progenitors.

2.3 Detection-weighted calculations

The distributions of the source properties observed by the gravitational-wave detectors are biased due to the selection effects. We account for such detection biases when we compare mass-ratio distributions of the synthetic population of DCO mergers (Section 4.2) with the population detected so far by The LIGO–Virgo–KAGRA Collaboration (LVK). We assume that a given merger is detectable if it has a signal-to-noise ratio (SNR) > 8 . The SNR for each merger can be expressed as $\rho = \rho_0 w > 8$, where ρ_0 is the SNR assuming the binary is optimally oriented and located in the sky, and $0 \leq w \leq 1$ is the projection factor that depends on the binary’s sky position and orientation. We calculate the SNRs using the waveform approximant IMRPhenomD (Khan et al. 2016), assuming LIGO mid-high sensitivity (corresponding to the O3 observing run).

For each binary within the detector’s horizon (i.e. $\rho_0 > 8$), we find that the probability that it will be detected is

$$p_{\text{det}} = P(8/\rho_0), \quad (4)$$

where $P(w)$ is the cumulative probability distribution function of w (Finn & Chernoff 1993). Each merger in our population is weighted by p_{det} to account for detector effects.

3 SINGLE STAR EVOLUTION

In this section, we show the results for new remnant mass formulas only for a single star evolution. We present the relations between the progenitor star mass at its zero-age main sequence (ZAMS) versus the final remnant mass (NS or BH), the total mass of the pre-SN star, and masses of pre-SN carbon oxygen (CO) and helium core (He) for different metallicities. For comparison, besides the two extreme examples of the new remnant mass formulas (Fryer et al. 2022), we provide similar results for the previous `STARTRACK` models: the rapid and delayed SN models (Fryer et al. 2012). In Section 3.2, we present how the different assumptions on the convection growth time-scale, corresponding to the different f_{mix} variants (see equation 2), impact the depth and width of the lower mass gap.

3.1 Remnant mass versus its stellar progenitor

In Figs 1–2, we present the final stellar remnant mass (NS or BH) as a function of its progenitor’s ZAMS mass for four models of SN: the two previous `STARTRACK` models, the so-called delayed and rapid SN models (Fig. 1), and the two models chosen from the spectrum provided by Fryer et al. (2022) (Fig. 2). The two examples of new SN models correspond to the extreme variants for the mixing parameter value: $f_{\text{mix}} = 0.5$ and $f_{\text{mix}} = 4.0$ (see Section 2). Every plot includes three panels which correspond to different stellar metallicities: at the top 1 per cent Z_{\odot} , in the middle 10 per cent Z_{\odot} , and at the bottom 100 per cent Z_{\odot} ($Z_{\odot} = 0.02$). For every model we show two variants for PSN limit (see Section 2). Note that the ZAMS mass range in the figures is extended up to $M_{\text{ZAMS}} = 300 M_{\odot}$, while in our cosmological simulations for the binary systems in the next sections we limit the possible initial mass of the star to $150 M_{\odot}$ for strong PPSN/PSN model and to $200 M_{\odot}$ for the revised PSN model (see Section 2).

3.1.1 Differences between previous and new SN models

The adopted core-collapse SN model plays a role up to some progenitor ZAMS mass threshold above which the fates of all collapsing stars end in the direct collapse to a BH with minimal mass ejection. After exceeding this threshold, which depends on metallicity, the relation between M_{ZAMS} and remnant mass of most massive stars (the right-hand side of the plots) looks the same for all SN models (Fig. 1–2).

The main difference between the previous and the new adopted formulas for remnant masses is that the new ones allow for probing convection growth time-scale on broad spectrum, which also means probing the depth and width of lower mass gap, instead of testing only the two extreme cases: delayed and rapid SN models. The extreme cases of the new formulas, $f_{\text{mix}} = 0.5$ and $f_{\text{mix}} = 4.0$, may be defined as substitutes of the previous delayed and rapid SN engines, respectively. Those models are, however, not exact equivalents, especially the previous rapid and the new $f_{\text{mix}} = 4.0$ differ by few important features. In order to compare the major features of SN models, we will divide them into two categories: the slow convection growth models: previous delayed SN and new $f_{\text{mix}} = 0.5$, and the fast convection growth models: previous rapid SN and new $f_{\text{mix}} = 4.0$.

The major difference between the slow and fast convection growth SN models is the limit on initial mass M_{ZAMS} threshold for a direct collapse into a BH (Figs 1 and 2). For the fast SN models, the threshold for M_{ZAMS} separating progenitors ending evolution in a direct collapse instead of successful SN explosion is noticeably lower than that of the slow SN models. This is because, when the

convection growth time-scale is fast (fast SN models) for progenitors with masses $M_{\text{ZAMS}} \geq 20 M_{\odot}$, convection is strongest when the material is still able to prevent an explosion. In contrast, for the same progenitors but once convection growth in slow time-scale (slow SN models), the peak in the convection occurs when the infalling ram pressure is weaker, allowing an explosion, see Fryer et al. (2012) and Belczynski et al. (2012). The threshold for direct collapse in fast SN models is around $M_{\text{ZAMS}} = 20 M_{\odot}$, while for slow SN models it is around $M_{\text{ZAMS}} = 35 M_{\odot}$ for lower metallicities (1 per cent and 10 per cent Z_{\odot}) and around $M_{\text{ZAMS}} = 80 M_{\odot}$ for 100 per cent Z_{\odot} as for such a high metallicity the stellar winds remove a significant part of the star’s mass.

SN models with a slow convection growth time-scale, so the previous delayed and the new model with $f_{\text{mix}} = 0.5$ give very similar results, with a small difference that the new model produces slightly lower SN remnant masses than the previous one. But between the two models with fast convection growth, previous rapid and the new model with $f_{\text{mix}} = 4.0$, there are two important differences. The low threshold for a direct collapse to a BH (around $M_{\text{ZAMS}} = 20 M_{\odot}$) results in a mass gap between NS and BH masses for both fast SN models. In the previous model, this mass gap was totally empty – zero compact objects produced in the mass range: $\sim 2\text{--}5 M_{\odot}$. Our new SN models, even the most rapid convection growth, with $f_{\text{mix}} = 4.0$, allow for formation of some compact objects within this range. However, the depth and width of the mass gap between NS and BH masses (fraction of compact objects with masses $\sim 2\text{--}5 M_{\odot}$) changes with the adopted value of f_{mix} (see Section 3.2 and Fig. 3). The new SN model with $f_{\text{mix}} = 4.0$, which corresponds to the most rapid convection growth, allows for a slight filling of the mass gap and is less extreme than the previous rapid model (Fryer et al. 2012). It is a result of the implementation of a better understanding of the growth time and narrowing the range of assumptions on mixing.

The second difference between the previous rapid and the new model with $f_{\text{mix}} = 4.0$ is the lack of an additional dip for remnant masses after exceeding the direct collapse threshold ($\sim M_{\text{ZAMS}} = 20 M_{\odot}$) in the new SN model. The origin of the dip in the previous rapid model was motivated by the feature observed in detailed evolutionary set of models (Woosley, Heger & Weaver 2002) for high-metallicity progenitors $Z = Z_{\odot}$ (Belczynski et al. 2012; Fryer et al. 2012). In those models, stars with their initial masses above the $M_{\text{ZAMS}} \geq 20 M_{\odot}$ due to increased mass-loss of the outer layers in stellar winds have their cores structure modified. As a consequence, the density of heavy oxygen and silicon layers may be decreased and the energy required to eject the outer part of the star is reduced. This, in turn leads to resuming successful SN explosions until the initial mass of progenitors reach other limits at which the final star is so massive that gravity leads to direct collapse to a BH. The position of this additional dip as well as its extent depends on the used detailed code and is sensitive to the choice of many input physical parameters such as mixing or mass-loss prescriptions. For example, in the versions of code used for studies by Fryer et al. (2022), the dip is less pronounced than it was for Fryer et al. (2012). Including dip modelling into new formulas would make them more complex and would require considering results for different star metallicity. This study does not include this effect.

3.1.2 Progenitor masses $M_{\text{ZAMS}} < 100 M_{\odot}$

There are few features in the relation between the ZAMS mass of the progenitor and the final remnant mass of the NS/BH which do not originate from the adopted SN model but from other physical processes. For example, LBV and Wolf–Rayet star (WR) winds play a role after exceeding a certain mass thresholds for progenitor initial

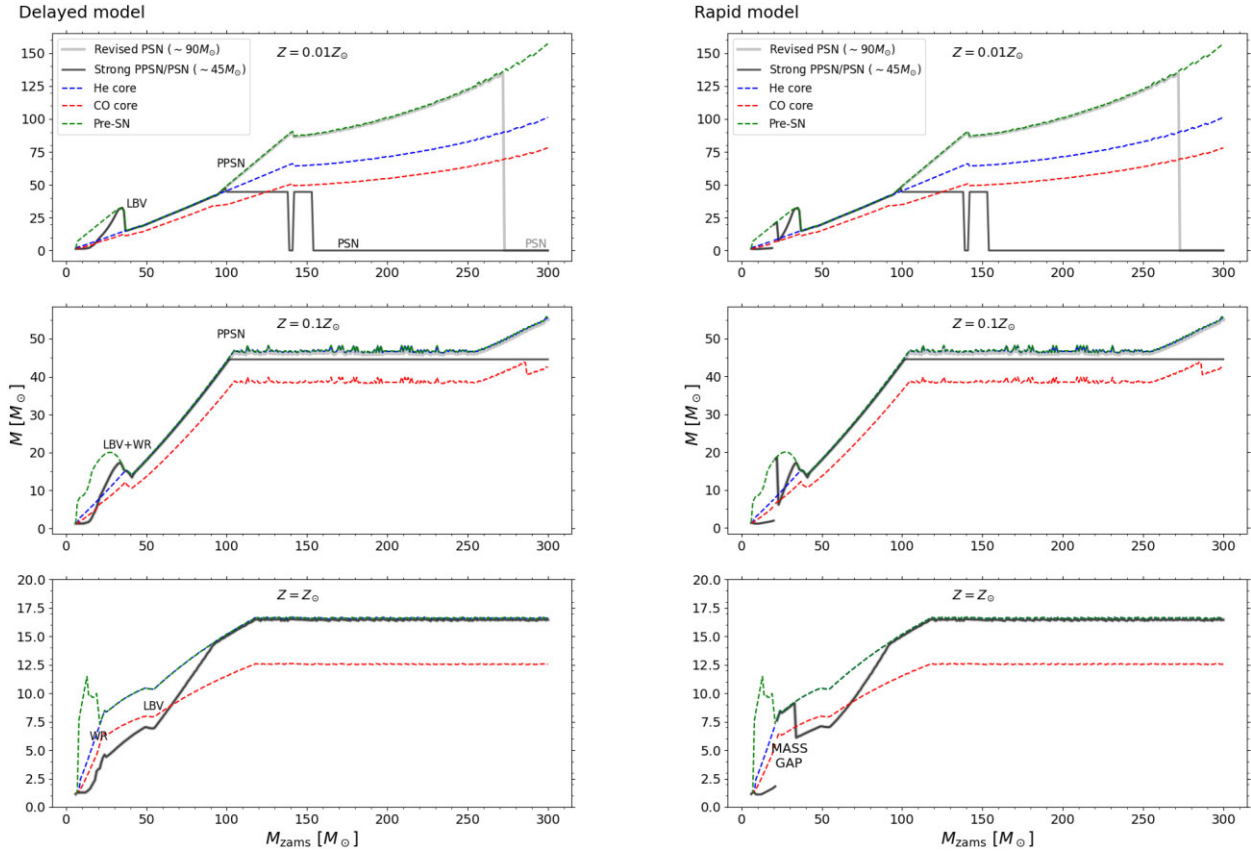


Figure 1. *Left-hand panels:* Remnant mass (NS or BH) and pre-SN star properties as a function of the progenitor ZAMS mass for the delayed SN model (Fryer et al. 2012). Top left panel: 1 per cent Z_{\odot} ; middle left panel: 10 per cent Z_{\odot} ; bottom left panel: 100 per cent Z_{\odot} ($Z_{\odot} = 0.02$). Black line: mass of the remnant (BH or NS) for strong PPSN/PSN model; grey line: mass of the remnant (BH or NS) for revised PSN model; blue dashed line: mass of the helium core of pre-SN star; red dashed line: mass of the carbon–oxygen core of pre-SN star; green dashed line: total mass of the pre-SN star. *Right-hand panels:* Same results for the rapid SN model (Fryer et al. 2012).

mass. Those thresholds, however, strongly depend on metallicity. In Table 1, we provide values of M_{ZAMS} for which massive stars in our simulations become a subject of increased mass-loss in the LBV or WR winds for three metallicities: 1 per cent Z_{\odot} , 10 per cent Z_{\odot} , and 100 per cent Z_{\odot} . We also marked the origin of features: LBV, WR, PPSN, and PSN in Fig. 1.

In all SN models (Fig. 1–2), we observe a clear dip in the final remnant mass at lower metallicities (1 per cent Z_{\odot} and 10 per cent Z_{\odot}) for progenitors with initial masses $M_{\text{ZAMS}} \gtrsim 32 M_{\odot}$ due to entering the effects LBV winds. The luminosity of such massive stars exceed Humphreys–Davidson limit (Humphreys & Davidson 1994) and stars are a subject of significant additional mass-loss in LBV stellar winds of order of $10^{-4} M_{\odot} \text{yr}^{-1}$ (Belczynski et al. 2010a). Massive stars with high metallicities (like 100 per cent Z_{\odot}) are also subject of LBV winds in our simulations. However, for high metallicities stars lose more mass in stellar winds during the the early evolutionary phases (main sequence). It removes significant fraction of star’s outer layers and shifts the threshold for LBV winds to larger progenitor masses $M_{\text{ZAMS}} \gtrsim 50 M_{\odot}$.

Another important threshold for M_{ZAMS} corresponds to WR-star winds (Hamann & Koesterke 1998). The minimum mass of stars to be a subject of WR winds, similar to LBV winds, depends on the metallicity. Metallicity also significantly impacts the duration of the WR phase (in our simulations the stripped helium core phase) and how much mass is lost in WR winds. In the case of WR winds, in contrast to LBV winds, the higher the metallicity, the lower the mass

M_{ZAMS} threshold for WR winds. Rich in metals, massive stars are subject of significant mass-loss in stellar winds during their earlier stage of evolution that may allow them to loose quickly hydrogen envelopes. Poor in metals, massive stars may also lose a significant part of their outer layers in stellar winds. However, it usually happens in the latter part of the evolution and therefore the duration of the WR phase (and its mass-loss) is also shorter. As an example, the same progenitor star with $M_{\text{ZAMS}} = 40 M_{\odot}$ at solar metallicity $Z = Z_{\odot}$ will lose $\sim 4 M_{\odot}$ during its WR phase, at $Z = 0.1Z_{\odot}$ around $\sim 1 M_{\odot}$, and at $Z = 0.01Z_{\odot}$ only $\sim 0.1 M_{\odot}$.

For stars with 100 per cent Z_{\odot} , the M_{ZAMS} threshold for WR winds starts for progenitors with $M_{\text{ZAMS}} \sim 24 M_{\odot}$ and is clearly visible in Figs 1 and 2. In the case of lower metallicities, 1 per cent and 10 per cent Z_{\odot} , the threshold at which WR winds activate is shifted to $M_{\text{ZAMS}} \sim 37 M_{\odot}$. However, note that for 1 per cent Z_{\odot} due to a relatively short WR phase the feature is negligible.

3.1.3 Progenitor masses $M_{\text{ZAMS}} \gtrsim 100 M_{\odot}$

Most massive stars $M_{\text{ZAMS}} \gtrsim 100 M_{\odot}$ may experience significant mass-loss in PPSN or complete disruption in the violent PSN explosion initiated by the creation of the electron–positron pairs which reduce the radial pressure in their cores (Woosley, Blinnikov & Heger 2007; Woosley 2017). However due to several uncertainties associated with physical processes in massive stellar cores, such as

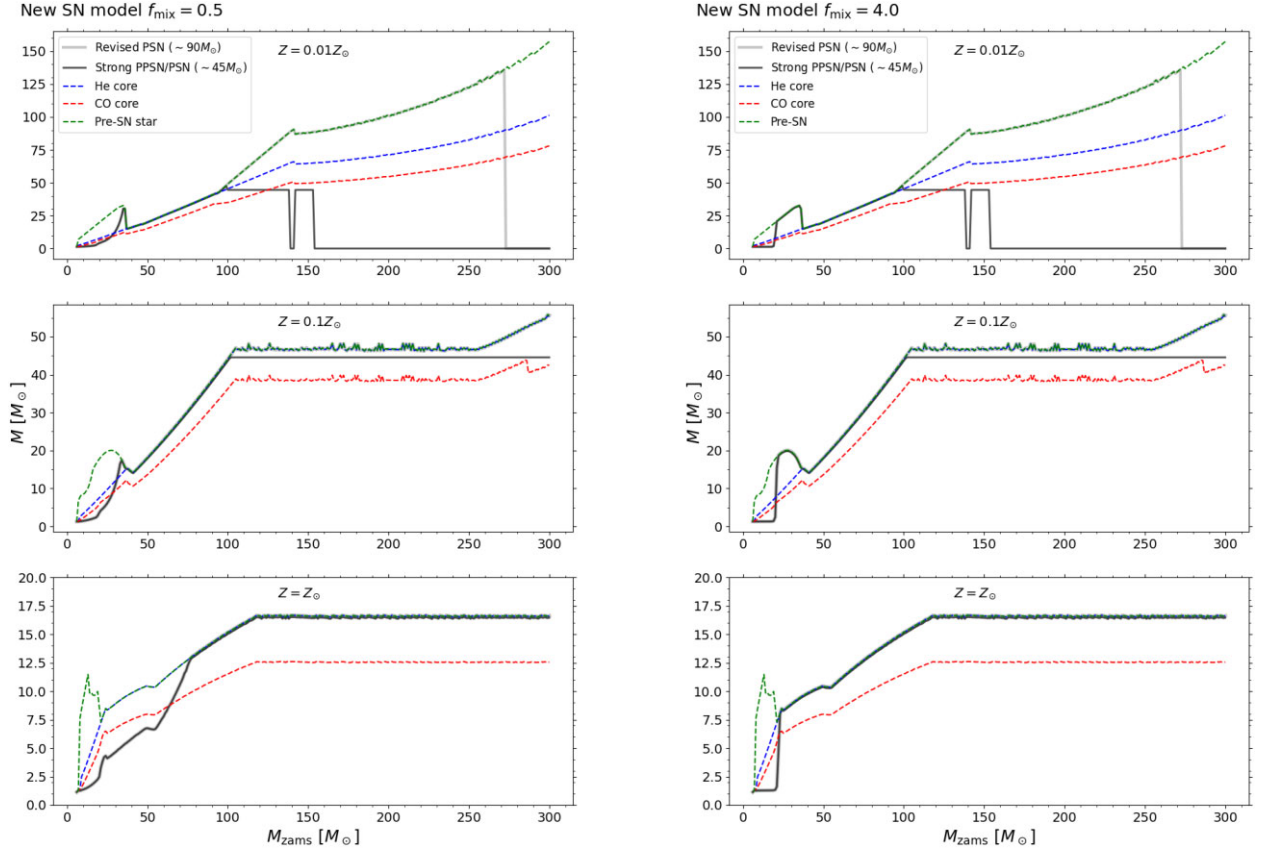


Figure 2. *Left-hand panels:* Remnant mass (NS or BH) and pre-SN star properties as a function of its progenitor ZAMS mass for the new SN model with $f_{\text{mix}} = 0.5$ (Fryer et al. 2022). Top left panel: 1 per cent Z_{\odot} ; middle left panel: 10 per cent Z_{\odot} ; bottom left panel: 100 per cent Z_{\odot} ($Z_{\odot} = 0.02$). Black line: mass of the remnant (BH or NS) for strong PPSN/PSN model; grey line: mass of the remnant (BH or NS) for revised PSN model; blue dashed line: mass of the helium core of pre-SN star; red dashed line: mass of the carbon–oxygen core of pre-SN star; green dashed line: total mass of the pre-SN star. *Right-hand panels:* Same results for the new SN model with $f_{\text{mix}} = 4.0$ (Fryer et al. 2022). Note that the new SN models with low values of $f_{\text{mix}} \approx 0.5$ (in equation 2) result in a shallow or no mass gap (similarly to old delayed SN model), while the high values such as $f_{\text{mix}} \approx 4.0$ result in deep mass gap (similarly to previous rapid SN model).

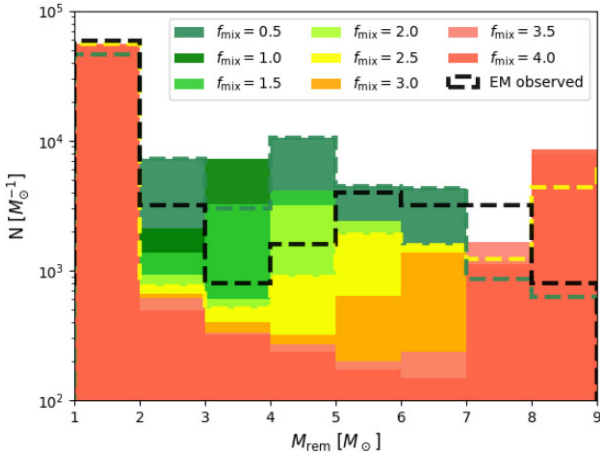


Figure 3. Histogram (binsize $1 M_{\odot}$) of the remnant masses of the probe of 10^5 single stars for the adopted IMF for eight new SN model prescriptions with f_{mix} in the range 0.5–4.0 and $Z = 1.0 Z_{\odot}$. Results for $M_{\text{crit}} = 5.75 M_{\odot}$ adopted for this study (see equation 2).

the rates for $^{12}\text{C}(\alpha, \gamma)^{16}\text{O}$ reaction, and a lack of strong observational constraints (The LIGO Scientific Collaboration 2021b), currently it is not well understood in what mass range star is a subject of

Table 1. Mass threshold for progenitors ZAMS mass to enter the regime of additional mass-loss in LBV/WR winds for three different metallicities.

	$M_{\text{ZAMS}, Z_{\odot}}$	$M_{\text{ZAMS}, 0.1 Z_{\odot}}$	$M_{\text{ZAMS}, 0.01 Z_{\odot}}$
LBV	$50 M_{\odot}$	$33 M_{\odot}$	$32 M_{\odot}$
WR	$24 M_{\odot}$	$38 M_{\odot}$	$37 M_{\odot}$

potential PPSN or PSN (Farmer et al. 2020; Costa et al. 2021; Woosley & Heger 2021). In this study, we test two different variants for the PSN limit. In our strong model (Belczynski et al. 2016), the maximum mass of the BH is limited to $\sim 45 M_{\odot}$. Stars with final helium cores $M_{\text{He}} > 45 M_{\odot}$ are subject of PPSN, while stars with $M_{\text{He}} > 65 M_{\odot}$ are completely disrupted in a PSN explosion. The second variant is a revised PSN model by Belczynski (2020). In the revised PSN model, we do not include PPSN mechanism while the limit for total star disruption in a PSN explosion is shifted to stars with final helium core masses $M_{\text{He}} > 90 M_{\odot}$. The total disruption of the star in a PSN explosion for both PSN models happens only for the lowest tested metallicity and the effect is visible only on the top panels (for 1 per cent Z_{\odot}) of Figs 1 and 2. In the strong PPSN/PSN model, stars with progenitor masses $M_{\text{ZAMS}} \gtrsim 100 M_{\odot}$ experience PPSN which decreases the final mass of BH to $45 M_{\odot}$. The non-linear, complex relation of stellar winds with the stellar mass and luminosity influences the final mass of the He core and makes it a

non-monotonic function of M_{ZAMS} . As an effect, the mass of He cores first exceeds $65 M_{\odot}$ (limit for complete disruption) for the progenitors with masses of $M_{\text{ZAMS}} = 138 M_{\odot}$. Then, for the progenitor stars with $138 < M_{\text{ZAMS}} \leq 153 M_{\odot}$, the final He core mass decreases a bit below the PSN limit and the star experience a PPSN instead. The limit for PSN is exceeded again for progenitors with initial masses $M_{\text{ZAMS}} > 153 M_{\odot}$. In the revised PSN variant, the limit for PSN is exceeded for most massive progenitors with $M_{\text{ZAMS}} > 250 M_{\odot}$. As in our binary evolution cosmological simulations (Section 4), we limit the initial stellar mass to $M_{\text{ZAMS}} = 200 M_{\odot}$. Therefore, a PSN in the revised treatment does not play a role in those results. Stars with 10 per cent Z_{\odot} do not experience PSN as the stellar winds reduce the He core mass below the PSN limit. However, in the strong PPSN/PSN model the most massive stars may be a subject of PPSN. Due to the overlap of the stellar winds with mass reduction in PPSN the remnant masses of 10 per cent Z_{\odot} stars is constantly $\sim 45 M_{\odot}$ for all the progenitors with initial masses $M_{\text{ZAMS}} > 105 M_{\odot}$. On the other hand, the results for revised PSN model do not differ much, as mass-loss with stellar winds allows for the formation of BH only to $\sim 47 M_{\odot}$ in the wide range of $105 M_{\odot} < M_{\text{ZAMS}} < 250 M_{\odot}$. For 100 per cent Z_{\odot} stars do not experience PPSN or PSN in both PSN variants as the strong stellar winds allow for the formation of BH with maximum mass of $\sim 20 M_{\odot}$.

3.2 Lower mass gap

Fig. 3 demonstrates how the lower mass gap changes with the assumed value of f_{mix} parameter corresponding to different convection time-scales growth (from rapid to delayed). These results are for high metallicity 100 per cent Z_{\odot} . In this paper, we assume f_{mix} takes a value from the range: 0.5 to 4.0 as suggested by Fryer et al. (2022) (see Section 2). In the figure we show results for eight f_{mix} values chosen from this range. The presented histogram, with a bin size of $1 M_{\odot}$, is made from the study of 10^5 single stars (for each SN model) with their initial masses $5 M_{\odot} < M_{\text{ZAMS}} < 150 M_{\odot}$ generated from three broken IMF (Kroupa, Tout & Gilmore 1993; Kroupa 2002) with the power-law exponent for massive stars ($M_{\text{ZAMS}} > 1 M_{\odot}$) equal $\alpha_3 = -2.3$. The distribution is shown in the range limited to remnant masses $1 < M_{\text{rem}} < 9 M_{\odot}$ in order demonstrate clearly the lower mass gap region.

In the same Fig. 3, we plot (black dashed line) the distribution NSs and low-mass BHs ($< 9 M_{\odot}$) observed in electromagnetic spectrum using data base collected by LVK LIGO-Virgo Mass Plot with the following provided references on system parameters: Deller et al. (2012), Heida et al. (2017), Alsing, Silva & Berti (2018), Thompson et al. (2019), Giesers et al. (2019), Ferdman et al. (2020), Fonseca et al. (2021), Jayasinghe et al. (2021), Haniewicz et al. (2021).

For all tested models, we observe a peak of NSs with masses in the range $M_{\text{rem}} \in 1-2 M_{\odot}$. The distribution for each f_{mix} varies significantly. In the model with the lowest $f_{\text{mix}} = 0.5$ (the most delayed convection growth), we get a high fraction ($\sim 10^4 M_{\odot}^{-1}$) of compact object remnants, massive NSs, and low-mass BHs, within the range of $2 M_{\odot} \leq M_{\text{rem}} < 7 M_{\odot}$. The corresponding number of more massive compact objects decreases by around an order of magnitude. The distribution of remnant masses for the most rapid model, $f_{\text{mix}} = 4.0$, behaves in the opposite way. After the NSs peak, there is a deep drop by approximately two orders of magnitude for compact objects in the mass bin $2 M_{\odot} \leq M_{\text{rem}} < 7 M_{\odot}$. The number of BHs increases by one to two orders of magnitude for $M_{\text{rem}} \in 7-9 M_{\odot}$ compared to mass range $M_{\text{rem}} \in 6-7 M_{\odot}$. The increase in the fraction of objects within the two most massive plotted bins, as already mentioned in Section 3.1, is due to peak in the convection of the rapid convection

time-scale for $f_{\text{mix}} = 4.0$ occurring earlier when the ram pressure of the infalling star is higher. The pre-SN star goes through direct collapse to a BH, with only mass-loss in neutrino flux, leaving more massive remnants than in case of successful SN explosion (e.g. $f_{\text{mix}} = 0.5$). The results for other f_{mix} alter the width and depth of the gap region. The models with f_{mix} values in the middle of possible range, e.g. $f_{\text{max}} = 2.5$, are promising as they reconstruct the reduced number of observed compact objects within the range $2-5 M_{\odot}$ but also do not completely prevent their formation. In this respect, such models are most compatible with small data base of NSs and low-mass BHs observed in electromagnetic spectrum (black dashed line). Note that here we compare results from simulations with the observed population of compact objects without taking into account many possible biases.

For comparison, apart from the results for $M_{\text{crit}} = 5.75 M_{\odot}$ adopted for this study (see equation 2), in Fig. A1 we provide same results but for different critical mass of carbon oxygen core for a BH formation, $M_{\text{crit}} = 4.75 M_{\odot}$. Different choice of M_{crit} parameter value may affect the range of produced mass gap.

4 BINARY EVOLUTION

In this section, we present the impact of the new remnant mass prescriptions for cosmological population of DCO mergers formed via the isolated binary evolution. Besides testing new formulas for remnant masses, we also show results for two different RLOF stability criteria and two PSN treatment, see method description in Section 2.1 for more details. In Sections 4.1 and 4.2, we present mass and mass ratio distributions of DCO mergers, respectively. In Section 4.3, we provide estimates of local merger rate densities for different types of DCO mergers.

4.1 Mass distribution of DCO mergers

In Figs 4 and 5, we present combined intrinsic distributions of remnant masses for all types of DCO which merge at redshift $z < 1.0$. The plots in Fig. 4 are the results of the standard CE STARTRACK development criteria, in which a vast majority of BH–BH binaries form via CE evolution. The plots in Fig. 5 show results for the revised CE development criteria, in which a majority of BH–BH binaries form via stable RLOF channel without any CE phase. For both figures, we provide plots with the entire spectrum of masses and with a mass range limited to low masses, $m < 15 M_{\odot}$, for a better visibility of the lower mass gap region. We show distributions of the more massive merger component (the primary, m_1), less massive merger component (secondary, m_2), and a sum of the two masses ($m_1 + m_2$). In every plot we provide results for three cases of new SN models: two extreme cases for convection growth time-scales, the most delayed with $f_{\text{mix}} = 0.5$, the most rapid with $f_{\text{mix}} = 4.0$, and the intermediate case for $f_{\text{mix}} = 1.0$. We also plot results for the two adopted limits for PSN.

In all distributions (for all remnant mass models and both CE development criteria), there is a large peak in the primary mass m_1 distribution in the mass range corresponding to typical masses of NSs. In the primary mass distribution for the model with $f_{\text{mix}} = 0.5$, there is a significant fraction of more massive NSs ($m_1 \in 1.5-2.0 M_{\odot}$), which we do not observe for two other tested SN models (corresponding to more rapid convection time-scale growth). For the model with $f_{\text{mix}} = 0.5$, the fraction of DCO mergers with their total masses in the range $m_1 + m_2 \in 3-4 M_{\odot}$ (massive NS–NS mergers) is about one order of magnitude higher than in other models. This may be an important feature for studying the origin of systems such as GW190425 (Abbott

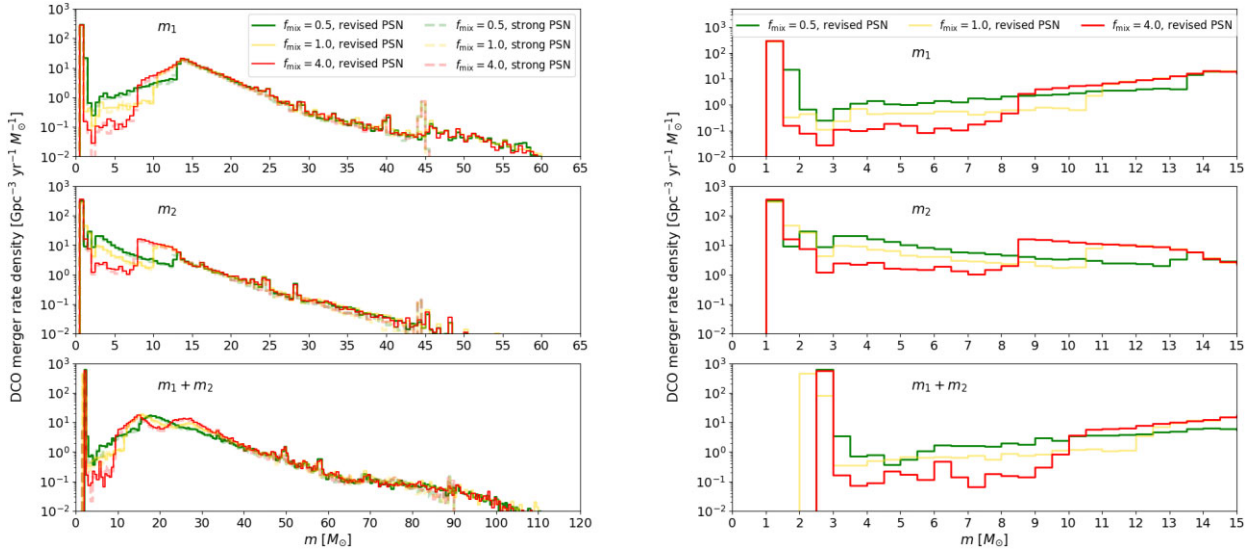


Figure 4. Intrinsic mass distribution of all types (NS–NS, BH–NS, BH–BH) of mergers at low redshifts ($z < 1.0$) for standard CE development criteria (BH–BH mergers forms via CE evolution). Results for three new remnant mass formulas with $f_{\text{mix}} = 0.5, 1.0, \text{ and } 4.0$ ($m_1 \geq m_2$). On the left the whole spectrum of masses for two PSN models: revised PSN (solid lines) and strong PPSN/PSN (dashed, semitransparent lines). On the right mass range is limited to $15 M_{\odot}$ (only revised PSN model). Note that our models allow for various depths of the lower mass gap, from deep (red line, the most rapid SN) to shallow (green line, the most delayed SN) gap depending on the development time-scale of neutrino supported convection SN engine. Full description is given in Section 4.

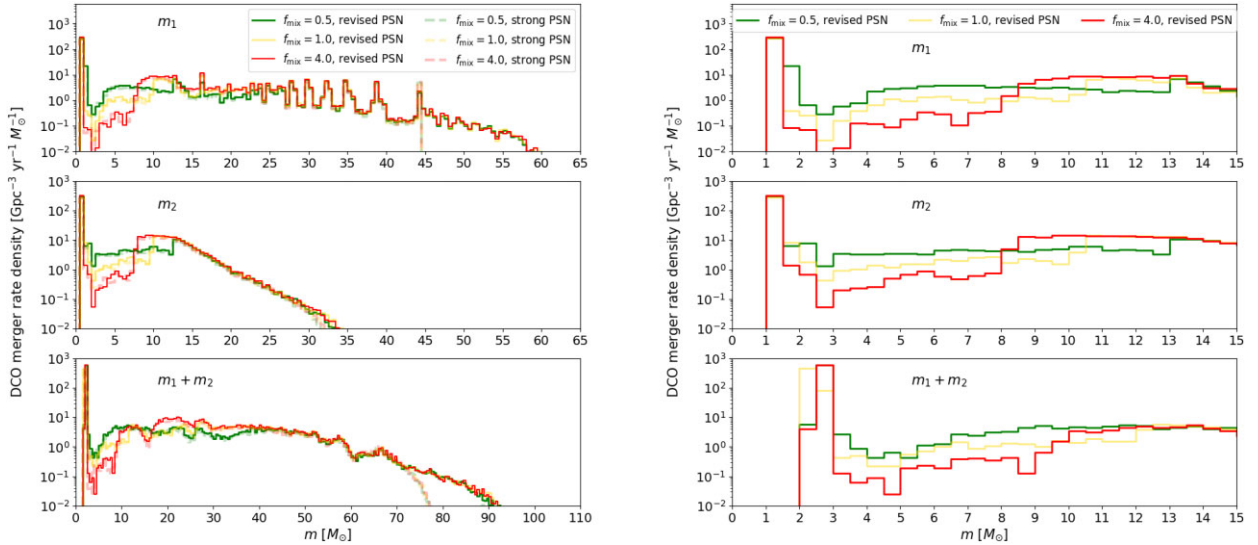


Figure 5. Intrinsic mass distribution of all types (NS–NS, BH–NS, BH–BH) of mergers at low redshifts ($z < 1.0$) for the revised criteria for mass transfer stability (BH–BH mergers forms via stable RLOF). Results for three new remnant mass formulas with $f_{\text{mix}} = 0.5, 1.0, \text{ and } 4.0$ ($m_1 \geq m_2$). On the left the whole spectrum of masses for two PSN models: revised PSN (solid lines) and strong PPSN/PSN (dashed, semitransparent lines). On the right mass range is limited to $15 M_{\odot}$ (only revised PSN model). Note that our models allow for various depths of the lower mass gap, from deep (red line, the most rapid SN) to shallow (green line, the most delayed SN) gap depending on the development time-scale of neutrino supported convection SN engine. Full description is given in Section 4.

et al. 2020) classified as a massive NS–NS merger with its component masses $m_1 \in 1.60\text{--}1.87 M_{\odot}$ and $m_2 \in 1.46\text{--}1.69 M_{\odot}$ for low-spin prior (or $m_1 \in 1.61\text{--}2.52$ and $m_2 \in 1.12\text{--}1.68 M_{\odot}$ with high-spin prior assumption).

The fraction of DCO mergers with components within the lower mass gap and slightly beyond it is systematically about one order of magnitude lower for the most rapid tested model with $f_{\text{mix}} = 4.0$ than for most delayed one $f_{\text{mix}} = 0.5$. The results corresponding to the intermediate case of convection growth time-scale ($f_{\text{mix}} = 1.0$) are usually somewhere between the two extreme cases. After exceeding

the masses of $m_1, m_2 \geq 8 M_{\odot}$ there is a reversal of trends in the behaviour of extreme SN models distributions. The fraction of DCO with $m_1, m_2 \in 9\text{--}15 M_{\odot}$ for $f_{\text{mix}} = 4.0$ is a few times larger than in $f_{\text{mix}} = 0.5$. In the case of $f_{\text{mix}} = 1.0$, the fraction of DCO mergers remains low for a wide range of masses $m_1, m_2 \in 2\text{--}10 M_{\odot}$ and increases by about an order of magnitude for $m_1, m_2 \gtrsim 11 M_{\odot}$. For the reasons already mentioned in Section 3, more rapid SN models (e.g. $f_{\text{mix}} = 4.0$) with successful explosions are unlikely to produce remnants with masses in the lower mass gap. Instead, stars either explode rapidly to form an NS below the gap or collapse directly to a

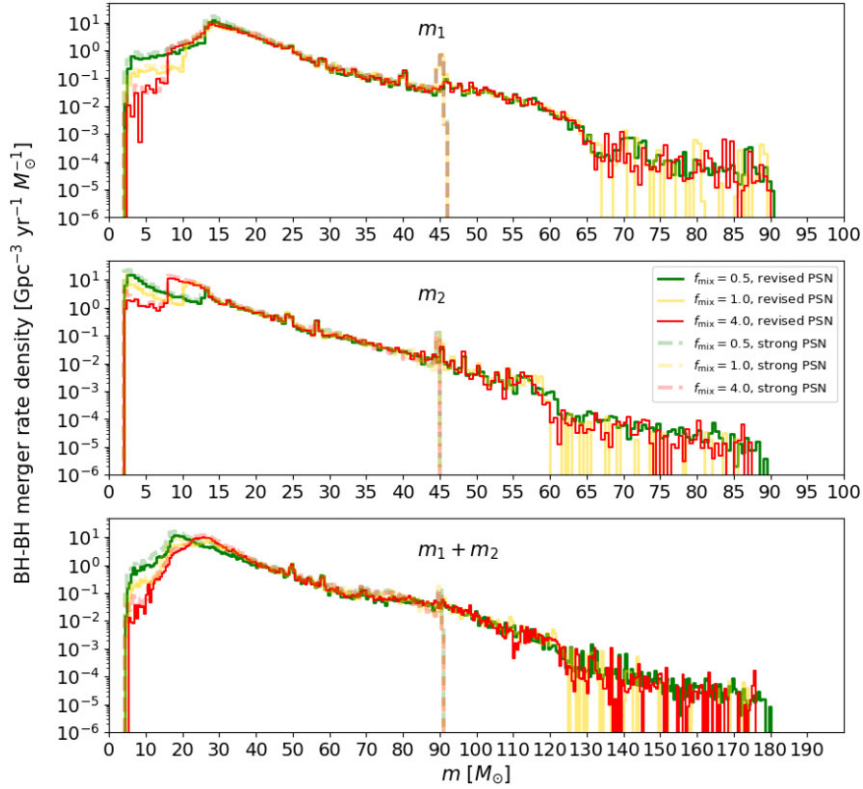


Figure 6. Intrinsic mass distribution of BH–BH mergers at low redshifts ($z < 1.0$) for standard CE development criteria (BH–BH mergers forms via CE evolution) divided into bins with $0.5 M_{\odot}$ size. Results for three new remnant mass formulas with $f_{\text{mix}} = 0.5, 1.0,$ and 4.0 ($m_1 \geq m_2$) for two PSN models: revised PSN (solid lines) and strong PPSN/PSN (dashed, semitransparent lines). Note that our models allow for various depths of the lower mass gap, from deep (red line, the most rapid SN) to shallow (green line, the most delayed SN) gap depending on the development time-scale of neutrino supported convection SN engine. Full description is given in Section 4.

BH with a mass above the gap. The influence of the adopted SN model is visible in the region of $m_1, m_2 \lesssim 17 M_{\odot}$ ($m_1 + m_2 \lesssim 35 M_{\odot}$). After that threshold, the massive stars in all tested models end their lives in a direct collapse to a BH, without a successful SN explosion. The different adopted approaches for the PSN limit does not affect much of the general picture of DCO mass distribution. The main difference is a tail of BHs with masses larger than $45 M_{\odot}$ in the model with revised PSN limit, while for a strong PPSN/PSN model there is a narrow peak around $45 M_{\odot}$ due to mass reduction by PPSN. The difference in the distribution of DCO mergers between two CE development criteria (Figs 4 and 5) is especially visible for massive systems ($m_1, m_2 \gtrsim 20 M_{\odot}$). BH–BH mergers formed in stable RLOF scenario (Fig. 5) are characterized by a significantly larger average total mass of DCO mergers, which was already noticed and explained by other recent studies, for example van Son et al. (2021) and Belczynski et al. (2022a). Massive BH–BH mergers are more likely to form via stable RLOF evolution as their progenitors avoid stellar merger while entering CE with Hertzsprung gap star donor (Olejak et al. 2021). The different approaches to the mass and orbital angular momentum loss mechanisms during stable and unstable RLOF also strongly affect mass ratio of BH–BH mergers (See Section 4.2). Additionally, in Figs 6 and 7, we show mass distribution only for BH–BH mergers for the two RLOF stability criteria. BH–BH mergers strongly dominate the detected GW signals thus far and therefore they are sometimes analysed separately from other types of DCO mergers.

4.2 Mass ratio distribution of BH–BH and BH–NS mergers

In Figs 8 and 9, we present the mass ratio distributions of BH–BH and BH–NS mergers (combined) obtained for three examples of new SN models: $f_{\text{mix}} = 0.5, f_{\text{mix}} = 1.0,$ and $f_{\text{mix}} = 4.0$ similarly as in Section 4.1. The mass ratio q is defined here as the mass of the secondary (less massive) to mass of the primary (more massive) component of merger ($q = \frac{m_2}{m_1}$). In Fig. 8, we plot the results for the standard CE development criteria, and in Fig. 9, the results for the revised criteria under which BH–BH mergers form mostly through stable RLOF. For both the standard and revised criteria, we show two separate figures corresponding to the two different PSN variants (see Section 2.1). On the left we show the results for the revised PSN model and, on the right the results for the strong PPSN/PSN model. On the top panel of the figures, we present the intrinsic (not redshifted nor detection-weighted) mass ratio distribution of BH–BH and BH–NS mergers population (combined) at redshift $z < 1.0$. On the bottom panel we also plot combined mass ratio distribution of BH–BH and BH–NS but weighted by detection biases according to a method described in Section 2.3 (only signals with estimated SNR > 8). The detection-weighted results are plotted together with a distribution built of publicly announced during O1 + O2 + O3 runs parameters of BH–BH and BH–NS mergers with a black dashed line (Abbott et al. 2016, b, c; The LIGO Scientific Collaboration 2021b).

In Table 2, for all the tested physical variants (see Section 2), we provide total fractions of unequal mass mergers with their mass ratios: $q < 0.3$ and $q < 0.5$. In the first column is the row number, in the

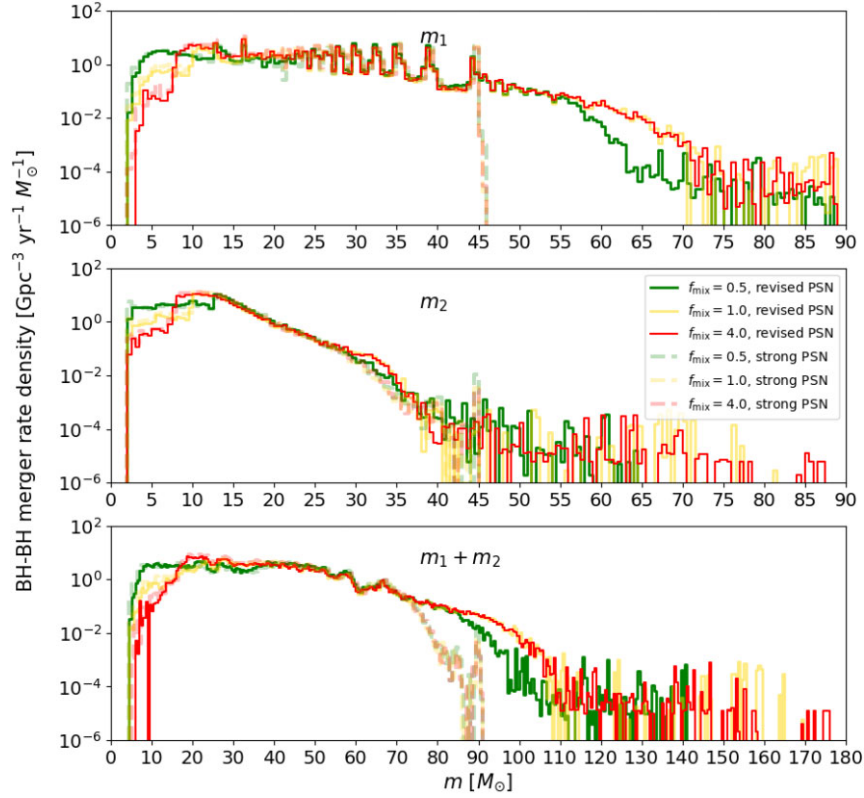


Figure 7. Intrinsic mass distribution of BH–BH mergers at low redshifts ($z < 1.0$) for revised mass transfer stability criteria (BH–BH mergers forms via stable RLOF) divided into bins with $0.5 M_{\odot}$ size. Results for three new remnant mass formulas with $f_{\text{mix}} = 0.5, 1.0,$ and 4.0 ($m_1 \geq m_2$) for two PSN models: revised PSN (solid lines) and strong PPSN/PSN (dashed, semitransparent lines). Note that our models allow for various depths of the lower mass gap, from deep (red line, the most rapid SN) to shallow (green line, the most delayed SN) gap depending on the development time-scale of neutrino supported convection SN engine. On the right mass range is limited to $15 M_{\odot}$. Full description is given in Section 4.

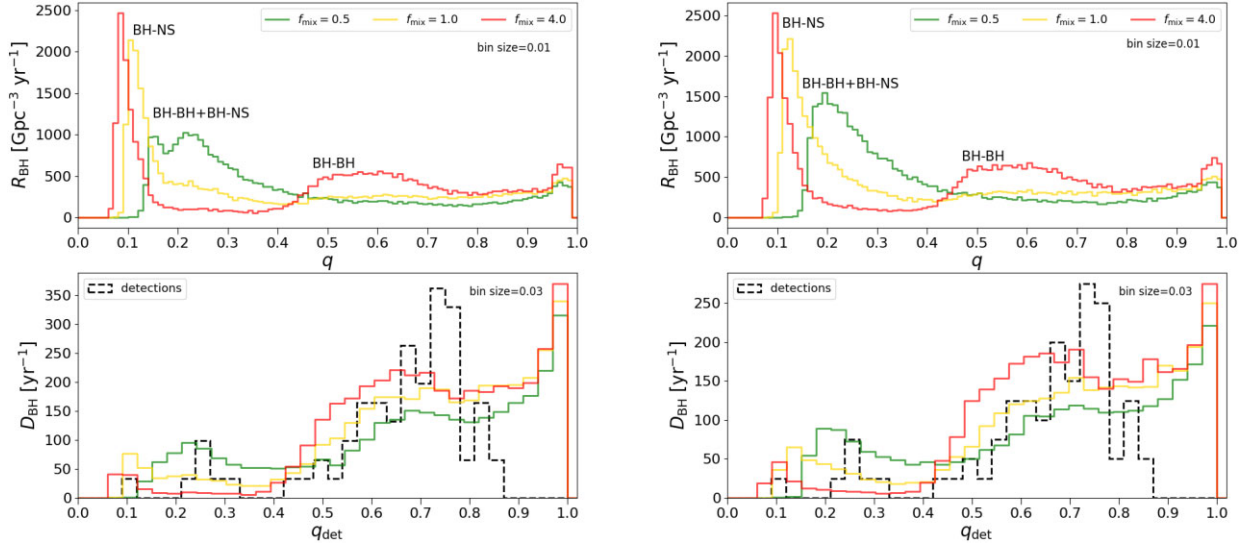


Figure 8. Mass ratio distribution for BH–BH and BH–NS mergers at low redshifts ($z < 1.0$) for the standard CE development criteria (BH–BH mergers formed via CE). On the upper panel intrinsic results (neither redshifted nor detection-weighted). On the bottom panel detection-weighted results together with the parameters of detected population of BH–BH and BH–NS mergers (O1+O2 + O3 runs). *On the left:* distribution for revised PSN model; *on the right:* distribution for strong PPSN/PSN.

second column we specify the adopted criteria for CE development: standard or revised. In the third column we define the used PSN model: strong (which limits BH mass to $\sim 45 M_{\odot}$) or revised (which

allows for more massive BHs formation). In the fourth column (SN model) we specify the adopted mixing parameter value for the new remnant mass formula: $f_{\text{mix}} = 0.5, 1.0,$ or 4.0 . In last four columns we

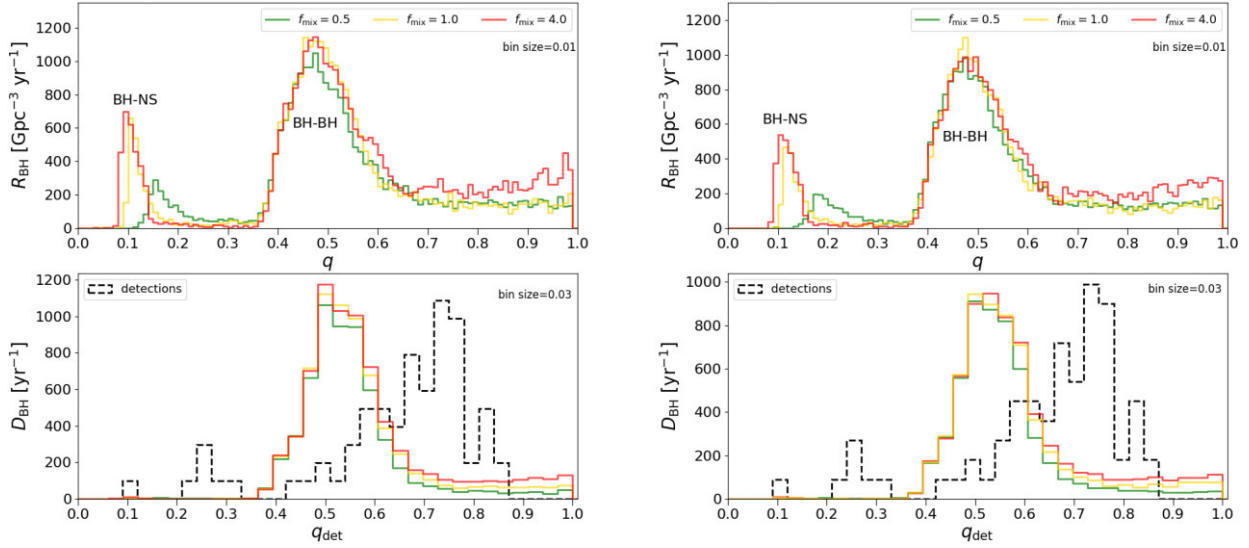


Figure 9. Mass ratio distribution for BH–BH and BH–NS mergers at low redshifts ($z < 1.0$) for the revised mass transfer stability criteria (BH–BH mergers formed via stable RLOF). On the upper panel intrinsic results (neither redshifted nor detection-weighted). On the bottom panel detection-weighted results together with parameters of detected population of BH–BHs and BH–NS mergers (O1+O2 + O3 runs). *On the left:* distribution for revised PSN; *on the right:* distribution for strong PPSN/PSN.

Table 2. Fractions of unequal mass BH–BH and BH–NS mergers (combined) in different tested models. The columns: CE criteria stands for adopted standard or revised CE development treatment; PSN limit stands for adopted strong ($\sim 45 M_{\odot}$) or revised ($\sim 90 M_{\odot}$) PSN limit; SN model stands for different adopted f_{mix} parameters (convection growth time); $q_{\text{intr}} < X$ is the intrinsic fraction of mergers with mass ratio less than X , while $q_{\text{det}} < Y$ is the fraction of mergers weighted by detection with mass ratio less than Y .

No.	CE criteria	PSN limit	SN model	$q_{\text{intr}} < 0.5$	$q_{\text{intr}} < 0.3$	$q_{\text{det}} < 0.5$	$q_{\text{det}} < 0.3$
1.	Standard	90 M_{\odot}	$f_{\text{mix}} = 0.5$	0.68	0.44	0.24	0.13
2.	Standard	90 M_{\odot}	$f_{\text{mix}} = 1.0$	0.61	0.47	0.15	0.08
3.	Standard	90 M_{\odot}	$f_{\text{mix}} = 4.0$	0.43	0.32	0.10	0.04
4.	Standard	45 M_{\odot}	$f_{\text{mix}} = 0.5$	0.68	0.43	0.26	0.13
5.	Standard	45 M_{\odot}	$f_{\text{mix}} = 1.0$	0.62	0.48	0.17	0.10
6.	Standard	45 M_{\odot}	$f_{\text{mix}} = 4.0$	0.43	0.32	0.11	0.04
7.	Revised	90 M_{\odot}	$f_{\text{mix}} = 0.5$	0.45	0.08	0.28	0.003
8.	Revised	90 M_{\odot}	$f_{\text{mix}} = 1.0$	0.66	0.10	0.26	0.003
9.	Revised	90 M_{\odot}	$f_{\text{mix}} = 4.0$	0.57	0.11	0.24	0.003
10.	Revised	45 M_{\odot}	$f_{\text{mix}} = 0.5$	0.44	0.07	0.26	0.003
11.	Revised	45 M_{\odot}	$f_{\text{mix}} = 1.0$	0.63	0.10	0.23	0.003
12.	Revised	45 M_{\odot}	$f_{\text{mix}} = 4.0$	0.54	0.11	0.21	0.003

give total fractions of unequal mass ratio mergers, first for intrinsic distributions q_{intr} (column fifth and sixth) and next for the detection-weighted results q_{det} (column seventh and eighth).

4.2.1 CE evolution

The intrinsic mass ratio distribution of BH–BH and BH–NS mergers (combined) in the case of CE evolution channel (top panel of Fig. 8) is significantly affected by the adopted model for the SN explosion. In the distribution for our model with $f_{\text{mix}} = 4.0$, which produces deep and wide lower mass gap, there are three peaks: a very high, thin peak at $q \approx 0.15$ composed of BH–NS mergers, a wide peak at $q \in 0.5–0.7$, and a slight peak at $q \approx 1.0$ both primarily composed of BH–BH mergers. The distribution for the model with $f_{\text{mix}} = 1.0$ is similar to that for the model with $f_{\text{mix}} = 4.0$ with a high peak for unequal mass BH–NS mergers.

In the mass ratio distribution for a model with $f_{\text{mix}} = 0.5$, there is a broad peak for unequal mass systems made of both BH–NS and BH–

BH mergers with mass ratios $q \in 0.1–0.3$. This SN model produces a higher fraction of massive NSs and low-mass BHs within the lower mass gap via a successful SN explosion compared to $f_{\text{mix}} = 4.0$ and $f_{\text{mix}} = 1.0$. Progenitors of BH–NS systems where both components are within the lower mass gap are expected to get high natal kicks at the time of an NS and BH formation. That makes such systems very easy to be disrupted or have orbits far too wide to merge in Hubble time. Therefore, despite producing massive NSs and low-mass BHs, we still get mainly unequal mass BH–NS, even for a model with $f_{\text{mix}} = 0.5$. The models with $f_{\text{mix}} = 1.0$ and $f_{\text{mix}} = 4.0$ produce more BH–NS mergers due to a bigger fraction of massive BHs formed via direct collapse without getting significant kicks. In such systems a BH is usually few times more massive than an NS, which explains the origin of the high peak of very unequal mass mergers for the models with $f_{\text{mix}} = 1.0$ or $f_{\text{mix}} = 4.0$. Assumption on PSN limit has negligible effect on mass ratio distribution.

Significant differences in intrinsic mass ratio distributions between SN models diminish while weighting the result by detection biases.

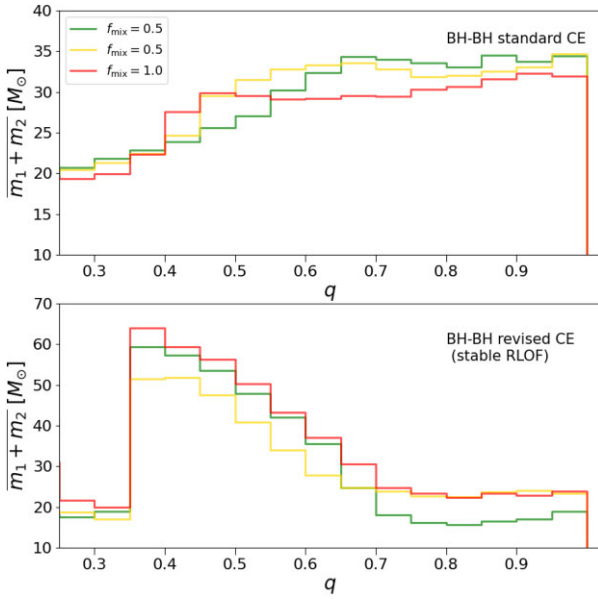


Figure 10. The relation between mass ratio q and the average total mass $m_1 + m_2$ of BH–BH mergers at $z < 2.0$. On the top panel results for standard CE development criteria (formation mainly via CE), on the bottom panel results for revised CE development criteria (formation mainly via stable RLOF). Green line: model with $f_{\text{mix}} = 0.5$, yellow line: model with $f_{\text{mix}} = 1.0$, and red line: model with $f_{\text{mix}} = 4.0$. Results for revised PSN model.

From the total BH–BH and BH–NS mergers population we choose only mergers with $\text{SNR} > 8$. The observational distribution of detectable sources is governed by their SNR, which depends on the masses of compact objects in addition to other extrinsic parameters (like redshift, sky position, etc.). The measured distribution of mass ratios from a population of detected binaries is significantly different from the intrinsic astrophysical distribution due to this selection bias. For stellar-mass compact objects, the SNR increases with the total mass of the binary for a fixed mass ratio. Also, for a given total mass, systems with equal mass components produce a higher SNR in the detectors and are easier to observe compared to binaries with asymmetric masses. Consequently, the relative fraction of observed sources becomes heavily biased in favour of higher mass ratios. The detection-weighted mass ratio distribution for CE evolution channel (bottom panel of Fig. 8) looks very different than the intrinsic one (top panel). The high peak of BH–NS mergers (and unequal mass BH–BH mergers for $f_{\text{mix}} = 0.5$) has been reduced with respect to more equal mergers. Detection-weighted distribution has a clear, high peak for equal mass systems with $q_{\text{det}} \approx 0.9–1.0$, while for intrinsic distribution this peak was barely visible. Fig. 10 for BH–BH mergers and Fig. 11 for BH–NS mergers help to understand the origin of this peak and the shape of the detection-weighted distributions. On the top panel of Fig. 10, we present the relation between mass ratio q and the average total mass $m_1 + m_2$ of BH–BH mergers at $z < 2.0$ for the standard CE development criteria. The plotted results indicate that in case of CE formation channel the more equal the BH–BH merger, the more massive it is on average. Average mass of unequal mass ratio BH–BH mergers $q = 0.3$ is around $20 M_{\odot}$. Equal mass BH–BH mergers ($q \in 0.9–1.0$) are significantly more massive, with the average mass around $35 M_{\odot}$. Therefore, equal mass mergers are more easily detected. The average mass of BH–NS mergers (up to $17 M_{\odot}$) for a given mass ratio bin is systematically lower than the average mass of BH–BH mergers. Despite that bias, the total fraction of the detectable unequal mass mergers with mass ratio $q_{\text{det}} < 0.5$

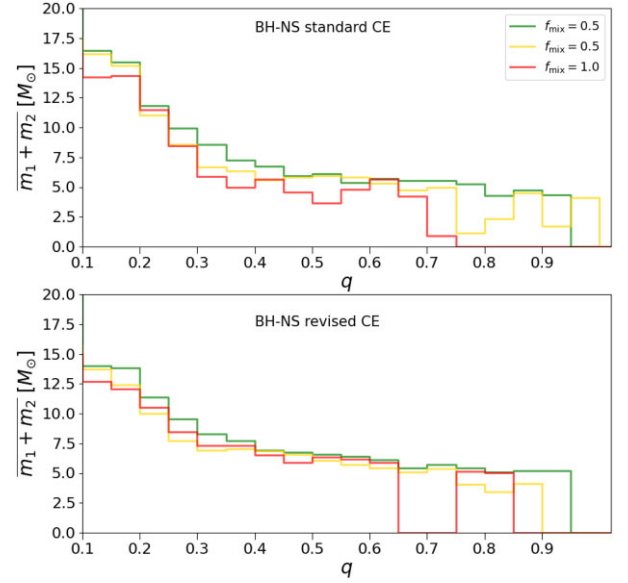


Figure 11. The relation between mass ratio q and the average total mass $m_1 + m_2$ of BH–NS mergers at $z < 2.0$. On the top panel results for standard CE development criteria, on the bottom panel results for revised CE development criteria. Green line: model with $f_{\text{mix}} = 0.5$, yellow line: model with $f_{\text{mix}} = 1.0$, and red line: model with $f_{\text{mix}} = 4.0$. Results for revised PSN model.

is significant for all SN models within the standard CE criteria, constituting ~ 24 per cent for $f_{\text{mix}} = 0.5$, ~ 15 per cent for $f_{\text{mix}} = 1.0$, and ~ 10 per cent for $f_{\text{mix}} = 4.0$ (Table 2).

4.2.2 Stable RLOF evolution

In the case of the revised CE development criteria (stable RLOF BH–BH formation channel, see Fig. 9) mass ratio distribution of BH–BH mergers is very similar for all tested variants of SN models and both PSN models. In the intrinsic distribution (top panels), the main difference between the remnant mass models is a peak of BH–NS mergers, which for models with $f_{\text{mix}} = 1.0$ and $f_{\text{mix}} = 4.0$ is two to three times higher and shifted towards more unequal mass ratios ($q \approx 0.1$) compared to the model with $f_{\text{mix}} = 0.5$ ($q \approx 0.2$). In all the tested SN models there is a second broad and high peak for mass ratios in the range $q \in 0.4–0.6$ which dominates the distribution of BH–BH mergers. This peak and its origin has already been noticed and explained in Olejak et al. (2021). In short, the peak is a consequence of overlap of restrict CE development criteria applied for massive donors with masses above $M_{\text{ZAMS}} > 18 M_{\odot}$ (BH progenitors) and the adopted assumptions of rather low orbital angular momentum mass-loss during non-conservative RLOF (Belczynski et al. 2008). In such physical conditions, it is possible to form tight BH–BH system which would merge in Hubble time only if the progenitor system had a significantly unequal mass ratio at the onset of the second RLOF.

The detection-weighted distribution for revised CE development criteria is, as with the the intrinsic distribution, strongly dominated by the peak made of BH–BH mergers with mass ratios $q \in 0.4–0.6$. However, the peak for unequal mass mergers with $q \in 0.1–0.2$, which was present in the intrinsic distribution, nearly disappears in the detection-weighted results with respect to the dominant BH–BH peak. The total fraction of unequal mass mergers with $q_{\text{det}} < 0.5$ is significant: around 25 per cent for all remnant mass models.

Table 3. Local merger rate densities ($z \approx 0$) for double compact objects (BH–BH, BH–NS, and NS–NS) for different tested physical models. In the first row(0.) we give recent (GWTC-3) estimates of LVK (Abbott et al. 2021d, e). The columns: CE criteria stands for adopted standard or revised CE development treatment; PSN limit stands for adopted strong ($\sim 45 M_{\odot}$) or revised ($\sim 90 M_{\odot}$) PSN limit; SN model stands for different adopted f_{mix} parameters (convection growth time); $\mathcal{R}_{\text{DCO}}[\text{Gpc}^{-3} \text{yr}^{-1}]$ stands for merger rate densities for different types of double compact object.

No.	CE criteria	PSN limit GWTC-3 $z \sim 0.2$	SN model	$\mathcal{R}_{\text{BH–BH}} [\text{Gpc}^{-3} \text{yr}^{-1}]$	$\mathcal{R}_{\text{BH–NS}} [\text{Gpc}^{-3} \text{yr}^{-1}]$	$\mathcal{R}_{\text{NS–NS}} [\text{Gpc}^{-3} \text{yr}^{-1}]$
				16–130 18–44	8–140	10–1700
1.	Standard	Revised	$f_{\text{mix}} = 0.5$	50	10	129
2.	Standard	Revised	$f_{\text{mix}} = 1.0$	43	21	119
3.	Standard	Revised	$f_{\text{mix}} = 4.0$	46	23	117
4.	Standard	Strong	$f_{\text{mix}} = 0.5$	61	11	155
5.	Standard	Strong	$f_{\text{mix}} = 1.0$	52	26	134
6.	Standard	Strong	$f_{\text{mix}} = 4.0$	58	27	143
7.	Revised	Revised	$f_{\text{mix}} = 0.5$	68	4	124
8.	Revised	Revised	$f_{\text{mix}} = 1.0$	75	5	116
9.	Revised	Revised	$f_{\text{mix}} = 4.0$	87	6	122
10.	Revised	Strong	$f_{\text{mix}} = 0.5$	80	5	154
11.	Revised	Strong	$f_{\text{mix}} = 1.0$	86	6	138
12.	Revised	Strong	$f_{\text{mix}} = 4.0$	102	7	144

However, for more extreme mass ratio mergers with $q_{\text{det}} < 0.3$ it quickly becomes negligible, constituting less than 1 per cent.

4.2.3 Mass ratio versus average mass of mergers

Figs 10 and 11 show trends in relation between mass ratios and masses of BH–BH and BH–NS mergers, respectively, for both RLOF stability criteria. On the bottom panel of Fig. 10, we plot the relation between mass ratio q and the average total mass $\overline{m_1 + m_2}$ of BH–BH mergers at $z < 2.0$ for the revised CE development criteria (stable RLOF formation channel). The trend is much different in the case of BH–BH binaries formed via the CE channel (top panel). The average mass of BH–BH mergers formed via stable RLOF is the largest ($\sim 50\text{--}60 M_{\odot}$) for unequal mass ratios corresponding to a peak $q \in 0.4\text{--}0.6$ and decreases moving towards equal mass ratio mergers.

4.2.4 Comparison with GW detections

Detection-weighted results for both the standard and revised CE development criteria do not fit all of the properties from the current data base of the LVK detection. In the case of the standard CE development criteria, the model with $f_{\text{mix}} = 0.5$ is able to reconstruct a significant fraction of unequal mass mergers ($q_{\text{det}} \leq 0.3$). All the three tested models of f_{mix} also produce a good fit to the LVK detections for the middle range of mass ratio values: $0.3 < q_{\text{det}} < 0.7$. For our simulations, we obtain a peak for equal mass ratio systems ($q_{\text{det}} > 0.9$), while the LVK detections show a peak at more unequal mergers: $q_{\text{det}} \in 0.7\text{--}0.8$.

In the case of the revised CE development criteria under which most BH–BH mergers formed via stable RLOF, the distribution is dominated by a high, broad peak similar to the LVK detections. However, in our simulations, the peak is shifted towards more unequal mergers, with its centre $q_{\text{det}} \approx 0.5$ instead of 0.7 (as for LVK). For those models we also do not produce a significant fraction of mergers with $q < 0.3$, which is visible in the distribution of the LVK detections.

Our results indicate that the distribution of the DCO mass ratio in the isolated binary evolution modelling is very sensitive to input

physical assumptions. A more extensive parameter study is needed in the future considering several assumptions on e.g. mass and orbital angular momentum loss during RLOF. Such studies could help to verify the model if we are able find an evolution model which fits the LVK observations well with the isolated binary evolution. If not, the LVK observations may require including other formation channels in order to produce all the features in mass ratio distribution of the detected DCO mergers.

4.3 Local merger rate density

In Table 3, we provide the local merger rate densities ($z \approx 0$) for our three new SN models and all tested physical models (see Section 2). The first column is the row number, in the second column we specify the used criteria for CE development: standard or revised. The third column stands for the PSN limit used: strong ($\sim 45 M_{\odot}$) and revised allowing for the formation of more massive BHs. In the fourth column we specify the adopted value of mixing parameter ($f_{\text{mix}} = 0.5, 1.0, \text{ or } 4.0$) for new remnant mass formula. In the fifth, sixth, and the seventh columns we provide the estimated values of the local merger rate densities ($z \approx 0$) for BH–BH, BH–NS, and NS–NS systems, respectively. We also provide a row with the current ranges for DCO merger rates given by recent LVK taking the union of 90 per cent credible intervals as provided by The LIGO Scientific Collaboration (2021b). For BH–BH mergers we give two variants of ranges, one with broader range under the assumption of constant rate density versus comoving volume (the upper value) and the second value given for $z = 0.2$ under the assumption that the BH–BH merger rate evolves with redshift (the lower value).

For all the tested models, the local merger rate densities (at $z \approx 0$) for NS–NS systems, which vary from 116 to 155 $\text{Gpc}^{-3} \text{yr}^{-1}$, are within the wide range constrained by the detections of LVK: 10–1700 $\text{Gpc}^{-3} \text{yr}^{-1}$ (the union of 90 per cent credible intervals). The local merger rate densities for BH–NS systems in our models are rather low and vary from 4 to 27 $\text{Gpc}^{-3} \text{yr}^{-1}$. Our values are within or close to the lower edge of the LVK range estimates for BH–NS merger rate densities: 8–140 $\text{Gpc}^{-3} \text{yr}^{-1}$ (the union of 90 per cent credible intervals). BH–BH merger rates for tested

models vary from 43 to $102 \text{ Gpc}^{-3} \text{ yr}^{-1}$. It falls into the broader variant of ranges for BH–BH merger rate densities given by LVK: $16\text{--}130 \text{ Gpc}^{-3} \text{ yr}^{-1}$ estimated (as for NS–NS and BH–NS) assuming a constant rate density versus comoving volume and taking the union of 90 per cent credible intervals (The LIGO Scientific Collaboration 2021b). However, our rates for BH–BH mergers vary from being close to the upper edge to even two times the upper edge of the narrow LVK range $18\text{--}44 \text{ Gpc}^{-3} \text{ yr}^{-1}$, which is the variant accounting for the BH–BH merger rate redshift evolution, estimated at a fiducial redshift ($z = 0.2$).

4.3.1 Impact of the SN model

The choice of the adopted SN model most significantly affects merger rates of BH–NS systems in standard CE development criteria. The rate estimated for model with $f_{\text{mix}} = 0.5$, $\sim 10 \text{ Gpc}^{-3} \text{ yr}^{-1}$, is more than two times lower than the rates estimated for models with $f_{\text{mix}} = 1.0$ and $f_{\text{mix}} = 4.0$. A similar effect has been already noticed for the previously used *STARTRACK* SN models: delay and rapid, and explained by Drozda et al. (2020). The increased efficiency in the formation of BH–NS mergers for models with more rapid convection growth time-scale, as described in more detail in Section 4.2, is due to the overlap of the produced mass distribution (particularly the lower mass gap) with the adopted assumption on NS and BH natal kicks. BHs formed via direct collapse in models $f_{\text{mix}} = 1.0$ and $f_{\text{mix}} = 4.0$ are more massive and get lower natal kicks than the low-mass BHs produced in the successful SN explosions in model $f_{\text{mix}} = 0.5$.

The different assumptions on the SN model do not significantly affect BH–BH and NS–NS merger rates, neither in the standard nor in the revised CE development criteria. In the case of NS–NS, the difference between results for tested remnant models is up to ~ 10 per cent, while for BH–BH mergers it is up to ~ 25 per cent.

4.3.2 Impact of assumption on PSN

The rates for all types of DCO mergers are slightly affected by the adopted PSN model (strong or revised) which changes them by around ~ 20 per cent due to different normalization caused by different IMF range (see Section 2). For the revised PSN model, we extend the range for the initial mass of the stars to $200 M_{\odot}$. This change makes it possible to create heavy BH–BH mergers with component masses $m_1 + m_2 \geq 100 M_{\odot}$. Such heavy BH–BH mergers are, however, rare (see Figs 6 and 7, Section 4.1) and do not constitute quantitatively significant fraction of all BH–BH mergers. Production of massive stars with initial masses $150\text{--}200 M_{\odot}$ takes some part of the total stellar mass (constant for all models) and slightly reduces the rates of DCO mergers in the revised PSN model.

4.3.3 Impact of RLOF stability criteria

Among all the tested models in this study factors, the merger rates of BH–BH and BH–NS are mostly affected by the used CE development criteria. As shown in Olejak et al. (2021), the different assumptions on RLOF stability may lead to different dominant formation scenario for DCO mergers. In the revised CE development criteria BH–BH and BH–NS progenitor systems are less likely to initiate a CE phase; for example, the massive donors with $M_{\text{ZAMS}} > 18 M_{\odot}$ (BH progenitors) RLOF are assumed to be stable for a much wider parameter space than in the standard criteria. The rates of BH–BH mergers between

the revised and the standard CE development criteria vary by up to a factor of ~ 2 , while BH–NS even by a factor of ~ 5 . However, due to a coincidence of the peak in star formation at $z \approx 2.0$ with the length of the BH–BH time delays,¹ which for stable RLOF phases are on average much longer than for CE formation channel, we obtain a non-intuitive result for BH–BH merger rates in the local Universe ($z \approx 0$). As shown in Fig. B1 (Appendix B), for most of the redshifts ($z \geq 0.5$) the BH–BH merger rate density is systematically a few times lower for the revised criteria dominated by stable RLOF formation channel than for the standard criteria dominated by CE formation channel. However, due to longer BH–BH time delays for stable RLOF channel, the peak in the merger rates related to increased star formation (at $z \approx 2.0$) is shifted towards lower redshifts. As a result of the lowest redshifts ($z \leq 0.5$) BH–BH merger rate density is approximately two times higher for the revised CE development criteria than for the standard one.

As discussed in Section 5, the physical parameter space tested within this study (12 models) is very limited and there are several other uncertain parameters and unconstrained processes which may significantly influence local merger rate densities. In this work, we focus on the impact of the adopted new remnant mass formulas. A few examples of works which provide estimates of DCO merger rates studying influence of other physical factors are Dominik et al. (2013), Neijssel et al. (2019), or Broekgaarden et al. (2022).

5 DISCUSSION OF CAVEATS AND UNCERTAINTIES

At this point we would like to mention some of the uncertainties in the calculations made in this work. In this study, we made a lot of assumptions related to the physical modelling of single and binary stellar evolution. Besides the stellar collapse and SN engine mechanism which is the main subject of this work, there are many other uncertain processes that dictate the formation of DCO mergers. Some examples of such processes or parameters which may significantly influence physical properties of DCO mergers are: the metallicity-specific star formation rate density and IMF (Chruślińska et al. 2020; Broekgaarden et al. 2021; Kroupa & Jerabkova 2021; Santoliquido et al. 2021; Briel et al. 2022), stellar winds (Vink et al. 2001; Sander et al. 2022), convection and overshooting (Klencki et al. 2021; Belczynski et al. 2022b), NS and BH natal kicks (Igoshev et al. 2021; Mandel et al. 2021), type and rate of mass transfer, and the outcome of stable/unstable RLOF (Bavera et al. 2020; Howitt et al. 2020; Vinciguerra et al. 2020; Olejak et al. 2021; Vigna-Gómez et al. 2022). The assumptions adopted for this work are described in Section 2. Here, we give examples of few uncertainties closely related to the new adopted formulas for SN remnant masses.

The *STARTRACK* population synthesis code uses analytic fits to the results of detailed evolution models given by Hurley, Pols & Tout (2000) and Hurley, Tout & Pols (2002). It has various possible consequences like a limited tested parameter space for detailed stellar physics or possible numerical artefacts. A specific example of possible overestimation or underestimation of the stellar structure parameters may be due to stopping the simulations before the star reaches collapse. The fits provided by Hurley et al. (2000) are based on results which tracked nuclear evolution of individual star and its structure parameters such as the core mass only till the end its core

¹Time delay is the time since the formation of a double compact object system (NS–NS, BH–NS, BH–BH) till its merger due to the gravitational waves emission.

helium-burning phase. However, the mass of the helium or carbon–oxygen core, the parameters which are used in this study e.g. in the new remnant mass formulas or in PSN modelling, still grow in the later part of the stellar evolution.

Using the carbon–oxygen core M_{CO} as a main tracer to estimate the fate of stellar collapse and the final remnant mass is not a perfect solution also for other reason. The value of M_{CO} does not capture the full structure of the pre-SN star nor the important features like the density gradient in the silicon and oxygen shells surrounding the iron core. Known in the literature as the compactness parameter, being a function of the density gradient, could be useful in making more precise predictions for remnant masses. Studies, e.g. Sukhbold & Woosley (2014), indicate that the compactness parameter may be a highly non-monotonic function of the ZAMS mass of the pre-SN star. Unfortunately, most of the population synthesis codes including *STARRACK* do not have an access to the detailed properties of stellar cores needed to estimate compactness parameter. In addition, it is known that, although the compactness parameter is a reasonable guide to the fate of the star, it also has its limitations (Alcock et al. 2001; Ertl et al. 2016; Burrows et al. 2020; Fryer et al. 2022). On the other hand, using fits to available results for the relation between ZAMS mass of pre-SN star and the final compactness parameter derived using detailed codes for single stellar evolution would not be a good approach as it would neglect the impact of mass transfer episodes (CE or stable RLOF), which are common and crucial for DCO mergers progenitors. Therefore, in this study we decided to use M_{CO} as the main parameter which seems to be the best compromise despite the caveats.

Another uncertainty is the M_{crit} parameter in formula (2) which in this work is set to $5.75 M_{\odot}$ and stands for the critical mass for the switch from NS to BH formation (threshold on mass of carbon–oxygen core). This is a parameter which is not yet constrained by observations. The different assumptions on M_{crit} impact the final remnant mass distribution, e.g. the width of the lower mass gap. See Fig. A1, where for comparison, we provide the same results as in Fig. 3 but for $M_{\text{crit}} = 4.75 M_{\odot}$.

Finally, we point out that the distribution of remnant masses could look very different for the rapidly rotating progenitors. If the angular momentum of the collapsing star is large enough, the SN explosion would be driven by a magnetar engine or NS accretion disc jet instead (See section 4 of Fryer et al. 2022). Rapidly rotating BH progenitors are believed to form accretion discs at the collapse and possibly drive an energetic jet. The jet could eject significant fraction of the stellar envelope and be responsible for long gamma-ray bursts phenomenon (Woosley 1993; MacFadyen, Woosley & Heger 2001). Such an additional ejection of mass would lead to the formation of less massive compact objects (NSs and BHs) compared to the remnant masses estimated by the new formulas applied for this study. However, as shown by Fryer et al. (2022) (see Fig. 11), such rapid rotators are not expected to constitute significant fraction of BH progenitors as the typical total angular momentum of pre-SN stars is usually expected to be way below the required limit. Also the underresolved simulations of magnetic field as well as the eventual jet production is not yet predictive.

6 CONCLUSIONS

In this study, we employ *STARRACK* population synthesis code to test how new formulas for SN models by Fryer et al. (2022) affect DCO mergers formed via the isolated binary evolution. New formulas for remnant masses allow to probe the convection growth time-scales in a wide spectrum in contrast to the previously used extreme cases

of delayed and rapid SN models (Fryer et al. 2012). The different assumptions for the convection growth time-scale impact the depth and width of the lower mass gap which may exist between the maximum possible mass of NS and the minimum mass of BH. In addition to the new models of SN, we test two variants of PSN: the strong PPSN/PSN model which limits BH mass to $\sim 45 M_{\odot}$ and the revised model which shifts the limit to higher BH masses (PSN for helium cores: $90 M_{\odot} < M_{\text{He}} < 175 M_{\odot}$). We also present results for the two CE development criteria: the standard model with BH–BH mergers formation mainly via CE and the revised model with BH–BH mergers formation mainly via a stable RLOF.

A summary of the results in this study is as follows:

(i) The different assumptions of the convection growth time-scale have a strong impact on the width and depth of the lower mass gap in remnant mass distribution for both single and binary evolution. The most-rapid SN model tested, the variant with $f_{\text{mix}} = 4.0$ (rapid growth of the convection $< 10\text{ms}$ that then develops an explosion in the first 100 ms), produces a wide and deep mass gap in the range $\sim 2\text{--}7 M_{\odot}$. In contrast, for the most-delayed SN model tested with $f_{\text{mix}} = 0.5$ (growth time closer to 100ms where the explosion can take up to 1s) the fraction of compact objects within the lower mass gap range is one to two orders of magnitude larger than in the model with $f_{\text{mix}} = 4.0$. Models with mixing parameter $f_{\text{mix}} \approx 2.5$ produce a gap in the range $\sim 2\text{--}5 M_{\odot}$, which is in good agreement with observations.

(ii) The mass distribution of DCO mergers, mass of the primary m_1 , secondary m_2 , and their sum, is sensitive to the adopted SN model up to total merger mass of $m_1 + m_2 \lesssim 35 M_{\odot}$.

(iii) The SN model with $f_{\text{mix}} = 0.5$ produces a significant fraction of massive NSs with mass $\in 1.5\text{--}2.5 M_{\odot}$, which may be important in studying the origin of massive NS systems like GW190425 (Abbott et al. 2020).

(iv) The choice of SN model affects significantly the intrinsic mass ratio distributions of BH–BH mergers but only in the CE formation scenario. In the intrinsic mass ratio distribution of BH–BH mergers (CE formation) with adopted $f_{\text{mix}} = 0.5$ there is a broad peak for unequal mass mergers $q \in 0.1\text{--}0.3$, while BH–BH mass ratio distribution for $f_{\text{mix}} = 4.0$ has two peaks at $q \in 0.5\text{--}0.7$ and for equal mass ratio systems $q \approx 1.0$ instead. Mass ratio distributions of BH–BH mergers formed mainly through stable RLOF is dominated by a broad, high peak for $q \in 0.4\text{--}0.6$ independently on SN model choice.

(v) The choice of SN model has the most significant effect on the local merger rates densities for BH–NS mergers. Rates of BH–NS mergers may even vary by a factor of ~ 3 between the two extreme cases $f_{\text{mix}} = 4.0$ and $f_{\text{mix}} = 0.5$. Such a difference is due to an overlap of the remnant mass distribution and the fraction of low-mass compact objects with our assumption of natal kicks (inversely proportional to the mass of compact object). The level of discrepancy between rates for different SN models is sensitive to other tested physical assumptions. Due to a wide mass gap, which means the dearth of massive NSs or low-mass BHs in model with $f_{\text{mix}} = 4.0$, there is a high peak for very unequal mass ratio BH–NS mergers with $q \sim 0.1$.

(vi) The different assumptions on PSN limit do not significantly influence the mass ratio distribution of BH–NS and BH–BH mergers. Extending the PSN limit to higher masses in revised PSN model allows to have a low tail of more massive mergers with total mass $m_1 + m_2 > 90 M_{\odot}$. For strong PPSN/PSN model the total mass of DCO mergers reaches up to $m_1 + m_2 \approx 90 M_{\odot}$, at which the value of the total merger mass has a slight peak due to partial mass ejection in PPSN.

(vii) The adopted CE development criteria differ only for BH progenitors and therefore the properties of NS–NS binaries are not affected by the used RLOF stability criteria. The choice of these criteria influences mainly the properties of BH–BH mergers, while BH–NS mergers are partly affected.

(viii) Our simulations for binary systems, similar to the results for single evolution presented in Fryer et al. (2022), show that the eventual stochasticity in stellar structure should not affect the statistical picture for a large probe of compact object population.

The SN models which partially fill the lower mass gap seem promising as such predictions could match the current EM observational results on the suppressed number of compact objects in the lower mass gap. In this work, we refrain from making any strong conclusions about the convection growth time-scale due to many uncertainties (see some caveats Section 5). We also still do not know what fraction of LVK mergers may come from different evolutionary channels (not necessarily the isolated binary evolution). However, further studies constraining detailed theoretical models by observations could bring progress towards understanding the evolution of massive stars (single and binary) and also the formation channels of detected DCO mergers. In addition, the number of future DCO detections is predicted to increase dramatically with the next-generation detectors (e.g. Borhanian & Sathyaprakash 2022). A much larger data base of parameters of DCO mergers will help to put more constraints on the SN mechanism and the origin of the detected signals.

ACKNOWLEDGEMENTS

KB and AO acknowledge support from the Polish National Science Center (NCN) grant Maestro (2018/30/A/ST9/00050). AO is also supported by the Foundation for Polish Science (FNP). The work by CLF was supported by the US Department of Energy through the Los Alamos National Laboratory. Los Alamos National Laboratory is operated by Triad National Security, LLC, for the National Nuclear Security Administration of U.S. Department of Energy (Contract No. 89233218CNA000001).

DATA AVAILABILITY

Data available on request. The results of simulations underlying this article will be shared on a request sent to the corresponding author: aolejak@camk.edu.pl.

REFERENCES

Abbott B. P. et al., 2016, *Phys. Rev. X*, 6, 041015
 Abbott B. P., Abbott R., Abbott T. D., Abraham S., LIGO Scientific Collaboration, Virgo Collaboration, 2019a, *Phys. Rev. X*, 9, 031040
 Abbott B. P., Abbott R., Abbott T. D., Abraham S., LIGO Scientific Collaboration, Virgo Collaboration, 2019b, *ApJ*, 882, L24
 Abbott B. P. et al., 2020, *ApJ*, 892, L3
 Abbott R. et al., 2021a, preprint ([arXiv:2108.01045](https://arxiv.org/abs/2108.01045))
 Abbott R. et al., 2021b, *Phys. Rev. X*, 11, 021053
 Abbott R. et al., 2021d, *ApJ*, 913, L7
 Abbott R. et al., 2021e, *ApJ*, 915, L5
 Alcock C. et al., 2001, *ApJ*, 550, L169
 Alsing J., Silva H. O., Berti E., 2018, *MNRAS*, 478, 1377
 Antonini F., Perets H. B., 2012, *ApJ*, 757, 27
 Antonini F., Toonen S., Hamers A. S., 2017, *ApJ*, 841, 77
 Arca-Sedda M., Capuzzo-Dolcetta R., 2019, *MNRAS*, 483, 152
 Arca-Sedda M., Li G., Kocsis B., 2021, *A&A*, 650, A189

Askar A., Szkudlarek M., Gondek-Rosińska D., Giersz M., Bulik T., 2017, *MNRAS*, 464, L36
 Bae Y.-B., Kim C., Lee H. M., 2014, *MNRAS*, 440, 2714
 Bailyn C. D., Jain R. K., Coppi P., Orosz J. A., 1998, *ApJ*, 499, 367
 Banerjee S., 2018, *MNRAS*, 473, 909
 Bavera S. S. et al., 2020, *A&A*, 635, A97
 Bavera S. S. et al., 2021, *A&A*, 647, A153
 Belczynski K., 2020, *ApJ*, 905, L15
 Belczynski K., Kalogera V., Bulik T., 2002, *ApJ*, 572, 407
 Belczynski K., Kalogera V., Rasio F. A., Taam R. E., Zezas A., Bulik T., Maccarone T. J., Ivanova N., 2008, *ApJS*, 174, 223
 Belczynski K., Bulik T., Fryer C. L., Ruiters A., Valsecchi F., Vink J. S., Hurley J. R., 2010a, *ApJ*, 714, 1217
 Belczynski K., Dominik M., Bulik T., O’Shaughnessy R., Fryer C. L., Holz D. E., 2010b, *ApJ*, 715, L138
 Belczynski K., Wiktorowicz G., Fryer C. L., Holz D. E., Kalogera V., 2012, *ApJ*, 757, 91
 Belczynski K. et al., 2016, *A&A*, 594, A97
 Belczynski K. et al., 2018, *A&A*, 615, A91
 Belczynski K. et al., 2020, *A&A*, 636, A104
 Belczynski K., Doctor Z., Zevin M., Olejak A., Banerjee S., Chattopadhyay D., 2022a, *ApJ*, 935, 126
 Belczynski K. et al., 2022b, *ApJ*, 925, 69
 Benacquista M. J., Downing J. M. B., 2013, *Living Rev. Relativ.*, 16, 4
 Blondin J. M., Mezzacappa A., DeMarino C., 2003, *ApJ*, 584, 971
 Bond J. R., Carr B. J., 1984, *MNRAS*, 207, 585
 Borhanian S., Sathyaprakash B. S., 2022, preprint ([arXiv:2202.11048](https://arxiv.org/abs/2202.11048))
 Briel M. M., Eldridge J. J., Stanway E. R., Stevance H. F., Chrimes A. A., 2022, *MNRAS*, 514, 1315
 Broekgaarden F. S. et al., 2021, *MNRAS*, 508, 5028
 Broekgaarden F. S. et al., 2022, *MNRAS*, preprint ([arXiv:2112.05763](https://arxiv.org/abs/2112.05763))
 Burrows A., Vartanyan D., Dolence J. C., Skinner M. A., Radice D., 2018, *Space Sci. Rev.*, 214, 33
 Burrows A., Radice D., Vartanyan D., Nagakura H., Skinner M. A., Dolence J. C., 2020, *MNRAS*, 491, 2715
 Chatterjee S., Rodriguez C. L., Kalogera V., Rasio F. A., 2017, *ApJ*, 836, L26
 Chruslińska M., Jeřábková T., Nelemans G., Yan Z., 2020, *A&A*, 636, A10
 Costa G., Bressan A., Mapelli M., Marigo P., Iorio G., Spera M., 2021, *MNRAS*, 501, 4514
 Couch S. M., Warren M. L., O’Connor E. P., 2020, *ApJ*, 890, 127
 Dabrowny M., Giacobbo N., Gerosa D., 2021, *Rendiconti Lincei. Scienze Fisiche e Naturali*, 32, 665
 de Mink S. E., Mandel I., 2016, *MNRAS*, 460, 3545
 Deller A. T. et al., 2012, *ApJ*, 756, L25
 Di Carlo U. N., Giacobbo N., Mapelli M., Pasquato M., Spera M., Wang L., Haardt F., 2019, *MNRAS*, 487, 2947
 Dominik M., Belczynski K., Fryer C., Holz D. E., Berti E., Bulik T., Mandel I., O’Shaughnessy R., 2013, *ApJ*, 779, 72
 Downing J. M. B., Benacquista M. J., Giersz M., Spurzem R., 2010, *MNRAS*, 407, 1946
 Drozda P., Belczynski K., O’Shaughnessy R., Bulik T., Fryer C. L., 2020, preprint ([arXiv:2009.06655](https://arxiv.org/abs/2009.06655))
 du Buisson L. et al., 2020, *MNRAS*, 499, 5941
 Eldridge J. J., Stanway E. R., 2016, *MNRAS*, 462, 3302
 Ertl T., Janka H. T., Woosley S. E., Sukhbold T., Ugliano M., 2016, *ApJ*, 818, 124
 Farmer R., Renzo M., de Mink S. E., Fishbach M., Justham S., 2020, *ApJ*, 902, L36
 Farr W. M., Sravan N., Cantrell A., Kreidberg L., Bailyn C. D., Mandel I., Kalogera V., 2011, *ApJ*, 741, 103
 Ferdman R. D. et al., 2020, *Nature*, 583, 211
 Fields C. E., Couch S. M., 2021, *ApJ*, 921, 28
 Finn L. S., Chernoff D. F., 1993, *Phys. Rev. D*, 47, 2198
 Fischer T., Whitehouse S. C., Mezzacappa A., Thielemann F. K., Liebendörfer M., 2010, *A&A*, 517, A80
 Fonseca E. et al., 2021, *ApJ*, 915, L12
 Fragione G., Kocsis B., 2019, *MNRAS*, 486, 4781

- Fragione G., Grishin E., Leigh N. W. C., Perets H. B., Perna R., 2019, *MNRAS*, 488, 47
- Fröhlich C. et al., 2006, *ApJ*, 637, 415
- Fryer C. L., Young P. A., 2007, *ApJ*, 659, 1438
- Fryer C. L., Belczynski K., Wiktorowicz G., Dominik M., Kalogera V., Holz D. E., 2012, *ApJ*, 749, 91
- Fryer C. L., Andrews S., Even W., Heger A., Safi-Harb S., 2018, *ApJ*, 856, 63
- Fryer C. L., Olejak A., Belczynski K., 2022, *ApJ*, 931, 94
- Giacobbo N., Mapelli M., Spera M., 2018, *MNRAS*, 474, 2959
- Giesers B. et al., 2019, *A&A*, 632, A3
- Gültekin K., Miller M. C., Hamilton D. P., 2004, *ApJ*, 616, 221
- Gültekin K., Miller M. C., Hamilton D. P., 2006, *ApJ*, 640, 156
- Hainich R. et al., 2018, *A&A*, 609, A94
- Hamann W. R., Koesterke L., 1998, *A&A*, 335, 1003
- Hamers A. S., Bar-Or B., Petrovich C., Antonini F., 2018, *ApJ*, 865, 2
- Haniewicz H. T., Ferdman R. D., Freire P. C. C., Champion D. J., Bunting K. A., Lorimer D. R., McLaughlin M. A., 2021, *MNRAS*, 500, 4620
- Hartwig T., Volonteri M., Bromm V., Klessen R. S., Barausse E., Magg M., Stacy A., 2016, *MNRAS*, 460, L74
- Heida M., Jonker P. G., Torres M. A. P., Chiavassa A., 2017, *ApJ*, 846, 132
- Herant M., Benz W., Hix W. R., Fryer C. L., Colgate S. A., 1994, *ApJ*, 435, 339
- Hoang B.-M., Naoz S., Kocsis B., Rasio F. A., Dosopoulou F., 2018, *ApJ*, 856, 140
- Hobbs G., Lorimer D. R., Lyne A. G., Kramer M., 2005, *MNRAS*, 360, 974
- Howitt G., Stevenson S., Vigna-Gómez A., Justham S., Ivanova N., Woods T. E., Neijssel C. J., Mandel I., 2020, *MNRAS*, 492, 3229
- Humphreys R. M., Davidson K., 1994, *PASP*, 106, 1025
- Hurley J. R., Pols O. R., Tout C. A., 2000, *MNRAS*, 315, 543
- Hurley J. R., Tout C. A., Pols O. R., 2002, *MNRAS*, 329, 897
- Hurley J. R., Sippel A. C., Tout C. A., Aarseth S. J., 2016, *MNRAS*, 33, e036
- Igoshev A. P., Chruslinska M., Dorozsmai A., Toonen S., 2021, *MNRAS*, 508, 3345
- Jayasinghe T. et al., 2021, *MNRAS*, 504, 2577
- Khan S., Husa S., Hannam M., Ohme F., Pürrer M., Jiménez Forteza X., Bohé A., 2016, *Phys. Rev. D*, 93, 044007
- King A. R., Davies M. B., Ward M. J., Fabbiano G., Elvis M., 2001, *ApJ*, 552, L109
- Kinugawa T., Inayoshi K., Hotokezaka K., Nakauchi D., Nakamura T., 2014, *MNRAS*, 442, 2963
- Klencki J., Nelemans G., Istrate A. G., Chruslinska M., 2021, *A&A*, 645, A54
- Kremer K. et al., 2020, *ApJS*, 247, 48
- Kroupa P., 2002, *Science*, 295, 82
- Kroupa P., Jerabkova T., 2021, preprint ([arXiv:2112.10788](https://arxiv.org/abs/2112.10788))
- Kroupa P., Tout C. A., Gilmore G., 1993, *MNRAS*, 262, 545
- Lam C. Y. et al., 2022, *ApJ*, 933, L23
- Laplace E., Justham S., Renzo M., Göteborg Y., Farmer R., Vartanyan D., de Mink S. E., 2021, *A&A*, 656, A58
- Lipunov V. M., Postnov K. A., Prokhorov M. E., 1997, *Astron. Lett.*, 23, 492
- Liu B., Lai D., 2018, *ApJ*, 863, 68
- Liu T., Wei Y.-F., Xue L., Sun M.-Y., 2021, *ApJ*, 908, 106
- Livescu D., Ristorcelli J. R., Gore R. A., Dean S. H., Cabot W. H., Cook A. W., 2009, *J. Turbul.*, 10, 13
- MacFadyen A. I., Woosley S. E., Heger A., 2001, *ApJ*, 550, 410
- MacLeod M., Ramirez-Ruiz E., 2015, *ApJ*, 803, 41
- MacLeod M., Antoni A., Murguia-Berthier A., Macias P., Ramirez-Ruiz E., 2017, *ApJ*, 838, 56
- Madau P., Fragos T., 2017, *ApJ*, 840, 39
- Magee R., Borhanian S., 2022, *ApJ*, 935, 139
- Mandel I., de Mink S. E., 2016, *MNRAS*, 458, 2634
- Mandel I., Müller B., Riley J., de Mink S. E., Vigna-Gómez A., Chattopadhyay D., 2021, *MNRAS*, 500, 1380
- Mapelli M., 2016, *MNRAS*, 459, 3432
- Marchant P., Langer N., Podsiadlowski P., Tauris T. M., Moriya T. J., 2016, *A&A*, 588, A50
- Marchant P., Renzo M., Farmer R., Pappas K. M. W., Taam R. E., de Mink S. E., Kalogera V., 2019, *ApJ*, 882, 36
- Melson T., Janka H.-T., Bollig R., Hanke F., Marek A., Müller B., 2015, *ApJ*, 808, L42
- Mennekens N., Vanbeveren D., 2014a, *A&A*, 564, A134
- Meurs E. J. A., van den Heuvel E. P. J., 1989, *A&A*, 226, 88
- Miller M. C., Hamilton D. P., 2002, *MNRAS*, 330, 232
- Mondal S., Belczyński K., Wiktorowicz G., Lasota J.-P., King A. R., 2020, *MNRAS*, 491, 2747
- Morawski J., Giersz M., Askar A., Belczynski K., 2018, *MNRAS*, 481, 2168
- Mroz P., Udalski A., Wyrzykowski L., Skowron J., Poleski R., Szymanski M., Soszynski I., Ulaczyk K., 2021, preprint ([arXiv:2107.13697](https://arxiv.org/abs/2107.13697))
- Neijssel C. J. et al., 2019, *MNRAS*, 490, 3740
- O’Leary R. M., O’Shaughnessy R., Rasio F. A., 2007, *Phys. Rev. D*, 76, 061504
- Olejak A., Belczynski K., 2021, *ApJ*, 921, L2
- Olejak A., Belczynski K., Ivanova N., 2021, *A&A*, 651, A100
- Özel F., Psaltis D., Narayan R., McClintock J. E., 2010, *ApJ*, 725, 1918
- Patton R. A., Sukhbold T., 2020, *MNRAS*, 499, 2803
- Pavlovskii K., Ivanova N., Belczynski K., Van K. X., 2017, *MNRAS*, 465, 2092
- Perego A., Hempel M., Fröhlich C., Ebinger K., Eichler M., Casanova J., Liebendörfer M., Thielemann F. K., 2015, *ApJ*, 806, 275
- Perna R., Wang Y.-H., Farr W. M., Leigh N., Cantiello M., 2019, *ApJ*, 878, L1
- Portegies Zwart S. F., McMillan S. L. W., 2000, *ApJ*, 528, L17
- Prša A. et al., 2016, *AJ*, 152, 41
- Qin Y., Wang Y.-Z., Dong-Hong, Wu, Meynet G., Song H., 2022, *ApJ*, 924, 129
- Ricker P. M., Taam R. E., 2008, *ApJ*, 672, L41
- Rodriguez C. L., Haster C.-J., Chatterjee S., Kalogera V., Rasio F. A., 2016, *ApJ*, 824, L8
- Rodriguez C. L., Amaro-Seoane P., Chatterjee S., Kremer K., Rasio F. A., Samsing J., Ye C. S., Zevin M., 2018, *Phys. Rev. D*, 98, 123005
- Sadowski A., Belczynski K., Bulik T., Ivanova N., Rasio F. A., O’Shaughnessy R., 2008, *ApJ*, 676, 1162
- Sahu K. C. et al., 2022, *ApJ*, 933, 83
- Samsing J., 2018, *Phys. Rev. D*, 97, 103014
- Sander A. A. C., Vink J. S., Higgins E. R., Shenar T., Hamann W.-R., Todt H., 2022, preprint ([arXiv:2202.04671](https://arxiv.org/abs/2202.04671))
- Santoliquido F., Mapelli M., Giacobbo N., Bouffanais Y., Artale M. C., 2021, *MNRAS*, 502, 4877
- Schneider F. R. N., Podsiadlowski Ph., Müller B., 2021, *A&A*, 645, A5
- Shao Y., Li X.-D., 2021, *ApJ*, 920, 81
- Silsbee K., Tremaine S., 2017, *ApJ*, 836, 39
- Spera M., Mapelli M., Giacobbo N., Trani A. A., Bressan A., Costa G., 2019, *MNRAS*, 485, 889
- Stegmann J., Antonini F., Schneider F. R. N., Tiwari V., Chattopadhyay D., 2022, *Phys. Rev. D*, 106, id.023014
- Stevenson S., Vigna-Gómez A., Mandel I., Barret J. W., Neijssel C. J., Perkins D., de Mink S. E., 2017, *Nat. Commun.*, 8, 14906
- Sukhbold T., Woosley S. E., 2014, *ApJ*, 783, 10
- Tagawa H., Haiman Z., Kocsis B., 2020, *ApJ*, 898, 25
- Tagawa H., Kocsis B., Haiman Z., Bartos I., Omukai K., Samsing J., 2021, *ApJ*, 908, 194
- The LIGO Scientific Collaboration, 2021a, preprint ([arXiv:2111.03606](https://arxiv.org/abs/2111.03606))
- The LIGO Scientific Collaboration, The Virgo Collaboration, The KAGRA Scientific Collaboration, 2021b, preprint ([arXiv:2111.03634](https://arxiv.org/abs/2111.03634))
- Thompson T. A. et al., 2019, *Science*, 366, 637
- Toonen S., Hamers A., Portegies Zwart S., 2016, *Comput. Astrophys. Cosmol.*, 3, 6
- Tutukov A. V., Yungelson L. R., 1993, *MNRAS*, 260, 675
- Ugliano M., Janka H.-T., Marek A., Arcones A., 2012, *ApJ*, 757, 69
- van den Heuvel E. P. J., Portegies Zwart S. F., de Mink S. E., 2017, *MNRAS*, 471, 4256
- van Son L. A. C. et al., 2021, *ApJ*, 931, id.17
- VanLandingham J. H., Miller M. C., Hamilton D. P., Richardson D. C., 2016, *ApJ*, 828, 77

Vigna-Gómez A., Toonen S., Ramirez-Ruiz E., Leigh N. W. C., Riley J., Haster C.-J., 2021, *ApJ*, 907, L19
 Vigna-Gómez A., Wassink M., Klencki J., Istrate A., Nelemans G., Mandel I., 2022, *MNRAS*, 511, 2326
 Vinciguerra S. et al., 2020, *MNRAS*, 498, 4705
 Vink J. S., de Koter A., Lamers H. J. G. L. M., 2001, *A&A*, 369, 574
 Woosley S. E., 1993, *ApJ*, 405, 273
 Woosley S. E., 2016, *ApJ*, 824, L10
 Woosley S. E., 2017, *ApJ*, 836, 244
 Woosley S. E., Heger A., 2021, *ApJ*, 912, L31
 Woosley S. E., Heger A., Weaver T. A., 2002, *Rev. Mod. Phys.*, 74, 1015
 Woosley S. E., Blinnikov S., Heger A., 2007, *Nature*, 450, 390
 Zevin M., Bavera S. S., 2022, *ApJ*, 933, 86
 Zevin M., Samsing J., Rodriguez C., Haster C.-J., Ramirez-Ruiz E., 2019, *ApJ*, 871, 91
 Zevin M., Spera M., Berry C. P. L., Kalogera V., 2020, *ApJ*, 899, L1

APPENDIX A: CRITICAL MASS FOR A BH FORMATION VERSUS LOWER MASS GAP

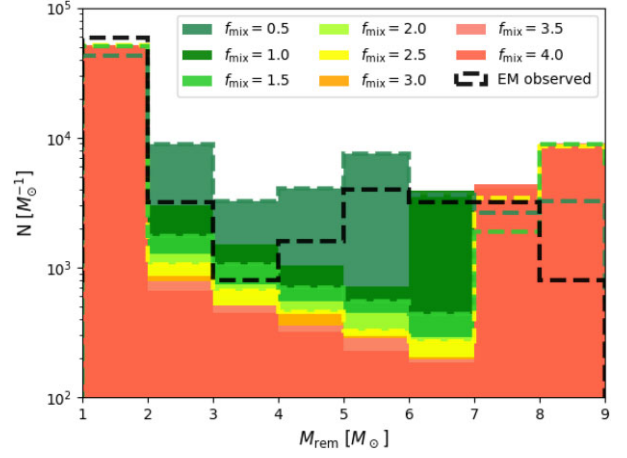


Figure A1. Histogram (binsize $1 M_{\odot}$) of the remnant masses of the probe of 10^5 single stars for the adopted IMF for eight new SN model prescriptions with f_{mix} in the range 0.5–4.0 and $Z = 1.0Z_{\odot}$. Results for different critical mass of carbon–oxygen core for a BH formation, $M_{\text{crit}} = 4.75M_{\odot}$ (see equation 2) than adopted for this study $M_{\text{crit}} = 5.75M_{\odot}$ (see Fig. 3).

APPENDIX B: REDSHIFT EVOLUTION OF MERGER RATE DENSITY OF BH–BH MERGERS

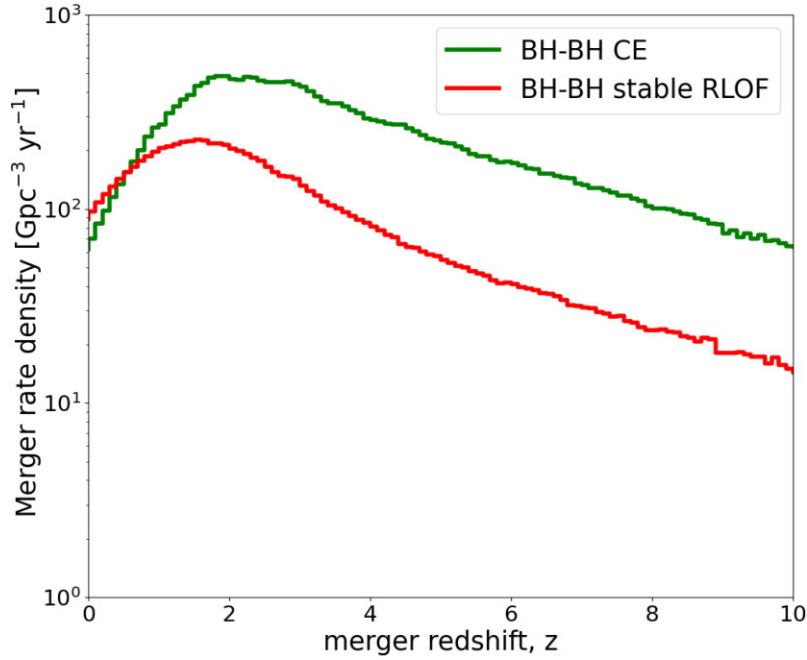


Figure B1. BH–BH merger rate density evolution with redshift z . Comparison between standard and revised CE development criteria. With the green line we plot the result for a model with the standard criteria for which BH–BH forms mainly through CE phase. The results for the revised criteria for which BH–BH forms mainly through stable RLOF is plotted with a red line. Note that, for most of the redshifts, the merger rate density for the revised criteria (BH–BH stable RLOF) is systematically a few times lower (up to one order of magnitude) than for the standard one. However, due to long time delays of BH–BH mergers in stable RLOF channel, the peak in merger rates related to a peak in star formation (at $z \approx 2.0$) is shifted to the left (towards lower redshifts). This leads to non-intuitive result that for the local Universe $z \approx 0$ BH–BH merger rate density is higher for stable RLOF than for CE formation channel.

APPENDIX C: STOCHASTICITY

Here, we check how assumption on some stochasticity in the pre-SN stellar structure, reported by several studies (Patton & Sukhbold 2020; Laplace et al. 2021; Schneider et al. 2021), may influence the mass distribution of cosmological DCO mergers in a similar way as Fryer et al. (2022) did for single star evolution. We mimic the stochasticity effect by including in our synthetic population a fraction of stars f_{stoch} which may have much different mass of their carbon–oxygen core M_{CO} at pre-SN evolution stage compared to the value predicted by standard `STARTRACK` calculations. For this fraction of stars we generate a value of M_{CO} from the flat distribution in range between 10 per cent of original value M_{CO} and the total pre-SN mass of the star, so

$$M_{\text{CO}}^{\text{stoch}} = \text{rand}(0.1M_{\text{CO}}, M_{\text{fin}}). \quad (\text{C1})$$

The results are shown in Figs C1 and C2, where we plot the mass distribution of DCO mergers for two examples of new SN models: $f_{\text{mix}} = 0.5$ and $f_{\text{mix}} = 4.0$, respectively. The figures show the results for the three variants of the included fractions of the stochastic-structure progenitors (equation C1). Those fractions are 0 per cent (red line), 30 per cent (blue line), and 50 per cent (green line). On the top panel we show the distribution of the primary mass m_1 , on the middle panel the secondary mass m_2 , and on the bottom panel the sum $m_1 + m_2$. The plotted results are for a physical model with a standard CE development criteria and a revised PSN limit (see Section 2).

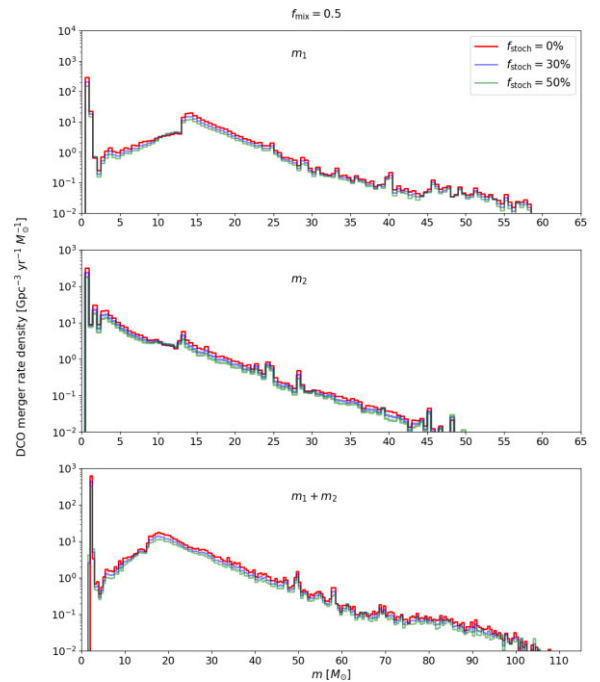


Figure C1. Mass distribution of DCO merger masses ($z < 1.0$) with different fractions of compact object progenitors with stochastic stellar structure (equation C1): 0 per cent (red line), 30 per cent (blue line), and 50 per cent (green line). The results for the new remnant mass formula with $f_{\text{mix}} = 0.5$, a standard CE development criteria, and a revised PSN limit (see Section 2). Top panel: distribution of primary mass m_1 , middle panel: secondary mass m_2 , bottom panel: $m_1 + m_2$.

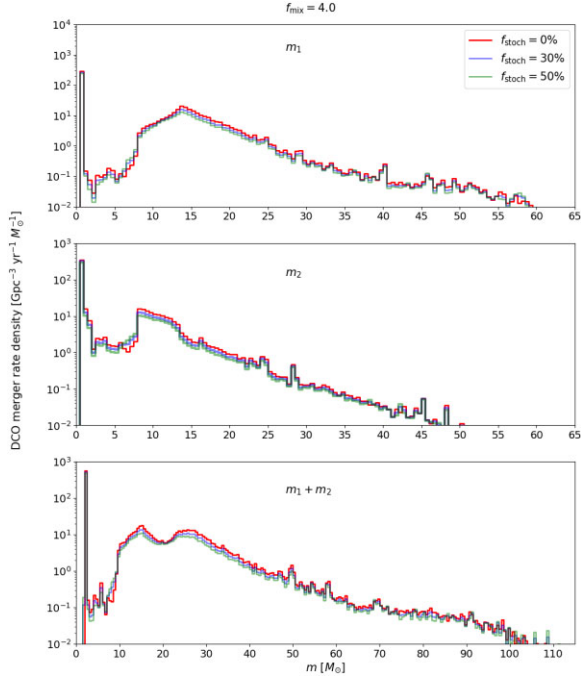


Figure C2. Mass distribution of DCO merger masses ($z < 1.0$) with different fractions of compact object progenitors with stochastic stellar structure (equation C1): 0 per cent (red line), 30 per cent (blue line), and 50 per cent (green line). Results for new remnant mass formula with $f_{\text{mix}} = 4.0$, a standard CE development criteria, and a revised PSN limit (see Section 2). Top panel: distribution of primary mass m_1 , middle panel: secondary mass m_2 , bottom panel: $m_1 + m_2$.

APPENDIX D: STARTRACK VERSUS MOBSE NEW REMNANT MASS PRESCRIPTIONS

In this section, we make a brief comparison of the outcomes of our new SN prescriptions parametrizing the convection growth time-scale with other recent prescription for stellar remnants parametrizing the fraction of the hydrogen envelope that is accreted by the BH during collapse (Dabrowny et al. 2021). The formula by Dabrowny et al. (2021) tested with MOBSE population synthesis code (Giacobbo, Mapelli & Spera 2018) uses compactness parameter $\zeta_{2.5}$ approximated with the formula

$$\zeta_{2.5} \approx 0.55 - 1.1(M_{\text{CO}}/1M_{\odot})^{-1}$$

as a threshold between NS and BH formation. The value used in their simulations $\zeta_{2.5} = 0.365$ was calibrated to match the results of the previous rapid SN model by Fryer et al. (2012). The mass of the BH is calculated with the formula

$$M_{\text{BH}} = M_{\text{He}} + f_{\text{H}}(M - M_{\text{He}}),$$

where M_{He} is the mass of the helium core, M is the pre-SN mass of the star, and f_{H} is the parameter which determines the assumed fraction of mass of the hydrogen envelope accreted on the BH during collapse. For the main tested model in their studies this fraction was $f_{\text{H}} = 0.9$.

In Fig. D1, we show the relation between the initial mass of the progenitor star and its final remnant mass for three cases of our new SN models and two variants of Dabrowny et al. (2021) formulas.

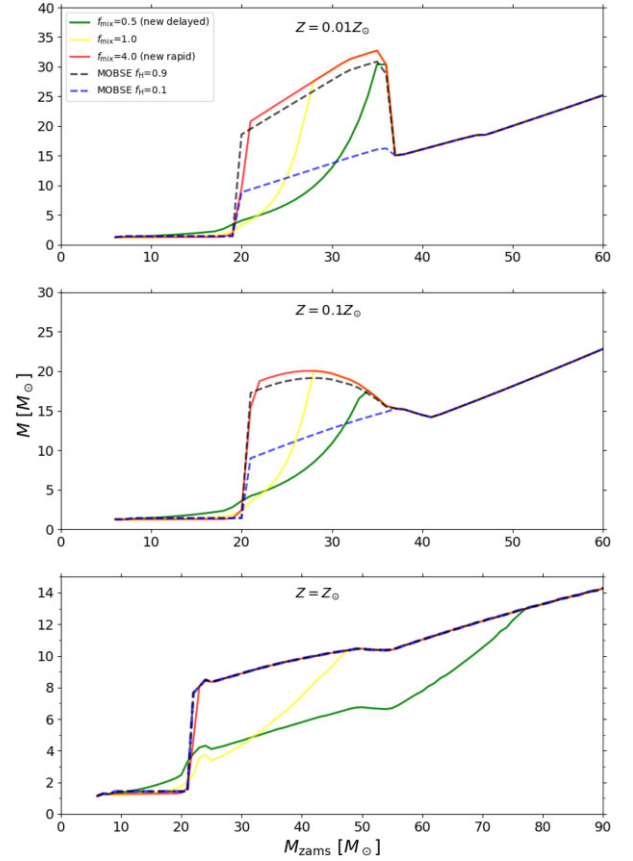


Figure D1. Relation between the initial mass M_{ZAMS} of the progenitor star and the final remnant mass for three new SN models (Fryer et al. 2022) parametrizing convection growth time-scale: $f_{\text{mix}} = 0.5$, $f_{\text{mix}} = 1.0$, and $f_{\text{mix}} = 4.0$ and two remnant mass variants parametrizing the fraction of the hydrogen envelope (Dabrowny et al. 2021): $f_{\text{H}} = 0.9$ and $f_{\text{H}} = 0.1$.

The threshold for BH formation in Dabrowny et al. (2021) was chosen to match the rapid SN model (Fryer et al. 2012). Moreover, their prescription with $f_{\text{H}} = 0.9$ assumes direct collapse of almost all star's mass to a BH. Therefore, as expected, the outcome for the model with $f_{\text{H}} = 0.9$ is almost the same as our new rapid SN model with $f_{\text{mix}} = 4.0$. We also test the other extreme assumption with a very low fraction of the accreted hydrogen envelope $f_{\text{H}} = 0.1$. If the final pre-SN star still has hydrogen envelope, this model produces systematically lower BH masses compared to our model with $f_{\text{mix}} = 4.0$ and Dabrowny et al.'s (2021) model with $f_{\text{H}} = 0.9$. However, as the minimum mass of a BH in Dabrowny et al. (2021) formulas is equal to its pre-SN helium core, this model produces a mass gap even for a low fraction of the accreted envelope $f_{\text{H}} = 0.1$ (there is steep increase between the masses of NSs and the lowest masses of BHs, see Fig. D1). Therefore, Dabrowny et al.'s (2021) parametrization would not allow for a smooth transition between having a deep mass gap and a remnant mass distribution filled with a significant number of 2–5 M_{\odot} compact objects as in the case of our Fryer et al. (2022) models with a wide spectrum of convection growth time-scales.

This paper has been typeset from a \LaTeX file prepared by the author.

7 Summary

7.1 Final conclusions

The current catalog of detected GW signals contains around 90 events, with the vast majority, roughly 90%, classified as BH-BH mergers [2; 3]. However, the origin of the detected compact object mergers and the contribution fraction of different formation channels is still unknown. There are several suggested formation scenarios, See Section 1.4. Some of them could reproduce all or a significant part of inferred merger rates for the given type of event (BH-BH, BH-NS or NS-NS) as well distribution of parameters of GW sources: their masses and spins. There are several not well constrained astrophysical processes related to each formation channel. The uncertain input assumptions, especially for the most exotic formation scenarios, cause the degeneracy of results for many models and make it hard to exclude or confirm contribution of any channel. Currently, it is even challenging to specify reasonable parameter space for GW sources that is confidently unavailable for a given formation scenario.

The main topic of this thesis is compact mergers' formation scenarios via isolated evolution of massive binary star systems, with a special focus on the population of BH-BH mergers. In the included studies, we try to reconstruct the parameters of detected GW systems, including unusual events such as highly unequal BH-BH mergers (See Section 3) or rapidly spinning BHs (see Section 5). We implement advancements in studies of highly uncertain astrophysical processes such as: CE development criteria (Sec. 4), and core-collapse SN (Sec. 6). We test the impact of various assumptions on the synthetic population of compact object mergers using the isolated binary evolution scenario. Our results indicate that commonly recognized characteristic properties of the GW sources which originate from isolated binaries, such as the tendency towards mass-equal mergers or negligible fraction of high spinning BHs, are not fully justified and model dependent. Within our models, we find formation scenarios for BH-BH mergers, with and without CE, which result in a spin distribution consistent with LVK detections (Sec. 5). Our articles bring attention to the gaps in our understanding of stellar binary evolution and consequences of several uncertain assumptions adopted in rapid population synthesis that affects predicted rates, masses, and spins of compact object mergers.

Unveiling the formation channel of detected GW sources is important as it would allow putting valuable constraints on single and binary evolution of massive stars, the mechanism of core-collapse SN, nature of dynamical interactions, properties of population III stars, and several other poorly understood astrophysical phenomena. Conversely, a better understanding of massive star evolution and their final fate using observations and numerical modeling may help to reduce degeneracy between models and identify formation scenarios of detected compact object mergers. These two things must go hand in hand. Therefore, it is necessary to further study the uncertain processes of mass transfer in massive binaries or core collapse SN systems and to look for other methods to constrain those phenomena using GW detections, observations of systems in the electromagnetic wave spectrum and future microlensing events. A deep understanding of the astrophysics processes responsible for compact object mergers formation is required to make any robust inferences based on parameters of detected systems.

7.2 Future of gravitational wave astrophysics

The future of GW astrophysics is bright and exciting. Currently, the community is getting prepared for the next observing runs using improved LIGO and Virgo interferometers, and looking further into the future, for the third generation of ground-based GW detectors Einstein Telescope (Europe) and the Cosmic Explorer (USA) [62; 63; 213; 273]. Advanced LIGO instruments with planned upgrades of squeezed light performance, mirrors with reduced thermal noise, and improved GW read-out method are supposed to increase their current sensitivity by more than a

factor of two [62]. The next LVK observing run O4 is scheduled to start on 24th May 2023 and is expected to provide a great number (tens or even hundreds) of new GW detections [274].

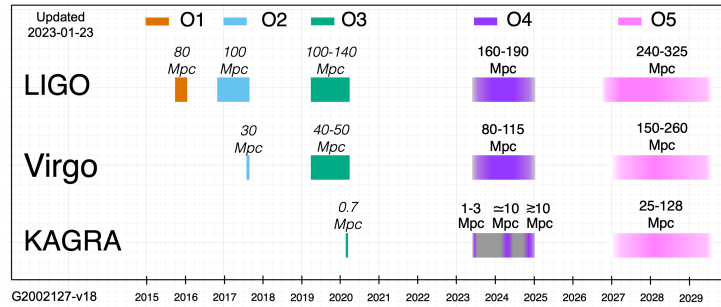


Fig. 18: Schedule of the LIGO, Virgo, and KAGRA observing runs (former and future) with the average distance at which the given GW instrument will be able to detect NS-NS merger. Credit: The LIGO-Virgo-KAGRA (LVK) Collaboration, source: <https://dcc-lho.ligo.org> [274].

GW detectors of the next generation: Einstein Telescope and Cosmic Explorer, expected to operate by the mid-2030s, are still in the rather early development phase. Einstein Telescope, planned to be built in Europe (the exact location is still undecided), will adopt new technological concepts and is going to be an underground infrastructure consisting of three 10 km arm interferometers in triangular configuration [62; 273]. Cosmic Explorer will adopt the former, already tested configuration of LIGO interferometers. However, the length of L-shape interferometer arms will be extended up to 40 km [62; 213]. There are two planned stages of implementation. In the first CE1 stage, mainly solutions of the Advanced LIGO will be adopted. The second CE2 stage provides for the possibility of implementing new technologies. [62].

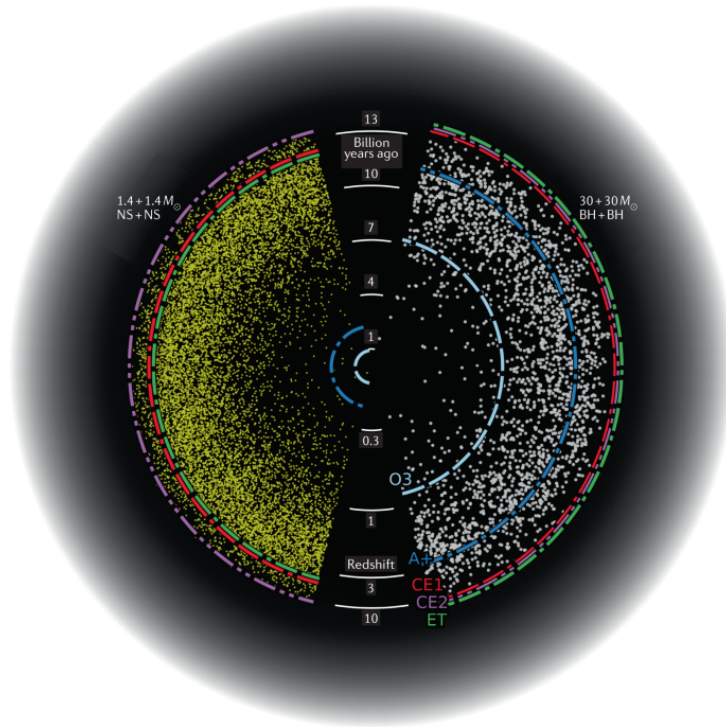


Fig. 19: Redshift and lookback time limits for the future detections of $1.4 M_{\odot}+1.4 M_{\odot}$ NS-NS mergers (left side) and massive, $30 M_{\odot}+30 M_{\odot}$ BH-BH mergers (right side) for different GW detectors. O3 (light blue) is the range of the current LVK detectors in the third joint observing run, A+ (dark blue) is the range for advanced LIGO interferometers after planned upgrades, CE (pink) is the range of the Cosmic Explorer and ET (green) the range of the Einstein telescope. Credit: Evan Hall, Salvatore Vitale/ MIT [62]

Both European and American GW instruments are going to continue to pursue the scientific goals of LVK collaboration. However, their sensitivity is going to be improved by an order of magnitude compared to the currently operating detectors [63]. Such sensitivity will allow following the evolution of rates and properties of compact object merger through the cosmic time. The optimal ranges for detections of each type of event will reach much higher redshifts, see Figure 19. Therefore, it will become possible to explore the very early stages of the universe, looking for eventual evidences for the first stellar populations or primordial BHs [63].

Assisted by planned space instrument LISA (Laser Interferometer Space Antenna) [275], future interferometers will cover a broad spectrum of frequencies, allowing for the detection of GWs from currently unavailable mass ranges and types of sources. Beside the origin of compact object mergers and constraints for their formation channels, many other astrophysical puzzles may be solved using the future GW data. Some examples are: the NS equation of state, the Universe expansion rate, the nature of dark matter, formation of super-massive BHs, primordial BHs, general relativity and modified theories of gravity, the structure of our Milky Way, type Ia supernovae mechanism and many others [62].

Acknowledgments

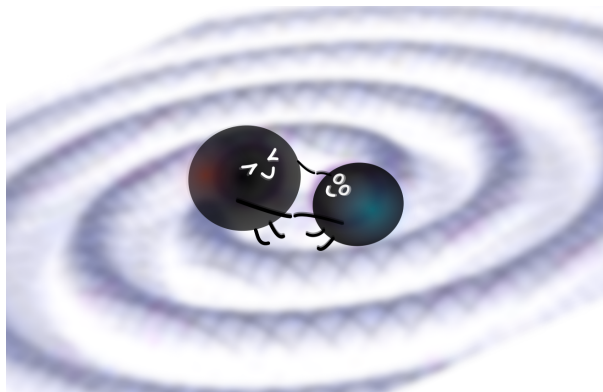
I would like to express my deepest gratitude to *Tomek Bulik*, who is a great example for me, both scientifically and in terms of ethical, and human values. I am very grateful for his advice, support, and kindness, especially in difficult situations. I would also like to thank *Krzysztof Belczyński* for the joint scientific projects, for introducing me to the field of gravitational wave astrophysics, for his constructive comments, and for the years of cooperation. I express my gratitude to *Jean-Pierre Lasota* for his reliable support, for ensuring the quality of our scientific articles, for interesting conversations, and for friendliness. I would also like to thank all the people I had the privilege to collaborate with, especially *Chris Fryer*, *Natasha Ivanova*, and *Bożena Czerny*.

During my doctoral studies at *Nicolaus Copernicus Astronomical Center*, I acknowledge support from *the Polish National Science Center (NCN) grant Maestro, Foundation for Polish Science (FNP)*, and *the Minister of Education and Science*.

Privately, I would like to thank my family with all my heart for their unconditional support and belief in my abilities. I express my deepest gratitude to my wonderful sisters *Karolina* and *Zuzia*, my mum *Ela*, my granddad *Antoni*, and my brother-in-law *Maciej*.

I thank *Marco* for motivating and cheering me up in the best and worst moments. I also thank a lot *Mateusz* for many years of our friendship and the fact that I can always count on him. I express my gratitude to my dear friends: *Dorota*, *Ola*, *Magda*, *Ewelina*, *Iza*, *Agata*, and *Bruno* for giving me a lot of joy and support during my doctoral studies as well as before. I thank my office mate *Chandra Shekhar* for his great company. I am also very grateful to the many other people who have been helpful and kind during the years of my studies at *Nicolaus Copernicus Astronomical Center*.

Finally, I would like to thank *Nara* for her feline company, which gave me encouragement during the final, intensive days of work on this thesis.



2

²Graphics by Marco Antonelli

Bibliography

- [1] The LIGO Scientific Collaboration et al. Observation of Gravitational Waves from a Binary Black Hole Merger. *Phys. Rev. Lett.*, 116(6):061102, February 2016. doi: 10.1103/PhysRevLett.116.061102.
- [2] The LIGO Scientific Collaboration et al. The population of merging compact binaries inferred using gravitational waves through GWTC-3. *arXiv e-prints*, art. arXiv:2111.03634, November 2021.
- [3] The LIGO Scientific Collaboration et al. GWTC-3: Compact Binary Coalescences Observed by LIGO and Virgo During the Second Part of the Third Observing Run. *arXiv e-prints*, art. arXiv:2111.03606, November 2021. doi: 10.48550/arXiv.2111.03606.
- [4] The LIGO Scientific Collaboration et al. GWTC-1: A Gravitational-Wave Transient Catalog of Compact Binary Mergers Observed by LIGO and Virgo during the First and Second Observing Runs. *Phys. Rev. X*, 9(3):031040, July 2019. doi: 10.1103/PhysRevX.9.031040.
- [5] The LIGO Scientific Collaboration et al. GWTC-2.1: Deep Extended Catalog of Compact Binary Coalescences Observed by LIGO and Virgo During the First Half of the Third Observing Run. *arXiv e-prints*, art. arXiv:2108.01045, August 2021. doi: 10.48550/arXiv.2108.01045.
- [6] The LIGO Scientific Collaboration et al. . GWTC-2: Compact Binary Coalescences Observed by LIGO and Virgo during the First Half of the Third Observing Run. *Physical Review X*, 11(2):021053, April 2021. doi: 10.1103/PhysRevX.11.021053.
- [7] The LIGO Scientific Collaboration et al. . Population Properties of Compact Objects from the Second LIGO-Virgo Gravitational-Wave Transient Catalog. *ApJL*, 913(1):L7, May 2021. doi: 10.3847/2041-8213/abe949.
- [8] The LIGO Scientific Collaboration et al. GW190814: Gravitational Waves from the Coalescence of a 23 Solar Mass Black Hole with a 2.6 Solar Mass Compact Object. *ApJL*, 896(2):L44, June 2020. doi: 10.3847/2041-8213/ab960f.
- [9] The LIGO Scientific Collaboration et al. GW190412: Observation of a binary-black-hole coalescence with asymmetric masses. *Phys. Rev. D*, 102(4):043015, August 2020. doi: 10.1103/PhysRevD.102.043015.
- [10] The LIGO Scientific Collaboration et al. GW190521: A Binary Black Hole Merger with a Total Mass of $150 M_{\odot}$. *Phys. Rev. Lett.*, 125(10):101102, September 2020. doi: 10.1103/PhysRevLett.125.101102.
- [11] Pavel Kroupa. On the variation of the initial mass function. *MNRAS*, 322(2):231–246, April 2001. doi: 10.1046/j.1365-8711.2001.04022.x.
- [12] Charles D. Bailyn, Raj K. Jain, Paolo Coppi, and Jerome A. Orosz. The mass distribution of stellar black holes. *The Astrophysical Journal*, 499(1):367–374, may 1998. doi: 10.1086/305614. URL <https://doi.org/10.1086/305614>.
- [13] Will M. Farr, Niharika Sravan, Andrew Cantrell, Laura Kreidberg, Charles D. Bailyn, Ilya Mandel, and Vicky Kalogera. THE MASS DISTRIBUTION OF STELLAR-MASS BLACK HOLES. *The Astrophysical Journal*, 741(2):103, oct 2011. doi: 10.1088/0004-637x/741/2/103. URL <https://doi.org/10.1088/0004-637x/741/2/103>.

- [14] Feryal Özel, Dimitrios Psaltis, Ramesh Narayan, and Jeffrey E. McClintock. The Black Hole Mass Distribution in the Galaxy. *ApJ*, 725(2):1918–1927, December 2010. doi: 10.1088/0004-637X/725/2/1918.
- [15] Laura Kreidberg, Charles D. Bailyn, Will M. Farr, and Vicky Kalogera. Mass Measurements of Black Holes in X-Ray Transients: Is There a Mass Gap? *ApJ*, 757(1):36, September 2012. doi: 10.1088/0004-637X/757/1/36.
- [16] J. Antoniadis, P. C. C. Freire, N. Wex, T. M. Tauris, R. S. Lynch, M. H. van Kerkwijk, M. Kramer, C. Bassa, V. S. Dhillon, T. Driebe, J. W. T. Hessels, V. M. Kaspi, V. I. Kondratiev, N. Langer, T. R. Marsh, M. A. McLaughlin, T. T. Pennucci, S. M. Ransom, I. H. Stairs, J. van Leeuwen, J. P. W. Verbiest, and D. G. Whelan. A Massive Pulsar in a Compact Relativistic Binary. *Science*, 340:448, April 2013. doi: 10.1126/science.1233232.
- [17] Samuel J. Swihart, Jay Strader, Tyrel J. Johnson, C. C. Cheung, David Sand, Laura Chomiuk, Asher Wasserman, Søren Larsen, Jean P. Brodie, Gregory V. Simonian, Evangelia Tremou, Laura Shishkovsky, Daniel E. Reichart, and Joshua Haislip. 2fgl j0846.02820: A new neutron star binary with a giant secondary and variable -ray emission. *ApJ*, 851(1):31, dec 2017. doi: 10.3847/1538-4357/aa9937. URL <https://doi.org/10.3847%2F1538-4357%2Faa9937>.
- [18] Vaibhav Tiwari and Stephen Fairhurst. The Emergence of Structure in the Binary Black Hole Mass Distribution. *ApJL*, 913(2):L19, June 2021. doi: 10.3847/2041-8213/abf7e7.
- [19] L. M. de Sá, A. Bernardo, R. R. A. Bachega, J. E. Horvath, L. S. Rocha, and P. H. R. S. Moraes. Quantifying the Evidence Against a Mass Gap between Black Holes and Neutron Stars. *ApJ*, 941(2):130, December 2022. doi: 10.3847/1538-4357/aca076.
- [20] Yong Shao. On the Neutron Star/Black Hole Mass Gap and Black Hole Searches. *Research in Astronomy and Astrophysics*, 22(12):122002, December 2022. doi: 10.1088/1674-4527/ac995e.
- [21] Stan Woosley and Thomas Janka. The physics of core-collapse supernovae. *Nature Physics*, 1(3):147–154, December 2005. doi: 10.1038/nphys172.
- [22] C. L. Fryer, K. Belczynski, G. Wiktorowicz, M. Dominik, V. Kalogera, and D. E. Holz. Compact Remnant Mass Function: Dependence on the Explosion Mechanism and Metallicity. *ApJ*, 749:91, April 2012. doi: 10.1088/0004-637X/749/1/91.
- [23] Tuguldur Sukhbold and S. E. Woosley. The Compactness of Presupernova Stellar Cores. *ApJ*, 783(1):10, March 2014. doi: 10.1088/0004-637X/783/1/10.
- [24] Tong Liu, Yun-Feng Wei, Li Xue, and Mou-Yuan Sun. Final Compact Remnants in Core-collapse Supernovae from 20 to 40 M_{\odot} : The Lower Mass Gap. *ApJ*, 908(1):106, February 2021. doi: 10.3847/1538-4357/abd24e.
- [25] Chris L. Fryer, Aleksandra Olejak, and Krzysztof Belczynski. The Effect of Supernova Convection On Neutron Star and Black Hole Masses. *ApJ*, 931(2):94, June 2022. doi: 10.3847/1538-4357/ac6ac9.
- [26] Aleksandra Olejak, Chris L. Fryer, Krzysztof Belczynski, and Vishal Baibhav. The role of supernova convection for the lower mass gap in the isolated binary formation of gravitational wave sources. *MNRAS*, 516(2):2252–2271, October 2022. doi: 10.1093/mnras/stac2359.

- [27] L. A. C. van Son, S. E. de Mink, M. Renzo, S. Justham, E. Zapartas, K. Breivik, T. Callister, W. M. Farr, and C. Conroy. No Peaks without Valleys: The Stable Mass Transfer Channel for Gravitational-wave Sources in Light of the Neutron Star-Black Hole Mass Gap. *ApJ*, 940(2):184, December 2022. doi: 10.3847/1538-4357/ac9b0a.
- [28] S. E. Woosley, S. Blinnikov, and Alexander Heger. Pulsational pair instability as an explanation for the most luminous supernovae. *Nature*, 450(7168):390–392, November 2007. doi: 10.1038/nature06333.
- [29] K. Belczynski, A. Heger, W. Gladysz, A. J. Ruiter, S. Woosley, G. Wiktorowicz, H. Y. Chen, T. Bulik, R. O’Shaughnessy, D. E. Holz, C. L. Fryer, and E. Berti. The effect of pair-instability mass loss on black-hole mergers. *A&A*, 594:A97, October 2016. doi: 10.1051/0004-6361/201628980.
- [30] Pablo Marchant, Mathieu Renzo, Robert Farmer, Kaliroe M. W. Pappas, Ronald E. Taam, Selma E. de Mink, and Vassiliki Kalogera. Pulsational Pair-instability Supernovae in Very Close Binaries. *ApJ*, 882(1):36, September 2019. doi: 10.3847/1538-4357/ab3426.
- [31] Simon Stevenson, Matthew Sampson, Jade Powell, Alejandro Vigna-Gómez, Coenraad J. Neijssel, Dorottya Szécsi, and Ilya Mandel. The Impact of Pair-instability Mass Loss on the Binary Black Hole Mass Distribution. *ApJ*, 882(2):121, September 2019. doi: 10.3847/1538-4357/ab3981.
- [32] S. E. Woosley and Alexander Heger. The Pair-instability Mass Gap for Black Holes. *ApJL*, 912(2):L31, May 2021. doi: 10.3847/2041-8213/abf2c4.
- [33] R. Farmer, M. Renzo, S. E. de Mink, M. Fishbach, and S. Justham. Constraints from Gravitational-wave Detections of Binary Black Hole Mergers on the $^{12}\text{C}(\alpha, \gamma)^{16}\text{O}$ Rate. *ApJL*, 902(2):L36, October 2020. doi: 10.3847/2041-8213/abbadd.
- [34] Guglielmo Costa, Alessandro Bressan, Michela Mapelli, Paola Marigo, Giuliano Iorio, and Mario Spera. Formation of GW190521 from stellar evolution: the impact of the hydrogen-rich envelope, dredge-up, and $^{12}\text{C}(\alpha, \gamma)^{16}\text{O}$ rate on the pair-instability black hole mass gap. *MNRAS*, 501(3):4514–4533, March 2021. doi: 10.1093/mnras/staa3916.
- [35] Maya Fishbach and Daniel E. Holz. Minding the Gap: GW190521 as a Straddling Binary. *ApJL*, 904(2):L26, December 2020. doi: 10.3847/2041-8213/abc827.
- [36] Alexander H. Nitz and Collin D. Capano. GW190521 May Be an Intermediate-mass Ratio Inspiral. *ApJL*, 907(1):L9, January 2021. doi: 10.3847/2041-8213/abccc5.
- [37] A. L. Sallaska, C. Iliadis, A. E. Champagne, S. Goriely, S. Starrfield, and F. X. Timmes. STARLIB: A Next-generation Reaction-rate Library for Nuclear Astrophysics. *ApJS*, 207(1):18, July 2013. doi: 10.1088/0067-0049/207/1/18.
- [38] Giacomo Fragione, Abraham Loeb, and Frederic A. Rasio. On the Origin of GW190521-like Events from Repeated Black Hole Mergers in Star Clusters. *ApJL*, 902(1):L26, October 2020. doi: 10.3847/2041-8213/abbc0a.
- [39] Francesco Paolo Rizzuto, Thorsten Naab, Rainer Spurzem, Mirek Giersz, J. P. Ostriker, N. C. Stone, Long Wang, Peter Berczik, and M. Rampp. Intermediate mass black hole formation in compact young massive star clusters. *MNRAS*, 501(4):5257–5273, March 2021. doi: 10.1093/mnras/staa3634.

- [40] Krzysztof Belczynski. The Most Ordinary Formation of the Most Unusual Double Black Hole Merger. *ApJL*, 905(2):L15, December 2020. doi: 10.3847/2041-8213/abcbf1.
- [41] A. Gal-Yam, P. Mazzali, E. O. Ofek, P. E. Nugent, S. R. Kulkarni, M. M. Kasliwal, R. M. Quimby, A. V. Filippenko, S. B. Cenko, R. Chornock, R. Waldman, D. Kasen, M. Sullivan, E. C. Beshore, A. J. Drake, R. C. Thomas, J. S. Bloom, D. Poznanski, A. A. Miller, R. J. Foley, J. M. Silverman, I. Arcavi, R. S. Ellis, and J. Deng. Supernova 2007bi as a pair-instability explosion. *Nature*, 462(7273):624–627, December 2009. doi: 10.1038/nature08579.
- [42] Jeff Cooke, Mark Sullivan, Avishay Gal-Yam, Elizabeth J. Barton, Raymond G. Carlberg, Emma V. Ryan-Weber, Chuck Horst, Yuuki Omori, and C. Gonzalo Díaz. Superluminous supernovae at redshifts of 2.05 and 3.90. *Nature*, 491(7423):228–231, November 2012. doi: 10.1038/nature11521.
- [43] Sebastian Gomez, Edo Berger, Matt Nicholl, Peter K. Blanchard, V. Ashley Villar, Locke Patton, Ryan Chornock, Joel Leja, Griffin Hosseinzadeh, and Philip S. Cowperthwaite. SN 2016iet: The Pulsational or Pair Instability Explosion of a Low-metallicity Massive CO Core Embedded in a Dense Hydrogen-poor Circumstellar Medium. *ApJ*, 881(2):87, August 2019. doi: 10.3847/1538-4357/ab2f92.
- [44] J. S. Vink, A. de Koter, and H. J. G. L. M. Lamers. New theoretical mass-loss rates of O and B stars. *A&A*, 362:295–309, October 2000. doi: 10.48550/arXiv.astro-ph/0008183.
- [45] Jorick S. Vink, A. de Koter, and H. J. G. L. M. Lamers. Mass-loss predictions for O and B stars as a function of metallicity. *A&A*, 369:574–588, April 2001. doi: 10.1051/0004-6361:20010127.
- [46] J. J. Eldridge and J. S. Vink. Implications of the metallicity dependence of Wolf-Rayet winds. *A&A*, 452(1):295–301, June 2006. doi: 10.1051/0004-6361:20065001.
- [47] Joachim Puls, Jorick S. Vink, and Francisco Najarro. Mass loss from hot massive stars. *A&AR*, 16(3-4):209–325, December 2008. doi: 10.1007/s00159-008-0015-8.
- [48] Krzysztof Belczynski, Tomasz Bulik, Chris L. Fryer, Ashley Ruitter, Francesca Valsecchi, Jorick S. Vink, and Jarrod R. Hurley. On the Maximum Mass of Stellar Black Holes. *ApJ*, 714(2):1217–1226, May 2010. doi: 10.1088/0004-637X/714/2/1217.
- [49] Jorick S. Vink. Very massive stars: a metallicity-dependent upper-mass limit, slow winds, and the self-enrichment of globular clusters. *A&A*, 615:A119, Jul 2018. doi: 10.1051/0004-6361/201832773.
- [50] Alex Camilo Gormaz-Matamala, Jorge Cuadra, Georges Meynet, and Michel Curé. Evolution of rotating massive stars with new hydrodynamic wind models. *arXiv e-prints*, art. arXiv:2303.13058, March 2023. doi: 10.48550/arXiv.2303.13058.
- [51] Coenraad J. Neijssel, Serena Vinciguerra, Alejandro Vigna-Gómez, Ryosuke Hirai, James C. A. Miller-Jones, Arash Bahramian, Thomas J. Maccarone, and Ilya Mandel. Wind Mass-loss Rates of Stripped Stars Inferred from Cygnus X-1. *ApJ*, 908(2):118, February 2021. doi: 10.3847/1538-4357/abde4a.
- [52] James C. A. Miller-Jones, Arash Bahramian, Jerome A. Orosz, Ilya Mandel, Lijun Gou, Thomas J. Maccarone, Coenraad J. Neijssel, Xueshan Zhao, Janusz Ziółkowski,

- Mark J. Reid, Phil Uttley, Xueying Zheng, Do-Young Byun, Richard Dodson, Victoria Grinberg, Taehyun Jung, Jeong-Sook Kim, Benito Marcote, Sera Markoff, María J. Rioja, Anthony P. Rushton, David M. Russell, Gregory R. Sivakoff, Alexandra J. Tetarenko, Valeriu Tudose, and Joern Wilms. Cygnus X-1 contains a 21-solar mass black hole—Implications for massive star winds. *Science*, 371(6533):1046–1049, March 2021. doi: 10.1126/science.abb3363.
- [53] K. Belczynski, J. Klencki, C. E. Fields, A. Olejak, E. Berti, G. Meynet, C. L. Fryer, D. E. Holz, R. O’Shaughnessy, D. A. Brown, T. Bulik, S. C. Leung, K. Nomoto, P. Madau, R. Hirschi, E. Kaiser, S. Jones, S. Mondal, M. Chruslinska, P. Drozda, D. Gerosa, Z. Doctor, M. Giersz, S. Ekstrom, C. Georgy, A. Askar, V. Baibhav, D. Wysocki, T. Natan, W. M. Farr, G. Wiktorowicz, M. Coleman Miller, B. Farr, and J. P. Lasota. Evolutionary roads leading to low effective spins, high black hole masses, and O1/O2 rates for LIGO/Virgo binary black holes. *A&A*, 636:A104, April 2020. doi: 10.1051/0004-6361/201936528.
- [54] Krzysztof Belczynski. The Most Ordinary Formation of the Most Unusual Double Black Hole Merger. *ApJL*, 905(2):L15, December 2020. doi: 10.3847/2041-8213/abcbf1.
- [55] N. Langer, W. R. Hamann, M. Lennon, F. Najarro, A. W. A. Pauldrach, and J. Puls. Towards an understanding of very massive stars. A new evolutionary scenario relating O stars, LBVs and Wolf-Rayet stars. *A&A*, 290:819–833, October 1994.
- [56] R. M. Humphreys and K. Davidson. Studies of luminous stars in nearby galaxies. III. Comments on the evolution of the most massive stars in the Milky Way and the Large Magellanic Cloud. *ApJ*, 232:409–420, September 1979. doi: 10.1086/157301.
- [57] Nathan Smith, Weidong Li, Jeffrey M. Silverman, Mohan Ganeshalingam, and Alexei V. Filippenko. Luminous blue variable eruptions and related transients: diversity of progenitors and outburst properties. *MNRAS*, 415(1):773–810, July 2011. doi: 10.1111/j.1365-2966.2011.18763.x.
- [58] Piero Madau and Mark Dickinson. Cosmic Star-Formation History. *ARAAS*, 52:415–486, August 2014. doi: 10.1146/annurev-astro-081811-125615.
- [59] Martyna Chruslinska and Gijs Nelemans. Metallicity of stars formed throughout the cosmic history based on the observational properties of star-forming galaxies. *MNRAS*, 488(4):5300–5326, October 2019. doi: 10.1093/mnras/stz2057.
- [60] Michela Mapelli, Nicola Giacobbo, Filippo Santoliquido, and Maria Celeste Artale. The properties of merging black holes and neutron stars across cosmic time. *MNRAS*, 487(1): 2–13, July 2019. doi: 10.1093/mnras/stz1150.
- [61] Martyna Chruslinska. Chemical evolution of the Universe and its consequences for gravitational-wave astrophysics. *arXiv e-prints*, art. arXiv:2206.10622, June 2022. doi: 10.48550/arXiv.2206.10622.
- [62] M. Bailes, B. K. Berger, P. R. Brady, M. Branchesi, K. Danzmann, M. Evans, K. Holley-Bockelmann, B. R. Iyer, T. Kajita, S. Katsanevas, M. Kramer, A. Lazzarini, L. Lehner, G. Losurdo, H. Lück, D. E. McClelland, M. A. McLaughlin, M. Punturo, S. Ransom, S. Raychaudhury, D. H. Reitze, F. Ricci, S. Rowan, Y. Saito, G. H. Sanders, B. S. Sathyaprakash, B. F. Schutz, A. Sesana, H. Shinkai, X. Siemens, D. H. Shoemaker,

- J. Thorpe, J. F. J. van den Brand, and S. Vitale. Gravitational-wave physics and astronomy in the 2020s and 2030s. *Nature Reviews Physics*, 3(5):344–366, January 2021. doi: 10.1038/s42254-021-00303-8.
- [63] Matthew Evans, Rana X Adhikari, Chaitanya Afle, Stefan W. Ballmer, Sylvia Biscoveanu, Ssohrab Borhanian, Duncan A. Brown, Yanbei Chen, Robert Eisenstein, Alexandra Gruson, Anuradha Gupta, Evan D. Hall, Rachael Huxford, Brittany Kamai, Rahul Kashyap, Jeff S. Kissel, Kevin Kuns, Philippe Landry, Amber Lenon, Geoffrey Lovelace, Lee McCuller, Ken K. Y. Ng, Alexander H. Nitz, Jocelyn Read, B. S. Sathyaprakash, David H. Shoemaker, Bram J. J. Slagmolen, Joshua R. Smith, Varun Srivastava, Ling Sun, Salvatore Vitale, and Rainer Weiss. A Horizon Study for Cosmic Explorer: Science, Observatories, and Community. *arXiv e-prints*, art. arXiv:2109.09882, September 2021. doi: 10.48550/arXiv.2109.09882.
- [64] Neha Singh, Tomasz Bulik, Krzysztof Belczynski, Marek Cieslar, and Francesca Calore. Reconstructing star formation rate for compact binary populations with Einstein telescope. *arXiv e-prints*, art. arXiv:2304.01341, April 2023. doi: 10.48550/arXiv.2304.01341.
- [65] Colm Talbot and Eric Thrane. Determining the population properties of spinning black holes. *Phys. Rev. D*, 96(2):023012, July 2017. doi: 10.1103/PhysRevD.96.023012.
- [66] Salvatore Vitale, Ryan Lynch, Vivien Raymond, Riccardo Sturani, John Veitch, and Philip Graff. Parameter estimation for heavy binary-black holes with networks of second-generation gravitational-wave detectors. *Phys. Rev. D*, 95(6):064053, March 2017. doi: 10.1103/PhysRevD.95.064053.
- [67] Shanika Galaudage, Colm Talbot, Tushar Nagar, Deepnika Jain, Eric Thrane, and Ilya Mandel. Building Better Spin Models for Merging Binary Black Holes: Evidence for Nonspinning and Rapidly Spinning Nearly Aligned Subpopulations. *ApJL*, 921(1):L15, November 2021. doi: 10.3847/2041-8213/ac2f3c.
- [68] Javier Roulet, Horng Sheng Chia, Seth Olsen, Liang Dai, Tejaswi Venumadhav, Barak Zackay, and Matias Zaldarriaga. Distribution of effective spins and masses of binary black holes from the LIGO and Virgo O1-O3a observing runs. *Phys. Rev. D*, 104(8):083010, October 2021. doi: 10.1103/PhysRevD.104.083010.
- [69] Thomas A. Callister, Simona J. Miller, Katerina Chatziioannou, and Will M. Farr. No Evidence that the Majority of Black Holes in Binaries Have Zero Spin. *ApJL*, 937(1):L13, September 2022. doi: 10.3847/2041-8213/ac847e.
- [70] Christian Adamcewicz and Eric Thrane. Do unequal-mass binary black hole systems have larger χ_{eff} ? Probing correlations with copulas in gravitational-wave astronomy. *MNRAS*, 517(3):3928–3937, December 2022. doi: 10.1093/mnras/stac2961.
- [71] Davide Gerosa and Emanuele Berti. Are merging black holes born from stellar collapse or previous mergers? *Phys. Rev. D*, 95(12):124046, June 2017. doi: 10.1103/PhysRevD.95.124046.
- [72] Maya Fishbach, Daniel E. Holz, and Ben Farr. Are LIGO’s Black Holes Made from Smaller Black Holes? *ApJL*, 840(2):L24, May 2017. doi: 10.3847/2041-8213/aa7045.
- [73] Jifeng Liu, Jeffrey E. McClintock, Ramesh Narayan, Shane W. Davis, and Jerome A. Orosz. Precise Measurement of the Spin Parameter of the Stellar-Mass Black Hole M33 X-7. *ApJL*, 679(1):L37, May 2008. doi: 10.1086/588840.

- [74] Christopher S. Reynolds. Observational Constraints on Black Hole Spin. *A&A*, 59:117–154, September 2021. doi: 10.1146/annurev-astro-112420-035022.
- [75] R. D. Blandford and R. L. Znajek. Electromagnetic extraction of energy from Kerr black holes. *MNRAS*, 179(3):433–456, 07 1977. ISSN 0035-8711. doi: 10.1093/mnras/179.3.433. URL <https://doi.org/10.1093/mnras/179.3.433>.
- [76] S. E. Woosley. Gamma-Ray Bursts from Stellar Mass Accretion Disks around Black Holes. *ApJ*, 405:273, March 1993. doi: 10.1086/172359.
- [77] Maya Fishbach and Vicky Kalogera. Apples and Oranges: Comparing Black Holes in X-Ray Binaries and Gravitational-wave Sources. *ApJL*, 929(2):L26, April 2022. doi: 10.3847/2041-8213/ac64a5.
- [78] Monica Gallegos-Garcia, Maya Fishbach, Vicky Kalogera, Christopher P. L Berry, and Zoheyr Doctor. Do High-spin High-mass X-Ray Binaries Contribute to the Population of Merging Binary Black Holes? *ApJL*, 938(2):L19, October 2022. doi: 10.3847/2041-8213/ac96ef.
- [79] H. C. Spruit. Dynamo action by differential rotation in a stably stratified stellar interior. *A&A*, 381:923–932, January 2002. doi: 10.1051/0004-6361:20011465.
- [80] Matias Zaldarriaga, Doron Kushnir, and Juna A. Kollmeier. The expected spins of gravitational wave sources with isolated field binary progenitors. *MNRAS*, 473(3):4174–4178, January 2018. doi: 10.1093/mnras/stx2577.
- [81] Kenta Hotokezaka and Tsvi Piran. Implications of the Low Binary Black Hole Aligned Spins Observed by LIGO. *ApJ*, 842(2):111, June 2017. doi: 10.3847/1538-4357/aa6f61.
- [82] Jim Fuller, Anthony L Piro, and Adam S Jermyn. Slowing the spins of stellar cores. *MNRAS*, 485(3):3661–3680, 02 2019. ISSN 0035-8711. doi: 10.1093/mnras/stz514. URL <https://doi.org/10.1093/mnras/stz514>.
- [83] R. G. Detmers, N. Langer, P. Podsiadlowski, and R. G. Izzard. Gamma-ray bursts from tidally spun-up Wolf-Rayet stars? *A&A*, 484:831–839, June 2008. doi: 10.1051/0004-6361:200809371.
- [84] D. Kushnir, M. Zaldarriaga, J. A. Kollmeier, and R. Waldman. Dynamical tides reexpressed. *MNRAS*, 467:2146–2149, May 2017. doi: 10.1093/mnras/stx255.
- [85] Y. Qin, T. Fragos, G. Meynet, J. Andrews, M. Sørensen, and H. F. Song. The spin of the second-born black hole in coalescing binary black holes. *A&A*, 616:A28, August 2018. doi: 10.1051/0004-6361/201832839.
- [86] A. Olejak and K. Belczynski. The Implications of High Black Hole Spins for the Origin of Binary Black Hole Mergers. *ApJL*, 921(1):L2, November 2021. doi: 10.3847/2041-8213/ac2f48.
- [87] Jim Fuller and Wenbin Lu. The spins of compact objects born from helium stars in binary systems. *MNRAS*, 511(3):3951–3964, April 2022. doi: 10.1093/mnras/stac317.
- [88] Périgois Carole, Mapelli Michela, Santoliquido Filippo, Bouffanais Yann, and Rufolo Roberta. Binary black hole spins: model selection with GWTC-3. *arXiv e-prints*, art. arXiv:2301.01312, January 2023.

- [89] Bill Paxton, Lars Bildsten, Aaron Dotter, Falk Herwig, Pierre Lesaffre, and Frank Timmes. Modules for Experiments in Stellar Astrophysics (MESA). *ApJS*, 192(1):3, January 2011. doi: 10.1088/0067-0049/192/1/3.
- [90] Bill Paxton, Matteo Cantiello, Phil Arras, Lars Bildsten, Edward F. Brown, Aaron Dotter, Christopher Mankovich, M. H. Montgomery, Dennis Stello, F. X. Timmes, and Richard Townsend. Modules for Experiments in Stellar Astrophysics (MESA): Planets, Oscillations, Rotation, and Massive Stars. *ApJS*, 208(1):4, September 2013. doi: 10.1088/0067-0049/208/1/4.
- [91] Bill Paxton, Pablo Marchant, Josiah Schwab, Evan B. Bauer, Lars Bildsten, Matteo Cantiello, Luc Dessart, R. Farmer, H. Hu, N. Langer, R. H. D. Townsend, Dean M. Townsley, and F. X. Timmes. Modules for Experiments in Stellar Astrophysics (MESA): Binaries, Pulsations, and Explosions. *ApJS*, 220(1):15, September 2015. doi: 10.1088/0067-0049/220/1/15.
- [92] Bill Paxton, Josiah Schwab, Evan B. Bauer, Lars Bildsten, Sergei Blinnikov, Paul Duffell, R. Farmer, Jared A. Goldberg, Pablo Marchant, Elena Sorokina, Anne Thoul, Richard H. D. Townsend, and F. X. Timmes. Modules for Experiments in Stellar Astrophysics (MESA): Convective Boundaries, Element Diffusion, and Massive Star Explosions. *ApJS*, 234(2):34, February 2018. doi: 10.3847/1538-4365/aaa5a8.
- [93] Adam S. Jermyn, Evan B. Bauer, Josiah Schwab, R. Farmer, Warrick H. Ball, Earl P. Bellinger, Aaron Dotter, Meridith Joyce, Pablo Marchant, Joey S. G. Mombarg, William M. Wolf, Tin Long Sunny Wong, Giulia C. Cinquegrana, Eoin Farrell, R. Smolec, Anne Thoul, Matteo Cantiello, Falk Herwig, Odette Toloza, Lars Bildsten, Richard H. D. Townsend, and F. X. Timmes. Modules for Experiments in Stellar Astrophysics (MESA): Time-dependent Convection, Energy Conservation, Automatic Differentiation, and Infrastructure. *ApJS*, 265(1):15, March 2023. doi: 10.3847/1538-4365/aca8d.
- [94] Nicola Giacobbo and Michela Mapelli. The progenitors of compact-object binaries: impact of metallicity, common envelope and natal kicks. *MNRAS*, 480(2):2011–2030, October 2018. doi: 10.1093/mnras/sty1999.
- [95] Krzysztof Belczynski, Grzegorz Wiktorowicz, Chris L. Fryer, Daniel E. Holz, and Vasiliki Kalogera. Missing Black Holes Unveil the Supernova Explosion Mechanism. *ApJ*, 757(1):91, September 2012. doi: 10.1088/0004-637X/757/1/91.
- [96] Simone S. Bavera, Tassos Fragos, Ying Qin, Emmanouil Zapartas, Coenraad J. Neijssel, Ilya Mandel, Aldo Batta, Sebastian M. Gaebel, Chase Kimball, and Simon Stevenson. The origin of spin in binary black holes. Predicting the distributions of the main observables of Advanced LIGO. *A&A*, 635:A97, March 2020. doi: 10.1051/0004-6361/201936204.
- [97] Carl L. Rodriguez, Michael Zevin, Chris Pankow, Vasiliki Kalogera, and Frederic A. Rasio. Illuminating Black Hole Binary Formation Channels with Spins in Advanced LIGO. *ApJL*, 832(1):L2, November 2016. doi: 10.3847/2041-8205/832/1/L2.
- [98] Michela Mapelli, Marco Dall’Amico, Yann Bouffanais, Nicola Giacobbo, Manuel Arca Sedda, M. Celeste Artale, Alessandro Ballone, Ugo N. Di Carlo, Giuliano Iorio, Filippo Santoliquido, and Stefano Torniamenti. Hierarchical black hole mergers in young, globular and nuclear star clusters: the effect of metallicity, spin and cluster properties. *MNRAS*, 505(1):339–358, July 2021. doi: 10.1093/mnras/stab1334.

- [99] Sambaran Banerjee, Aleksandra Olejak, and Krzysztof Belczynski. Symmetry breaking in merging binary black holes from young massive clusters and isolated binaries. *arXiv e-prints*, art. arXiv:2302.10851, February 2023. doi: 10.48550/arXiv.2302.10851.
- [100] Michael Zevin, Simone S. Bavera, Christopher P. L. Berry, Vicky Kalogera, Tassos Fragos, Pablo Marchant, Carl L. Rodriguez, Fabio Antonini, Daniel E. Holz, and Chris Pankow. One Channel to Rule Them All? Constraining the Origins of Binary Black Holes Using Multiple Formation Pathways. *ApJ*, 910(2):152, April 2021. doi: 10.3847/1538-4357/abe40e.
- [101] P. C. Peters. Gravitational radiation and the motion of two point masses. *Phys. Rev.*, 136: B1224–B1232, Nov 1964. doi: 10.1103/PhysRev.136.B1224. URL <https://link.aps.org/doi/10.1103/PhysRev.136.B1224>.
- [102] R. O’Shaughnessy, V. Kalogera, and Krzysztof Belczynski. Binary Compact Object Coalescence Rates: The Role of Elliptical Galaxies. *ApJ*, 716(1):615–633, June 2010. doi: 10.1088/0004-637X/716/1/615.
- [103] Michela Mapelli and Nicola Giacobbo. The cosmic merger rate of neutron stars and black holes. *MNRAS*, 479(4):4391–4398, October 2018. doi: 10.1093/mnras/sty1613.
- [104] Carl L. Rodriguez and Abraham Loeb. Redshift Evolution of the Black Hole Merger Rate from Globular Clusters. *ApJL*, 866(1):L5, October 2018. doi: 10.3847/2041-8213/aee377.
- [105] Fabio Antonini and Mark Gieles. Merger rate of black hole binaries from globular clusters: Theoretical error bars and comparison to gravitational wave data from GWTC-2. *Phys. Rev. D*, 102(12):123016, December 2020. doi: 10.1103/PhysRevD.102.123016.
- [106] A. Olejak, K. Belczynski, and N. Ivanova. Impact of common envelope development criteria on the formation of LIGO/Virgo sources. *A&A*, 651:A100, July 2021. doi: 10.1051/0004-6361/202140520.
- [107] L. A. C. van Son, S. E. de Mink, T. Callister, S. Justham, M. Renzo, T. Wagg, F. S. Broekgaarden, F. Kummer, R. Pakmor, and I. Mandel. The Redshift Evolution of the Binary Black Hole Merger Rate: A Weighty Matter. *ApJ*, 931(1):17, May 2022. doi: 10.3847/1538-4357/ac64a3.
- [108] J. R. Bond and B. J. Carr. Gravitational waves from a population of binary black holes. *MNRAS*, 207:585–609, April 1984. doi: 10.1093/mnras/207.3.585.
- [109] A. V. Tutukov and L. R. Yungelson. The merger rate of neutron star and black hole binaries. *MNRAS*, 260:675–678, February 1993. doi: 10.1093/mnras/260.3.675.
- [110] V. M. Lipunov, K. A. Postnov, and M. E. Prokhorov. Black holes and gravitational waves: Possibilities for simultaneous detection using first-generation laser interferometers. *Astronomy Letters*, 23:492–497, July 1997.
- [111] R. Voss and T. M. Tauris. Galactic distribution of merging neutron stars and black holes - prospects for short gamma-ray burst progenitors and LIGO/VIRGO. *MNRAS*, 342:1169–1184, July 2003. doi: 10.1046/j.1365-8711.2003.06616.x.
- [112] K. Belczynski, M. Dominik, T. Bulik, R. O’Shaughnessy, C. L. Fryer, and D. E. Holz. The effect of metallicity on the detection prospects for gravitational waves. *ApJL*, 715: L138–L141, June 2010. doi: 10.1088/2041-8205/715/2/L138.

- [113] M. Dominik, K. Belczynski, C. Fryer, D. Holz, B. Berti, T. Bulik, I. Mandel, and R. O’Shaughnessy. Double compact objects I: The significance of the common envelope on merger rates. *ApJ*, 759:52, November 2012.
- [114] T. Kinugawa, K. Inayoshi, K. Hotokezaka, D. Nakauchi, and T. Nakamura. Possible indirect confirmation of the existence of Pop III massive stars by gravitational wave. *MNRAS*, 442:2963–2992, August 2014. doi: 10.1093/mnras/stu1022.
- [115] T. Hartwig, M. Volonteri, V. Bromm, R. S. Klessen, E. Barausse, M. Magg, and A. Stacy. Gravitational waves from the remnants of the first stars. *MNRAS*, 460:L74–L78, July 2016. doi: 10.1093/mnrasl/slw074.
- [116] I. Mandel and S. E. de Mink. Merging binary black holes formed through chemically homogeneous evolution in short-period stellar binaries. *MNRAS*, 458:2634–2647, May 2016. doi: 10.1093/mnras/stw379.
- [117] M. Spera, N. Giacobbo, and M. Mapelli. Shedding light on the black hole mass spectrum. *Mem. Societa Astronomica Italiana*, 87:575, 2016.
- [118] K. Belczynski, D. E. Holz, T. Bulik, and R. O’Shaughnessy. The first gravitational-wave source from the isolated evolution of two stars in the 40-100 solar mass range. *Nature*, 534:512–515, June 2016. doi: 10.1038/nature18322.
- [119] J. J. Eldridge and E. R. Stanway. BPASS predictions for binary black hole mergers. *MNRAS*, 462:3302–3313, November 2016. doi: 10.1093/mnras/stw1772.
- [120] S. E. Woosley. The Progenitor of GW150914. *ApJL*, 824:L10, June 2016. doi: 10.3847/2041-8205/824/1/L10.
- [121] E. P. J. van den Heuvel, S. F. Portegies Zwart, and S. E. de Mink. Forming short-period Wolf-Rayet X-ray binaries and double black holes through stable mass transfer. *MNRAS*, 471:4256–4264, November 2017. doi: 10.1093/mnras/stx1430.
- [122] S. Stevenson, A. Vigna-Gómez, I. Mandel, J. W. Barrett, C. J. Neijssel, D. Perkins, and S. E. de Mink. Formation of the first three gravitational-wave observations through isolated binary evolution. *Nature Communications*, 8:14906, April 2017. doi: 10.1038/ncomms14906.
- [123] Matthias U. Kruckow, Thomas M. Tauris, Norbert Langer, Michael Kramer, and Robert G. Izzard. Progenitors of gravitational wave mergers: binary evolution with the stellar grid-based code COMBINE. *MNRAS*, 481(2):1908–1949, December 2018. doi: 10.1093/mnras/sty2190.
- [124] R. Hainich, L. M. Oskinova, T. Shenar, P. Marchant, J. J. Eldridge, A. A. C. Sander, W.-R. Hamann, N. Langer, and H. Todt. Observational properties of massive black hole binary progenitors. *A&A*, 609:A94, January 2018. doi: 10.1051/0004-6361/201731449.
- [125] P. Marchant, M. Renzo, R. Farmer, K. M. W. Pappas, R. E. Taam, S. de Mink, and V. Kalogera. Pulsational pair-instability supernovae in very close binaries. *arXiv e-prints*, October 2018.
- [126] M. Spera, M. Mapelli, N. Giacobbo, A. A. Trani, A. Bressan, and G. Costa. Merging black hole binaries with the SEVN code. *MNRAS*, 485:889–907, May 2019. doi: 10.1093/mnras/stz359.

- [127] Coenraad J. Neijssel, Alejandro Vigna-Gómez, Simon Stevenson, Jim W. Barrett, Sebastian M. Gaebel, Floor S. Broekgaarden, Selma E. de Mink, Dorottya Szécsi, Serena Vinciguerra, and Ilya Mandel. The effect of the metallicity-specific star formation history on double compact object mergers. *MNRAS*, 490(3):3740–3759, December 2019. doi: 10.1093/mnras/stz2840.
- [128] Simone S. Bavera, Tassos Fragos, Michael Zevin, Christopher P. L. Berry, Pablo Marchant, Jeff J. Andrews, Scott Coughlin, Aaron Dotter, Konstantinos Kovelakas, Devina Misra, Juan G. Serra-Perez, Ying Qin, Kyle A. Rocha, Jaime Román-Garza, Nam H. Tran, and Emmanouil Zapartas. The impact of mass-transfer physics on the observable properties of field binary black hole populations. *A&A*, 647:A153, March 2021. doi: 10.1051/0004-6361/202039804.
- [129] Ying Qin, Yuan-Zhu Wang, Dong-Hong Wu, Georges Meynet, and Hanfeng Song. On the Angular Momentum Transport Efficiency within the Star Constrained from Gravitational-wave Observations. *arXiv e-prints*, art. arXiv:2108.04821, August 2021.
- [130] Krzysztof Belczynski, Zoheyr Doctor, Michael Zevin, Aleksandra Olejak, Sambaran Banerje, and Debatri Chattopadhyay. Black Hole-Black Hole Total Merger Mass and the Origin of LIGO/Virgo Sources. *ApJ*, 935(2):126, August 2022. doi: 10.3847/1538-4357/ac8167.
- [131] K. Pavlovskii, N. Ivanova, K. Belczynski, and K. X. Van. Stability of mass transfer from massive giants: double black hole binary formation and ultraluminous X-ray sources. *MNRAS*, 465:2092–2100, February 2017. doi: 10.1093/mnras/stw2786.
- [132] Pablo Marchant, Kaliröe M. W. Pappas, Monica Gallegos-Garcia, Christopher P. L. Berry, Ronald E. Taam, Vicky Kalogera, and Philipp Podsiadlowski. The role of mass transfer and common envelope evolution in the formation of merging binary black holes. *A&A*, 650:A107, June 2021. doi: 10.1051/0004-6361/202039992.
- [133] Monica Gallegos-Garcia, Christopher P. L. Berry, Pablo Marchant, and Vicky Kalogera. Binary Black Hole Formation with Detailed Modeling: Stable Mass Transfer Leads to Lower Merger Rates. *ApJ*, 922(2):110, December 2021. doi: 10.3847/1538-4357/ac2610.
- [134] Yong Shao and Xiang-Dong Li. Population Synthesis of Black Hole Binaries with Compact Star Companions. *arXiv e-prints*, art. arXiv:2107.03565, July 2021.
- [135] Jakub Klencki, Gijs Nelemans, Alina G. Istrate, and Martyna Chruslinska. It has to be cool: Supergiant progenitors of binary black hole mergers from common-envelope evolution. *A&A*, 645:A54, January 2021. doi: 10.1051/0004-6361/202038707.
- [136] Andris Dorozsmai and Silvia Toonen. Importance of stable mass transfer and stellar winds for the formation of gravitational wave sources. *arXiv e-prints*, art. arXiv:2207.08837, July 2022. doi: 10.48550/arXiv.2207.08837.
- [137] M. M. Briel, H. F. Stevance, and J. J. Eldridge. Understanding the high-mass binary black hole population from stable mass transfer and super-Eddington accretion in BPASS. *MNRAS*, 520(4):5724–5745, April 2023. doi: 10.1093/mnras/stad399.
- [138] S. E. de Mink, M. Cantiello, N. Langer, O. R. Pols, I. Brott, and S. Ch. Yoon. Rotational mixing in massive binaries. Detached short-period systems. *A&A*, 497(1):243–253, April 2009. doi: 10.1051/0004-6361/200811439.

- [139] S. E. de Mink, M. Cantiello, N. Langer, and O. R. Pols. Chemically Homogeneous Evolution in Massive Binaries. In Vicky Kalogera and Marc van der Sluys, editors, *International Conference on Binaries: in celebration of Ron Webbink's 65th Birthday*, volume 1314 of *American Institute of Physics Conference Series*, pages 291–296, December 2010. doi: 10.1063/1.3536387.
- [140] P. Marchant, N. Langer, P. Podsiadlowski, T. M. Tauris, and T. J. Moriya. A new route towards merging massive black holes. *A&A*, 588:A50, April 2016. doi: 10.1051/0004-6361/201628133.
- [141] S. E. de Mink and I. Mandel. The chemically homogeneous evolutionary channel for binary black hole mergers: rates and properties of gravitational-wave events detectable by advanced LIGO. *MNRAS*, 460:3545–3553, August 2016. doi: 10.1093/mnras/stw1219.
- [142] Ilya Mandel and Selma E. de Mink. Merging binary black holes formed through chemically homogeneous evolution in short-period stellar binaries. *MNRAS*, 458(3):2634–2647, May 2016. doi: 10.1093/mnras/stw379.
- [143] Jeff Riley, Ilya Mandel, Pablo Marchant, Ellen Butler, Kaila Nathaniel, Coenraad Neijssel, Spencer Shortt, and Alejandro Vigna-Gómez. Chemically homogeneous evolution: a rapid population synthesis approach. *MNRAS*, 505(1):663–676, July 2021. doi: 10.1093/mnras/stab1291.
- [144] A. Maeder. Evidences for a bifurcation in massive star evolution. The ON-blue stragglers. *A&A*, 178:159–169, May 1987.
- [145] C. A. Nelson and P. P. Eggleton. A Complete Survey of Case A Binary Evolution with Comparison to Observed Algol-type Systems. *ApJ*, 552(2):664–678, May 2001. doi: 10.1086/320560.
- [146] Simon F. Portegies Zwart and Stephen L. W. McMillan. Black Hole Mergers in the Universe. *ApJL*, 528(1):L17–L20, Jan 2000. doi: 10.1086/312422.
- [147] M. C. Miller and D. P. Hamilton. Production of intermediate-mass black holes in globular clusters. *MNRAS*, 330:232–240, February 2002. doi: 10.1046/j.1365-8711.2002.05112.x.
- [148] M. C. Miller and D. P. Hamilton. Four-Body Effects in Globular Cluster Black Hole Coalescence. *ApJ*, 576:894–898, September 2002. doi: 10.1086/341788.
- [149] S. F. Portegies Zwart, H. Baumgardt, P. Hut, J. Makino, and S. L. W. McMillan. Formation of massive black holes through runaway collisions in dense young star clusters. *Nature*, 428:724–726, April 2004. doi: 10.1038/nature02448.
- [150] K. Gültekin, M. C. Miller, and D. P. Hamilton. Growth of Intermediate-Mass Black Holes in Globular Clusters. *ApJ*, 616:221–230, November 2004. doi: 10.1086/424809.
- [151] K. Gültekin, M. C. Miller, and D. P. Hamilton. Three-Body Dynamics with Gravitational Wave Emission. *ApJ*, 640:156–166, March 2006. doi: 10.1086/499917.
- [152] R. M. O’Leary, R. O’Shaughnessy, and F. A. Rasio. Dynamical interactions and the black-hole merger rate of the Universe. *Phys. Rev. D*, 76(6):061504, September 2007. doi: 10.1103/PhysRevD.76.061504.

- [153] A. Sadowski, K. Belczynski, T. Bulik, N. Ivanova, F. A. Rasio, and R. O’Shaughnessy. The Total Merger Rate of Compact Object Binaries in the Local Universe. *ApJ*, 676: 1162-1169, April 2008. doi: 10.1086/528932.
- [154] M. J. Benacquista and J. M. B. Downing. Relativistic Binaries in Globular Clusters. *Living Reviews in Relativity*, 16:4, March 2013. doi: 10.12942/lrr-2013-4.
- [155] N. Mennekens and D. Vanbeveren. Massive double compact object mergers: gravitational wave sources and r-process element production sites. *A&A*, 564:A134, April 2014. doi: 10.1051/0004-6361/201322198.
- [156] Y.-B. Bae, C. Kim, and H. M. Lee. Compact binaries ejected from globular clusters as gravitational wave sources. *MNRAS*, 440:2714–2725, May 2014. doi: 10.1093/mnras/stu381.
- [157] Sourav Chatterjee, Carl L. Rodriguez, Vicky Kalogera, and Frederic A. Rasio. Dynamical Formation of Low-mass Merging Black Hole Binaries like GW151226. *ApJL*, 836 (2):L26, February 2017. doi: 10.3847/2041-8213/aa5caa.
- [158] M. Mapelli. Massive black hole binaries from runaway collisions: the impact of metallicity. *MNRAS*, 459:3432–3446, July 2016. doi: 10.1093/mnras/stw869.
- [159] J. R. Hurley, A. C. Sippel, C. A. Tout, and S. J. Aarseth. A Dynamical Gravitational Wave Source in a Dense Cluster. *MNRAS*, 33:e036, August 2016. doi: 10.1017/pasa.2016.30.
- [160] C. L. Rodriguez, C.-J. Haster, S. Chatterjee, V. Kalogera, and F. A. Rasio. Dynamical Formation of the GW150914 Binary Black Hole. *ApJL*, 824:L8, June 2016. doi: 10.3847/2041-8205/824/1/L8.
- [161] J. H. VanLandingham, M. C. Miller, D. P. Hamilton, and D. C. Richardson. The Role of the Kozai–Lidov Mechanism in Black Hole Binary Mergers in Galactic Centers. *ApJ*, 828:77, September 2016. doi: 10.3847/0004-637X/828/2/77.
- [162] A. Askar, M. Szkudlarek, D. Gondek-Rosińska, M. Giersz, and T. Bulik. MOCCA-SURVEY Database - I. Coalescing binary black holes originating from globular clusters. *MNRAS*, 464:L36–L40, January 2017. doi: 10.1093/mnras/slw177.
- [163] M. Arca-Sedda and R. Capuzzo-Dolcetta. The MEGaN project II. Gravitational waves from intermediate-mass and binary black holes around a supermassive black hole. *MNRAS*, 483(1):152–171, February 2019. doi: 10.1093/mnras/sty3096.
- [164] J. Samsing. Eccentric Black Hole Mergers Forming in Stellar Clusters. *ArXiv e-prints*, November 2017.
- [165] Jakub Morawski, M. Giersz, A. Askar, and K. Belczynski. MOCCA-SURVEY Database I: Assessing GW kick retention fractions for BH-BH mergers in globular clusters. *MNRAS*, 481(2):2168–2179, December 2018. doi: 10.1093/mnras/sty2401.
- [166] S. Banerjee. Stellar-mass black holes in young massive and open stellar clusters and their role in gravitational-wave generation - II. *MNRAS*, 473:909–926, January 2018. doi: 10.1093/mnras/stx2347.
- [167] Ugo N. Di Carlo, Nicola Giacobbo, Michela Mapelli, Mario Pasquato, Mario Spera, Long Wang, and Francesco Haardt. Merging black holes in young star clusters. *MNRAS*, 487(2):2947–2960, August 2019. doi: 10.1093/mnras/stz1453.

- [168] M. Zevin, J. Samsing, C. Rodriguez, C.-J. Haster, and E. Ramirez-Ruiz. Eccentric Black Hole Mergers in Dense Star Clusters: The Role of Binary Binary Encounters. *ApJ*, 871: 91, January 2019. doi: 10.3847/1538-4357/aaf6ec.
- [169] C. L. Rodriguez, P. Amaro-Seoane, S. Chatterjee, K. Kremer, F. A. Rasio, J. Samsing, C. S. Ye, and M. Zevin. Post-Newtonian dynamics in dense star clusters: Formation, masses, and merger rates of highly-eccentric black hole binaries. *Phys. Rev. D*, 98(12): 123005, December 2018. doi: 10.1103/PhysRevD.98.123005.
- [170] R. Perna, Y.-H. Wang, W. M. Farr, N. Leigh, and M. Cantiello. Constraining the Black Hole Initial Mass Function with LIGO/Virgo Observations. *ApJL*, 878:L1, June 2019. doi: 10.3847/2041-8213/ab2336.
- [171] Kyle Kremer, Claire S. Ye, Nicholas Z. Rui, Newlin C. Weatherford, Sourav Chatterjee, Giacomo Fragione, Carl L. Rodriguez, Mario Spera, and Frederic A. Rasio. Modeling Dense Star Clusters in the Milky Way and Beyond with the CMC Cluster Catalog. *ApJS*, 247(2):48, April 2020. doi: 10.3847/1538-4365/ab7919.
- [172] Fabio Antonini, Mark Gieles, Fani Dosopoulou, and Debatri Chattopadhyay. Coalescing black hole binaries from globular clusters: mass distributions and comparison to gravitational wave data from GWTC-3. *MNRAS*, 522(1):466–476, 03 2023. ISSN 0035-8711. doi: 10.1093/mnras/stad972. URL <https://doi.org/10.1093/mnras/stad972>.
- [173] D. C. Heggie. Binary evolution in stellar dynamics. *MNRAS*, 173:729–787, December 1975. doi: 10.1093/mnras/173.3.729.
- [174] Lyman Spitzer. *Dynamical evolution of globular clusters*. 1987.
- [175] J. M. B. Downing, M. J. Benacquista, M. Giersz, and R. Spurzem. Compact binaries in star clusters - I. Black hole binaries inside globular clusters. *MNRAS*, 407:1946–1962, September 2010. doi: 10.1111/j.1365-2966.2010.17040.x.
- [176] Alan P. Lightman and Stuart L. Shapiro. The dynamical evolution of globular clusters. *Reviews of Modern Physics*, 50(2):437–481, April 1978. doi: 10.1103/RevModPhys.50.437.
- [177] Hideaki Mouri and Yoshiaki Taniguchi. Runaway Merging of Black Holes: Analytical Constraint on the Timescale. *ApJL*, 566(1):L17–L20, February 2002. doi: 10.1086/339472.
- [178] Giacomo Fragione, Bence Kocsis, Frederic A. Rasio, and Joseph Silk. Repeated Mergers, Mass-gap Black Holes, and Formation of Intermediate-mass Black Holes in Dense Massive Star Clusters. *ApJ*, 927(2):231, March 2022. doi: 10.3847/1538-4357/ac5026.
- [179] Kyle Kremer, Mario Spera, Devin Becker, Sourav Chatterjee, Ugo N. Di Carlo, Giacomo Fragione, Carl L. Rodriguez, Claire S. Ye, and Frederic A. Rasio. Populating the Upper Black Hole Mass Gap through Stellar Collisions in Young Star Clusters. *ApJ*, 903(1):45, November 2020. doi: 10.3847/1538-4357/abb945.
- [180] H Baumgardt, C He, S M Sweet, M Drinkwater, A Sollima, J Hurley, C Usher, S Kamann, H Dalglish, S Dreizler, and T-O Husser. No evidence for intermediate-mass black holes in the globular clusters ω Cen and NGC 6624. *MNRAS*, 488(4):5340–5351, 07 2019. ISSN 0035-8711. doi: 10.1093/mnras/stz2060. URL <https://doi.org/10.1093/mnras/stz2060>.

- [181] H. Sana, J. B. Le Bouquin, S. Lacour, J. P. Berger, G. Duvert, L. Gauchet, B. Norris, J. Olofsson, D. Pickel, G. Zins, O. Absil, A. de Koter, K. Kratter, O. Schnurr, and H. Zinnecker. Southern Massive Stars at High Angular Resolution: Observational Campaign and Companion Detection. *ApJS*, 215(1):15, November 2014. doi: 10.1088/0067-0049/215/1/15.
- [182] H. Sana, S. E. de Mink, A. de Koter, N. Langer, C. J. Evans, M. Gieles, E. Gosset, R. G. Izzard, J.-B. Le Bouquin, and F. R. N. Schneider. Binary Interaction Dominates the Evolution of Massive Stars. *Science*, 337:444–, July 2012. doi: 10.1126/science.1223344.
- [183] Maxwell Moe and Rosanne Di Stefano. Mind Your Ps and Qs: The Interrelation between Period (P) and Mass-ratio (Q) Distributions of Binary Stars. *ApJS*, 230(2):15, June 2017. doi: 10.3847/1538-4365/aa6fb6.
- [184] Tokovinin, A. A. Msc - a catalogue of physical multiple stars*. *Astron. Astrophys. Suppl. Ser.*, 124(1):75–84, 1997. doi: 10.1051/aas:1997181. URL <https://doi.org/10.1051/aas:1997181>.
- [185] L. G. Kiseleva, P. P. Eggleton, and J. P. Anosova. A note on the stability of hierarchical triple stars with initially circular orbits. *MNRAS*, 267(1):161–166, 03 1994. ISSN 0035-8711. doi: 10.1093/mnras/267.1.161. URL <https://doi.org/10.1093/mnras/267.1.161>.
- [186] M. L. Lidov. The evolution of orbits of artificial satellites of planets under the action of gravitational perturbations of external bodies. *P&SS*, 9(10):719–759, October 1962. doi: 10.1016/0032-0633(62)90129-0.
- [187] Yoshihide Kozai. Secular perturbations of asteroids with high inclination and eccentricity. *AJ*, 67:591–598, November 1962. doi: 10.1086/108790.
- [188] Fabio Antonini, Silvia Toonen, and Adrian S. Hamers. Binary Black Hole Mergers from Field Triples: Properties, Rates, and the Impact of Stellar Evolution. *ApJ*, 841(2):77, June 2017. doi: 10.3847/1538-4357/aa6f5e.
- [189] Kedron Silsbee and Scott Tremaine. Lidov-Kozai Cycles with Gravitational Radiation: Merging Black Holes in Isolated Triple Systems. *ApJ*, 836(1):39, February 2017. doi: 10.3847/1538-4357/aa5729.
- [190] Manuel Arca Sedda, Gongjie Li, and Bence Kocsis. Order in the chaos. Eccentric black hole binary mergers in triples formed via strong binary-binary scatterings. *A&A*, 650:A189, June 2021. doi: 10.1051/0004-6361/202038795.
- [191] Bin Liu and Dong Lai. Black Hole and Neutron Star Binary Mergers in Triple Systems: Merger Fraction and Spin-Orbit Misalignment. *ApJ*, 863(1):68, August 2018. doi: 10.3847/1538-4357/aad09f.
- [192] Giacomo Fragione and Bence Kocsis. Black hole mergers from quadruples. *MNRAS*, 486(4):4781–4789, July 2019. doi: 10.1093/mnras/stz1175.
- [193] S. Toonen, S. Portegies Zwart, A. S. Hamers, and D. Bandopadhyay. The evolution of stellar triples. The most common evolutionary pathways. *A&A*, 640:A16, August 2020. doi: 10.1051/0004-6361/201936835.

- [194] Alejandro Vigna-Gómez, Silvia Toonen, Enrico Ramirez-Ruiz, Nathan W. C. Leigh, Jeff Riley, and Carl-Johan Haster. Massive Stellar Triples Leading to Sequential Binary Black Hole Mergers in the Field. *ApJL*, 907(1):L19, January 2021. doi: 10.3847/2041-8213/abd5b7.
- [195] Jakob Stegmann, Fabio Antonini, and Maxwell Moe. Evolution of massive stellar triples and implications for compact object binary formation. *MNRAS*, 516(1):1406–1427, October 2022. doi: 10.1093/mnras/stac2192.
- [196] F. Antonini and H. B. Perets. Secular Evolution of Compact Binaries near Massive Black Holes: Gravitational Wave Sources and Other Exotica. *ApJ*, 757:27, September 2012. doi: 10.1088/0004-637X/757/1/27.
- [197] Giacomo Fragione, Evgeni Grishin, Nathan W. C. Leigh, Hagai B. Perets, and Rosalba Perna. Black hole and neutron star mergers in galactic nuclei. *MNRAS*, 488(1):47–63, September 2019. doi: 10.1093/mnras/stz1651.
- [198] Amy Secunda, Jillian Bellovary, Mordecai-Mark Mac Low, K. E. Saavik Ford, Barry McKernan, Nathan W. C. Leigh, Wladimir Lyra, and Zsolt Sándor. Orbital Migration of Interacting Stellar Mass Black Holes in Disks around Supermassive Black Holes. *ApJ*, 878(2):85, June 2019. doi: 10.3847/1538-4357/ab20ca.
- [199] Fabio Antonini and David Merritt. Dynamical Friction around Supermassive Black Holes. *ApJ*, 745(1):83, January 2012. doi: 10.1088/0004-637X/745/1/83.
- [200] Adrian S. Hamers, Ben Bar-Or, Cristobal Petrovich, and Fabio Antonini. The Impact of Vector Resonant Relaxation on the Evolution of Binaries near a Massive Black Hole: Implications for Gravitational-wave Sources. *ApJ*, 865(1):2, September 2018. doi: 10.3847/1538-4357/aadae2.
- [201] Bao-Minh Hoang, Smadar Naoz, Bence Kocsis, Frederic A. Rasio, and Fani Dosopoulou. Black Hole Mergers in Galactic Nuclei Induced by the Eccentric Kozai-Lidov Effect. *ApJ*, 856(2):140, April 2018. doi: 10.3847/1538-4357/aaafce.
- [202] A. Heger and S. E. Woosley. The nucleosynthetic signature of population iii. *The Astrophysical Journal*, 567(1):532, mar 2002. doi: 10.1086/338487. URL <https://dx.doi.org/10.1086/338487>.
- [203] David Sobral, Jorrit Matthee, Behnam Darvish, Daniel Schaerer, Bahram Mobasher, Huub J. A. Röttgering, Sérgio Santos, and Shoubaneh Hemmati. Evidence for PopIII-like Stellar Populations in the Most Luminous Lyman- α Emitters at the Epoch of Reionization: Spectroscopic Confirmation. *ApJ*, 808(2):139, August 2015. doi: 10.1088/0004-637X/808/2/139.
- [204] Nozomu Tominaga, Hideyuki Umeda, and Ken’ichi Nomoto. Supernova Nucleosynthesis in Population III 13-50 M_{Solar} Stars and Abundance Patterns of Extremely Metal-poor Stars. *ApJ*, 660(1):516–540, May 2007. doi: 10.1086/513063.
- [205] Keith A. Olive and David Thomas. Generalized limits to the number of light particle degrees of freedom from big bang nucleosynthesis. *Astroparticle Physics*, 11(4):403–411, September 1999. doi: 10.1016/S0927-6505(99)00009-2.
- [206] P. Marigo, L. Girardi, C. Chiosi, and P. R. Wood. Zero-metallicity stars. I. Evolution at constant mass. *A&A*, 371:152–173, May 2001. doi: 10.1051/0004-6361:20010309.

- [207] S. C. Yoon, A. Dierks, and N. Langer. Evolution of massive Population III stars with rotation and magnetic fields. *A&A*, 542:A113, June 2012. doi: 10.1051/0004-6361/201117769.
- [208] Tomoya Kinugawa, Takashi Nakamura, and Hiroyuki Nakano. Formation of binary black holes similar to GW190521 with a total mass of $\sim 150 M_{\odot}$ from Population III binary star evolution. *MNRAS*, 501(1):L49–L53, February 2021. doi: 10.1093/mnras/slaa191.
- [209] Yuzuru Yoshii, Hiroaki Sameshima, Takuji Tsujimoto, Toshikazu Shigeyama, Timothy C. Beers, and Bruce A. Peterson. Potential signature of population iii pair-instability supernova ejecta in the blr gas of the most distant quasar at $z = 7.54^*$. *AJ*, 937(2):61, sep 2022. doi: 10.3847/1538-4357/ac8163. URL <https://dx.doi.org/10.3847/1538-4357/ac8163>.
- [210] Krzysztof Belczynski, Taeho Ryu, Rosalba Perna, Emanuele Berti, Takamitsu L. Tanaka, and Tomasz Bulik. On the likelihood of detecting gravitational waves from Population III compact object binaries. *MNRAS*, 471(4):4702–4721, November 2017. doi: 10.1093/mnras/stx1759.
- [211] Ataru Tanikawa, Takashi Yoshida, Tomoya Kinugawa, Alessandro A. Trani, Takashi Hosokawa, Hajime Susa, and Kazuyuki Omukai. Merger Rate Density of Binary Black Holes through Isolated Population I, II, III and Extremely Metal-poor Binary Star Evolution. *ApJ*, 926(1):83, February 2022. doi: 10.3847/1538-4357/ac4247.
- [212] Taeho Ryu, Takamitsu L. Tanaka, and Rosalba Perna. Formation, disruption and energy output of Population III X-ray binaries. *MNRAS*, 456(1):223–238, February 2016. doi: 10.1093/mnras/stv2629.
- [213] LIGO Scientific Collaboration et al. and J Harms. Exploring the sensitivity of next generation gravitational wave detectors. *Classical and Quantum Gravity*, 34(4):044001, jan 2017. doi: 10.1088/1361-6382/aa51f4. URL <https://dx.doi.org/10.1088/1361-6382/aa51f4>.
- [214] Neha Singh, Tomasz Bulik, Krzysztof Belczynski, and Abbas Askar. Exploring compact binary populations with the Einstein Telescope. *A&A*, 667:A2, November 2022. doi: 10.1051/0004-6361/202142856.
- [215] Ya. B. Zel’dovich and I. D. Novikov. The Hypothesis of Cores Retarded during Expansion and the Hot Cosmological Model. *Soviet Astronomy*, 10:602, February 1967.
- [216] S. W. Hawking. Black hole explosions? *Nature*, 248(5443):30–31, March 1974. doi: 10.1038/248030a0.
- [217] G. F. Chapline. Cosmological effects of primordial black holes. *Nature*, 253(5489):251–252, January 1975. doi: 10.1038/253251a0.
- [218] Bernard Carr and Florian Kühnel. Primordial Black Holes as Dark Matter: Recent Developments. *Annual Review of Nuclear and Particle Science*, 70:355–394, October 2020. doi: 10.1146/annurev-nucl-050520-125911.
- [219] Anne M Green and Bradley J Kavanagh. Primordial black holes as a dark matter candidate. *Journal of Physics G: Nuclear and Particle Physics*, 48(4):043001, feb 2021. doi: 10.1088/1361-6471/abc534. URL <https://dx.doi.org/10.1088/1361-6471/abc534>.

- [220] Guillem Domènech, Chunshan Lin, and Misao Sasaki. Gravitational wave constraints on the primordial black hole dominated early universe. *Journal of Cosmology and Astroparticle Physics*, 2021(04):062, apr 2021. doi: 10.1088/1475-7516/2021/04/062. URL <https://dx.doi.org/10.1088/1475-7516/2021/04/062>.
- [221] B. J. Carr, Kazunori Kohri, Yuuiti Sendouda, and Jun’Ichi Yokoyama. New cosmological constraints on primordial black holes. *Phys. Rev. D*, 81(10):104019, May 2010. doi: 10.1103/PhysRevD.81.104019.
- [222] Bernard Carr, Kazunori Kohri, Yuuiti Sendouda, and Jun’ichi Yokoyama. Constraints on primordial black holes. *Reports on Progress in Physics*, 84(11):116902, November 2021. doi: 10.1088/1361-6633/ac1e31.
- [223] Oscar Barco. Primordial black hole origin for thermal gamma-ray bursts. *MNRAS*, 506(1):806–812, 06 2021. ISSN 0035-8711. doi: 10.1093/mnras/stab1747. URL <https://doi.org/10.1093/mnras/stab1747>.
- [224] Simeon Bird, Ilias Cholis, Julian B. Muñoz, Yacine Ali-Haïmoud, Marc Kamionkowski, Ely D. Kovetz, Alvise Raccanelli, and Adam G. Riess. Did ligo detect dark matter? *Phys. Rev. Lett.*, 116:201301, May 2016. doi: 10.1103/PhysRevLett.116.201301. URL <https://link.aps.org/doi/10.1103/PhysRevLett.116.201301>.
- [225] Misao Sasaki, Teruaki Suyama, Takahiro Tanaka, and Shuichiro Yokoyama. Primordial Black Hole Scenario for the Gravitational-Wave Event GW150914. *Phys. Rev. Lett.*, 117(6):061101, August 2016. doi: 10.1103/PhysRevLett.117.061101.
- [226] A. M Green. Astrophysical uncertainties on stellar microlensing constraints on multi-Solar mass primordial black hole dark matter. *ArXiv e-prints*, May 2017.
- [227] Sébastien Clesse and Juan García-Bellido. The clustering of massive Primordial Black Holes as Dark Matter: Measuring their mass distribution with advanced LIGO. *Physics of the Dark Universe*, 15:142–147, Mar 2017. doi: 10.1016/j.dark.2016.10.002.
- [228] Bernard Carr and Joseph Silk. Primordial black holes as generators of cosmic structures. *MNRAS*, 478(3):3756–3775, Aug 2018. doi: 10.1093/mnras/sty1204.
- [229] V. De Luca, V. Desjacques, G. Franciolini, P. Pani, and A. Riotto. GW190521 Mass Gap Event and the Primordial Black Hole Scenario. *Phys. Rev. Lett.*, 126(5):051101, February 2021. doi: 10.1103/PhysRevLett.126.051101.
- [230] Kaze W. K. Wong, Gabriele Franciolini, Valerio De Luca, Vishal Baibhav, Emanuele Berti, Paolo Pani, and Antonio Riotto. Constraining the primordial black hole scenario with bayesian inference and machine learning: The gwtc-2 gravitational wave catalog. *Phys. Rev. D*, 103:023026, Jan 2021. doi: 10.1103/PhysRevD.103.023026. URL <https://link.aps.org/doi/10.1103/PhysRevD.103.023026>.
- [231] LIGO Scientific Collaboration et al. Search for Subsolar-Mass Binaries in the First Half of Advanced LIGO’s and Advanced Virgo’s Third Observing Run. *PRL*, 129(6):061104, August 2022. doi: 10.1103/PhysRevLett.129.061104.
- [232] Krzysztof Belczynski, Vassiliki Kalogera, Frederic A. Rasio, Ronald E. Taam, Andreas Zezas, Tomasz Bulik, Thomas J. Maccarone, and Natalia Ivanova. Compact Object Modeling with the StarTrack Population Synthesis Code. *ApJS*, 174(1):223–260, January 2008. doi: 10.1086/521026.

- [233] A. Olejak, K. Belczynski, T. Bulik, and M. Sobolewska. Synthetic catalog of black holes in the Milky Way. *A&A*, 638:A94, June 2020. doi: 10.1051/0004-6361/201936557.
- [234] Piero Madau and Tassos Fragos. Radiation Backgrounds at Cosmic Dawn: X-Rays from Compact Binaries. *ApJ*, 840(1):39, May 2017. doi: 10.3847/1538-4357/aa6af9.
- [235] H. Jabran Zahid, Gabriel I. Dima, Rolf-Peter Kudritzki, Lisa J. Kewley, Margaret J. Geller, Ho Seong Hwang, John D. Silverman, and Daichi Kashino. The Universal Relation of Galactic Chemical Evolution: The Origin of the Mass-Metallicity Relation. *ApJ*, 791(2):130, August 2014. doi: 10.1088/0004-637X/791/2/130.
- [236] U. Kolb, A. R. King, and H. Ritter. The cataclysmic variable period gap: still there. *MNRAS*, 298(2):L29–L33, August 1998. doi: 10.1046/j.1365-8711.1998.01854.x.
- [237] Steve B. Howell, Lorne A. Nelson, and Saul Rappaport. An Exploration of the Paradigm for the 2-3 Hour Period Gap in Cataclysmic Variables. *ApJ*, 550(2):897–918, April 2001. doi: 10.1086/319776.
- [238] Jonas Goliašch and Lorne Nelson. Population Synthesis of Cataclysmic Variables. I. Inclusion of Detailed Nuclear Evolution. *ApJ*, 809(1):80, August 2015. doi: 10.1088/0004-637X/809/1/80.
- [239] A. V. Fedorova, A. V. Tutukov, and L. R. Yungelson. Type-Ia Supernovae in Semidetached Binaries. *Astronomy Letters*, 30:73–85, February 2004. doi: 10.1134/1.1646692.
- [240] A. G. Kuranov, K. A. Postnov, and M. E. Prokhorov. Formation of Low-Mass X-Ray Novae with Black Holes from Triple Systems. *Astronomy Reports*, 45(8):620–630, August 2001. doi: 10.1134/1.1388927.
- [241] Grzegorz Wiktorowicz, Małgorzata Sobolewska, Jean-Pierre Lasota, and Krzysztof Belczynski. The Origin of the Ultraluminous X-Ray Sources. *ApJ*, 846(1):17, September 2017. doi: 10.3847/1538-4357/aa821d.
- [242] Grzegorz Wiktorowicz, Jean-Pierre Lasota, Krzysztof Belczynski, Youjun Lu, Jifeng Liu, and Krystian Iłkiewicz. Wind-powered Ultraluminous X-ray Sources. *ApJ*, 918(2):60, September 2021. doi: 10.3847/1538-4357/ac0cf7.
- [243] Krzysztof Belczynski, Tomasz Bulik, and Bronisław Rudak. Study of Gamma-Ray Burst Binary Progenitors. *ApJ*, 571(1):394–412, May 2002. doi: 10.1086/339860.
- [244] Paulina Karczmarek, Radosław Smolec, Gergely Hajdu, Grzegorz Pietrzyński, Wolfgang Gieren, Weronika Narloch, Grzegorz Wiktorowicz, and Krzysztof Belczynski. Synthetic population of binary cepheids. i. the effect of metallicity and initial parameter distribution on characteristics of cepheids’ companions. *The Astrophysical Journal*, 930(1):65, may 2022. doi: 10.3847/1538-4357/ac6354. URL <https://dx.doi.org/10.3847/1538-4357/ac6354>.
- [245] S. B. Popov and M. E. Prokhorov. REVIEWS OF TOPICAL PROBLEMS: Population synthesis in astrophysics. *Physics Uspekhi*, 50(11):1123–1146, November 2007. doi: 10.1070/PU2007v050n11ABEH006179.
- [246] Jarrod R. Hurley, Onno R. Pols, and Christopher A. Tout. Comprehensive analytic formulae for stellar evolution as a function of mass and metallicity. *MNRAS*, 315(3):543–569, July 2000. doi: 10.1046/j.1365-8711.2000.03426.x.

- [247] Jarrod R. Hurley, Christopher A. Tout, and Onno R. Pols. Evolution of binary stars and the effect of tides on binary populations. *MNRAS*, 329(4):897–928, February 2002. doi: 10.1046/j.1365-8711.2002.05038.x.
- [248] K. Belczynski, A. Romagnolo, A. Olejak, J. Klencki, D. Chattopadhyay, S. Stevenson, M. Coleman Miller, J. P. Lasota, and Paul A. Crowther. The Uncertain Future of Massive Binaries Obscures the Origin of LIGO/Virgo Sources. *ApJ*, 925(1):69, January 2022. doi: 10.3847/1538-4357/ac375a.
- [249] Erin R. Higgins and Jorick S. Vink. Massive star evolution: rotation, winds, and overshooting vectors in the mass-luminosity plane. I. A calibrated grid of rotating single star models. *A&A*, 622:A50, February 2019. doi: 10.1051/0004-6361/201834123.
- [250] A. Schootemeijer, N. Langer, N. J. Grin, and C. Wang. Constraining mixing in massive stars in the Small Magellanic Cloud. *A&A*, 625:A132, May 2019. doi: 10.1051/0004-6361/201935046.
- [251] Simone S. Bavera, Michael Zevin, and Tassos Fragos. Approximations of the Spin of Close Black Hole-Wolf-Rayet Binaries. *Research Notes of the American Astronomical Society*, 5(5):127, May 2021. doi: 10.3847/2515-5172/ac053c.
- [252] A. Romagnolo, K. Belczynski, J. Klencki, P. Agrawal, T. Shenar, and D. Szécsi. The role of stellar expansion on the formation of gravitational wave sources. *arXiv e-prints*, art. arXiv:2211.15800, November 2022. doi: 10.48550/arXiv.2211.15800.
- [253] Carl L. Rodriguez, Kyle Kremer, Michael Y. Grudić, Zachary Hafen, Sourav Chatterjee, Giacomo Fragione, Astrid Lamberts, Miguel A. S. Martinez, Frederic A. Rasio, Newlin Weatherford, and Claire S. Ye. GW190412 as a Third-generation Black Hole Merger from a Super Star Cluster. *ApJ*, 896(1):L10, June 2020. doi: 10.3847/2041-8213/ab961d.
- [254] Adrian S. Hamers and Mohammadtaher Safarzadeh. Was GW190412 Born from a Hierarchical 3 + 1 Quadruple Configuration? *ApJ*, 898(2):99, August 2020. doi: 10.3847/1538-4357/ab9b27.
- [255] Davide Gerosa, Salvatore Vitale, and Emanuele Berti. Astrophysical Implications of GW190412 as a Remnant of a Previous Black-Hole Merger. *Phys. Rev. Lett.*, 125(10):101103, September 2020. doi: 10.1103/PhysRevLett.125.101103.
- [256] A. Olejak, M. Fishbach, K. Belczynski, D. E. Holz, J. P. Lasota, M. C. Miller, and T. Bulik. The Origin of Inequality: Isolated Formation of a 30+10 M Binary Black Hole Merger. *ApJL*, 901(2):L39, October 2020. doi: 10.3847/2041-8213/abb5b5.
- [257] B. Paczynski. Common Envelope Binaries. In Peter Eggleton, Simon Mitton, and John Whelan, editors, *Structure and Evolution of Close Binary Systems*, volume 73, page 75, January 1976.
- [258] R. F. Webbink. Double white dwarfs as progenitors of R Coronae Borealis stars and type I supernovae. *ApJ*, 277:355–360, February 1984. doi: 10.1086/161701.
- [259] N. Ivanova, S. Justham, X. Chen, O. De Marco, C. L. Fryer, E. Gaburov, H. Ge, E. Glebbeek, Z. Han, X. D. Li, G. Lu, T. Marsh, P. Podsiadlowski, A. Potter, N. Soker, R. Taam, T. M. Tauris, E. P. J. van den Heuvel, and R. F. Webbink. Common envelope evolution: where we stand and how we can move forward. *Astronomy and Astrophysics Reviews*, 21:59, February 2013. doi: 10.1007/s00159-013-0059-2.

- [260] Mario Livio and Noam Soker. The Common Envelope Phase in the Evolution of Binary Stars. *ApJ*, 329:764, Jun 1988. doi: 10.1086/166419.
- [261] Katelyn Breivik, Scott Coughlin, Michael Zevin, Carl L. Rodriguez, Kyle Kremer, Claire S. Ye, Jeff J. Andrews, Michael Kurkowski, Matthew C. Digman, Shane L. Larson, and Frederic A. Rasio. COSMIC Variance in Binary Population Synthesis. *ApJ*, 898(1):71, July 2020. doi: 10.3847/1538-4357/ab9d85.
- [262] H. C. Spruit. Differential rotation and magnetic fields in stellar interiors. *A&A*, 349:189–202, September 1999.
- [263] Christopher L. Fryer and Patrick A. Young. Late-Time Convection in the Collapse of a 23 M_{Solar} Star. *ApJ*, 659(2):1438–1448, April 2007. doi: 10.1086/513003.
- [264] C. Fröhlich, P. Hauser, M. Liebendörfer, G. Martínez-Pinedo, F. K. Thielemann, E. Bravo, N. T. Zinner, W. R. Hix, K. Langanke, A. Mezzacappa, and K. Nomoto. Composition of the Innermost Core-Collapse Supernova Ejecta. *ApJ*, 637(1):415–426, January 2006. doi: 10.1086/498224.
- [265] T. Fischer, S. C. Whitehouse, A. Mezzacappa, F. K. Thielemann, and M. Liebendörfer. Protoneutron star evolution and the neutrino-driven wind in general relativistic neutrino radiation hydrodynamics simulations. *A&A*, 517:A80, July 2010. doi: 10.1051/0004-6361/200913106.
- [266] Marcella Ugliano, Hans-Thomas Janka, Andreas Marek, and Almudena Arcones. Progenitor-explosion Connection and Remnant Birth Masses for Neutrino-driven Supernovae of Iron-core Progenitors. *ApJ*, 757(1):69, September 2012. doi: 10.1088/0004-637X/757/1/69.
- [267] A. Perego, M. Hempel, C. Fröhlich, K. Ebinger, M. Eichler, J. Casanova, M. Liebendörfer, and F. K. Thielemann. PUSHing Core-collapse Supernovae to Explosions in Spherical Symmetry I: the Model and the Case of SN 1987A. *ApJ*, 806(2):275, June 2015. doi: 10.1088/0004-637X/806/2/275.
- [268] Andrej Prša, Petr Harmanec, Guillermo Torres, Eric Mamajek, Martin Asplund, Nicole Capitaine, Jørgen Christensen-Dalsgaard, Éric Depagne, Margit Haberreiter, and Saskia Hekker. Nominal Values for Selected Solar and Planetary Quantities: IAU 2015 Resolution B3. *AJ*, 152(2):41, Aug 2016. doi: 10.3847/0004-6256/152/2/41.
- [269] T. Ertl, H. Th. Janka, S. E. Woosley, T. Sukhbold, and M. Ugliano. A Two-parameter Criterion for Classifying the Explodability of Massive Stars by the Neutrino-driven Mechanism. *ApJ*, 818(2):124, February 2016. doi: 10.3847/0004-637X/818/2/124.
- [270] Chris L. Fryer, Sydney Andrews, Wesley Even, Alex Heger, and Samar Safi-Harb. Parameterizing the Supernova Engine and Its Effect on Remnants and Basic Yields. *ApJ*, 856(1):63, March 2018. doi: 10.3847/1538-4357/aaaf6f.
- [271] Marc Herant, Willy Benz, W. Raphael Hix, Chris L. Fryer, and Stirling A. Colgate. Inside the Supernova: A Powerful Convective Engine. *ApJ*, 435:339, November 1994. doi: 10.1086/174817.
- [272] Sean M. Couch, MacKenzie L. Warren, and Evan P. O’Connor. Simulating Turbulence-aided Neutrino-driven Core-collapse Supernova Explosions in One Dimension. *ApJ*, 890(2):127, February 2020. doi: 10.3847/1538-4357/ab609e.

- [273] M Punturo, M Abernathy, F Acernese, B Allen, N Andersson, K Arun, F Barone, B Barr, M Barsuglia, M Beker, N Beveridge, S Birindelli, S Bose, L Bosi, S Braccini, C Bradaschia, T Bulik, E Calloni, G Cella, E Chassande Mottin, S Chelkowski, A Chincarini, J Clark, E Coccia, C Colacino, J Colas, A Cumming, L Cunningham, E Cuoco, S Danilishin, K Danzmann, G De Luca, R De Salvo, T Dent, R De Rosa, L Di Fiore, A Di Virgilio, M Doets, V Fafone, P Falferi, R Flaminio, J Franc, F Frasconi, A Freise, P Fulda, J Gair, G Gemme, A Gennai, A Giazotto, K Glampedakis, M Granata, H Grote, G Guidi, G Hammond, M Hannam, J Harms, D Heinert, M Hendry, I Heng, E Hennes, S Hild, J Hough, S Husa, S Huttner, G Jones, F Khalili, K Kokeyama, K Kokkotas, B Krishnan, M Lorenzini, H Lück, E Majorana, I Mandel, V Mandic, I Martin, C Michel, Y Minenkov, N Morgado, S Mosca, B Mours, H Müller–Eberhardt, P Murray, R Nawrodt, J Nelson, R Oshaughnessy, C D Ott, C Palomba, A Paoli, G Parguez, A Pasqualetti, R Passaquieti, D Passuello, L Pinard, R Poggiani, P Popolizio, M Prato, P Puppo, D Rabeling, P Rapagnani, J Read, T Regimbau, H Rehbein, S Reid, L Rezzolla, F Ricci, F Richard, A Rocchi, S Rowan, A Rüdiger, B Sassolas, B Sathyaprakash, R Schnabel, C Schwarz, P Seidel, A Sintes, K Somiya, F Speirits, K Strain, S Strigin, P Sutton, S Tarabrin, A Thüring, J van den Brand, C van Leewen, M van Veggel, C van den Broeck, A Vecchio, J Veitch, F Vetrano, A Vicere, S Vyatchanin, B Willke, G Woan, P Wolfango, and K Yamamoto. The einstein telescope: a third-generation gravitational wave observatory. *Classical and Quantum Gravity*, 27(19):194002, sep 2010. doi: 10.1088/0264-9381/27/19/194002. URL <https://dx.doi.org/10.1088/0264-9381/27/19/194002>.
- [274] The Ligo Scientific Collaboration et al. Prospects for observing and localizing gravitational-wave transients with Advanced LIGO, Advanced Virgo and KAGRA. *Living Reviews in Relativity*, 21(1):3, April 2018. doi: 10.1007/s41114-018-0012-9.
- [275] Karsten Danzmann and the LISA study team. Lisa: laser interferometer space antenna for gravitational wave measurements. *Classical and Quantum Gravity*, 13(11A):A247, nov 1996. doi: 10.1088/0264-9381/13/11A/033. URL <https://dx.doi.org/10.1088/0264-9381/13/11A/033>.